Study of Natural Ventilation in Buildings with Large Eddy Simulation

by

Yi Jiang

M.E. Mechanical Engineering
Washington State University, 1998

Submitted to the Department of Architecture
in partial fulfillment of the
requirements for the Degree of Doctor of Philosophy
in the field of Architecture: Building Technology

at the

Massachusetts Institute of Technology

June 2002

Signature of Author _____
Department of Architecture
May 3, 2002

Certified by _____
Qingyan Chen
Associate Professor of Building Technology
Thesis supervisor

Accepted by _____
Stanford Anderson
Head, Department of Architecture
Chairman, Departmental Committee on Graduate Students

Thesis Committee:
Qingyan Chen, Associate Professor of Building Technology
Leon R. Glicksman, Professor of Building Technology and Mechanical Engineering
Leslie K. Norford, Associate Professor of Building Technology

Study of Natural Ventilation in Buildings with Large Eddy Simulation

by
Yi Jiang

Submitted to the Department of Architecture
on May 3, 2002 in partial fulfillment of the
requirements for the Degree of Doctor of Philosophy
in the field of Architecture: Building Technology

ABSTRACT

With the discovery of many economic, environmental, and health problems in sealed and mechanically ventilated buildings, the concept of natural ventilation has been revived. "Buildings that breathe" have become more and more desired by ordinary people and architects. Although natural ventilation is conceptually simple, it is difficult to design and control. At present, methods to study natural ventilation are either inaccurate or costly. This study aims at solving these problems by using large eddy simulation (LES).

In LES, a three-dimensional, time-dependent method, the contribution of the large, energy-carrying structures is computed directly and only the smallest scales of turbulence are modeled. This investigation has identified a filtered dynamic subgrid-scale model of LES to study natural ventilation. The experimental data from a wind tunnel, a full-scale test chamber, and other research data have been used to validate the LES program.

Methods have been developed to solve the problems encountered in validating LES models for natural ventilation studies. Studying the characteristics of different indoor and outdoor airflows helps to identify the best SGS model for those flows. By comparing the results of using large and small computational domains, an appropriate domain size is recommended to save computing time. It is also found that simulating the transient properties of incoming wind, such as the principal frequency of the turbulent fluctuations, influences the pressure distributions around buildings.

The mechanism of natural ventilation is investigated using the numerical and experimental results. The fundamental impact of turbulence characteristics on ventilation rate is discussed and a new definition to calculate the ventilation rate is introduced. The distributions of velocities, pressures, temperature and energy spectra, and the computed ventilation rates, suggest that natural ventilation performance is significantly affected by thermal conditions and geometry of a building. LES provides the best tool to predict the effects under those conditions. Finally, with the implementation of a Lagrangian particle model, LES is applied to compute particle dispersion in buildings, which provides valuable information to improve indoor air quality. Good results were found for particles larger than 10 micrometers. Further work is needed for smaller particles.

Thesis Supervisor: Qingyan Chen
Title: Associate Professor of Building Technology

Acknowledgements

First of all, I would like to express my sincere thanks to my advisor, Professor Qingyan (Yan) Chen, for his tireless support and sound guidance during my four-year study at MIT. I feel grateful for having the opportunity to work with him. His knowledge and encouragement have helped me to deeply understand the problems and quickly build up my research approaches. His attitude and insight about research have a beneficial influence on me and have let me know what a good researcher should think and what a good researcher should do.

I would like to thank my thesis committee members, Professor Leon Glicksman and Professor Les Norford, for providing me with valuable comments and advisement to improve the thesis.

I would like to thank Dr. Wei Zhang, Dr. Minde Su, and Dr. Claudine Beghein for their precious help in the fields of large eddy simulation and particle model. I thank Zhiqiang Zhai, Allocca Camille, Jeffery Huang, Henry Spindler, Yang Gao, and Brent Griffith, for their time and knowledgeable help in natural ventilation studies and thesis preparation. I also thank Nabukazu Kobayashi, Donald Alexander, Huw Jenkins, Rob Arthur, and Professor Phil Jones for their help and advice on my experimental setup and measurements. My special thanks are to Dorrit Schuchter and Kathleen Ross for their considerate and kind supports so that I can focus on my research.

The financial support from U.S. National Science Foundation, MIT Kann-Rasmussen Program, and Martin Family Society of Fellows for Sustainability are acknowledged. I would also like to thank Professor Tadahisa Katayama from Kyushu University, Japan for providing the experimental data and building plans and for many useful discussions.

Dedication

To my husband, unborn baby, parents, brother's family and Professor Karen Polenske.

Contents

Chapter 1

Introduction

Natural ventilation has become an important sustainable strategy in building designs. This chapter reviews the problems associated with the current methodology for predicting and designing natural ventilation, and indicates the need to use an advanced tool, large eddy simulation, to provide accurate and detailed results for natural ventilation studies.

1.1 Why Natural Ventilation

The design, construction, and operation of buildings has a major impact on the environment and natural resources. In the United States, buildings account for one-third of all the energy and two-thirds of all electricity consumption (U.S. Energy Information Administration, 1995). Various mechanical systems comprise the major part of the energy consumption in residential and office buildings. Among them, the heating, ventilating, and air-conditioning (HVAC) system is the most commonly used and is the largest energy consumer.

The construction and operation of buildings generates pollutions that cause urban air quality problems and climate change. Producing energy for buildings uses a large amount of natural resources and is a major source of pollutants. The pollutants from buildings account for 49 percent of total sulfur dioxide emissions, 25 percent of total nitrous oxide emissions, and 10 percent of total particulate emissions, all of which worsen urban air quality. Buildings also generate 35 percent of total carbon dioxide emissions, which are believed to contribute to global warming (U.S. Department of Energy, 1997).

On the other hand, the use of HVAC systems in buildings does not necessarily create a healthy and comfortable indoor environment. Indeed, reports of symptoms and other health complaints related to indoor environments have been increasing. Evidences from the literature show that poor indoor environment significantly increase the rate of respiratory illness, allergy and asthma symptoms, and sick building symptoms; as a consequence, worker performance is adversely affected. Conversely, households and companies will benefit from better indoor environments. In the USA, the estimated potential annual savings and productivity gains are $6 to $14 billion from reduced respiratory disease, $1 to $4 billion from reduced allergies and asthma, $10 to $30 billion from reduced sick building syndrome symptoms, and $20 to $160 billion from direct improvements in worker performance that are unrelated to heath (Fisk, 2000).

An investigation conducted by National Institute for Occupational Safety and Health (NIOSH, 1999) shows that poor indoor environmental conditions are mainly related to indoor air quality issues, such as microbiological and chemical exposures. Other factors that affect people's perception of indoor environment include: physical conditions, such as temperature, humidity, lighting and noise, and social/psychological stresses. Several studies

suggest that there is a relationship between mechanical ventilation systems and complaints related to indoor air quality (Zweers, *et al.*, 1992, and Doughty, *et al.*, 2002). Other studies show that in mechanical ventilation systems, the system-produced condensed water may serve for microbial growth (Singh, 2001), the system itself could be a significant source of volatile organic compounds (VOC) (Wolkoff, 1999), and the system-produced air could contribute to dissatisfaction with perceived air quality (Jaakkola and Miettinen, 1995). As pointed out by Godish and Spengler (1996), the mechanical ventilation system could be a source of indoor contaminants that would contribute to building-related health symptoms. On the other hand, a naturally ventilated building does not encounter the problems that the mechanically ventilated building might have if outdoor air quality is good. Muzi *et al.* (1998) found that the symptom rate in mechanically ventilated buildings is much higher than naturally ventilated buildings. Therefore, natural ventilation is a promising solution for the indoor air quality problems introduced by mechanical ventilation systems.

In addition, the thermal comfort survey conducted in Bangkok by Busch (1992) suggests that people can tolerate higher temperature in a naturally ventilated building than in a mechanically ventilated building. Brager and De Dear (2000) confirmed this by analyzing thermal comfort field experiments inside 160 different office buildings located on four continents and covering a broad spectrum of climatic zones. They found that occupants in naturally ventilated buildings tolerated a wider range of temperature when compared to occupants in mechanically conditioned buildings. Therefore, if natural ventilation is used in a building, the period of air conditioning can be significantly reduced or eliminated. This would help to reduce the energy consumption in buildings.

Natural ventilation, which can provide occupants good indoor air quality and a high level of thermal comfort and reduce energy costs, has become an important sustainable strategy in building designs, and is thus attracting considerable interests from designers (Etheridge and Sandberg, 1996, and Allard, 1998).

1.2 Difficulties in Predicting and Designing Natural Ventilation

Although natural ventilation is conceptually simple, it is difficult to design and control. The following factors need to be considered:

- Driving forces. In a naturally ventilated building, air is driven in and out due to pressure differences produced by wind and/or buoyancy forces. Wind-driven natural ventilation is caused by temporal changes in wind speed and direction around the building and its neighbors. Buoyancy-driven natural ventilation is caused by temperature difference between indoor and outdoor air. Understanding of the two driving forces is crucial to natural ventilation design.

- Opening type. Natural ventilation can be further divided into cross ventilation and single-sided ventilation, depending on the opening type. Cross ventilation works for

indoor spaces with openings on more than one facade, while single-sided ventilation has openings only on one facade. Cross ventilation is normally more effective than single-sided ventilation, and therefore it should be used whenever possible. However, if a building is too thick or has solid internal partitions, it may prelude effective cross ventilation, and single-sided ventilation must be used. In both ventilation types, the size and position of the openings are critical in achieving effective ventilation.

- Site, form and orientation of the building. Natural ventilation, especially wind-driven, is directly affected by the airflow around the building. Topography, surrounding buildings, and the shape, orientation, and dimension of the building in turn determine the airflow.

1.3 Methods to Study Natural Ventilation

The previous section suggests that many factors have an impact on natural ventilation and they should be carefully examined. To study these impacts on natural ventilation in buildings, there are three different approaches: analytical methods, experimental measurements, and computational fluid dynamics (CFD) simulations.

1.3.1 Analytical methods

Two simple analytical methods have been developed to study natural ventilation in buildings. The first empirical models combine the airflow with the temperature difference, wind velocity and possibly a fluctuating term in order to give a bulk evaluation of the airflow rate or the air velocity in a building. These models use simplified formula and have been commonly used by designers because they offer a fast first estimate of building ventilation effectiveness. All of the empirical models are derived from Bernoulli theory and require empirical parameters that are obtained under specific building conditions (British Standards, 1980, ASHRAE Fundamentals, 1997, Aynsley, *et al.*, 1977, and De Gidds and Phaff, 1982). Normally, very simple building shapes and surroundings are used to generate the empirical parameters. For a complex building situation, therefore, the empirical models may give incorrect results. Furthermore, the empirical models regard a building as a single zone and can only provide a bulk airflow rate or a mean air velocity for the building. In reality, the airflow inside a building is not uniformly distributed and the building may be divided into different zones, which requires a multi-zone airflow network analysis to better understand the ventilation effectiveness of the building. Therefore, the empirical models cannot be used as a general methodology to provide accurate and detailed airflow information for natural ventilation studies.

The second analytical method is network models, which divide the building into a number of nodes that represent the simulated zones and the exterior environment. Network models can provide detailed airflow information at various zones inside a building in contrast to empirical models. Some examples of developed network models are ESP (Clarke, 1993),

AIRNET (Walton, 1988), CONTAM (Dols, *et al.*, 2000), COMIS (Feustel, *et al.* 1990), and PASSPORT-AIR (Dascalaki and Santamouris, 1995). Network simulation requires the knowledge of the exterior pressure distributions and empirical coefficients, such as the pressure discharge coefficients, to compute the pressure and velocity values within the interior nodes. However, it is difficult to estimate those data because they are strongly dependent on the building's form and surrounding conditions, which vary from case to case.

1.3.2 Experimental measurements

Experimental measurements can give much more accurate results than analytical models. Three types of measurements can be used to study natural ventilation: scale model, wind tunnel measurements, and full-scale measurements.

Scale models use water or various gases as the working fluid. Because of the viscosity difference between the working fluid and air, buildings can be scaled down significantly while keeping the same dimensionless parameters, such as Grashof number. A scale model can be used to test the impacts of different factors on natural ventilation at a reasonable cost and informative images can be generated. However, it is difficult to simulate different types of heat sources and openings and account complex surrounding conditions using a scale model (Linden *et al.*, 1990). Furthermore, Olson *et al.* (1990) found that scale models did not always reproduce the flow characteristics found in real buildings because of the difference in Prandtl numbers between the working fluid and air.

Wind tunnels have been widely used to study airflows around buildings for structure analysis and outdoor thermal comfort design. A wind tunnel can simulate an atmospheric boundary layer at a very high air speed so that buildings can be scaled down while having the same Reynolds number. Wind tunnels can be used to study the impact of different factors on natural ventilation caused by wind. The mean flow characteristics, such as velocity and pressure, can be adequately measured (Dagliesh, 1975, and Petersen, 1987). However, measurement data from wind tunnels is normally limited to a few points, and the instrumentation used for the flow field measurements can disturb flow patterns and lead to inaccuracies (Murakami *et al.*, 1991). Furthermore, the fluctuating components of the flow characteristics, such as the fluctuation of wind directions, are difficult to reproduce (Tieleman, *et al.* 1981, and Surry, 1989). In general, wind-tunnel tests are expensive and time consuming. Our study only uses a wind tunnel experiment to provide accurate flow data for validating the results of computer simulations.

One key limitation of wind tunnels is that they cannot be used to study natural ventilation with combined wind and buoyancy effects. This is because similarity theory would lead to contradictory scaling factors for wind and buoyancy effects. Even for purely buoyancy-driven natural ventilation, it is difficult to simulate the Grashof number found in real building cases. Therefore, experimental study of natural ventilation with buoyancy or combined wind and buoyancy must be studied in a full-scale facility.

A full-scale facility used for wind-driven and buoyancy-driven ventilation studies can provide reliable airflow information. Katayama, *et al.* (1992), Dascalaki, *et al.* (1996), and Fernandez and Bailey (1992) measured ventilation rate and airflow distributions around and inside a full-scale room with natural ventilation. Experiments in full-scale facilities are very expensive and time consuming, so they are mainly used to obtain data for validating computer modeling results and for deriving empirical models. In addition, due to the difficulties of controlling the wind and thermal conditions in the experimental facility, it is not feasible to study the impacts of all different factors on natural ventilation in a full-scale facility. Nevertheless, since full-scale measurement is reliable, the current study will use a full-scale facility to obtain some buoyancy effect data to validate the computational results.

1.3.3 Computation fluid dynamics

Computational fluid dynamics (CFD) is another approach to study natural ventilation. CFD is becoming popular due to its informative results and low labor and equipment costs, made possible by developments in turbulence modeling and in computer speed and capacity (Chen, 1996, Murakami, 1998, and Spalart, 2000). There are three different CFD methods: direct numerical simulation (DNS), Reynolds-averaged Navier-Stokes (RANS) modeling, and large eddy simulation (LES).

DNS

DNS directly solves the Navier-Stokes equation without approximation. The model requires the use of very fine grid resolutions so that the smallest eddies (the order of the Kolmogorov length scale or about 0.001 m in natural ventilation study) can be computed. for a small building and its surroundings, DNS would require a grid number of 10^{11}. Current super computers can handle a grid resolution as fine as 10^{8}. Therefore, the computer capacity is still far too small to solve natural ventilation airflows.

LES

Unlike DNS, which needs to solve the smallest eddies of the order of the Kolmogorov length scale, LES only solves the large, energy-carrying eddies, which are assumed to be directly affected by the boundary conditions and carry most of the Reynolds stress. Since the small eddies tend to be more homogeneous and universal and less affected by the boundary conditions than the large ones, the small scale eddies are modeled, and the models are expected to be simple and require few adjustments.

LES solves three-dimensional, time-dependent airflow fields. Since one of the major driving forces in natural ventilation is wind, which changes its direction and magnitude over time, a transient simulation is required in such a study. LES can simulate transient airflows, and moreover, the detailed turbulence information provided by LES can be used for thermal comfort analysis.

LES has been successfully applied to several indoor airflow studies (Davidson and Nielsen, 1996, Emmerich and McGrattan, 1998, Zhang and Chen, 2000). Furthermore, as reviewed by Murakami (1998), LES produces accurate results both at the mean and turbulent levels for airflows around buildings. Since natural ventilation studies require correct prediction of both indoor and outdoor airflows, LES is an ideal candidate for natural ventilation studies. The Fundamentals of LES in terms of governing equations, models and numerical solutions will be discussed in Chapter 2.

RANS

Reynolds-averaged Navier-Stokes (RANS) modeling determines ensemble-averaged flow parameters, such as air velocity and temperature, by using turbulence modeling. This modeling is the most widely used CFD method in many industrial applications and requires much less computing time than LES.

In studying natural ventilation, however, RANS modeling has several problems. First, RANS modeling cannot correctly predict airflows around and inside buildings. Chen (1996) compared five different k-ε models of RANS modeling for indoor airflows. All of the models failed to predict the anisotropic turbulence and secondary recirculation of indoor airflow. Lakehal and Rodi (1997) compared the computed results of airflow around a bluff body by using various RANS models. They found that most RANS models cannot generate the separation region on the top and all RANS models over-predict the recirculation region behind the body. On the other hand, the LES models did not encounter these problems and the results agreed well with the experimental data (Rodi, *et al.*, 1997). Second, as mentioned above, the unsteadiness caused by fluctuations in the wind-driven force requires a transient simulation. The RANS modeling, which performs an ensemble-averaging process, cannot perform such a simulation.

To overcome the difficulties encountered by RANS modeling, some special methods have been used to add a time scale to RANS modeling, which results in a so-called unsteady RANS modeling (Spalart and Allmaras, 1994, and Durbin, 1995). These methods are expected to provide unsteady flow fields and to be faster than LES models although slower than a regular RANS model.

Unsteady RANS modeling, however, still lacks the accuracy for detailed flow prediction and analysis as required by natural ventilation studies. For example, Gianluca and Durbin (2000) used an unsteady RANS model to compute the airflow around a bluff body, which was computed by Lakehal and Rodi (1997) with regular RANS models and by Shah (1998) with LES models. The computed results with unsteady RANS model are better than the regular RANS models. However, compared with experimental data (confirmed by LES results), unsteady RANS modeling still over-predicts the extent of the recirculation region behind the block by nearly 20% and is unable to correctly capture the separated boundary layer on the cube roof. Another example of the accuracy problems associated with the unsteady RANS modeling is in the study of airflows around a smooth body, such as a circular cylinder. The computed flow field using unsteady RANS modeling (Shur, *et al.*

1996) cannot capture as many flow details as the LES models can (Travin, *et al.*, 2000) as shown in Figure 1.1. As a result, the drag coefficient predicted by the unsteady RANS modeling is over 40% higher than the experimental result, but LES can correctly predict the drag coefficient. It is interesting to point out that at lower Reynolds number, a laminar model also gives good agreement for the drag coefficient. Spalart (2000) also pointed out that in the study of airflows around a cylinder, the unsteady RANS models had difficulties generating the coherent structure of turbulence motions and introduced a separation of time scales between that of the visible shedding and that of the putative residual turbulence, which did not occur in experimental measurements. Travin *et al.* (2000) explained the accuracy problems associated with the unsteady RANS modeling as follows. The airflow past a body, such as a building, causes massive three-dimensional separation. In contrast to LES, which resolves the complete range of random motion, the unsteady RANS only captures a single frequency of airflow motion. The hope that RANS turbulence models will soon achieve engineering accuracy in these regions is not supported by their rate of progress over the last twenty years, even at the highest complexity level, such as Reynolds-stress transport, and even with the benefit of unsteady solutions. Reynolds averaging may create an unsurmountable problem when the dominant eddies are highly geometry-specific and wide-ranged, such as in the airflows around buildings.

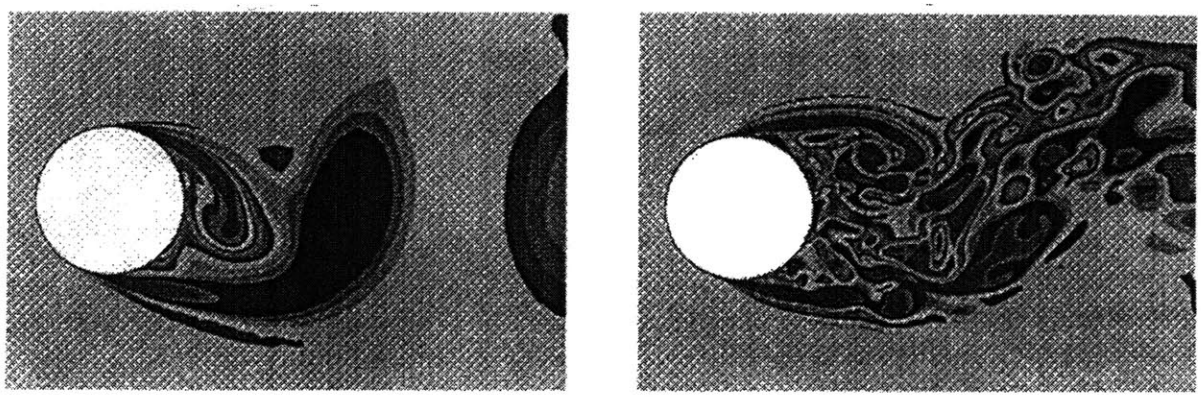

(a) unsteady RANS model (Shur et al., 1996) *(b) LES (Travin et al., 2000)*

***Figure 1.1** Simulation of flow past circular cylinder by various CFD methods.*

Another problem with the unsteady RANS modeling is that it has difficulties producing correct airflow fields under an unsteady inflow condition, such as an incoming wind varied with speed and/or direction. Scotti and Piomelli (2002) studied the channel flows under an unsteady boundary condition with four unsteady RANS models. They found that although the unsteady RANS models can give reasonable results for mean velocity, all of them failed to correctly predict the second-order flow fields, such as Reynolds stresses, kinetic energy and dissipation rate. However, the information from the second-order flow fields is very important in the prediction and design of natural ventilation and study of thermal comfort.

Therefore, unsteady RANS modeling with its extra time cost does not seem to be superior to regular RANS modeling for natural ventilation studies.

Computing costs with different CFD models

When using CFD to study airflows, the computing cost is a critical issue. Although DNS is the most accurate CFD method, it cannot be used for airflow studies in buildings due to the tremendous computing cost, which is not currently affordable. The reason that RANS modeling has been widely used is that it can give reasonable results for many industrial flows with an affordable computing cost. This section gives a broad overview of the CFD methods with order of magnitude estimates of their respective computing costs. The computing time is calculated based on a fast workstation. The target flows are those over a building at a Reynolds number of about 10^6 or those over an airliner at a Reynolds number of about 10^8. The driving-force in those flows is wind. For the simulation of buoyancy-driven airflows, more computing time is needed.

Table 1.1 compares the computing costs of different CFD methods. Two versions of LES are included. IN LES*, some empirical models are added to LES, such as a wall model or a RANS model for the simulation of the whole boundary layer, in oder to reduce the grid number in the near-wall or boundary-layer regions. In LES**, no such empirical models are added to the near-wall or boundary-layer regions. Therefore, to fully describe the airflows in those regions, the grid spacing in all directions (or at least in the two directions parallel to the wall) would scale with the boundary-layer thickness, which requires a huge number of grids. Hence, the computing time required by LES** is much longer than for LES*.

Table 1.1 shows that for the study of airflows around and in buildings, the RANS and unsteady RANS models only require several hours of computing time. LES with an empirical model, such as a wall model, requires 4~5 days of computing time. The computing costs using LES without any empirical models and DNS are too high to be affordable at present. For the study of airflows around an airline or an automobile, an acceptable tool would be unsteady RANS modeling. However, with the supports of super-computers and parallel schemes, LES with an empirical model is also possible.

The comparison shows that LES requires a large-capacity, high-speed computer to study airflows related to buildings. However, the computing cost for LES with an empirical model, which has been widely used for both indoor and outdoor airflow studies, is not too expensive to be affordable. Since LES can produce accurate and detailed airflow information for natural ventilation studies, which cannot be achieved by RANS or unsteady RANS models, and the computing cost can be easily reduced in the near future due to the rapid development in computer capacity and speed, LES is used as the main tool to study natural ventilation in the present investigation.

Table 1.1 *Comparison of the computing costs among different CFD methods*

Name	Unsteady	Empiricism	Grid		Steps		Computing cost	
			Building Re~10^6	Airline Re~10^8	Building Re~10^6	Airline Re~10^8	Building Re~10^6	Airline Re~10^8
RANS	No	Strong	10^5	10^7	10^3	10^3	2 hour	200 hours
Unsteady RANS	Yes	Strong	10^5	10^7	$10^{3.5}$	$10^{3.5}$	6 hours	600 hours
LES*	Yes	Slightly	10^6	10^8	10^4	10^4	100 hours	1 year
LES**	Yes	Weak	10^8	$10^{11.5}$	$10^{5.5}$	$10^{6.7}$	35 years	10^6 years
DNS	Yes	None	10^{11}	10^{16}	10^6	$10^{7.7}$	10^5 years	10^{12} years

* Special treatments of the boundary layer with either a wall model or a RANS model.
** No special treatments of the boundary layer.

1.4 Objectives of the Present Study

The discussions in previous sections indicate that predicting and designing natural ventilation needs to take into account the incoming wind speed and direction, building shape and density, surrounding landscape, thermal conditions in and around buildings, opening type, size and locations, and building interior layout, among other factors. The current methods for natural ventilation studies have their limitations. Empirical models cannot be used as a general methodology because they are developed under specific building circumstances; experimental design tools are expensive; and RANS modeling may be inaccurate. Since the fast development in computer power has made the study of airflows around and inside buildings with LES more realistic, LES is a good approach for natural ventilation studies.

Therefore, the overall objective of this thesis is to determine if LES is the best methodology to study natural ventilation by in terms of accuracy and costs and to improve the LES models to analyze the mechanism of natural ventilation in buildings. More specifically, the present study aims to:

- To compare in details the pros and cons of different methods for studying natural ventilation, such as wind-tunnel and full-scale measurements, empirical models, RANS modeling, and LES.

- To examine the performance of LES and its applicability for solving complex airflow in and around buildings with natural ventilation.

- To understand the impacts of driving forces, opening type, and site layout on ventilation effectiveness of a building with natural ventilation.

- To apply LES for studying realistic ventilation problems, such as natural ventilation in a dense urban environment and particle dispersion in a multi-room building.

1.5 The Structure of the Thesis

This thesis is organized as follows:

- Chapter 2 introduces the fundamentals of LES, which include the filtered governing equations for LES; the subgrid-scale (SGS) models of LES that are used in the current study; the numerical methods in terms of the computational grid system, the discretization schemes, the numerical procedure, and the determination of the time step size used to solve the governing equations; and the boundary conditions for wall treatment, and inflow and outflow settings.

- Chapter 3 illustrates two sets of experiments related to natural ventilation. One is conducted in a wind tunnel to study natural ventilation driven by wind forces. Both cross ventilation and single-sided ventilation are investigated. The other one is conducted in a full-scale environmental chamber to study buoyancy-driven natural ventilation. Single-sided ventilation with two different opening sizes is investigated.

- Chapter 4 applies the SGS models of LES to study the mechanism of indoor and outdoor airflows, through which the performances of the LES models is evaluated. This helps to evaluate the capability of the LES models to study airflows related to buildings.

- Chapter 5 validates the LES models with experimental data for natural ventilation obtained from the literature and from the experiments described in Chapter 3. The performances of the LES models under wind-driven and buoyancy-driven natural ventilation conditions are investigated. The standard k-ε model of RANS modeling and empirical models are also used as a comparison.

- Chapter 6 implements a Lagrangian particle model in LES to study particle dispersion in buildings. This is an extension of the natural ventilation study, which helps to design an effective natural ventilation system to provide good indoor air quality.

- Chapter 7 summarizes the conclusions arising from the study and provides recommendations for future studies.

Chapter 2

Fundamentals of Large Eddy Simulation

This chapter first describes the governing equations for LES in an incompressible fluid. Then the subgrid-scale models of LES that were used in the current study are discussed. The numerical methods used to solve the governing equations and the boundary conditions for walls, inflow and outflow are also presented.

2.1 Filtering and Governing Equations of Large Eddy Simulation

In LES, the contribution of the large, energy-carrying structures to momentum and energy transfer is computed directly, and only the smallest scales of turbulence are modeled. To separate the large from the small scales, LES is based on a filtering operation. This section introduces the definition and characteristics of this filtering operation, provides the governing equations of LES, and discusses the subgrid-scale (SGS) stresses that are obtained through the filtering operation.

The current study uses the Cartesian coordinate system, in which the coordinates and velocity components are represented by the following symbols: x_1 (or x), x_2 (or y), and x_3 (or z) represent the three spatial coordinates where x is in the streamwise direction, y in the vertical direction, and z in the spanwise direction; u_1, u_2, u_3 or u, v, w are velocity components along the streamwise, vertical and spanwise directions respectively.

2.1.1 Filtering operation

In LES, the flow field is divided into a large scale, $\overline{u}_i$, and a subgrid scale (SGS), u_i'

$$u_i = \overline{u}_i + u_i' \tag{2. 1}$$

The large scale is defined by a filtering process (Leonard, 1974). For example, a one-dimensional filtered velocity can be obtained from

$$\overline{u_i} = \int G(x,x')\, u_i(x')\, dx' \tag{2. 2}$$

where the bar represents grid filtering, and $G(x,x')$ is the filter kernel, which is a localized function. $G(x,x')$ is large only when (x-x′) is less than a length scale or a filter width. The length scale is a length over which averaging is performed. The filtering procedure removes spatial fluctuations that are narrower than the characteristic length scale. Flow eddies larger than the length scale are "large eddies" and smaller than the length scale are "small eddies".

There are three commonly used filter kernels:

(1) Gaussian filter

$$G(x_i) = \sqrt{\frac{6}{\pi\Delta_i^2}}\exp\left\{-\frac{6x_i^2}{\Delta_i^2}\right\} \tag{2.3}$$

(2) Cutoff spectral filter

$$G(x_i) = \frac{2\sin\left\{\frac{\pi x_i}{\Delta_i}\right\}}{\pi x_i} \tag{2.4}$$

(3) Top-hat/Box filter

$$G(x_i) = \begin{cases} \dfrac{1}{\Delta_i} & \left(|x_i| \le \dfrac{\Delta_i}{2}\right) \\ 0 & \left(|x_i| > \dfrac{\Delta_i}{2}\right) \end{cases} \tag{2.5}$$

where Δ_i is the filter width. Piomelli *et al.* (1987) pointed out that the Fourier and Gaussian filters were normally used for LES that applied spectral methods. For finite volume or finite difference methods, it was natural to use the box filter. Since the finite difference method is used in this investigation, the box filter is adopted.

The filtering technique uses the following relationships

$$u = \bar{u} + u', \qquad \overline{\frac{\partial u}{\partial x}} = \frac{\partial \bar{u}}{\partial x}, \qquad \overline{\frac{\partial^n u}{\partial x^n}} = \frac{\partial^n \bar{u}}{\partial x^n} \tag{2.6}$$

and unlike conventional averaging, in general

$$\bar{\bar{u}} \neq \bar{u}, \qquad u' \neq 0 \tag{2.7}$$

2.1.2 Governing equations

The filter process provides a formal definition of the averaging process and separates the resolvable scales from the subgrid scales. With filtering, we are able to derive the

resolvable-scale equations for incompressible flows. The original governing equations of the flows are

$$\frac{\partial u_i}{\partial t} + \frac{\partial}{\partial x_j}(u_i u_j) = -\frac{1}{\rho}\frac{\partial p}{\partial x_i} + \nu\frac{\partial^2 u_i}{\partial x_j \partial x_j} + g_j\beta(\theta - \theta_0)\delta_{ij} \tag{2. 8}$$

$$\frac{\partial u_i}{\partial x_i} = 0 \tag{2. 9}$$

$$\frac{\partial \theta}{\partial t} + \frac{\partial u_j \theta}{\partial x_j} = \frac{\partial}{\partial x_j}\left(\frac{\nu}{Pr}\frac{\partial \theta}{\partial x_j}\right) \tag{2. 10}$$

where ρ = air density (m^3/s)
p = air pressure (Pa)
ν = kinetic viscosity (m/s^2)
Pr = molecular Prandtl number
θ = air temperature (^oC)

By applying the box filter (Equation 2.5), Equations (2.8 – 2.10) are filtered as

$$\frac{\partial \overline{u_i}}{\partial t} + \frac{\partial}{\partial x_j}(\overline{u_i u_j}) = -\frac{1}{\rho}\frac{\partial \overline{p}}{\partial x_i} + \nu\frac{\partial^2 \overline{u_i}}{\partial x_j \partial x_j} + g_j\beta(\overline{\theta} - \theta_0)\delta_{ij} \tag{2. 11}$$

$$\frac{\partial \overline{u_i}}{\partial x_i} = 0 \tag{2. 12}$$

$$\frac{\partial \overline{\theta}}{\partial t} + \frac{\partial \overline{u_j \theta}}{\partial x_j} = \frac{\partial}{\partial x_j}\left(\frac{\nu}{Pr}\frac{\partial \overline{\theta}}{\partial x_j}\right) \tag{2. 13}$$

where the bar represents the box filtering. Two non-linear terms are derived through this filtering procedure, $\overline{u_i u_j}$ and $\overline{u_j \theta}$, which are decomposed into a filtered field and a SGS term, respectively

$$\overline{u_i u_j} = \overline{u}_i \overline{u}_j + (\overline{u_i u_j} - \overline{u}_i \overline{u}_j) = \overline{u}_i \overline{u}_j + \tau_{ij} \tag{2. 14}$$

$$\overline{u_j \theta} = \overline{u}_j \overline{\theta} + (\overline{u_j \theta} - \overline{u}_j \overline{\theta}) = \overline{u}_j \overline{\theta} + h_j \tag{2. 15}$$

where τ_{ij} and h_j are the SGS Reynolds stresses and the SGS heat fluxes, respectively,

$$\tau_{ij} = \overline{u_i u_j} - \overline{u}_i \overline{u}_j \tag{2. 16}$$

$$h_j = \overline{u_j \theta} - \overline{u}_j \overline{\theta} \tag{2. 17}$$

and must be modeled. By replacing the two non-linear terms in Equations (2.11) and (2.13) with Equations (2.14) and (2.15), one can obtain the governing equations of LES

$$\frac{\partial \overline{u_i}}{\partial t} + \frac{\partial}{\partial x_j}(\overline{u_i u_j}) = -\frac{1}{\rho}\frac{\partial \overline{p}}{\partial x_i} + \nu \frac{\partial^2 \overline{u}_i}{\partial x_j \partial x_j} - \frac{\partial \tau_{ij}}{\partial x_j} + g_j \beta(\overline{\theta} - \theta_0)\delta_{ij} \tag{2. 18}$$

$$\frac{\partial \overline{u_i}}{\partial x_i} = 0 \tag{2. 19}$$

$$\frac{\partial \overline{\theta}}{\partial t} + \frac{\partial \overline{u}_j \overline{\theta}}{\partial x_j} = \frac{\partial}{\partial x_j}\left(\frac{\nu}{Pr}\frac{\partial \overline{\theta}}{\partial x_j}\right) - \frac{\partial h_j}{\partial x_j} \tag{2. 20}$$

The models to simulate the SGS Reynolds stresses and heat fluxes will be discussed in Section 2.2.

2.2 Subgrid-scale Models of Large Eddy Simulation

This section introduces the SGS models of LES that are used in the present study. It is assumed that the subgrid scales are nearly isotropic and that their contribution to turbulence kinetic energy and momentum transfer are small, so that simple models can be used to describe these SGS eddies.

2.2.1 Smagorinsky subgrid-scale model

The Smagorinsky subgrid-scale (SS) model is the first SGS model of LES (Smagorinsky, 1963), and has been widely used since the pioneer work by Deardorff (1970). The SS model assumes that the SGS Reynolds stresses, τ_{ij}, are proportional to the rate of strain tensor,

$$\tau_{ij} = -2\nu_{SGS}\overline{S_{ij}} \tag{2. 21}$$

where $\overline{S}_{ij}$ are the rates of strain tensor,

$$\overline{S}_{ij} = \frac{1}{2}\left(\frac{\partial \overline{u}_i}{\partial x_j} + \frac{\partial \overline{u}_j}{\partial x_i}\right) \tag{2. 22}$$

and ν_{SGS} is the SGS eddy viscosity defined as

$$\nu_{SGS} = (C_{SGS}\overline{\Delta})^2 \left|\overline{S}\right| = C\,\overline{\Delta}^2\,(2\overline{S_{ij}}\cdot\overline{S_{ij}})^{\frac{1}{2}} \tag{2. 23}$$

where C_{SGS} = the Smagorinsky constant
$\overline{\Delta}$ = the length scale of a typical SGS eddy
C = $(C_{SGS})^2$, the model coefficient

The length scale $\overline{\Delta}$ is related to the grid size and is usually represented as

$$\overline{\Delta} = (\Delta x\,\Delta y\,\Delta z)^{1/3} \tag{2. 24}$$

In analogy to the SGS Reynolds stresses, the subgrid heat fluxes in the filtered energy equation are modeled as

$$h_j = -\alpha_{SGS}\frac{\partial \overline{\theta}}{\partial x_j} \tag{2. 25}$$

where α_{SGS}, is the SGS eddy diffusivity, and is defined as

$$\alpha_{SGS} = C\,\overline{\Delta}^2\,\frac{\left|\overline{S}\right|}{Pr_{SGS}} \tag{2. 26}$$

The subgrid heat fluxes are then solved with

$$h_j = C\,\overline{\Delta}^2\,\frac{\left|\overline{S}\right|}{Pr_{SGS}}\frac{\partial \overline{\theta}}{\partial x_j} \tag{2. 27}$$

where Pr_{SGS} = 0.5 - 0.9.

The SS model is an adaptation of the mixing length model of RANS modeling to the SGS model of LES. The Smagorinsky constant, C_{SGS}, needs to be specified prior to a simulation. In the available literature on the SS model (Deardoff, 1970, Piomelli *et al.*, 1987 and Murakami, 1998), there is no consensus on an appropriate value of C_{SGS}. It depends on the flow type, the filter being used, and the numerical method employed.

2.2.2 Dynamic subgrid-scale model

The SS model requires a priori specification of the Smagorinsky coefficient, C_{SGS}, or the model coefficient, C. It is difficult to specify the model coefficient in advance, and the coefficient may not be a constant. In order to solve this problem, Germano *et al.* (1991) developed a SGS model with a dynamic procedure, which is usually called a dynamic subgrid-scale (DS) model. This model can determine the coefficient as a function of time and location. The DS model, which does not have a prescribed coefficient, is physically sound, and therefore is very attractive.

The DS model assumes that there is an algebraic identity between the SGS stresses at two different filtered levels, the test filtered level and the grid filtered level, and the resolved turbulent stresses. The characteristic width of the test filter, $\widetilde{\Delta}$, is assumed to be larger than the gird filter width, $\overline{\Delta}$, and is normally set as $\widetilde{\Delta} = 2\overline{\Delta}$. By applying the test filter (~) to the filtered (—) governing equations of LES (Equations (2.18)-(2.20)), one can obtain

$$\frac{\partial \widetilde{\overline{u}}_i}{\partial t} + \frac{\partial}{\partial x_j}(\widetilde{\overline{u}}_i \widetilde{\overline{u}}_j) = -\frac{1}{\rho}\frac{\partial \widetilde{\overline{p}}}{\partial x_i} + \nu \frac{\partial^2 \widetilde{\overline{u}}_i}{\partial x_j \partial x_j} - \frac{\partial T_{ij}}{\partial x_j} + g_j \beta(\widetilde{\overline{\theta}} - \theta_0)\delta_{ij} \qquad (2.28)$$

$$\frac{\partial \widetilde{\overline{u}}_i}{\partial x_i} = 0 \qquad (2.29)$$

$$\frac{\partial \widetilde{\overline{\theta}}}{\partial t} + \frac{\partial \widetilde{\overline{u}}_j \widetilde{\overline{\theta}}}{\partial x_j} = \frac{\partial}{\partial x_j}\left(\frac{\nu}{Pr}\frac{\partial \widetilde{\overline{\theta}}}{\partial x_j}\right) - \frac{\partial H_j}{\partial x_j} \qquad (2.30)$$

where the SGS stresses and heat fluxes at the test level are

$$T_{ij} = \widetilde{\overline{u_i u_j}} - \widetilde{\overline{u}}_i \widetilde{\overline{u}}_j \qquad (2.31)$$

$$H_j = \widetilde{\overline{u_j \theta}} - \widetilde{\overline{u}}_j \widetilde{\overline{\theta}} \qquad (2.32)$$

The first term on the right side of Equation (2.31) cannot be determined directly, like the one in Equation (2.16). Substituting Equation (2.31) from Equation (2.16) with a test filter leads to

$$T_{ij} - \tilde{\tau}_{ij} = L_{ij} \qquad (2.33)$$

where

$$L_{ij} = \widetilde{\overline{u}_i \overline{u}_j} - \tilde{\overline{u}}_i \tilde{\overline{u}}_j \tag{2.34}$$

The resolved turbulent stresses in Equation (2.34), L_{ij}, can be calculated explicitly. With the definition of the SS model, the stresses with the test filter, T_{ij}, and that of the grid filter, τ_{ij}, are

$$T_{ij} = -2C_T \tilde{\Delta}^2 \left|\tilde{\overline{S}}\right| \tilde{\overline{S}}_{ij} = -C_T \alpha_{ij} \tag{2.35}$$

$$\tau_{ij} = -2C_\tau \overline{\Delta}^2 \left|\overline{S}\right| \overline{S}_{ij} = -C_\tau \beta_{ij} \tag{2.36}$$

where $\overline{\Delta}$ is the grid filter width, and $\tilde{\Delta}$ the test filter width. C_τ and C_T are the coefficients of the grid and test filters, respectively. Furthermore,

$$\tilde{\overline{S}}_{ij} = \frac{1}{2}\left(\frac{\partial \tilde{\overline{u}}_i}{\partial x_j} + \frac{\partial \tilde{\overline{u}}_j}{\partial x_i}\right), \qquad \left|\tilde{\overline{S}}\right| = \sqrt{2\tilde{\overline{S}}_{ij}\tilde{\overline{S}}_{ij}} \tag{2.37}$$

Substitution of Equations (2.35) and (2.36) into Equation (2.34) gives

$$L_{ij} - \frac{1}{3}\delta_{ij} L_{kk} = C_T \alpha_{ij} - \widetilde{C_\tau \beta_{ij}} \tag{2.38}$$

where $\alpha_{ij} = 2\tilde{\Delta}^2 \left|\tilde{\overline{S}}\right| \tilde{\overline{S}}_{ij}$ and $\beta_{ij} = 2\overline{\Delta}^2 \left|\overline{S}\right| \overline{S}_{ij}$. The C_τ in Equation (2.38) cannot be solved explicitly because it is in the test filtering operation. Germano *et al.* (1991) extracted this term from the filtering operation, and assumed that

$$C \approx C_\tau \approx C_T \tag{2.39}$$

$$\widetilde{C_\tau \beta_{ij}} = C_\tau \tilde{\beta}_{ij}, \tag{2.40}$$

With the least-square approach suggested by Lilly (1992), C can be solved for with

$$C = \frac{< L_{ij} M_{ij} >}{< M_{ij} M_{ij} >} \tag{2.41}$$

where $M_{ij} = (\alpha_{ij} - \widetilde{\beta}_{ij})$ and $< >$ denotes a plane averaging over a homogeneous direction. Without an averaging process over the homogenous direction, C fluctuates significantly, making the results unstable. The averaging procedure helps to damp large fluctuations of the C, and produces good results for a simple flow with at least one homogeneous direction, such as a turbulent channel flow.

The derivation procedure to compute the model coefficient, C, can be used to determine the SGS Prandtl number, Pr_{SGS} (Equation (2.27)). Lilly (1992) modeled the SGS heat fluxes, $h_j = \overline{u_j\theta} - \overline{u}_j\overline{\theta}$, with a simplified Boussinesq approximation and the SGS Prandtl number, Pr_{SGS}, can be calculated as

$$\frac{1}{Pr_{SGS}} = \frac{1}{C}\frac{P_j R_j}{R_j^2} \tag{2.42}$$

where

$$P_j = \widetilde{\overline{u}_j\overline{\theta}} - \widetilde{\overline{u}}_j\widetilde{\overline{\theta}} \tag{2.43}$$

$$R_j = \widetilde{\overline{\Delta}}^2\left|\widetilde{\overline{S}}\right|\frac{\partial\widetilde{\overline{\theta}}}{\partial x_j} - \overline{\Delta}^2\left|\overline{S}\right|\frac{\partial\overline{\theta}}{\partial x_j} \tag{2.44}$$

To compute the model coefficient, C, of the DS model, an averaging procedure over a homogeneous direction is needed to stabilize the results. However, in complex flows, such as the airflows around and inside buildings, it is difficult, if not impossible, to find a homogeneous direction. Therefore, a new SGS model has to be developed to remove the large fluctuation of the model coefficient without the averaging procedure over a homogeneous direction. The next section discusses such a new model.

2.2.3 Filtered dynamic subgrid-scale model

The DS model has the key features of proper asymptotic behavior near walls and the SGS eddy viscosity can vanish in the regions of laminar flow. However, this DS model can lead to numerical instability if the SGS eddy viscosity remains negative for too long (Shah, 1998). To overcome this difficulty, Germano *et al.* (1991) averaged the flow variables over a homogenous direction. For a channel flow, it is possible to identify the homogeneous direction. For the airflow in buildings, where no homogeneous direction exists, Zhang and Chen (2000) introduced a filtered dynamic subgrid-scale (FDS) model to stabilize the calculation.

As described in Section 2.2.2, Germano *et al.* (1991) were able to calculate the model coefficient by introducing a test filter. The first term on the right side of Equation (2.31) is unknown, and can be calculated with Equation (2.33). The terms $(\widetilde{\overline{u}_i \overline{u}_j} - \widetilde{\overline{u}}_i \widetilde{\overline{u}}_j)$ in Equation (2.34) can be solved and, consequently, the model coefficient can be calculated. However, all the terms in Equation (2.33) are within the test filter scale. Therefore, the model coefficient C in Equation (2.41) without the averaging procedure can be considered valid only for the test filter scale. In other words, the model coefficient, C, without an averaging process cannot be used to determine the stress tensor, τ_{ij}, that is defined by the grid filter scale. Strictly speaking, the C obtained with the grid filter scale can be used to calculate τ_{ij}, because the SGS model is defined with the grid filter scale. Applying the coefficient C obtained in Equation (2.41) without the averaging procedure to calculate τ_{ij} may lead to inaccurate results.

The FDS model overcomes the difficulties mentioned above by introducing a grid filter to Equation (2.33). Since the SGS Reynolds stresses, τ_{ij}, are defined with the grid filter ($\overline{\Delta}$), the model coefficient, C, should be related to the grid filter ($\overline{\Delta}$). Thus, applying a grid filter to Equation (2.33) yields:

$$\overline{T}_{ij} - \widetilde{\overline{\tau}}_{ij} = \overline{L}_{ij} \tag{2.45}$$

In order to obtain a new model coefficient from Equation (2.45), the τ_{ij} and T_{ij} in Equation (2.45) are modeled by using the SS model or the mixed model (Zang *et al*, 1994). However, this modeling would lead to an error in satisfying Equation (2.45), τ_{ij}^{model}

$$e_{ij} = \overline{L}_{ij} - (\overline{T}_{ij}^{model} - \widetilde{\overline{\tau}}_{ij}^{model}) \tag{2.46}$$

For simplicity, this investigation used the Smagorinsky model. The corresponding error is

$$e_{ij} = \overline{L}_{ij} - \overline{2C_T \widetilde{\overline{\Delta}}^2 \left|\widetilde{\overline{S}}\right| \widetilde{\overline{S}}_{ij}} + 2\widetilde{C_\tau \overline{\Delta}^2 |\overline{S}| \overline{S}}_{ij} \tag{2.47}$$

Using a definition of $\alpha_{ij} = 2\widetilde{\Delta}^2 \left|\widetilde{\overline{S}}\right| \widetilde{\overline{S}}_{ij}, \beta_{ij} = 2\overline{\Delta}^2 |\overline{S}| \overline{S}_{ij}$, Equation (2.47) can be re-written as

$$e_{ij} = \overline{L}_{ij} - \overline{C_T \alpha_{ij}} + \widetilde{\overline{C_\tau \beta_{ij}}} \tag{2.48}$$

If we assume that

$$\overline{C_T \alpha_{ij}} \approx \overline{C}_T \overline{\alpha}_{ij} \tag{2.49}$$

$$\overline{\widetilde{C_\tau \beta_{ij}}} \approx \overline{\widetilde{C}}_\tau \overline{\widetilde{\beta}}_{ij} \tag{2.50}$$

$$C \approx \overline{\widetilde{C}}_\tau \approx \overline{C}_T \tag{2.51}$$

then Equation (2.47) becomes

$$e_{ij} = \overline{L}_{ij} - \overline{C_T \alpha_{ij}} + \overline{\widetilde{C_\tau \beta_{ij}}} = \overline{L}_{ij} - C\overline{M}_{ij} \tag{2.52}$$

where $M_{ij} = \alpha_{ij} - \widetilde{\beta}_{ij}$.

Meneveau *et al.* (1996) used DNS data to analyze the two hypotheses above (Equations (2.39) and (2.40)). They filtered the DNS data at both the grid level and the test level and then compared the coefficients obtained with or without an averaging procedure (Lagrangian time averaging). Although the two coefficients are not equal without averaging, they are similar with the Lagrangian time averaging:

$$C^{DNS}{}_\tau \neq C^{DNS}{}_T \tag{2.53}$$

$$\left\{C^{DNS}{}_\tau\right\} \approx \left\{C^{DNS}{}_T\right\} \tag{2.54}$$

where $\{\}$ denotes time averaging. Meneveau *et al.* (1996) also discussed the minimal error caused by approximating $\widetilde{C_\tau \beta_{ij}} = \widetilde{C}_\tau \widetilde{\beta}_{ij}$ with or without using the averaging technique. Their study shows that the minimal error with the averaging is smaller than that without the averaging

$$\text{Error}_{\min}\left(\left\{\widetilde{C}_\tau \widetilde{\beta}_{ij}\right\}, \left\{\widetilde{C_\tau \beta_{ij}}\right\}\right) << \text{Error}_{\min}\left(\widetilde{C}_\tau \widetilde{\beta}_{ij}, \widetilde{C_\tau \beta_{ij}}\right) \tag{2.55}$$

Since the filtering technique is averaging, the results obtained by Meneveau *et al.* (1996) may be extended to a grid filtering technique. Therefore, the assumptions used in Equations (2.49), (2.50), and (2.51) may be valid as well, although they need to be further examined.

Zhang and Chen (2000) used the least-square approach to obtain the model coefficient, C in Equation (2.52), as suggested by Lilly (1992). At any given point in a space, **x**, e_{ij} is a function of C. In order to obtain an optimal C, e_{ij} should be integrated over the entire flow domain. On the other hand, the least-square approach requires optimization over the entire

flow domain with a smoothing function because the square of the residual, $e_{ij}e_{ij}$, may have locally violent changes. Thus, the integrated square of the error function, $E_{ij}(C)$, is

$$E_{ij}(C) = \int G(\mathbf{x},\mathbf{x}')e_{ij}(\mathbf{x}')e_{ij}(\mathbf{x}')d\mathbf{x}' \tag{2.56}$$

where $G_f(\mathbf{x},\mathbf{x}')$ is a smoothing function. Substituting Equation (2.52) into Eqution (2.56), we get

$$\begin{aligned} E_{ij}(C) &= \int G(\mathbf{x},\mathbf{x}')(\overline{L}_{ij} - C\overline{M}_{ij})^2 d\mathbf{x}' \\ &= \int G(\mathbf{x},\mathbf{x}')\overline{L}_{ij}\overline{L}_{ij}d\mathbf{x}' - 2\int G(\mathbf{x},\mathbf{x}')C\overline{L}_{ij}\overline{M}_{ij}d\mathbf{x}' + \int G(\mathbf{x},\mathbf{x}')C^2\overline{M}_{ij}\overline{M}_{ij}d\mathbf{x}' \end{aligned} \tag{2.57}$$

Since the least square condition for Equation (2.57) is $\frac{\partial E_{ij}(C)}{\partial C} = 0$, the optimal model coefficient C is obained as

$$C = \frac{\int G(\mathbf{x},\mathbf{x}')\overline{L}_{ij}\overline{M}_{ij}d\mathbf{x}'}{\int G(\mathbf{x},\mathbf{x}')\overline{M}_{ij}\overline{M}_{ij}d\mathbf{x}'} \tag{2.58}$$

The computed C is obviously a function of time and space, and it can be applied to inhomogeneous flows. The smooth function G ($\boldsymbol{x}$, $\boldsymbol{x}$') should be chosen for the entire flow domain and may depend on the turbulence scales. Although the smooth function can be in many forms, a box filter (Equation (2.5)) may be the most convenient. This is because, according to the definition of large eddy simulation, a filter may be used as a smooth function. The filter can be either a grid filter or a test filter:

$$C = \frac{\overline{\overline{L}_{ij}\overline{M}_{ij}}}{\overline{\overline{M}_{kl}\overline{M}_{kl}}} \qquad \text{(with the grid filter)} \tag{2.59}$$

or

$$C = \frac{\widetilde{\overline{L}_{ij}\overline{M}_{ij}}}{\widetilde{\overline{M}_{ij}\overline{M}_{ij}}} \qquad \text{(with the test filter)} \tag{2.60}$$

Equations (2.59) and (2.60) are now defined as the filtered dynamic SGS model (FDS model). The FDS_G has the grid filter in Equation (2.59), and FDS_T has the test filter in Equation (2.60). The function of the grid filter is to average the coefficient and to smooth large fluctuations of the coefficient. The filter technique can provide a stable numerical

solution. The FDSM can be considered a simple model compared with those proposed by Ghosal *et al.* (1996) and Meneveau *et al.* (1996).

The FDS-G or FDS-T can also be negative locally. According to Piomelli *et al.*(1991), a negative C indicates a negative eddy viscosity and implies an energy transfer from small scales to the resolved scales or backscatter. However, the negative C can also lead to numerical instability. In order to avoid this instability, the present investigation uses

$$C = \text{Max}\ (0.0, \text{Equation (2.59)}, \text{Equation (2.60)}) \tag{2. 61}$$

which has been also used others (Murakami, *et al.*, 1995).

Similarly, we can calculate the Prandtl number in the dynamic subgrid heat fluxes with the same procedure. The subgrid heat flux on the test filter ($\widetilde{G}$ filter) is

$$H_j = \widetilde{\overline{u_j \theta}} - \widetilde{\overline{u}}_j \widetilde{\overline{\theta}} \tag{2. 62}$$

Substitute Equation (2.62) from Equation (2.17) with a test filter

$$H_j - \widetilde{h}_j = R_j \tag{2. 63}$$

where $R_j = \widetilde{\overline{u}_j \overline{\theta}} - \widetilde{\overline{u}}_j \widetilde{\overline{\theta}}$. Applying a grid filter to Equation (2.63), the equation becomes

$$\overline{H}_j - \overline{\widetilde{h}}_j = \overline{R}_j \tag{2. 64}$$

Now all the terms in Equation (2.64) are related to the grid filter. If h_j and H_j in Equation (2.64) are replaced by a simplified Boussinesq approximation, the replacement leads to an error in satisfying Equation (2.64). The error associated with a model, h_j^{model}, is given by

$$e^h{}_j = \overline{R}_j - (\overline{H}_j^{model} - \overline{\widetilde{h}}_j^{model}) \tag{2. 65}$$

With the simplified Boussinesq approximation,

$$h_j = 2C_\tau \overline{\Delta}^2 \frac{|\overline{S}|}{Pr^h{}_{SGS}} \frac{\partial \overline{\theta}}{\partial x_j} \tag{2. 66}$$

$$H_j = 2C_T \widetilde{\overline{\Delta}}^2 \frac{|\widetilde{\overline{S}}|}{Pr^H{}_{SGS}} \frac{\partial \widetilde{\overline{\theta}}}{\partial x_j} \tag{2. 67}$$

If we define $\alpha^{H}{}_{j} = 2\tilde{\bar{\Delta}}^{2}\left|\tilde{\bar{S}}\right|\frac{\partial\tilde{\bar{\theta}}}{\partial x_j}$ and $\beta^{h}{}_{j} = 2\bar{\Delta}^{2}\left|\bar{S}\right|\frac{\partial\bar{\theta}}{\partial x_j}$, then Equation (2.65) can be rewritten as

$$e_j^h = \bar{R}_j - \overline{(C_T \frac{1}{Pr_{SGS}^H}\alpha_j^H - C_\tau \frac{1}{Pr_{SGS}^h}\beta_j^h)} \approx \bar{R}_j - C(\overline{\frac{1}{Pr_{SGS}^H}\alpha_j^H} - \overline{\frac{1}{Pr_{SGS}^h}\beta_j^h}) \qquad (2.68)$$

With the following assumptions

$$\overline{\alpha_j^H \frac{1}{Pr_{SGS}^H}} \approx \bar{\alpha}_j^H \overline{\frac{1}{Pr_{SGS}^H}} \qquad (2.69)$$

$$\overline{\tilde{\beta}_j^h \frac{1}{Pr_{SGS}^h}} \approx \bar{\tilde{\beta}}_j^h \overline{\frac{1}{Pr_{SGS}^h}} \qquad (2.70)$$

$$\overline{\frac{1}{Pr_{SGS}^h}} \approx \overline{\frac{1}{Pr_{SGS}^H}} \approx \frac{1}{Pr_{SGS}} \qquad (2.71)$$

Eq. (2.66) becomes,

$$e_j^h = \bar{R}_j - C\frac{1}{Pr_{SGS}}\bar{P}_j \qquad (2.72)$$

where $P_j = \alpha_j^H - \tilde{\beta}_j^h$.

By using the least-square approach, we also can obtain an optimal $\frac{1}{Pr_{SGS}}$. The integrated square of the error function, $E_j^h(\frac{1}{Pr_{SGS}})$, is

$$E^h{}_j(\frac{1}{Pr_{SGS}}) = \int G_f^h(\mathbf{x},\mathbf{x}')\, e^h{}_j(\mathbf{x}')\, e^h{}_j(\mathbf{x}')\, d\mathbf{x}' \qquad (2.73)$$

where $G_f^h(\mathbf{x},\mathbf{x}')$ is a smooth function. Substitute Equation (2.72) into Equation (2.73), giving

$$E^h{}_j\left(\frac{1}{Pr_{SGS}}\right) = \int G_f^h(\mathbf{x},\mathbf{x}')\left(\overline{R}_j - C\frac{1}{Pr_{SGS}}\overline{P}_j\right)^2 d\mathbf{x}' \qquad (2.74)$$

Since the least square condition for the Equation (2.74) is $\frac{\partial E_j^h\left(\frac{1}{Pr_{SGS}}\right)}{\partial\left(\frac{1}{Pr_{SGS}}\right)} = 0$, then the optimal subgrid turbulent Prandtl number $\frac{1}{Pr_{SGS}}$ is

$$\frac{1}{Pr_{SGS}} = \frac{1}{C}\frac{\int G_f^h(\mathbf{x},\mathbf{x}')\overline{R}_j\overline{P}_j d\mathbf{x}'}{\int G_f^h(\mathbf{x},\mathbf{x}')\overline{P}_j\overline{P}_j d\mathbf{x}'} \qquad (2.75)$$

To be consistent with Equations (2.56) and (2.57), a box filter (Equation (2.5)) can be used as the smooth function, $G_f^h(\mathbf{x},\mathbf{x}')$. Then the SGS Prandtl number $\left(\frac{1}{Pr_{SGS}}\right)$ is

$$\frac{1}{Pr_{SGS}} = \frac{1}{C}\frac{\overline{\overline{P}_j\overline{R}_j}}{\overline{\overline{P}_j\overline{P}_j}} \qquad \text{(with the grid filter)} \qquad (2.76)$$

or

$$\frac{1}{Pr_{SGS}} = \frac{1}{C}\frac{\widetilde{\overline{P}_j\overline{R}_j}}{\widetilde{\overline{P}_j\overline{P}_j}} \qquad \text{(with the test filter)} \qquad (2.77)$$

The FDS model takes 20% more computing time than the SS model because the model coefficient, C, in the FDS model needs to be calculated. In the current investigation, both the FDS model and the SS model are used.

2.3 Numerical Methods

This section describes the numerical method used to solve the governing equations presented in Section 2.1. The computational grid adopted in the current study is introduced first. The discretization schemes for spatial terms and time advancement are then described. The procedure to solve the equations is introduced and the method to solve the Poisson equation is presented. Finally, the determination of the time step size is discussed.

2.3.1 Computational grid

The Navier-Stokes equations are discretized on a staggered Cartesian grid (Harlow and Welch, 1965). For the airflows around and inside buildings, the grid is usually non-uniform in all three directions due to the inhomogeneous characteristics of the airflows. A two-dimensional computational cell (i, j) is illustrated in Figure 2.1. The velocity components (u, v) are defined on the cell surfaces, whereas the pressure, p, and the temperature, θ, are defined at the center of the cell.

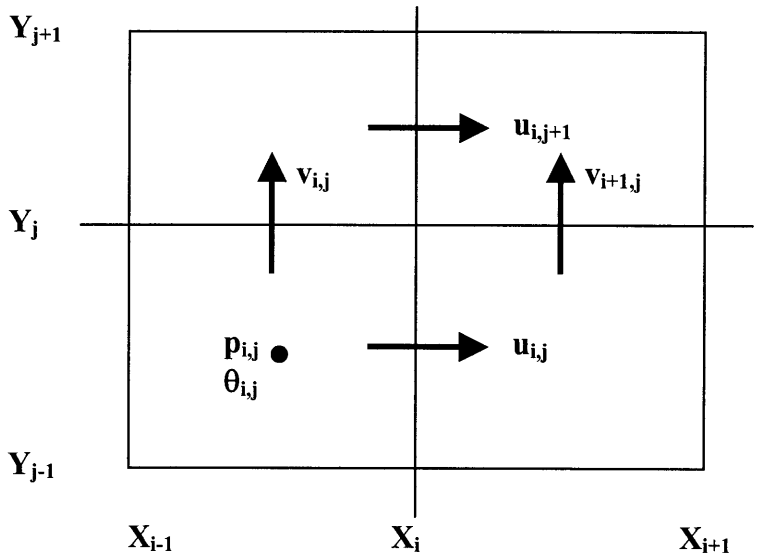

Figure 2.1 *Staggered computational grid in two dimensions.*

2.3.2 Discretization schemes

The current study uses a second-order finite-difference method to discretize the governing equations of LES (Equations (2.18) - (2.20)). Since there is no time derivative term in the continuity equation of LES (Equation (2.19)), the continuity equation cannot be solved directly. Techniques have been developed to correlate the continuity equation with the momentum equations, which will be discussed in Section 2.3.3. Therefore, only the spatial terms in the momentum and energy equations need to be discretized. Equations (2.78) and (2.79) list the spatial terms that need to be discretized. The schemes for time advancement of velocity and temperature are also discussed. For convenience, the overbar indicating filtered variables is dropped in this section.

$$\frac{\partial \overline{u_i}}{\partial t} + \underbrace{\frac{\partial}{\partial x_j}(\overline{u_i u_j})}_{\text{Spatial Term 1}} = \underbrace{-\frac{1}{\rho}\frac{\partial \overline{p}}{\partial x_i}}_{\text{Spatial Term 2}} + \underbrace{\nu \frac{\partial^2 \overline{u}_i}{\partial x_j \partial x_j} - \frac{\partial \tau_{ij}}{\partial x_j}}_{\text{Spatial Term 3}} + g_j \beta(\overline{\theta} - \theta_0)\delta_{ij} \qquad (2.78)$$

$$\frac{\partial \overline{\theta}}{\partial t} + \underbrace{\frac{\partial \overline{u}_j \overline{\theta}}{\partial x_j}}_{\text{Spatial Term 4}} = \underbrace{\frac{\partial}{\partial x_j}\left(\frac{\nu}{Pr}\frac{\partial \overline{\theta}}{\partial x_j}\right) - \frac{\partial h_j}{\partial x_j}}_{\text{Spatial Term 5}} \qquad (2.79)$$

Spatial derivatives

In the LES program, the second-order central scheme is used for spatial terms.

- Spatial Term 1: the convection term for the u component is discretized as

$$\frac{\partial(uu)}{\partial x} = \frac{\left(u_{i+\frac{1}{2},j,k}\right)^2 - \left(u_{i-\frac{1}{2},j,k}\right)^2}{\Delta x}$$

$$= \frac{\left[\frac{1}{2}(u_{i,j,k} + u_{i+1,j,k})\right]^2 - \left[\frac{1}{2}(u_{i,j,k} + u_{i-1,j,k})\right]^2}{x_{i+\frac{1}{2}} - x_{i-\frac{1}{2}}} \qquad (2.80)$$

$$\frac{\partial(uv)}{\partial y} = \frac{\left(u_{i,j+\frac{1}{2},k}\right)\left(v_{i+\frac{1}{2},j,k}\right) - \left(u_{i,j-\frac{1}{2},k}\right)\left(v_{i+\frac{1}{2},j-1,k}\right)}{\Delta y}$$

$$= \frac{\left[\frac{1}{2}(u_{i,j,k} + u_{i,j+1,k})\right]\left[\frac{1}{2}(v_{i,j,k} + v_{i+1,j,k})\right] - \left[\frac{1}{2}(u_{i,j,k} + u_{i,j-1,k})\right]\left[\frac{1}{2}(v_{i,j-1,k} + v_{i+1,j-1,k})\right]}{y_j - y_{j-1}} \qquad (2.81)$$

$$\frac{\partial(uw)}{\partial z} = \frac{\left(u_{i,j,k+\frac{1}{2}}\right)\left(w_{i+\frac{1}{2},j,k}\right) - \left(u_{i,j,k-\frac{1}{2}}\right)\left(w_{i+\frac{1}{2},j,k-1}\right)}{\Delta z}$$

$$= \frac{\left[\frac{1}{2}(u_{i,j,k} + u_{i,j,k+1})\right]\left[\frac{1}{2}(w_{i,j,k} + w_{i+1,j,k})\right] - \left[\frac{1}{2}(u_{i,j,k} + u_{i,j,k-1})\right]\left[\frac{1}{2}(w_{i+1,j,k-1} + w_{i+1,j,k-1})\right]}{z_k - z_{k-1}} \tag{2.82}$$

- Spatial Term 2: the pressure term for the u component is discretized as

$$\frac{1}{\rho}\frac{\partial p}{\partial x} = \frac{1}{\rho}\frac{(p_{i,j,k} - p_{i-1,j,k})}{(x_{i+\frac{1}{2}} - x_{i-\frac{1}{2}})} \tag{2.83}$$

- Spatial Term 3: the dissipation term for the u component, which includes both a molecular term and the SGS term, is discretized as

$$2.0\frac{\partial}{\partial x}\left[(\nu + \nu_{SGS})\frac{\partial u}{\partial x}\right] + \frac{\partial}{\partial y}\left[(\nu + \nu_{SGS})\left(\frac{\partial v}{\partial x} + \frac{\partial u}{\partial y}\right)\right] + \frac{\partial}{\partial z}\left[(\nu + \nu_{SGS})\left(\frac{\partial w}{\partial x} + \frac{\partial u}{\partial z}\right)\right]$$

$$= 2.0\left\{\left[(\nu + \nu_{SGS})\frac{\partial u}{\partial x}\right]_{i+1} - \left[(\nu + \nu_{SGS})\frac{\partial u}{\partial x}\right]_{i}\right\}/\Delta x$$

$$+ \left\{\left[(\nu + \nu_{SGS})\left(\frac{\partial v}{\partial x} + \frac{\partial u}{\partial y}\right)\right]_{j+1} - \left[(\nu + \nu_{SGS})\left(\frac{\partial v}{\partial x} + \frac{\partial u}{\partial y}\right)\right]_{j}\right\}/\Delta y$$

$$+ \left\{\left[(\nu + \nu_{SGS})\left(\frac{\partial w}{\partial x} + \frac{\partial u}{\partial z}\right)\right]_{k+1} - \left[(\nu + \nu_{SGS})\left(\frac{\partial w}{\partial x} + \frac{\partial u}{\partial z}\right)\right]_{k}\right\}/\Delta z \tag{2.84}$$

- Spatial Term 4: the convection term for temperature is discretized as

$$\frac{\partial(u_j\theta)}{\partial x_j}$$

$$= \frac{\theta_{i+\frac{1}{2},j,k}u_{i,j,k} - \theta_{i-\frac{1}{2},j,k}u_{i-1,j,k}}{\Delta x} + \frac{\theta_{i,j+\frac{1}{2},k}v_{i,j,k} - \theta_{i,j-\frac{1}{2},k}v_{i,j-1,k}}{\Delta y} + \frac{\theta_{i,j,k+\frac{1}{2}}w_{i,j,k} - \theta_{i,j,k-\frac{1}{2}}w_{i,j,k-1}}{\Delta z}$$

$$= \frac{\frac{1}{2}(\theta_{i,j,k}+\theta_{i+1,j,k})u_{i,j,k} - \frac{1}{2}(\theta_{i,j,k}+\theta_{i-1,j,k})u_{i-1,j,k}}{x_i - x_{i-1}}$$
$$+ \frac{\frac{1}{2}(\theta_{i,j,k}+\theta_{i,j+1,k})v_{i,j,k} - \frac{1}{2}(\theta_{i,j,k}+\theta_{i,j-1,k})v_{i,j-1,k}}{y_j - y_{j-1}}$$
$$+ \frac{\frac{1}{2}(\theta_{i,j,k}+\theta_{i,j,k+1})w_{i,j,k} - \frac{1}{2}(\theta_{i,j,k}+\theta_{i,j,k-1})w_{i,j,k-1}}{z_k - z_{k-1}} \qquad (2.85)$$

- Spatial Term 5: the dissipation term, which includes both the molecular term and the SGS term, is discretized as

$$\frac{\partial}{\partial x_j}\left(\frac{\nu}{Pr} + \frac{\nu_{SGS}}{Pr_{SGS}}\right)\frac{\partial\overline{\theta}}{\partial x_j}$$

$$= \left[\left(\frac{\nu}{Pr} + \frac{\nu_{SGS}}{Pr_{SGS}}\right)\frac{(\theta_{i+1,j,k} - \theta_{i,j,k})}{x_{i+\frac{1}{2}} - x_{i-\frac{1}{2}}} - \left(\frac{\nu}{Pr} + \frac{\nu_{SGS}}{Pr_{SGS}}\right)\frac{(\theta_{i-1,j,k} - \theta_{i,j,k})}{x_{i-\frac{1}{2}} - x_{i-\frac{3}{2}}}\right] / (x_i - x_{i-1})$$
$$+ \left[\left(\frac{\nu}{Pr} + \frac{\nu_{SGS}}{Pr_{SGS}}\right)\frac{(\theta_{i,j+1,k} - \theta_{i,j,k})}{y_{j+\frac{1}{2}} - y_{j-\frac{1}{2}}} - \left(\frac{\nu}{Pr} + \frac{\nu_{SGS}}{Pr_{SGS}}\right)\frac{(\theta_{i,j-1,k} - \theta_{i,j,k})}{y_{j-\frac{1}{2}} - y_{j-\frac{3}{2}}}\right] / (y_j - y_{j-1})$$
$$+ \left[\left(\frac{\nu}{Pr} + \frac{\nu_{SGS}}{Pr_{SGS}}\right)\frac{(\theta_{i,j,k+1} - \theta_{i,j,k})}{z_{k+\frac{1}{2}} - z_{k-\frac{1}{2}}} - \left(\frac{\nu}{Pr} + \frac{\nu_{SGS}}{Pr_{SGS}}\right)\frac{(\theta_{i,j,k-1} - \theta_{i,j,k})}{z_{k-\frac{1}{2}} - z_{k-\frac{3}{2}}}\right] / (z_k - z_{k-1}) \qquad (2.86)$$

Since the discretization of convection terms is a major source of numerical errors in an LES calculation, it is very important to choose an appropriate scheme for this operation. Although an upwind scheme to discretize the convection terms can provide a stable result,

it introduces a built-in numerical dissipation that can be larger than the dissipation introduced by the SGS stresses. Mittal and Moin (1997) found that an upwind scheme produces poor velocity power spectra compared with a central scheme. Therefore, the current calculation uses a second-order central differencing scheme to discretize the convection terms. This central differencing scheme may exhibit oscillating behavior due to insufficient grid resolution. Nevertheless, the convection terms should not be solved using an upwind scheme, especially not a lower order upwind scheme (Shah, 1998).

Time advancement

The velocities and temperature in the momentum and energy equations (Equations (2.78) and (2.79)) are discretized by the explicit Adams-Bashforth scheme, which is also a second-order differencing scheme (Lilly 1965). Therefore, the overall accuracy is second order. The velocity at the $(n+1)^{-th}$ time step is calculated as

$$
\begin{aligned}
& u_i^{n+1} \\
& = u_i^{n} + \Delta t \times \\
& \left\{ -\frac{3\times\left[\frac{\partial}{\partial x_j}(u_i u_i)\right]^{n} - \left[\frac{\partial}{\partial x_j}(u_i u_i)\right]^{n-1}}{2} - \frac{1}{\rho}\frac{\Delta p^{n+1/2}}{\Delta x_i} \right. \\
& \left. + (\nu+\nu_{SGS})\left[\frac{3\times\left(\frac{\partial^2 u_i}{\partial x_j \partial x_j}\right)^{n} - \left(\frac{\partial^2 u_i}{\partial x_j \partial x_j}\right)^{n-1}}{2}\right] + g_j\beta(\theta-\theta_0)\delta_{ij} \right\}
\end{aligned}
\qquad (2.87)
$$

The temperature at the $(n+1)^{-th}$ time step is calculated as

$$
\begin{aligned}
& t^{n+1} \\
& = t^{n} + \Delta t \times
\end{aligned}
$$

$$\left\{ -\frac{3\times\left[\frac{\partial}{\partial x_j}(u_j\theta)\right]^n-\left[\frac{\partial}{\partial x_j}(u_j\theta)\right]^{n-1}}{2} \right.$$

$$\left. +\frac{3\times\left[\frac{\partial}{\partial x_j}\left(\frac{\nu}{Pr}+\frac{\nu_{SGS}}{Pr_{SGS}}\right)\frac{\partial\bar{\theta}}{\partial x_j}\right]^n-\left[\frac{\partial}{\partial x_j}\left(\frac{\nu}{Pr}+\frac{\nu_{SGS}}{Pr_{SGS}}\right)\frac{\partial\bar{\theta}}{\partial x_j}\right]^{n-1}}{2} \right\} \qquad (2.88)$$

In Equations (2.87) and (2.88), the time advancement of the velocities, u_i^{n+1} and temperature, θ^{n+1}, are calculated explicitly based on the solved flow field from previous time steps.

2.3.3 Solution procedure

With the SGS model, the present study uses the simplified marker and cell method (SMAC) (Harlow and Welch, 1965) to solve the governing equations of LES. In order to correlate the momentum equation and the continuity equation, the SMAC method first solves the momentum equations without the pressure term. So the velocity obtained, $\bar{u}_i^*$, is a pseudo-velocity.

$$\frac{\partial\bar{u}_i^*}{\partial t}+\frac{\partial}{\partial x_j}(\overline{u_i u_j})=\nu\frac{\partial^2\bar{u}_i}{\partial x_j\partial x_j}-\frac{\partial\tau_{ij}}{\partial x_j}+g_j\beta(\bar{\theta}-\theta_0)\delta_{ij} \qquad (2.89)$$

Subtracting Equation (2.18) from Equation (2.89) yields:

$$\frac{\partial(\bar{u}_i^*-\bar{u}_i)}{\partial t}=\frac{1}{\rho}\frac{\partial p}{\partial x_i} \qquad (2.90)$$

Then, by differentiating both sides of Equation (2.90) and using Equation (2.19), we have

$$\frac{\partial}{\partial t}\left(\frac{\partial\bar{u}_i^*}{\partial x_i}\right)=\frac{1}{\rho}\frac{\partial^2 p}{\partial x_i^{\,2}} \qquad (2.91)$$

Equation (2.91) is a Poisson equation, whose solution will be discussed in the next section. With the solution of the Poisson equation for pressure, the real velocity can be calculated with

$$\bar{u}_i = \bar{u}_i^* - \frac{\Delta t}{\rho}\frac{\partial p}{\partial x_i} \tag{2.92}$$

2.3.4 Poisson equation

The Poisson equation for pressure (2.91) can be rewritten in the following form

$$\frac{\partial^2 p}{\partial x_i^{\,2}} = q \tag{2.93}$$

where $q = \frac{\rho}{\Delta t}\left(\frac{\partial \bar{u}_i^*}{\partial x_i}\right)$ is a source term of the Poisson equation.

With the second-order center-differencing scheme, the corresponding differencing equation for Equation (2.93) is

$$\frac{\dfrac{p_{i+1,j,k}-p_{i,j,k}}{\Delta x_{i+1/2}} - \dfrac{p_{i,j,k}-p_{i-1,j,k}}{\Delta x_{i-1/2}}}{\Delta x_i} + \frac{\dfrac{p_{i,j+1,k}-p_{i,j,k}}{\Delta y_{j+1/2}} - \dfrac{p_{i,j,k}-p_{i,j-1,k}}{\Delta y_{j-1/2}}}{\Delta y_j} + \frac{\dfrac{p_{i,j,k+1}-p_{i,j,k}}{\Delta z_{k+1/2}} - \dfrac{p_{i,j,k}-p_{i,j,k-1}}{\Delta z_{k-1/2}}}{\Delta z_k} = q_{i,j,k} \tag{2.94}$$

which can be simplified in form to yield

$$a_{W,i}p_{i-1,j,k} + a_{S,j}p_{i,j-1,k} + a_{B,i}p_{i,j,k-1} - a_{P,i,j,k}p_{i,j,k} + a_{E,i}p_{i+1,j,k} + a_{N,i}p_{i,j+1,k} + a_{I,k}p_{i,j,k+1} = q_{i,j,k} \tag{2.95}$$

where

$$a_{W,i} = \frac{1}{\Delta x_i \Delta x_{i-1/2}}, \quad a_{S,j} = \frac{1}{\Delta y_j \Delta y_{j-1/2}}, \quad a_{B,k} = \frac{1}{\Delta z_k \Delta z_{k-1/2}},$$

$$a_{E,i} = \frac{1}{\Delta x_i \Delta x_{i+1/2}}, \quad a_{N,j} = \frac{1}{\Delta y_j \Delta y_{j+1/2}}, \quad a_{T,k} = \frac{1}{\Delta z_k \Delta z_{k+1/2}},$$

$$a_{P,i,j,k} = a_{W,i} + a_{E,i} + a_{S,j} + a_{N,j} + a_{B,k} + a_{T,k}$$

In Equation (2.95), known quantities are represented by a's. The p's represent unknown quantities. Since one such equation exists for each grid point (i, j, k), there is a total of

$$N = (I+1)\,(J+1)\,(K+1) \tag{2.96}$$

equations in the N unknown pressures. In the transient problem, one such set arises at each time step. These equations can be solved directly by elimination or by one of several iterative methods, such as relaxation, successive over-relaxation, or alternating direction iteration (ADI). Stone (1968) proposed a strong-implicit iterative procedure that converges much faster than other methods. In the strong-implicit method, the original set of Equation (2.95) is modified to make it amenable for direct elimination of a set of equations and rapid convergence of the iterative procedure. The advantage of applying this method is more significant for larger sets of equations and transient simulations, which characterize the current situations.

Although fast Fourier transformation (FFT) requires less computing time than the strong-implicit method, the FFT method requires uniform grid distribution along at least one direction. This situation might work well for airflows with at least one homogeneous direction. However, for airflows around and inside buildings, the grids along all three directions are normally non-uniformly distributed due to the strongly inhomogeneous characteristics of the airflows.

2.3.5 Time step

Since turbulence is an inherently unsteady flow, temporal accuracy is essential. The temporal accuracy of the calculation is dependent on the time step Δt. To choose a suitable time step, the following criteria have to be considered:

(1) Stability limit of the time advancement scheme. The stability limit for the explicit Adams-Bashforth scheme is determined by the Courant-Fredrichs-Lewy (CFL) number, which is defined as

$$CFL = \Delta t \left(\frac{|u|}{\Delta x}, \frac{|v|}{\Delta y}, \frac{|w|}{\Delta z} \right)_{max} \tag{2.97}$$

The present study set CFL = 1 as the upper limit.

(2) Physical consideration. To correctly predict the statistical characteristics of turbulent flows, all events contributing to turbulence need to be solved. It was found that the statistical characteristics of turbulence could be correctly represented if the time step size was larger than the Kolmogorov time scale, ν/u_τ^2 (Moin, *et al.* 1996). In the current study, the CFL limit produces a time step much larger than the Kolmogorov time scale.

2.4 Boundary Conditions

Boundary conditions, including the treatments of walls, and inflow and outflow conditions are discussed in this section.

2.4.1 Wall models

For the airflows around and inside buildings, Reynolds numbers are usually very high and walls are normally rough. If a non-slip boundary condition is used in such conditions, a large number of fine grids close to the walls are needed, which is not practical at present due to computer limitations. Therefore, a macroscopic boundary condition, a wall model, has to be introduced into the airflow study in buildings.

The current study uses the wall model suggested by Werner and Wengle (1991). This model can be applied to both fully developed turbulent regions and regions of unsteady laminar flow, which are common in airflows around and inside buildings. The model specifies the boundary conditions at walls by assuming that at a point close to the wall (P),

(1) the instantaneous velocity tangential to the wall is in phase with the instantaneous wall shear stress, τ_w.

(2) the instantaneous velocity distribution follows a linear law at the wall

$$u^+ = y^+ \qquad \text{for } y^+ \le 11.81 \tag{2. 98}$$

and a power-law

$$u^+ = A(y^+)^B \qquad \text{for } y^+ > 11.81 \tag{2. 99}$$

where A = 8.3 and B = 1/7, and the dimensionless velocity, u^+, and the distance, y^+, are defined as

$$u^+ \equiv \frac{u}{u_\tau} \tag{2. 100}$$

$$y^+ \equiv \frac{u_\tau y}{\nu} \tag{2. 101}$$

where the friction velocity, u_τ, is defined by

$$u_\tau \equiv \sqrt{\frac{\tau_w}{\rho}} \tag{2. 102}$$

Therefore, the wall shear stresses, τ_w, can be solved analytically,

$$|\tau_{wall}| = \frac{2\rho\nu|u|}{\Delta y} \qquad \text{for } |u| \le \frac{\nu}{2\Delta y} A^{\frac{2}{1-B}}$$

$$|\tau_w| = \rho\left[\frac{1-B}{2} A^{\frac{1+B}{1-B}} \left(\frac{\nu}{\Delta y}\right)^{1+B} + \frac{1+B}{A}\left(\frac{\nu}{\Delta y}\right)^{B} |u|\right]^{\frac{2}{1+B}}$$

$$\text{for } |u| > \frac{\nu}{2\Delta y} A^{\frac{2}{1-B}} \tag{2. 103}$$

where Δy is the vertical width of the grid volume next to the wall. Equation (2.98) shows that the non-slip boundary condition is used when $y^+ \le 11.81$.

2.4.2 Inflow condition

When applying LES to study airflow around buildings, the boundary conditions at open boundaries, which include inflow and outflow conditions, are complicated due to the effects of up and down-stream obstacles, free stream turbulence etc. This section discusses the inflow condition and the next section will discuss the outflow condition.

There are two types of inflow conditions, a windless situation and a windy situation. For the windless situation, there is no airflow introduced to a computational domain and the air movement inside the domain is driven only by buoyancy forces. Therefore, a zero-gradient condition,

$$\frac{\partial u_i}{\partial x_1} = 0 \tag{2. 104}$$

can be applied. If the computational domain is large enough, a symmetrical or non-slip condition can also be adopted.

In a windy condition, the technique for generating a realistic wind at the inflow boundary is very important. Since the inflow is always turbulent, it is not practical to use a non-turbulent mean velocity profile at the inlet or periodic boundary conditions along the streamwise direction. This is because a very long domain would be required to ensure that the turbulence is fully developed before it reaches the investigated buildings. Therefore, some techniques are required to generate the turbulent inflow. The simplest method is to store the time history of velocity fluctuations given from a preliminary LES computation (Werner and Wengle, 1991, and Shah, 1998). However, this method requires an extra computational cost to generate a series of transient flow fields and a large amount of memory to store the data. Therefore, it is not possible to use this technique in an airflow study for buildings. The current study uses random fluctuations superimposed on a mean velocity profile at the inlet. The fluctuations are constructed to be of the same magnitude as the real wind. This method was adopted by Akselvoll and Moin (1995).

2.4.3 Outflow condition

The treatment of an outflow boundary condition is also important. The boundary condition at the exit should cause a minimum of upstream influence and should permit eddies in the flow to exit the domain without any adverse effect on the flow field inside the computational domain. The current investigation uses the zero-gradient condition that has been used successfully for a long time. Although the convective boundary condition

$$\frac{\partial u_i}{\partial t} + U_c \frac{\partial u_i}{\partial x_1} = 0 \qquad (2.\ 105)$$

has been used in recent years, there is no established method to give a suitable value of the convective velocity, U_c.

2.5 Conclusions

This chapter describes the governing equations for LES, the SGS models of LES that are used in the current study, the numerical methods used to solve the governing equations, and the boundary conditions.

In LES, the large-scale eddies are computed directly and only the smallest scales of turbulence are modeled. To separate the large from the small scales, LES is based on a filtering operation, though which the governing equations of LES are obtained. In the LES equations, the unknown SGS Reynolds stresses and heat fluxes are characterized with SGS models. Two models are introduced and used in the current study, the SS model and the FDS model that is a modification based on the DS model.

The simplified marker and cell method (SMAC) is used to solve the LES governing equations and a second-order finite-difference method is used to discretize the governing

equations. The boundary conditions in terms of wall treatments, inflow and outflow conditions, and determination of the time step are discussed.

Chapter 3

Measurements of Natural Ventilation

In a naturally ventilated building, air is driven in and out due to pressure differences produced by wind or buoyancy forces. This chapter deals with measurements of natural ventilation caused by both types of forces.

To investigate natural ventilation driven by wind forces, a wind-tunnel experiment was conducted, and both cross ventilation and single-sided ventilation were investigated. Detailed airflow fields, including parameters such as mean and fluctuating velocity and pressure distributions inside and around building-like models were measured. In the wind tunnel, a Laser Doppler Anemometer (LDA) was used to provide accurate and detailed velocity data. The limitations of the experiment are discussed and the mechanism of natural ventilation driven by wind forces is examined by turbulence statistical analysis.

To investigate natural ventilation driven by buoyancy forces, a full-scale room with a heat source and a large opening was used to simulate an indoor environment and the room was placed in a large laboratory space that simulates a calm outdoor environment. Single-sided ventilation with two different opening sizes was investigated. Detailed airflow characteristics inside and outside of the room, such as mean velocity, fluctuating velocity and temperature distributions were measured with anemometers and other instrumentation. A modified constant injection method was used to measure the ventilation rate of the room with a tracer-gas system. The mechanism of this buoyancy-driven single-sided ventilation is discussed.

3.1 Measurements of Wind-Driven Natural Ventilation in a Wind Tunnel

In the wind-tunnel experiment, detailed measurements of airflow around and within a simple, cubic, building-like model were carried out in a boundary-layer wind tunnel. Two-dimensional mean and fluctuating velocity components were captured using Laser Doppler Anemometer (LDA) equipment. Measurement points were arranged in front, inside, and behind the model. The pressure distributions along the model surface were also measured. Three different natural ventilation cases were studied: single-sided ventilation with an opening in the windward wall, single-sided ventilation with an opening in the leeward wall, and cross ventilation with openings in both windward and leeward walls.

3.1.1 Experimental methodology

Facilities

The present investigation used the boundary layer wind tunnel at Cardiff University, UK that offers a working section 2.0 m × 2.0 m in area and 1.0 m in height. A 6.0 m upstream fetch in the tunnel uses a combination of blockages, fences and surfaces roughness (Lego

Duplo blocks) to simulate the lower part of an urban atmospheric boundary layer. The maximum wind speed in the tunnel is about 12.0 m/s. The layout of the wind tunnel is shown in Figure 3.1.

The instrument to measure the velocity distributions around and inside building models is a one-dimensional Laser Doppler Anemometer (LDA) commercially produced by Dantec (Figure 3.2). This system allows accurate velocity measurement in highly turbulent and recirculating flows without intruding into those flows. The equipment has a measurement resolution of ±0.05 m/s. The probe is positioned by a computer controlled traversing arm that provides a resolution of ±0.5 mm vertically and ±1.0 mm horizontally. Seeding for the LDA system was achieved using a fog mist introduced at the inlet of the tunnel.

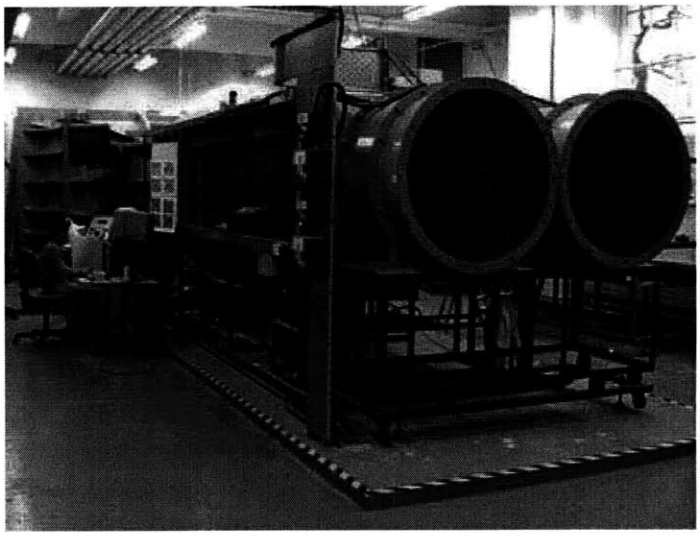

Figure 3.1 *The layout of the wind tunnel.*

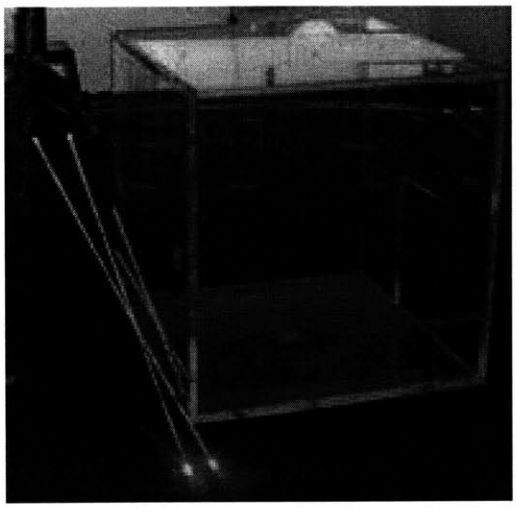

Figure 3.2 *The LDA used in the experiment.*

The velocity measurements were conducted on a grid plane at the center-section of the building. The velocities were measured along 10 vertical lines, and there were 18 measuring points at each line. The distance intervals between the bottom 16 points were 25 mm, and 50 mm for the top 2 points. Therefore, the measured height along each vertical line was 500 mm from the tunnel floor. Figure 3.3 shows the locations of the measuring lines.

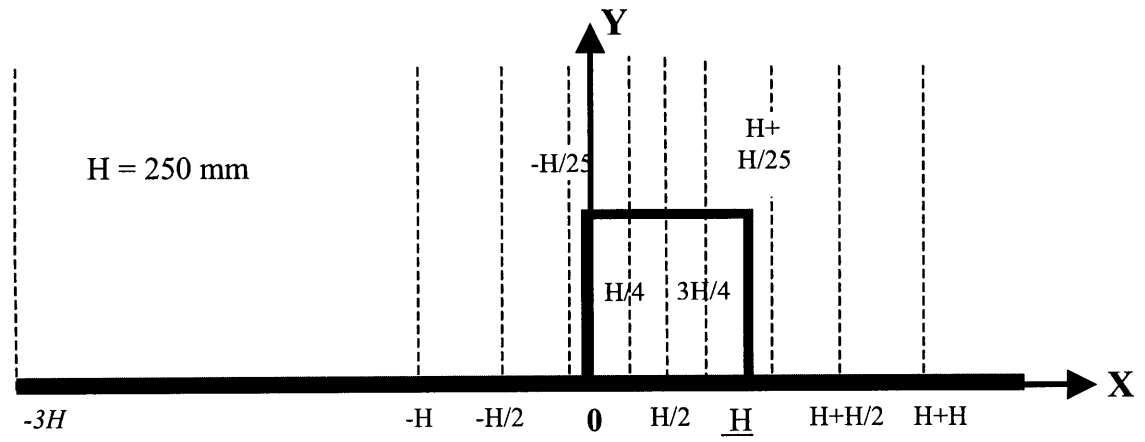

Figure 3.3 *Air velocities measurement locations (The thick block represents the building model).*

Data for several thousand measurements were collected at each grid point to provide both mean and fluctuating velocities. The LDA system available was one-dimensional, so measurements in the streamwise and vertical directions had to be taken in separate runs, with the probe repositioned between runs. Tunnel speed was monitored continuously so that the two components could be normalized; the variation in tunnel speed between measurement runs was less than 2%. Since the measurement was conducted along the center-section of the building and the model was symmetrical, the velocities along the spanwise direction were expected to be close to zero, and were not measured.

In addition to the velocity measurements, mean surface pressures along the center-section of the building surface were measured, using Furness Control differential pressure transducers coupled to Scanivalve port selectors. Pressure measurement accuracy is better than ±1%. Tunnel reference pressure head, as measured by a pitot tube positioned away from flow disturbances caused by the model, was used to calculate the surface pressure coefficient Cp.

Building Models

Two building-like models were made for the wind tunnel tests. One had only one opening in one wall, and the other one had openings in two opposite walls. To distinguish the

impact of the opening location on natural ventilation, the sizes of these two models and the openings were the same. For simplicity, the shape of the models was cubic, and the model size was 250 mm × 250 mm × 250 mm. The size of each opening was 84 mm × 125 mm (length × height), and the thickness of all the walls was 6 mm. For the model with only one opening, the opening could be placed on either the windward direction or the leeward direction. Three cases were conducted:

- Case 1 - single-sided ventilation with opening in windward wall
- Case 2 - single-sided ventilation with opening in leeward wall
- Case 3 - cross ventilation with openings in both windward and leeward walls

As noted previously, the wind tunnel models were intended to be "building-like," rather than a scale model of a building. Both the sizes of the model, and of the openings, are large to facilitate measurement.

The building models were made of transparent Perspex, to allow penetration of the LDA beam to the interior. Figure 3.4 shows a schematic view of the building model with one opening in the windward wall (Case 1).

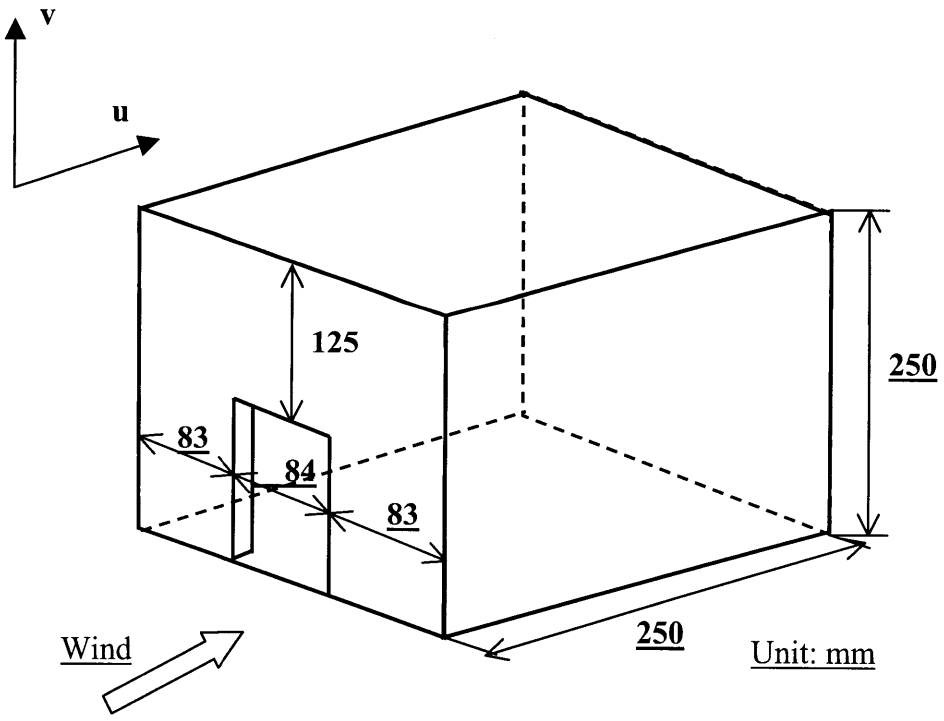

Figure 3.4 *A schematic view of the building model in Case 1 (single-sided ventilation with one opening in windward wall).*

3.1.2 Results and discussions

Detailed two-dimensional mean and fluctuating velocities measured around and inside the building model and the pressure distributions along the model surface will be presented in Chapter 5 as a comparison with the numerical results. In this section, three aspects of the experiment are discussed in more general terms. First, the airflow field is investigated in terms of flow patterns and motions. Second, the impacts of the seeding for the LDA system on the measured results are discussed. Third, the energy spectra of the flow field in the vicinity of the opening are studied to investigate the mechanism of this wind-driven natural ventilation.

Airflow field study

Figure 3.5 shows the measured flow field in the central section for all of the three cases. It was found that the airflow motions inside the building model for the cross ventilation case were much stronger than the two single-sided ventilation cases. Although the ventilation rates were not measured in the experiment, it is expected that the ventilation rate for cross ventilation is much higher than those for the single-sided ventilation cases. For single-sided ventilation with an opening in the windward direction, a complete, small and nearly-stationary eddy was formed at the opening, and functioned like a barrier, preventing large airflows entering (Figure 3.5 (a)). For single-sided ventilation with an opening in the leeward direction, the entering airflow does not encounter this difficulty because the airflow is within a large recirculation region downstream of the building, leading the airflow to the opening. Therefore, it is expected that the ventilation rate in the leeward case would be higher than that in the windward case. The ventilation rates computed with LES models for these cases are discussed in Chapter 5.

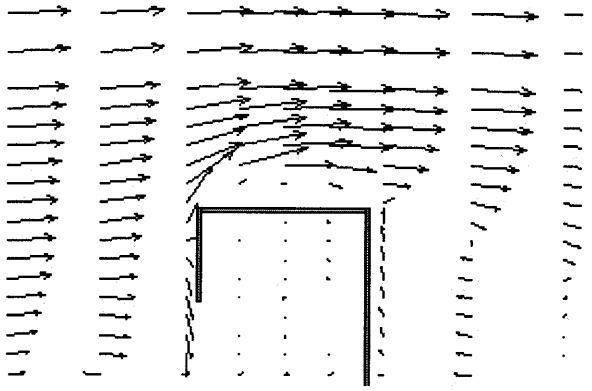

(a) single-sided, windward ventilation

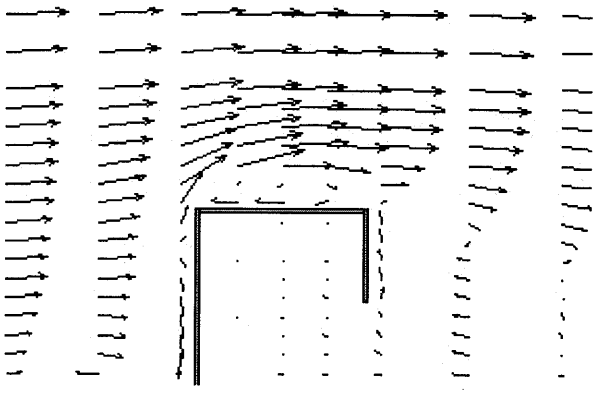

(b) single-sided, leeward ventilation

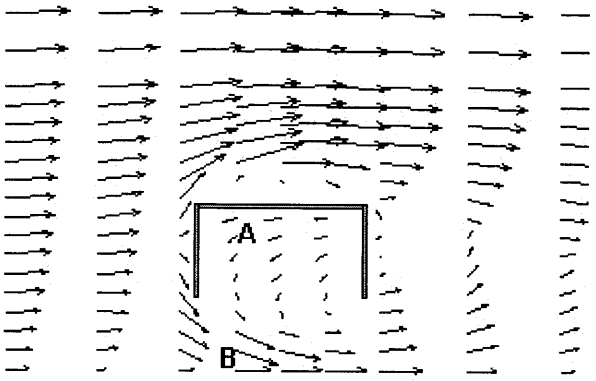

(c) Cross ventilation (A and B are the positions of the two demonstration points for energy spectral analysis).

Figure 3.5 *The measured mean flow field in the central section.*

Impacts of the seeding on the measured results

In the current experiment, to conduct LDA measurements of the airflow velocity, a fog mist was introduced at the inlet of the tunnel. The seeding particles from the fog mist injected into the flow field can be captured by the LDA system. Therefore, the velocities of the particles, which represent the airflow velocities at the corresponding locations, can be recorded. In order to obtain accurate velocity information, a large number of data points is needed at each measuring position. This requires abundant seeding particles at each measurement point. In most open and high-velocity flow fields, where the airflow motion is strong and particles can reach all areas without any difficulties, the needed amount of seeding particles can be collected quickly and easily. However, in some recirculation and low-velocity regions, such as the indoor airflow in the single-sided ventilation cases, it was difficult to seed the interior of the model due to weak flow motions. Although much longer measurement times were used in those regions, fewer particles were generally collected than in high-velocity regions. The difficulties in collecting particles in the interior and low-velocity regions led to the following two problems.

First, the fluctuating velocities in most of the interior and low-velocity regions were higher than the magnitudes of the mean velocities. In order to obtain accurate velocity information, a much larger amount of data points would be needed than those in the open (outdoor), high-velocity regions. However, as mentioned above, it was difficult to obtain the needed information. Therefore, the measured fluctuating velocities in the interior and low-velocity regions were not very meaningful.

Second, although the measured velocity data can be used to do energy spectral analysis, caution must be used in the recirculation and low-velocity regions. This is because the energy spectral analysis requires that variations of the airflow velocity be measured continuously. The energy spectrum of the velocity fluctuations, E(n), is defined as

$$\int_0^\infty E(n)\,dn = \overline{u'^2} \qquad (3.1)$$

where $\overline{u'^2}$ is the root-mean-square of the velocity fluctuation. However, as mentioned above, in the interior and low-velocity regions, it was hard for seeding particles to penetrate even though longer measurement times were used. Therefore, the measured energy spectra from these regions may not represent the real characteristics of the flow field, but the characteristics of the data collecting frequency. To demonstrate this problem, two measurement points were used to do the energy spectral analysis (Figure 3.5 (c)). In Figure 3.5 (c), Point A is in a low-velocity and recirculation region, and Point B is in a high-velocity region.

Figure 3.6 (a) shows how the velocity measured at Point A changes with time. Here, the "arrival time" means the time at which the seeding particles arrive at the measured point.

The time interval between collected data could be as large as from 35 to 55 seconds. This would lead to an artificial peak energy at low frequency, where most energy was contained in low-frequency regions (Figure 3.6 (b)). However, this is due to the difficulties in collecting the seeding particles in the measurements, and it does not represent real flow properties. Figure 3.7 (a) shows how the velocity varies with time at Point B. In this case, the velocities were collected continuously within a short time period. The computed energy spectra represent the characteristics of the flow field and not the characteristics of the collecting frequency (Figure 3.7 (b)).

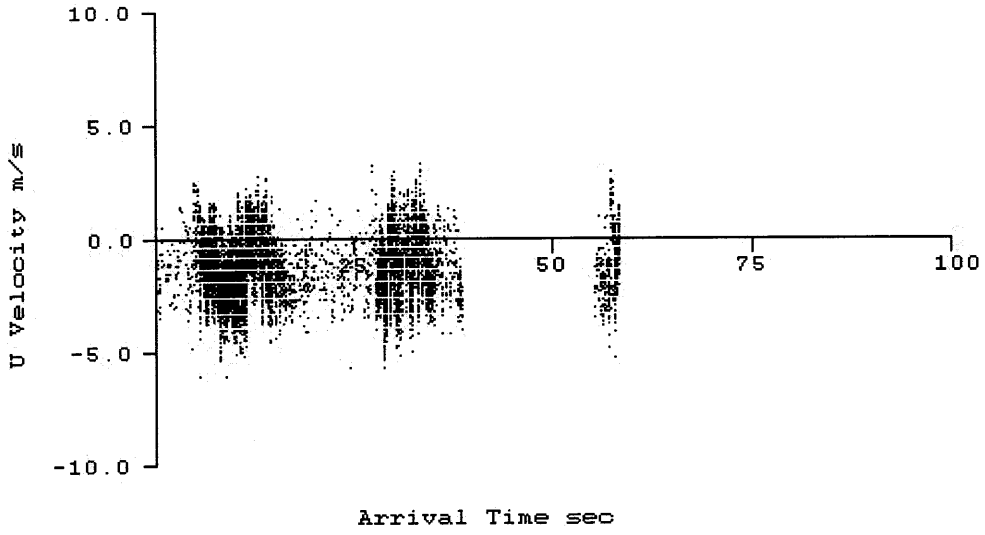

(a) Time series of the velocity component, u.

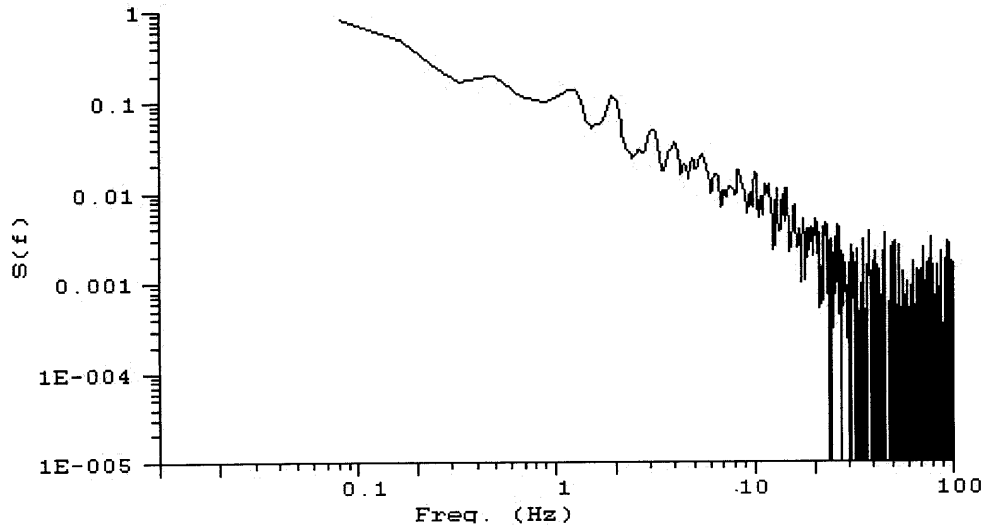

(b) Energy spectra of the velocity component, u.

Figure 3.6 *Flow field analysis at Point A (X = H/4 and Y= 0.8 H) in cross ventilation case.*

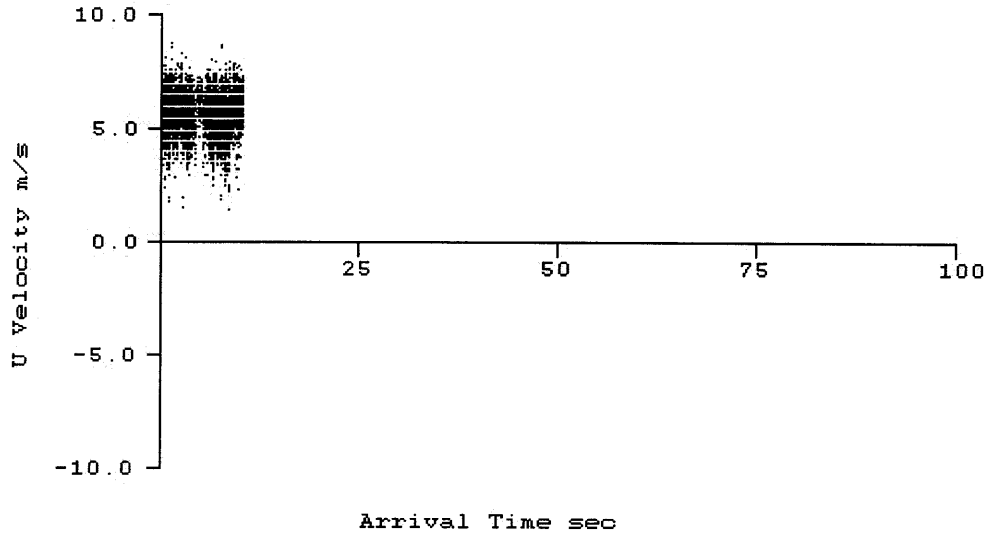

(a) Time series of velocity component, u.

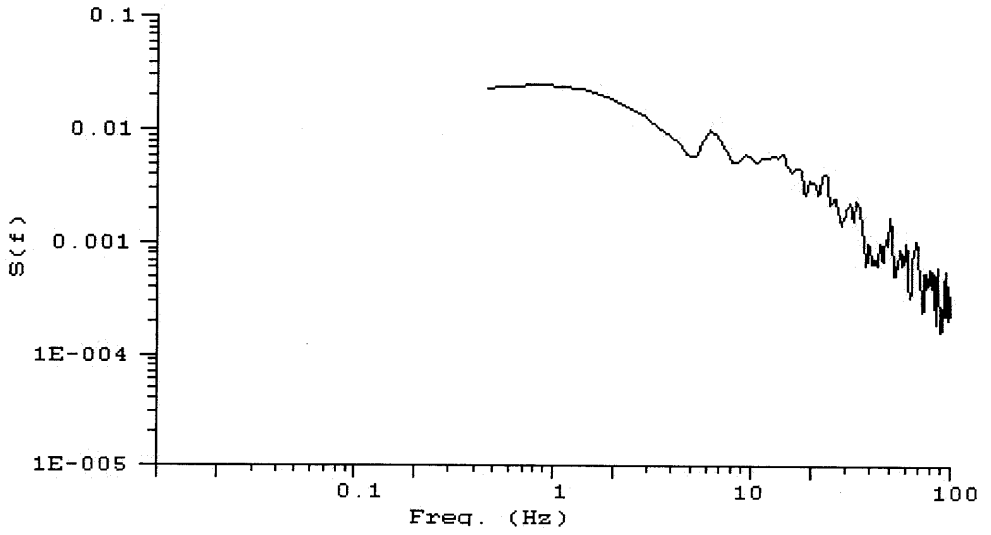

(b) Energy spectra of the velocity component, u.

Figure 3.7 *Flow field analysis at Point A (X = H/4 and Y= 0.1 H) in cross ventilation case.*

Energy spectral study

The examples give above illustrate the necessity for continous collection of velocity data if meaningful energy spectral analysis is to be performed. Thus, each time series to be analyzed was tested first to ensure that the collected velocities were continuously distributed within a short period of time. It was found that in the two single-sided ventilation cases, the time series of the collected velocities inside the building models were mostly not continuously distributed, and the variations of the velocity with time are similar to those shown in Figure 3.6 (a) due to weak flow motions in those regions. Therefore, it is not practical to do energy analysis inside the building model for those two cases, and only the energy spectra outside of the model close to the opening are studied.

Figures 4.8 and 4.9 show the energy spectral distributions outside of the building model. As pointed out by Hanzawa, *et al.* (1987), the study of energy spectra could help to reveal the impacts of turbulence on thermal comfort, which is an important factor in evaluating natural ventilation performance. In the current investigation, it was found that the spectral curve contains a wide range from 0.1 Hz to 100 Hz, and the peak energy is at about 1 Hz. Ohba *et al.* (2001) did a wind-tunnel experiment of cross ventilation, and they obtained similar results. This suggests that in the wind-tunnel generated ventilation cases, both low-frequency large eddies and high-frequency small eddies are contained in the flow field. However, whether this conclusion represents a real situation should be tested by detailed measurements of real winds inside and outside of buildings. Furthermore, it is very interesting to investigate how the energy spectral distribution affects the thermal comfort of human beings. These two types of experiments are suggested for future study of natural ventilation.

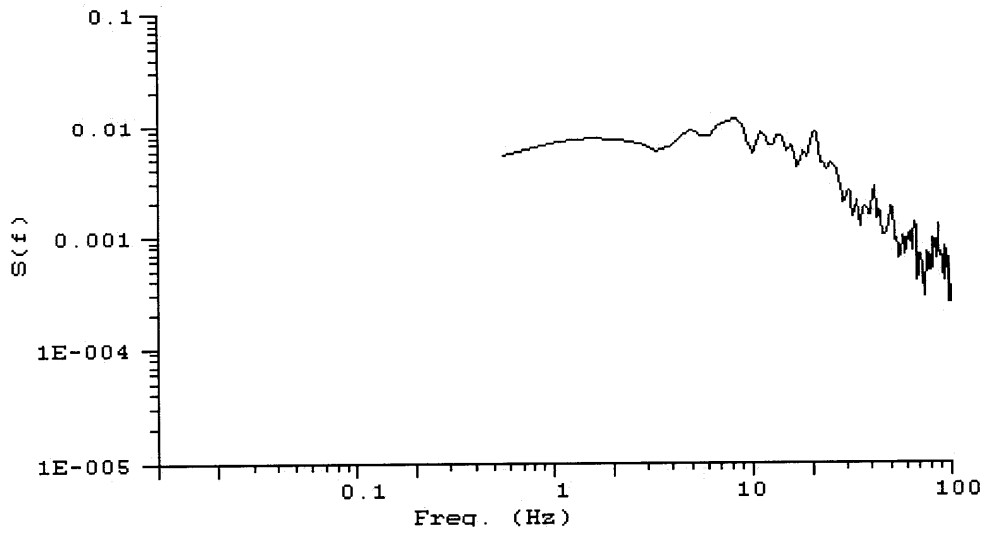

(a) Y = 0.3 H

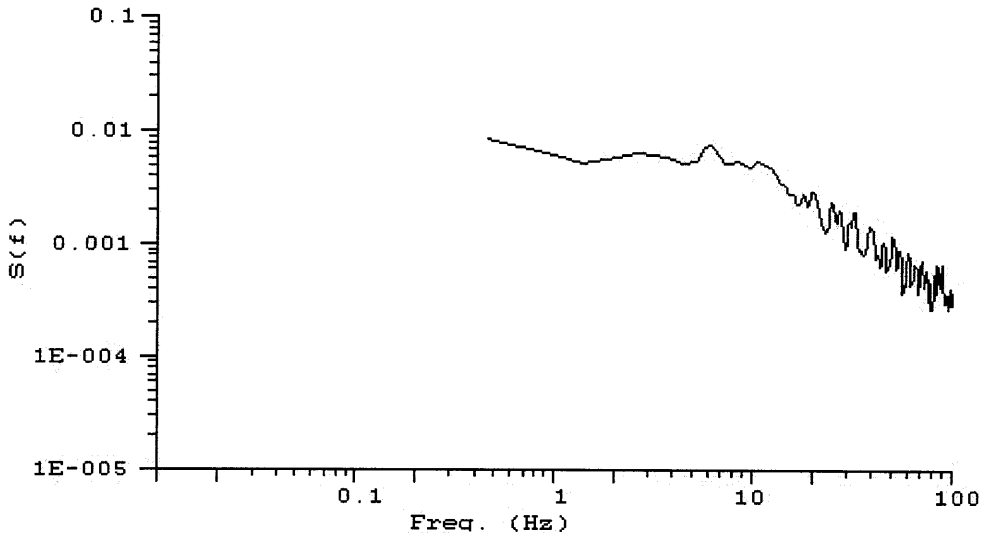

(b) Y = 0.5 H

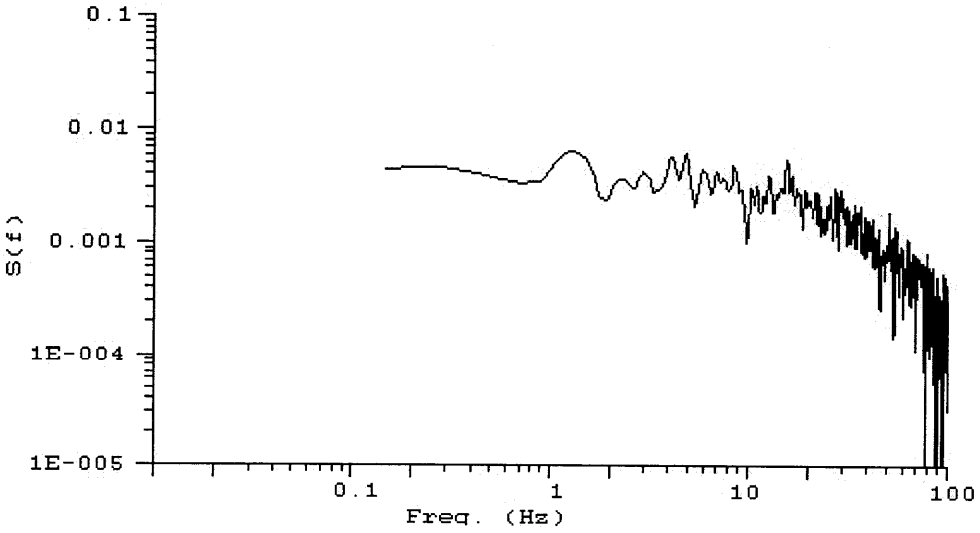

(c) Y = 0.8 H

Figure 3.8 *The energy spectra of the velocity component, u, outside of the building model in the single-side, windward ventilation case at X = -H/25.*

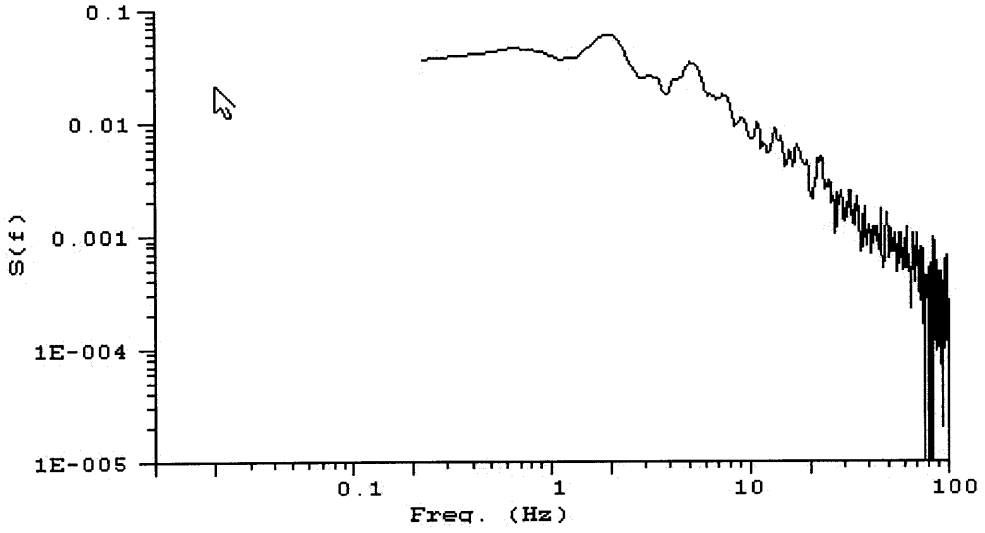
0.1
0.01
0.001
1E-004
1E-005
S(f)
0.1
1
10
100
Freq. (Hz)

(a) Y = 0.3 H

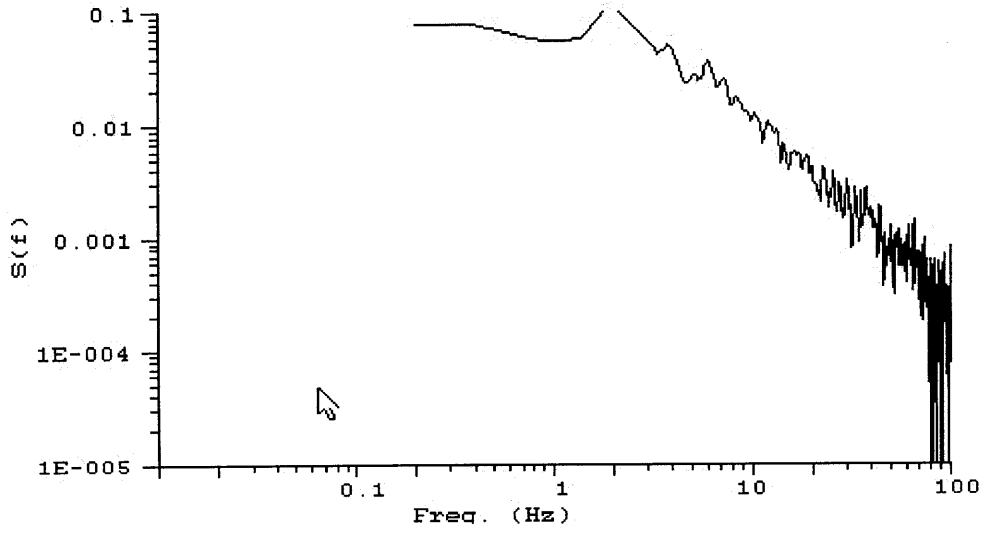
0.1
0.01
0.001
1E-004
1E-005
S(f)
0.1
1
10
100
Freq. (Hz)

(b) Y = 0.5 H

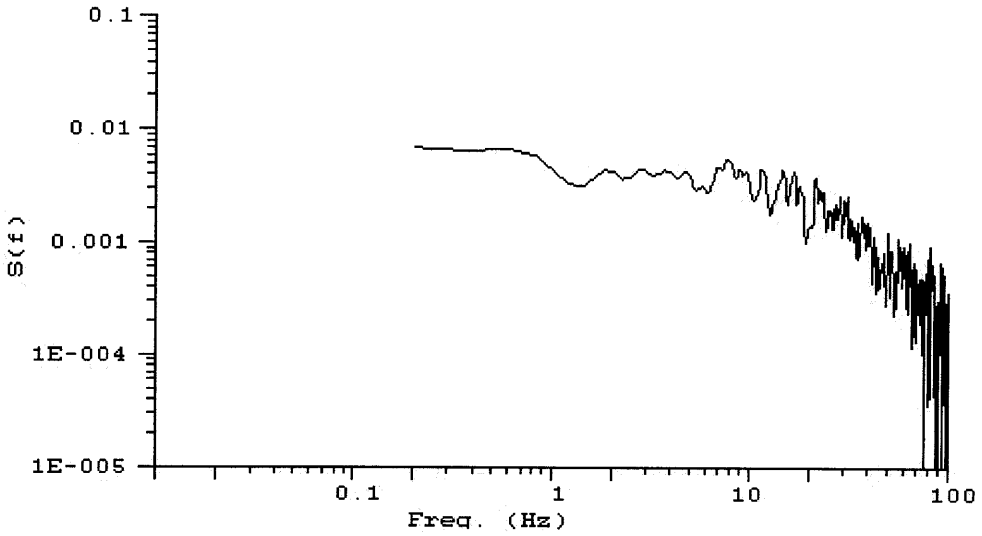

(c) Y = 0.8 H

Figure 3.9 *The energy spectra of the velocity component, u, outside of the building model in the single-side, leeward ventilation case at X = H+H/25.*

For the cross ventilation case, the energy spectra can be used to analyze both the inside and outside of the building model in the vicinity of the opening. Figure 3.10 shows the energy spectral distribution near the opening. The turbulence energy spectra of the air velocity are almost the same both outside and inside of the building model. This means that the airflow maintains its turbulence characteristics after going through the opening. Again, the spectral curves are very similar to those obtained in single-sided ventilation cases.

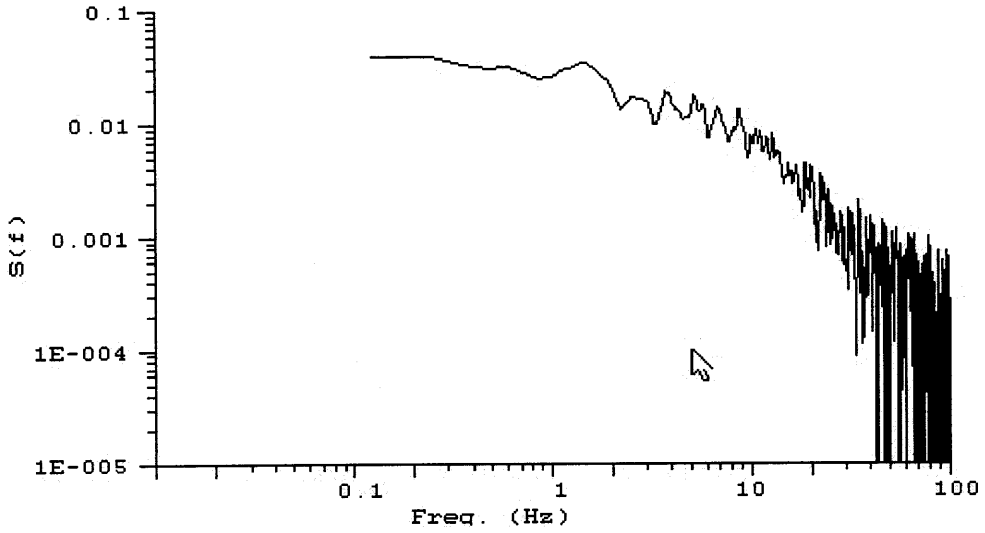

(a) Outside of the room at X = -H/25 and Y = 0.1 H.

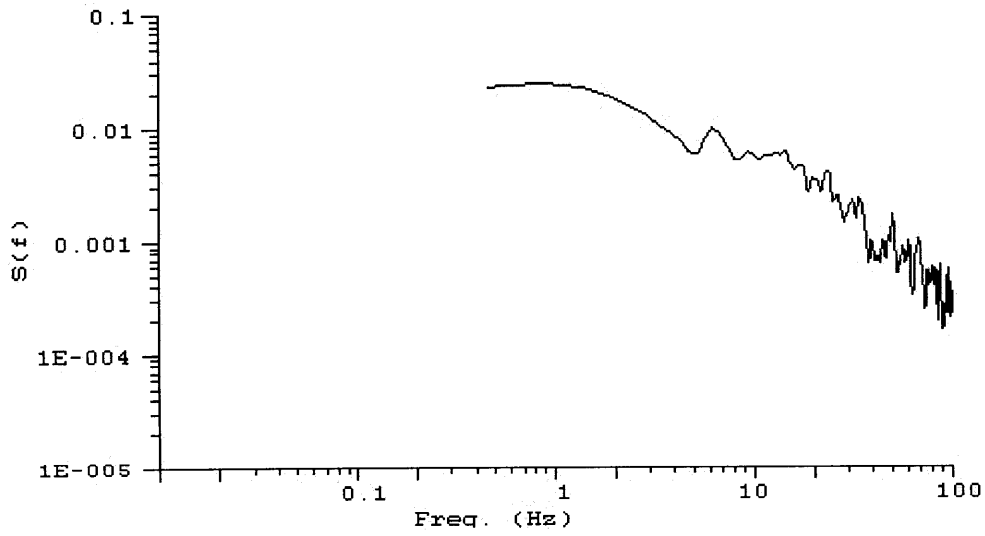

(b) Inside the room at X = H/4 and Y = 0.1 H.

Figure 3.10 *The energy spectra of the velocity component, u, in the vicinity of the opening in the cross-ventilation case.*

3.2 Measurements of Buoyancy-driven Natural Ventilation in a Full-scale Chamber

Unlike wind-driven natural ventilation, few detailed experimental measurements for buoyancy-driven natural ventilation have been done in the past. It is difficulty to conduct such experiments and to provide detailed flow information for numerical model validations.

Wind-tunnel experiments cannot be used in this type of experiments due to the difficulties in generating high-Grashof number airflows analogous to a full-scale situation as required by similarity theory. Although small-scale modeling with water as the working fluid (Linden *et al.*, 1990) can be used to investigate the mechanism of buoyancy-driven forces produced by salinity differences within the fluid, the information obtained is limited and cannot be used for a CFD model validation. Therefore, a full-scale measurement is the optimal.

For full-scale experiments, however, it is hard to find a windless day in nature. Although Flourentzou, *et al.* (1997) did full-scale experiments in a windless situation, they only measured the airflow patterns and a few points at the openings in order to determine the discharge coefficients. Again, these data cannot be used to fully validate a CFD model. Therefore, the outdoor thermal and boundary conditions should be controlled in the experiment. The current investigation places a full-scale test room in a large laboratory environment so that the "outdoor environment" is windless.

3.2.1 Experimental methodology

The experimental facility consists of two chambers, a test chamber and an environmental chamber, placed in a large laboratory as shown in Figure 3.11. The current study used the test chamber to simulate an indoor environment and the laboratory space to simulate a windless outdoor environment. A 1,500 W baseboard heater was placed in the test chamber to generate buoyancy forces. The door of the test chamber was open to the laboratory. This resulted in single-sided ventilation driven by buoyancy forces. When the lower half of the door was blocked, the situation corresponds to a room with an open "window."

The air velocity and temperature distributions were measured with six hot-sphere anemometers at different heights (0.1m, 0.5m, 0.9m, 1.3m, 1.7m, and 2.1m from the floor) in five different locations (P1 through P5) inside and outside of the test chamber as shown in Figure 3.12. The anemometers have large uncertainty if the air velocity is lower than 0.1 m/s, and the temperature measurement error is 0.3 K. The measurement frequency was 10 Hz. The experiment also used a SF_6 tracer gas system to measure the ventilation rate of the room.

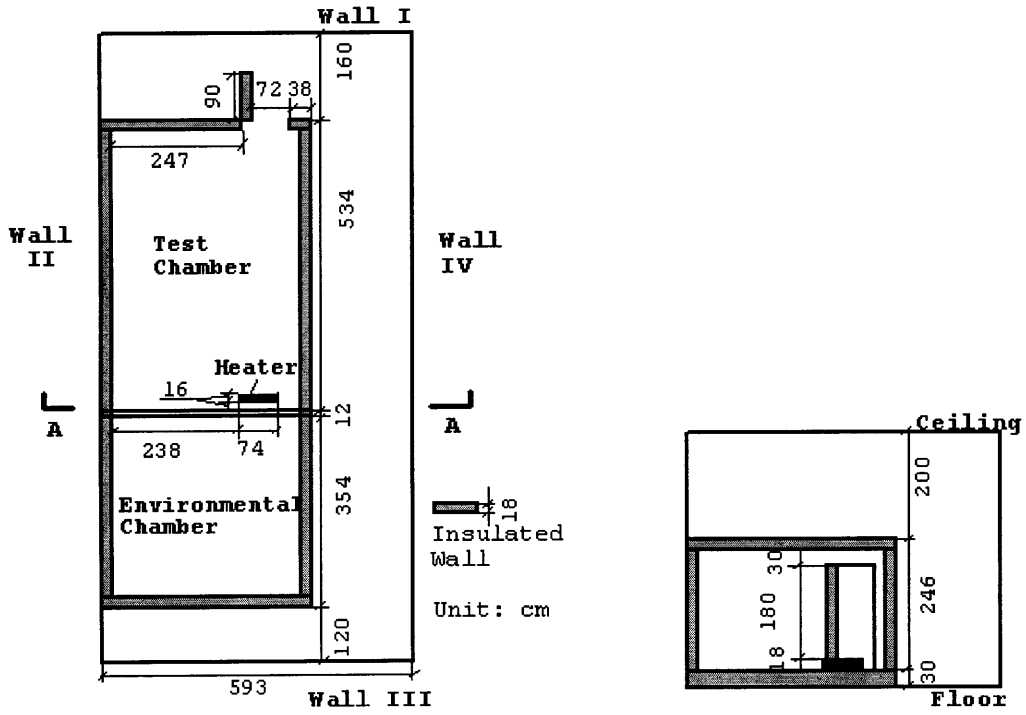

(a) The plan of the laboratory *(b) A-A section*

Figure 3.11 *The configuration of the laboratory.*

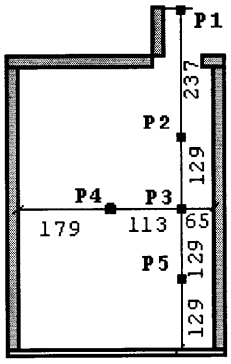

Figure 3.12 *The measuring positions.*

3.2.2 Results and discussions

This section discusses the impacts of the boundary conditions on the measured results and a modified constant injection method for the ventilation rate measurement.

Impacts of "outdoor" temperature variation on the measurements

The laboratory space outside of the test and environmental chambers was used to simulate a windless "outdoor" environment. However, the "outdoor" air temperature was not stable, and its temperature variation would affect the "indoor" temperature. This section discusses the impacts of this "outdoor" temperature variation on the measured results.

The measurements were performed in May and June 2001 in Greater Boston, Massachusetts, USA, during which the real outdoor air temperature varied significantly from day to day. Since Wall IV and the roof of the laboratory (Figure 3.11) were exterior, their surface temperatures were affected directly by the weather. Since each measurement took eight hours, the temperature on these exterior surfaces and that of the laboratory air varied during the measurements. The surface temperatures varied as much as 3.5 K as shown in Table 3.1. However, when the measured air temperature and velocity were non-dimensionalized, the differences among the three door cases (the same indoor conditions but measured on three different days) were generally within 5% as shown in Figure 3.13. Therefore, the weather did not affect the non-dimensional results.

Figure 3.13 also shows the measured results from the window case. Although the airflow distributions in the window case are very similar to those in the door case, there are three major differences. First, the temperature stratification outside of the room (at P1) in the window case is larger than that in the door case (Figure 3.13 (a)). Second, the air velocity at the lower part of P2 in the window case is higher than that in the door case (Figure 3.13 (b)). Third, the root-mean-square (RMS) velocities at the lower part of P2 and P3 in the window case are higher than those in the door case. These differences show that the airflow motion in the window case was stronger than that in the door case due to a larger temperature difference between inside and outside in the window case.

Table 3.1 *The surface temperatures of the laboratory (°C).*

Case Type	Door Case			Window Case
Test Number	Test 1	Test 2	Test 3	Test 4
Ceiling	25.11	23.11	26.67	26.46
Floor	22.78	22.11	24.78	24.28
Wall I	24.57	23.01	26.11	26.10
Wall II	24.39	22.83	25.58	25.47
Wall III	24.40	22.90	25.72	25.63
Wall IV	22.67	20.94	24.53	24.02

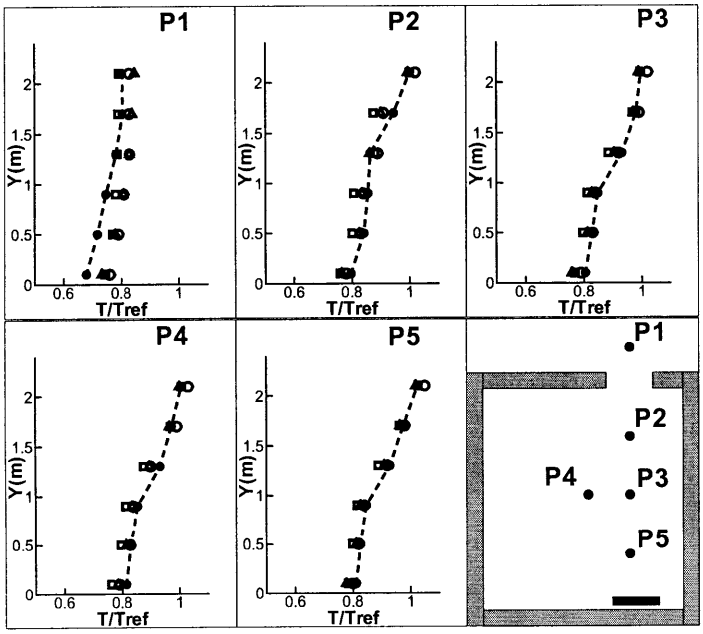

(a) Mean air temperature profiles

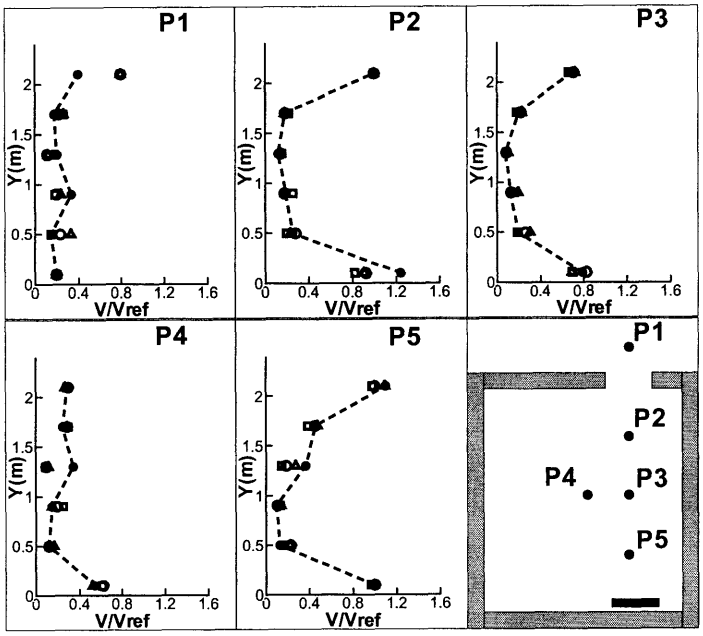

(b) Mean air velocity profiles

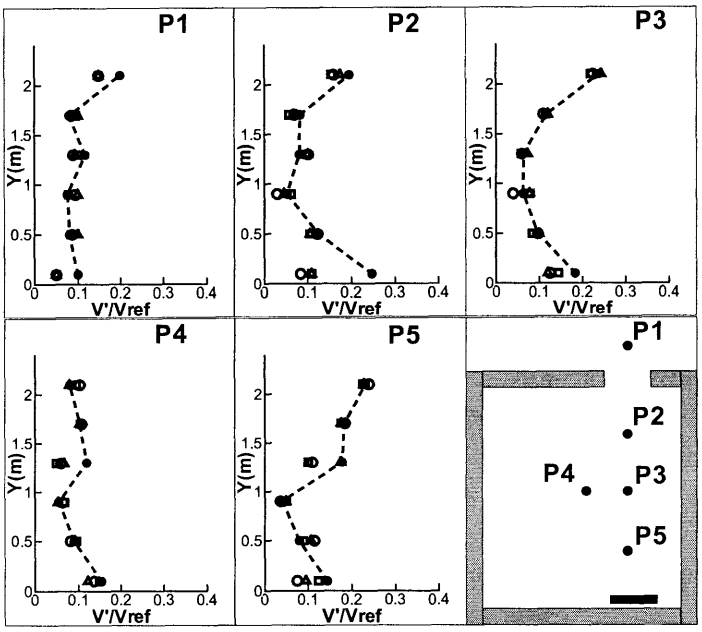

(c) Root-mean-square (RMS) velocity profiles

Figure 3.13 *Measured airflow distributions at the five locations (Non-dimensional values). Circles: Test 1; Squares: Test 2; Deltas: Test 3; Black dots with dashed lines: Test 4.*

Tracer gas measurement

With a tracer gas system, several methods can be used to measure the ventilation rate of a building. The current investigation applied a constant injection method, in which the tracer gas, SF_6, was injected into the chamber at a constant rate, and the SF_6 concentration in the chamber was measured.

By assuming that the concentration of the tracer gas in the test chamber was uniform at all times and the SF_6 concentration from the laboratory air was very low, one can obtain the ventilation rate (Etheridge and Sandberg, 1996)

$$Q = \frac{\dot{m}}{\frac{\int_{t_1}^{t_2} C^i(t)dt}{t_2 - t_1}} \tag{3.2}$$

Axley and Persily (1988) pointed out that this constant injection method could provide accurate estimates of the mean ventilation rate regardless of the amplitude of the flow variation if the variation period of the flow field was small compared to the mean flow nominal time constant. The variation period of the flow field is the inverse of the peak frequency of the flow energy spectra, and the mean flow nominal time constant, τ_n, is defined as

$$\tau_n = \frac{V}{Q} \tag{3.3}$$

In the current investigation, τ_n was about 500 s, and the variation period of the flow field was about 10 s. Therefore, Equation (3.2) gives accurate estimates of the mean ventilation rate. The flow fields studied in the current case were pseudo-steady and the SF_6 concentration and the ventilation rate did not change over time.

Since the SF_6 concentration in the laboratory air was not "low", Equation (3.2) must be modified for the current case. In the experiment, there was a time delay between the tracer gas entering the chamber and the tracer gas leaving the chamber. The delay was of the same order as the mean flow nominal time constant. Thus, the modified formula to compute the ventilation rate becomes

$$Q = \frac{\dot{m}}{\frac{\int_{t_1}^{t_2} [C^i(t) - C^e(t - \tau_n)]dt}{t_2 - t_1}} \tag{3.4}$$

When the flow field reaches a steady state, $[C^i(t) - C^e(t - \tau_n)]$ will become a constant. Since Q and τ_n are unknown, they can be determined by solving Equations (3.3) and (3.4) together.

When using the constant injection method, the SF_6 concentration in the chamber was assumed to be uniform at all times, namely $C^i(t)$ does not vary with position. In reality, the SF_6 concentration may not be uniformly distributed and was measured at different locations. In Test 1, SF_6 concentration was measured at P2 through P5 at 1.7 m above the floor. Figure 3.14 shows that the SF_6 concentrations are almost the same in the four indoor locations. In Tests 2, 3, and 4, SF_6 concentrations at 1.7 m from the floor in P4 and at 1.7 m from the floor at the opening were measured to represent the internal concentrations of SF_6 (Figures 3.15 ~ 3.17). Since in Tests 2 and 4, there were concentration differences between these two measured points (Figures 3.15 and 3.17), the ventilation rate was within a range instead of a single value. In all of four tests, the SF_6 concentration of the entering air was measured at the lower part of the opening (0.3 m from the floor for the door case and 1.3 m from the floor for the window case).

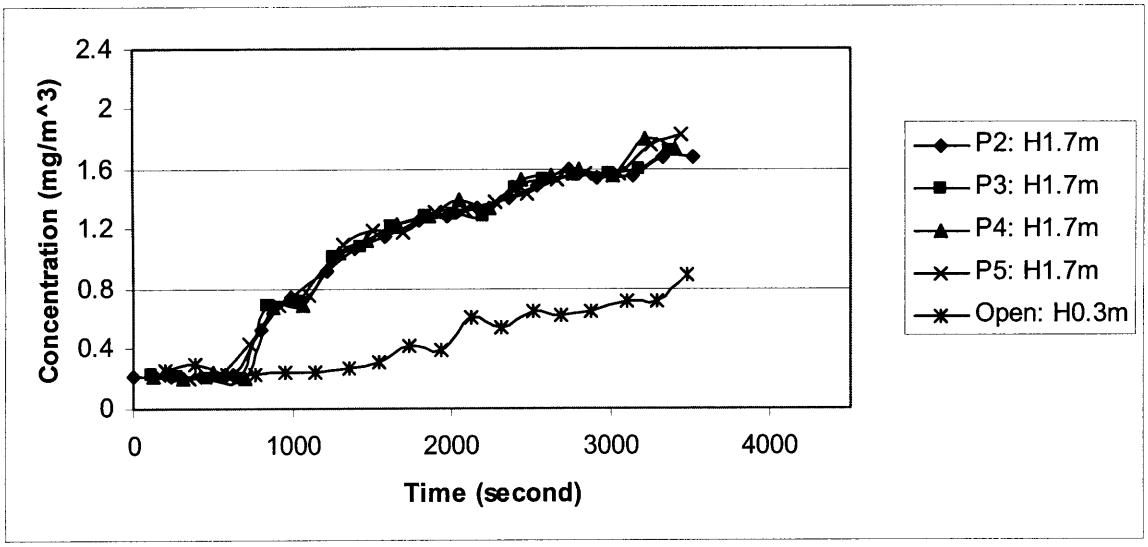

Figure 3.14 *The measured SF_6 at 1.7 m above the floor in P2 through P5 and 0.3 m above the floor in the opening for Test 1.*

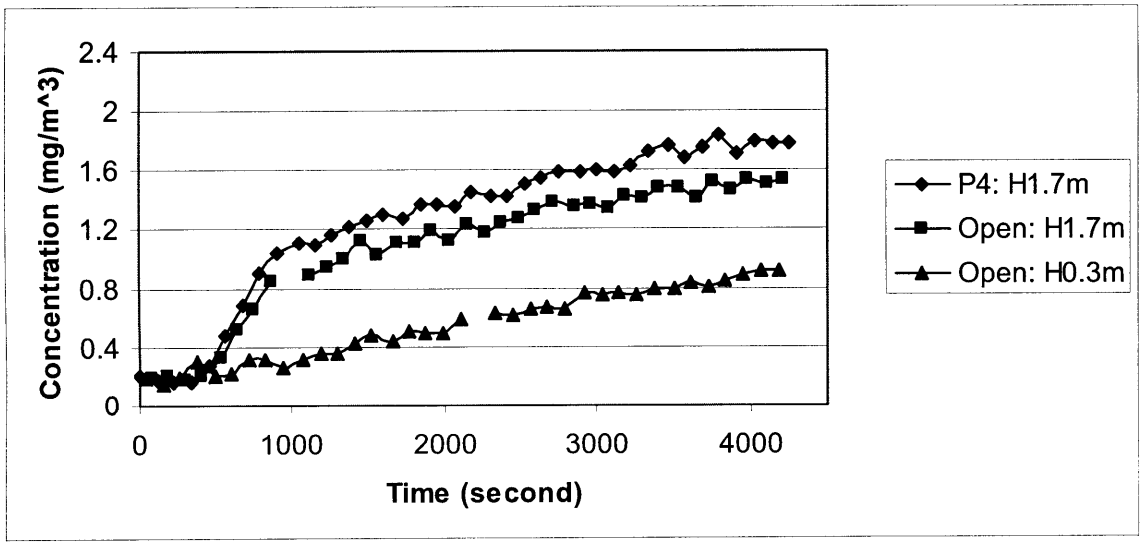

Figure 3.15 *The measured SF_6 at 1.7 m above the floor in P4, 0.3 m and 1.7 m above the floor at the opening for Test 2.*

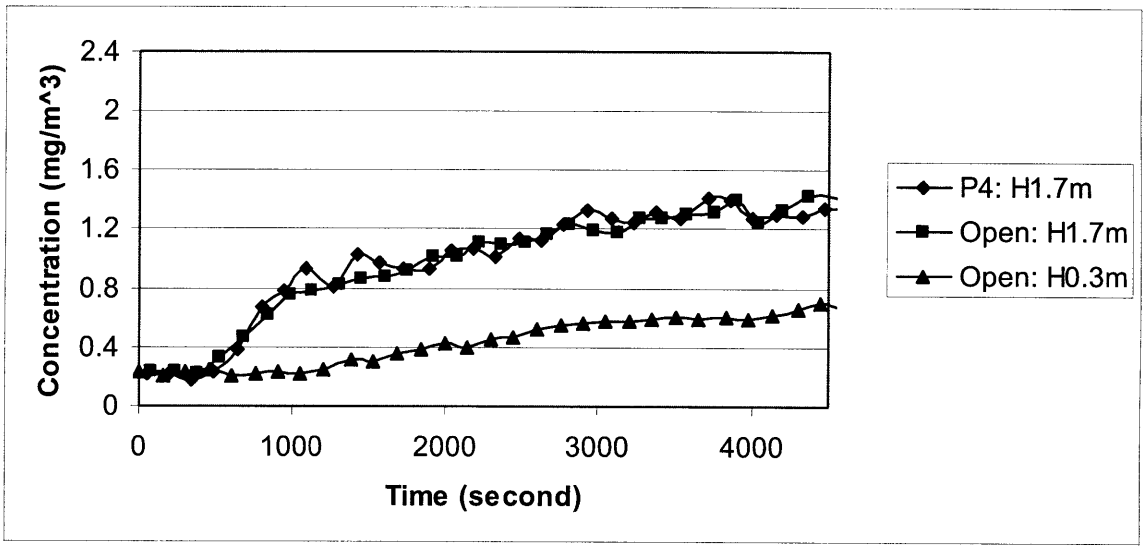

Figure 3.16 *The measured SF_6 at 1.7 m above the floor in P4, 0.3 m and 1.7 m above the floor at the opening for Test 3.*

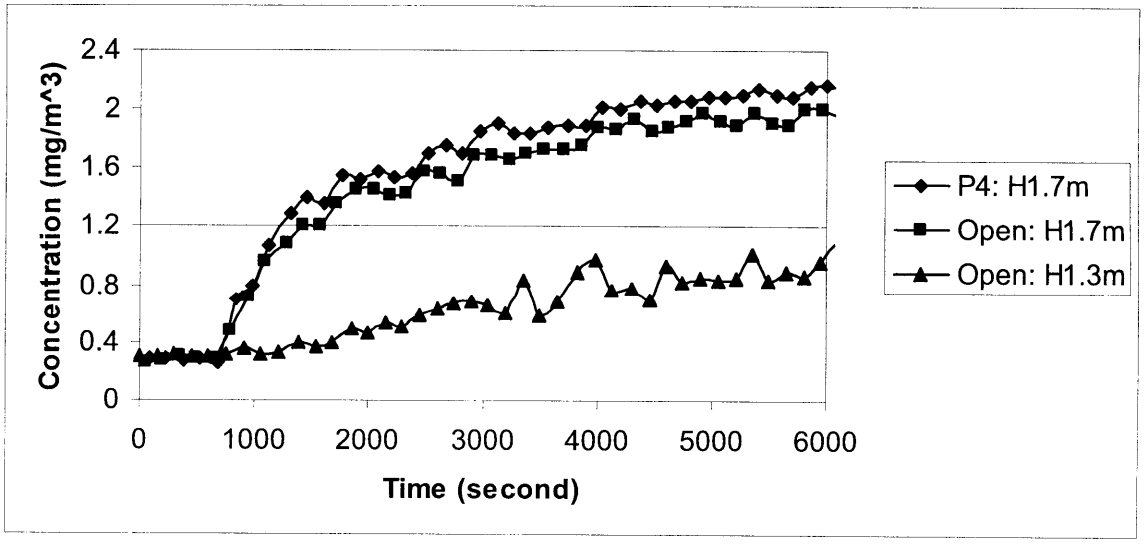

Figure 3.17 *The measured SF_6 at 1.7 m above the floor in P4, 0.3 m and 1.7 m above the floor at the opening for Test 4.*

Based on the measured data and with Equations (3.2) and (3.3), the ventilation rates shown in Table 3.2 were calculated. Table 3.2 shows that although the opening size of the window was only half that of the door, the ventilation rate of the window case was more than half of that in the door case. This is mainly due to the stronger airflow motion in the window case than that in the door case as observed in Figure 3.13.

Table 3.2 *The measured ventilation rates in the four tests.*

Case Type	Door Case			Window Case
Test number	Test 1	Test 2	Test 3	Test 4
Ventilation rate (m^3/s)	0.107	0.102~0.140	0.127	0.075~0.088
Ventilation rate (ACH)	9.63	9.18~12.60	11.43	6.75~7.92

Statistical analysis

Figures 3.18 and 3.19 show the measured turbulence energy spectra of the air speed near the opening (at P1 and P2) for the door and window cases, respectively. The turbulence energy spectra of the air velocity remain almost the same when entering the room from outside or leaving the room from inside. This means that the airflow maintains its turbulence characteristics after going through the opening. The figures also show that the spectral curve contains eddies from 0.01 Hz to 1 Hz, a narrower range than that observed in the wind-tunnel cases (Section 3.1.2). The peak energy is about 0.1 Hz, which is one order of magnitude lower than that in the wind-tunnel cases. Ohba *et al.* (2001) pointed out that wind whose energy was mostly contained in low-frequency regions would be more comfortable than wind consisting of small eddies in high-frequency regions. Therefore, this buoyancy-driven airflow in the full-scale chamber should be more comfortable than the wind-driven airflow in the high-speed wind tunnel if the temperature and humidity are the same.

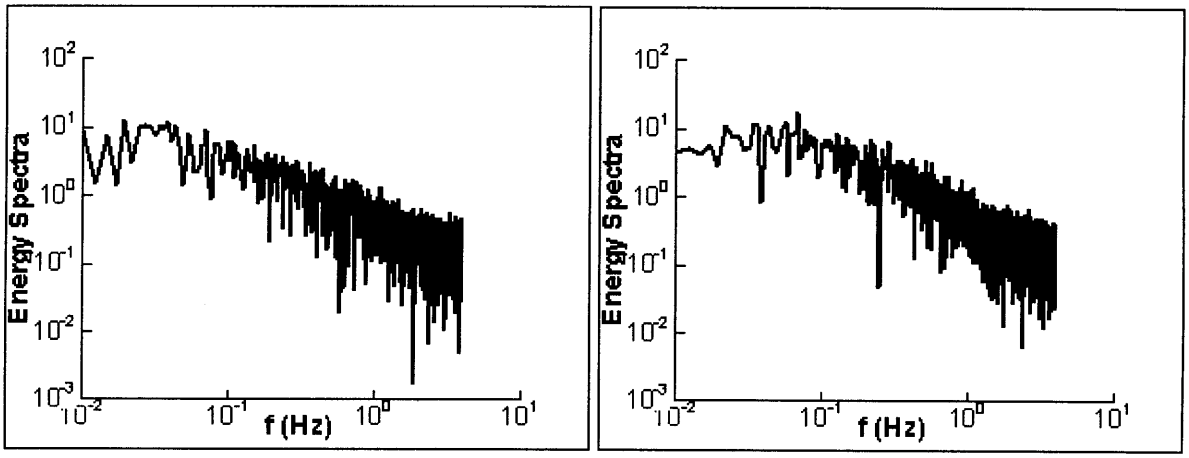

(a) H=0.5 m from the floor at P1.

(b) H=0.5 m from the floor at P2.

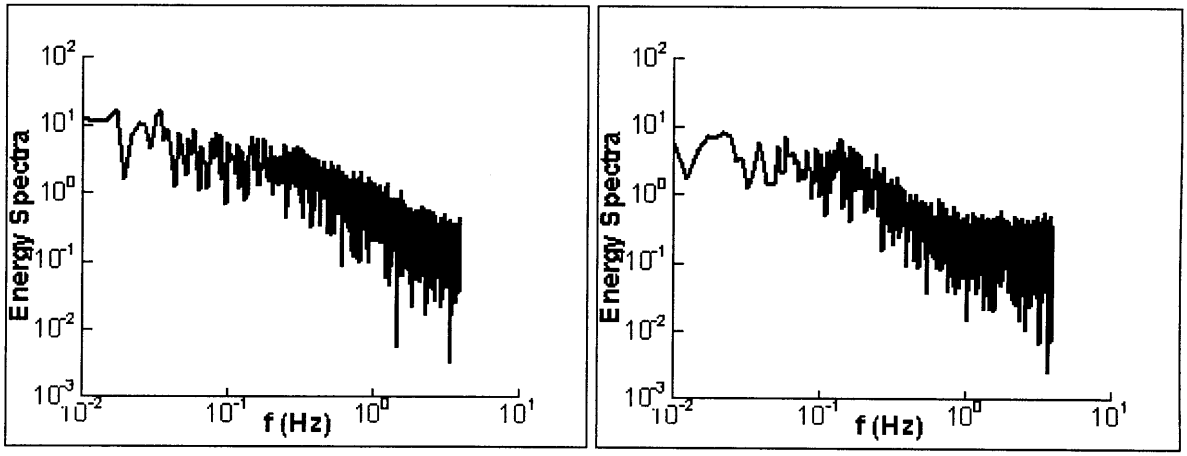

(c) H=1.7 m from the floor at P1.

(d) H=1.7 m from the floor at P2.

Figure 3.18 *The measured turbulence energy spectra in the opening vicinity for the open door case.*

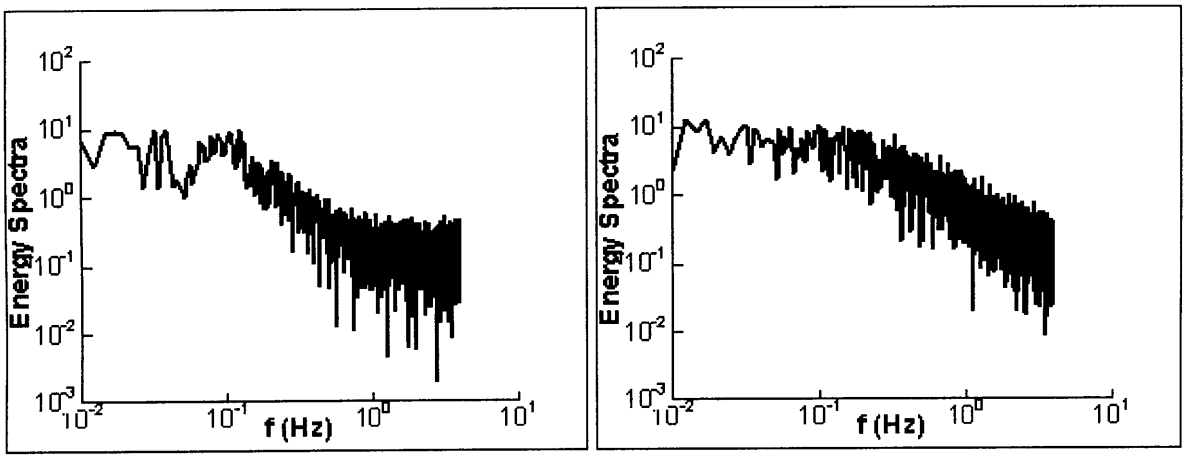

(a) H=0.5 m from the floor at P1.

(b) H=0.5 m from the floor at P2.

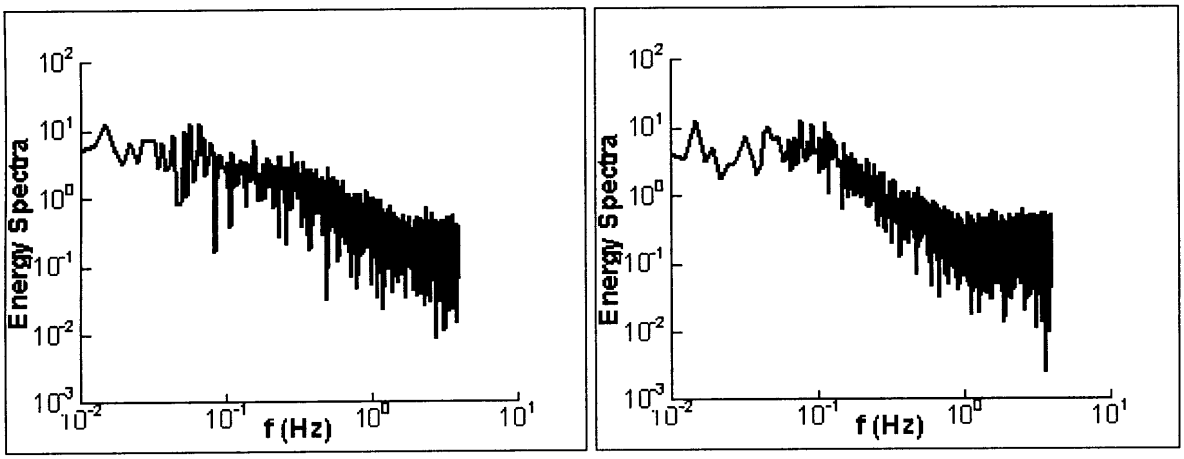

(c) H=1.7 m from the floor at P1.

(d) H=1.7 m from the floor at P2.

Figure 3.19 *The measured turbulence energy spectra in the opening vicinity for the open window case.*

3.3 Conclusions

Two different sets of experiments were conducted to provide detailed airflow characteristics inside and outside of building models or a full-scale chamber. The limitations in the experiments and some modified methods were discussed, and the mechanisms of natural ventilation driven by wind forces and buoyancy forces were investigated through energy spectral analysis. The following conclusions were drawn.

3.3.1 Wind-driven natural ventilation in a wind tunnel

For the wind-tunnel experiment, two-dimension mean and fluctuating velocities inside and around the building model and the pressure distributions along the model surface were measured. Three ventilation cases; single-sided ventilation with an opening in the windward wall, single-sided ventilation with an opening in the leeward wall, and cross ventilation were considered.

(1) The airflow motions inside the building model for the cross ventilation case are much stronger than for the two single-sided ventilation cases. For single-sided ventilation with an opening in the windward direction, a complete small eddy formed at the opening, and functioned like a barrier, preventing large airflows from entering. For single-sided ventilation with an opening in the leeward direction, the airflow does not encounter this difficulty. Therefore, relatively larger ventilation rate is expected in the leeward case than that in the windward case.

(2) It is difficult to measure some of the fluctuating velocities inside the building model due to the limitations of the experiment.

(3) To do energy spectral analysis, the variations of the airflow velocity should be measured continuously within a short period of time. However, in the recirculation and low-velocity regions, it was hard for seeding particles to penetrate even though longer measurement times were used. Therefore, the measured energy spectra from these regions do not represent the characteristics of the real flow field.

3.3.2 Buoyancy-driven natural ventilation in a full-scale chamber

For the full-scale experiment, single-sided natural ventilation driven by buoyancy forces was studied for a room with an open door or an open window. The experiment used a full-scale test room with an opening to simulate an indoor environment, and placed the test room in a large laboratory space that simulated an "outdoor" environment. Sophisticated measuring equipment, such as anemometers and a tracer-gas analyzer, were used to measure the distributions of air temperature and speed and ventilation rate. The following conclusions were made.

(1) In the measurements, it took a long time to obtain steady flow conditions. The control of the "outdoor" environment was difficult due to the impacts from the real outdoor weather on the enclosure of the laboratory.

(2) Although the results from the experimental measurements are generally considered to be reliable, it is difficult to measure low air velocities.

(3) In the experiment, since the "outdoor" space was limited and the airflow distributions inside the room were not uniformly distributed, a modified constant injection method was developed to correctly predict the ventilation rate.

3.3.3 Comparison between two ventilation situations driven by different forces

(1) For wind-driven natural ventilation, the airflow motions are mainly determined by ventilation types and incoming wind direction and speed. However, for buoyancy-driven ventilation, the airflow motions are determined by ventilation types, indoor temperature distributions, and temperature differences between indoor and outdoor areas.

(2) The study of energy spectra helps to reveal the impacts of turbulence on thermal comfort, which is an important factor in evaluating natural ventilation performance. For the wind-tunnel generated wind, the energy spectra of the wind velocity contains a wide range from 0.1 Hz to 100 Hz. However, for the buoyancy-driven wind generated in a full-scale chamber, the spectral curve contains eddies from 0.01 Hz to 1 Hz. Furthermore, the peak energy of the buoyancy-driven wind is about 0.1 Hz, which is one order of magnitude lower than that in the wind-tunnel cases. This suggests that in the wind-tunnel generated ventilation cases, both low-frequency large eddies and high-frequency small eddies are contained in the flow field, while in the buoyancy-driven cases, most energy is contained in low-frequency large eddies. However, whether this conclusion represents the real situation should be further tested by detailed measurements of real winds inside and outside of buildings.

Chapter 4

Study of the Mechanism of Indoor and Outdoor Airflows with Large Eddy Simulation

In this chapter, both the SS model and the FDS model of LES introduced in Chapter 2 are used to study outdoor and indoor airflows. This study improves the understanding of the characteristics of building airflows contributes to evaluation of the performance of LES models applied to different types of airflows.

The study of natural ventilation requires knowledge of both indoor and outdoor airflows. Normally, the features of indoor and outdoor airflows are significantly different. For indoor airflow, the Reynolds number ranges from 5,000 to 10,000, and the flow has both turbulent and laminar characteristics. The Reynolds number of outdoor airflows is usually an order of magnitude higher than that of indoor airflow due to large building scales and high wind speeds, and the outdoor airflow is usually characterized by fully developed turbulence. A model that can simulate both indoor and outdoor airflows successfully should be used to study natural ventilation.

4.1 Outdoor Airflow Study: Airflow around a Bluff Body

Successful simulation of the airflow around buildings helps to provide correct boundary conditions when studying natural ventilation in buildings. In this case, a shear flow that has a 1/4 power-law profile was generated in a wind tunnel, and a 2H × 2H × 1H block was mounted on one wall in the tunnel as shown in Figure 4.1. The Architecture Institue of Japan (AIJ) working group (1994) conducted experimental measurements on pressure coefficients for this situation. These experimental data are used to validate both the SS and FDS models.

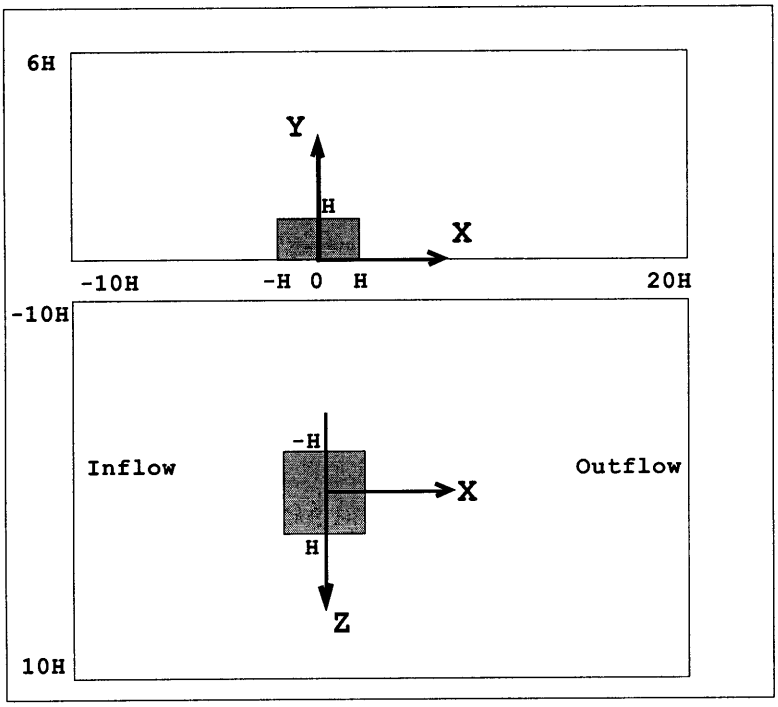

Figure 4.1 *The computational domain for the flow over a bluff body (top figure is the section view, and bottom figure is the plan view).*

4.1.1 Case setup

This section discusses the computational grid and boundary conditions defined and the turbulence length scale used.

In the numerical study, the Reynolds number is 10^5, the non-dimensional characteristic length is 1, and the expected Kolmogorov scale is about 10^{-4}. The smallest non-dimensional grid size, which is close to the block edge, is 0.02. The non-dimensional time step size is 0.005. The number of grid points is 120 x 50 x 90. The computational domain has a downstream length of 18H, an upstream length of 9H, and a lateral length of 9H on both sides of the block. A vertical height of 5H from the ground is used.

The profile of the mean velocity in the streamwise direction, x, follows a power law with an exponent of 1/4, and the mean velocities in the other two directions are zero. The turbulence is added to the mean velocity at the inflow: the fluctuations of the inflow velocity in all three directions are generated by superposing random perturbations with an intensity, u′/U, of 10%.

The frequency of the turbulence disturbance added to the inflow has a significant impact on the turbulence integral length scale, which is a measure of the average spatial extent or

coherence of the fluctuations. For a particular point in a flow field, the magnitude of the turbulence length scale depends on the correlation properties and on the direction of separation between the investigated point and its correlative point. The turbulence integral length scale along the streamwise direction, L_x, can normally be obtained through the measured autocorrelation coefficient, $R(\tau)$, and the mean velocity, U, based on Taylor's hypothesis ($x \approx U\tau$) (Reynolds 1974):

$$L_x = \int_0^\infty R(x)dx = \int_0^\infty R(U\tau)d(U\tau) \tag{4.1}$$

The turbulence autocorrelation coefficient, $R(\tau)$, which can be obtained from experiments, is defined as:

$$R(\tau) = \frac{\overline{u(t)u(t+\tau)}}{\overline{u'u'}} \tag{4.2}$$

where u' = root-mean-square (RMS) velocity, m/s
$u(t)$ = velocity at time t, m/s
$u(t+\tau)$ = velocity at time $(t+\tau)$, m/s
$\overline{\quad}$ = averaging process

Hence, the turbulence integral length scale along the streamwise direction, L_x, is related to the time history, and the disturbance frequency of the added turbulence plays an important role in determining the turbulence length scale. The current study investigates three cases with a time step of 0.01 seconds: case 1 with no disturbance (f_{dis} = 0), case 2 with one disturbance per hundred time steps (f_{dis} = 1 Hz), and case 3 with one disturbance per time step (f_{dis} = 100 Hz).

4.1.2 Impacts of inflow condition

It was found that both the SS model and the FDS model gave similar results in all cases. The SS model is therefore used to investigate the impacts of inflow conditions on the airflow distributions. The reason for the similarity of the SS and FDS model results is discussed below.

Figure 4.2 shows the history of the u-component velocity at a point, which is y/H = 1 (at the block height), x/H = –2 (1 H in front of the block), and z/H = 0 (at the middle section). The results show that the higher the disturbance frequency, the larger the velocity fluctuation. Turbulence scales can quantify these characteristics.

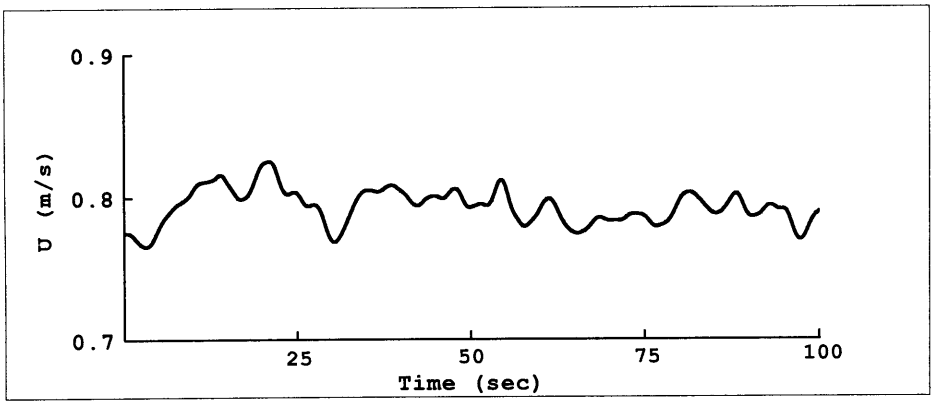

(a) Disturbance frequency f_{dis}= 0 Hz

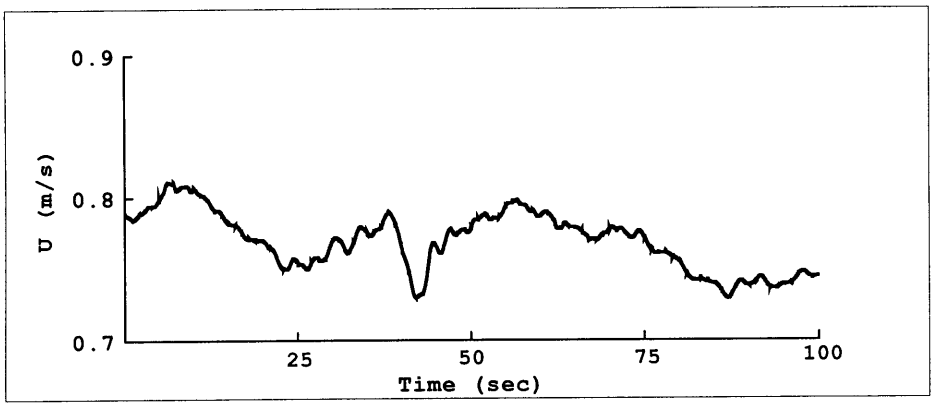

(b) Disturbance frequency f_{dis} = 1 Hz

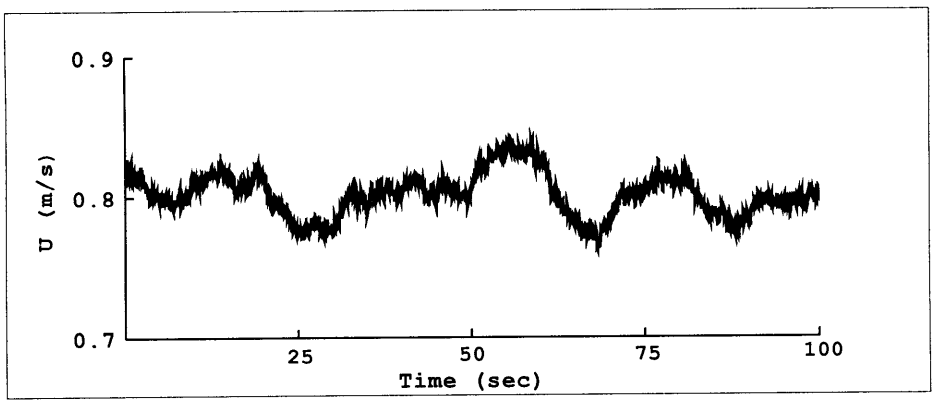

(c) Disturbance frequency f_{dis} = 100 Hz

Figure 4.2 *The history of the u-component velocity at a point in front of the block with different disturbance frequencies.*

Table 4.1 shows that the turbulence length scale varies with disturbance frequency at point x/H = –2, y/H = 1, and z/H = 0. The turbulence length scale decreases with increasing disturbance frequency. Thus, large-scale turbulence is equivalent to a flow with slowly varying velocity (Figure 4.2 (a)).

On the other hand, Figure 4.3 shows that the turbulence intensity is not sensitive changing disturbance frequency. The disturbance frequency has a major influence on turbulence length scales, but not on turbulence intensity.

Table 4.1 *Turbulence length scale in front of the body edge*

f_{dis}	0 Hz	1 Hz	100 Hz
Turbulence length scale ratio, L_x / H	9.3	6.3	3.1

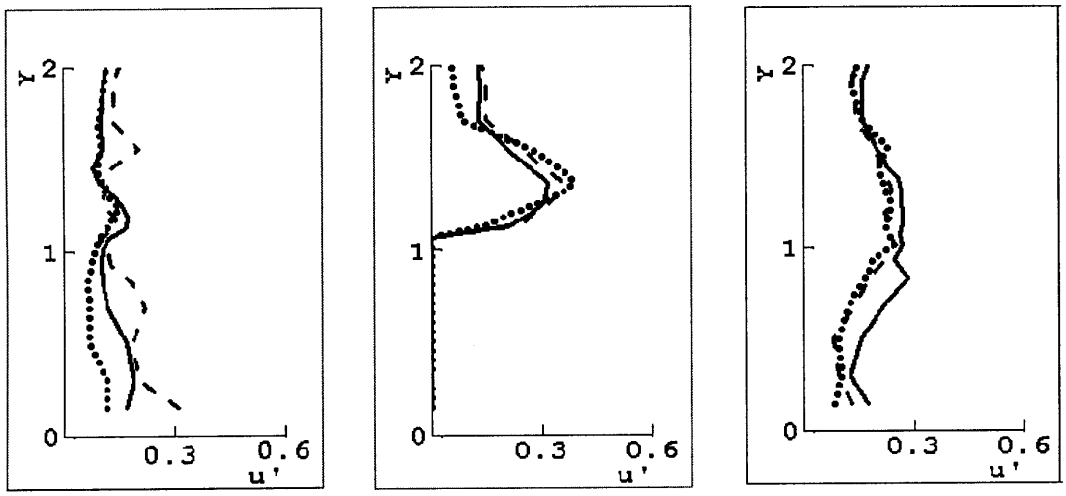

(a) *(b)* *(c)*

Figure 4.3 *The RMS velocity profiles, u', around the bluff body. Dotted lines: f_{dis}= 0 Hz; Dashed lines: f_{dis} =1 Hz; Solid lines: f_{dis} = 100 Hz. (a) In front of the block, X=-2H; (b) Above the block, X=0; and (c) Behind the block, X=2H.*

In addition, the turbulence length scale of an incoming wind may have a significant effect on the mean pressure distributions around a building (Nakamura and Ozono 1987). The mean pressure can be represented by a mean pressure coefficient,

$$C_p = \frac{\left(\overline{P} - \overline{P}_0\right)}{\frac{1}{2}\rho U^2} \tag{4.3}$$

where $\overline{P}$ = mean air pressure, Pa

$\overline{P}_0$ = mean reference pressure of the incoming flow at the building height, Pa

ρ = air density, m^3/s

U = mean reference velocity of the incoming flow at the building height, m

When the disturbance frequency is 100 Hz (Case 3), the incoming turbulence length-scale ratio is 3.1, close to that in the experiment, 2.1 ~ 3.5 (The AIJ working group 1994). In this situation, the computed mean pressure distribution is in good agreement with the experimental data (Figure 4.4). With increasing turbulence length scale, the negative peak pressure coefficient on the block roof decreases.

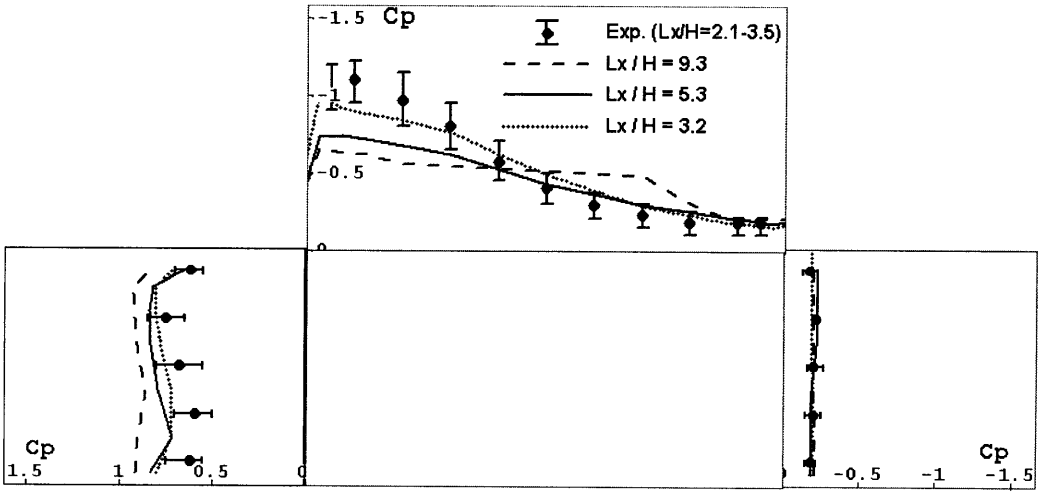

Figure 4.4 *The distribution of the mean pressure coefficient, Cp, along the bluff body at the middle section.*

That the highest negative peak pressure occurs when L_x is in the range of body-size scale, L_x/h = 2~3, can be explained by analyzing the energy spectra of velocity fluctuations. Reynolds (1974) described how to calculate the energy spectra, $\Phi(\varpi)$, with autocorrelation coefficients.

$$\Phi(\varpi) = \frac{2}{\pi}\int_0^\infty R(\tau)\cos\varpi\tau d\tau \tag{4.4}$$

Figure 4.5 shows the energy spectra of the u-component velocity fluctuation at two points, one is close to the leading edge of the block (x/H = –1.5, y/H = 1, and z/H = 0), and the other one is in the vortex region behind the body (x/H = 1.5, y/H = 1, and z/H = 0). Figures 4.5 (a) and (b) show that when the incoming turbulence scales are much larger than the body-size scale, L_x/D = 2~3, the vortex shedding cannot be stimulated, and most energy is contained in low frequency eddies, which fluctuate slowly. Figure 4.5 (c) shows that when the incoming turbulence scale is in the range of the body-size scale (f_{dis} = 100 Hz), the incoming turbulence strongly interacts with the vortex shedding behind the block. Figure 4.6 shows the instantaneous velocity distributions around the block with f_{dis} = 100 Hz. In Figure 4.6, there are intensive interactions of vortex eddies around the block, which help to draw more energy to the high frequency eddies, thus leading the vortex shedding to fluctuate intensively. This effect can be called resonant interaction. Therefore, the intensified backward vortex draws more fluid from the roof of the block, and results in a high negative peak pressure on the roof (Figure 4.4).

Figure 4.6 shows significant wind fluctuation along the block surfaces, especially on the downstream surface. This fluctuation indicates variations of the wind pressure and velocity distributions. Therefore, if there were any openings on the downstream surface, the fluctuating wind pressure would draw considerable amount of airflow in and out of the building, which has an important impact on the ventilation rate calculation. Etheridge (2000) showed that fluctuating wind pressures played an important role in natural ventilation design.

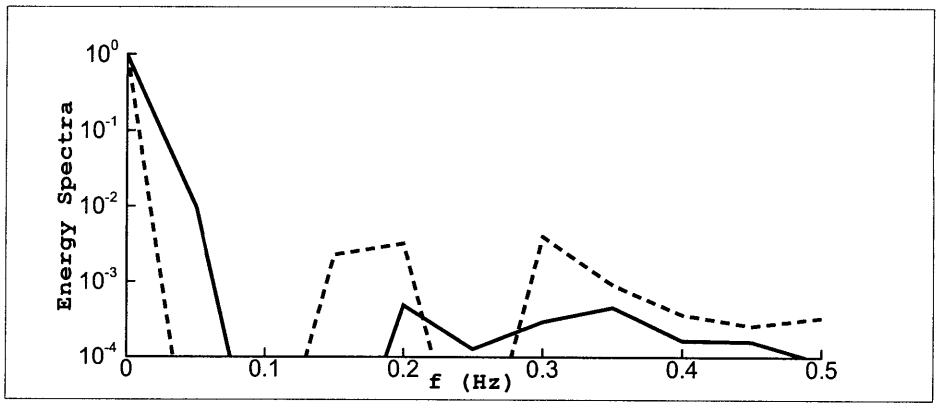

(a)

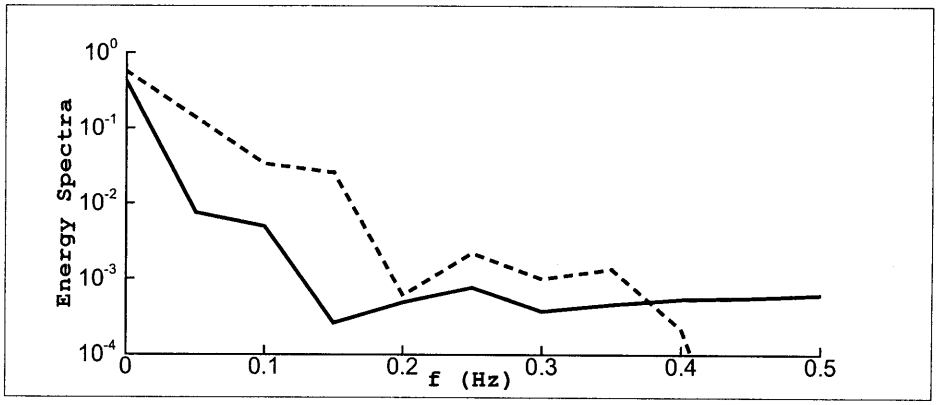

(b)

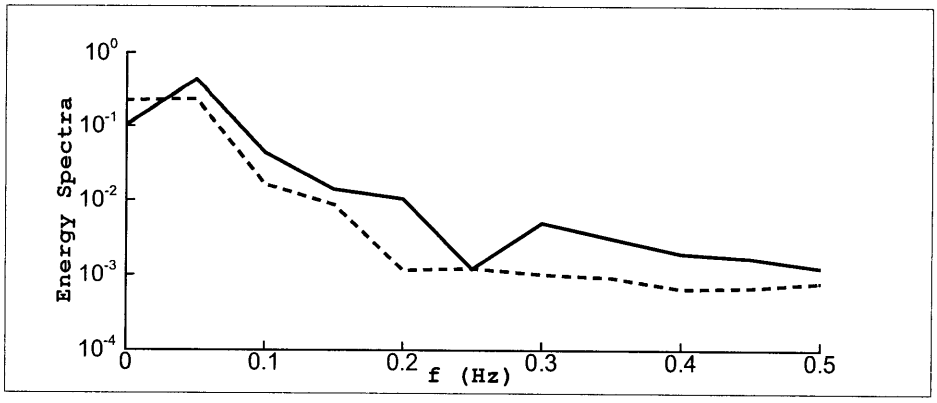

(c)

Figure 4.5 *Energy Spectra of the u-component Velocity Fluctuations at a Point H/2 in front of the Block (Solid Lines) and H/2 behind the Block (Dashed Line). Both Points are at the Building Height. (a) Disturbance frequency* f_{dis} *= 0 Hz; (b) disturbance frequency* f_{dis} *= 1 Hz; and (c) disturbance frequency* f_{dis} *= 100 Hz.*

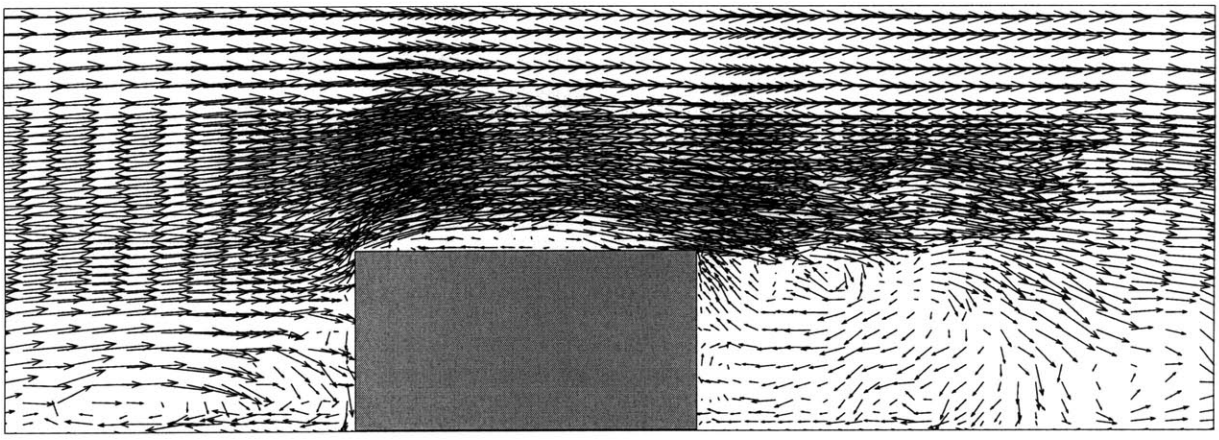

(a)

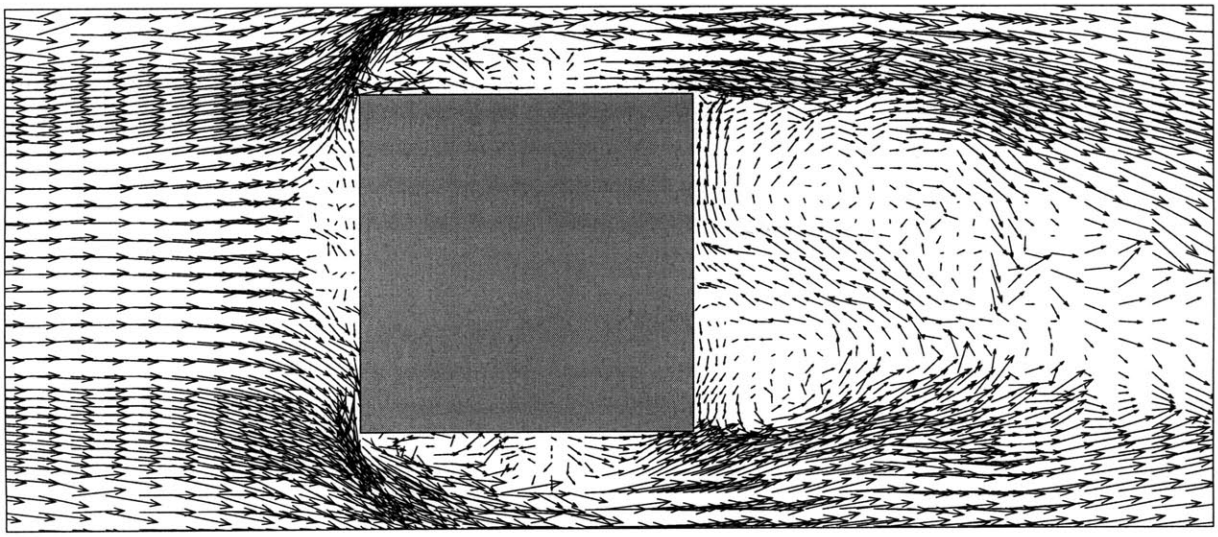

(b)

Figure 4.6 *Instantaneous velocity distributions at f_{dis} = 100 Hz. (a) In the middle section of the blockage; and (b) at the H/2 height of the plan.*

It would be interesting to increase the disturbance frequency, which results in a smaller turbulence length scale, to study the effect of the small turbulence scale on pressure distributions around a building. However, increasing the disturbance frequency to 1000 Hz requires a time step size of 0.001 seconds or less, which would require a much more computing time. Furthermore, previous experimental observation (Nakamura and Ozono 1987) shows that the mean pressure distribution around a rectangular block is insensitive to changing turbulence scale up to $L_x/h = 2$. Theses two factors explain why the current study does not include turbulence length scales below the building size.

4.1.3 Impacts of subgrid-scale models

The previous section shows that setting the disturbance frequency at 100 Hz, produces an incoming turbulence length-scale ratio close to that in the experiment, with the computed mean pressure distribution in good agreement with the experimental data. Therefore, in this section, the disturbance frequency is set at 100 Hz, and both the SS and FDS models are used for comparison.

Figure 4.7 shows the computed and measured distributions of the mean pressure coefficients, Cp, along the block. Both the SS and FDS models show good agreement with the experimental data. The difference between the results obtained with the two SGS models is small. The FDS model performs slightly better on the sidewalls but slightly worse on the roof than the SS model.

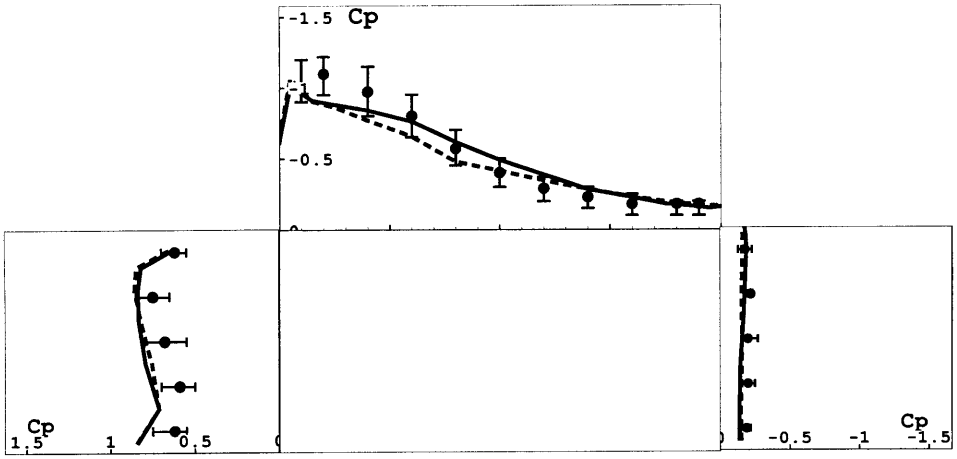

(a) middle section of the block

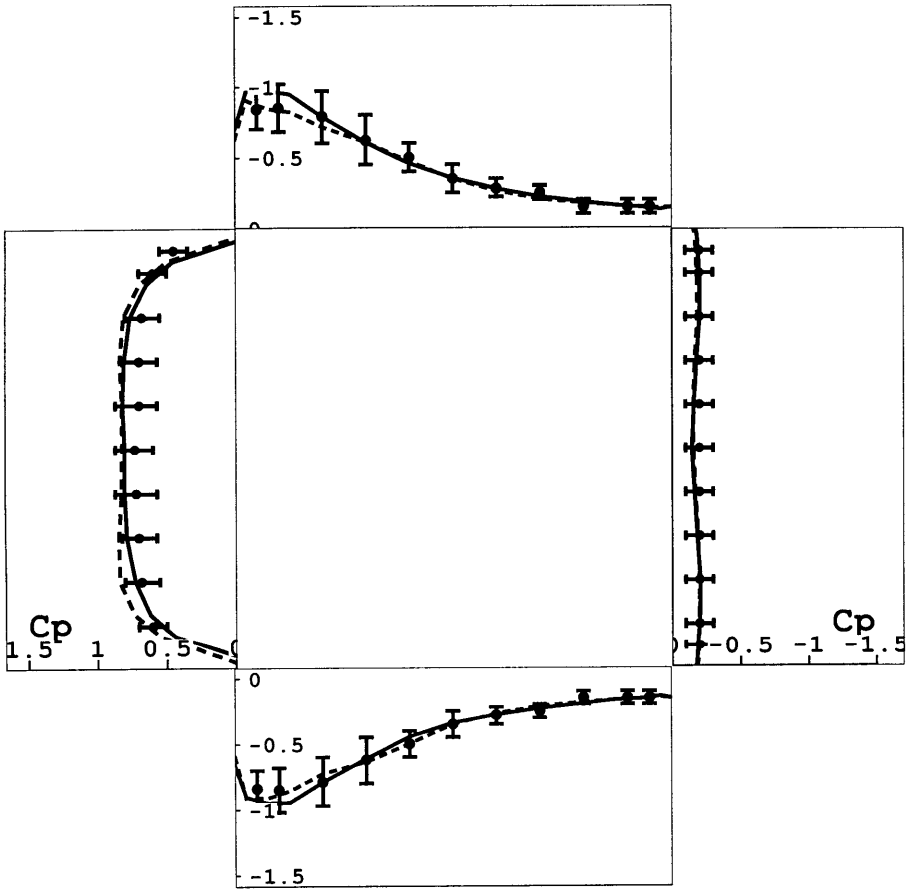

(b) plan at height of H/2

Figure 4.7 *Distributions of the mean pressure coefficients. Dots with error bars: Experiment; Solid line: SS model; Dashed line: FDS model.*

Rodi, *et al.* (1997) and Shah (1998) also found that different SGS models produced similar results when studying the airflow around a cube with a Reynolds number of 40,000. This phenomenon can be explained by analyzing the magnitudes of different terms in the momentum equation. The filtered momentum equation (Equation (2.18)) is Reynolds averaged to examine the importance of the SGS term:

$$\frac{\partial}{\partial x_j}\left\langle(\overline{u_i}\cdot\overline{u_j})\right\rangle = -\frac{1}{\rho}\frac{\partial\left\langle\overline{p}\right\rangle}{\partial x_i} + \upsilon\frac{\partial^2\left\langle\overline{u_i}\right\rangle}{\partial x_i\partial x_j} - \frac{\partial\left\langle\tau_{ij}\right\rangle}{\partial x_j} - \frac{\partial\left\langle R_{ij}\right\rangle}{\partial x_j} \tag{4.5}$$

where $\langle ... \rangle$ denotes Reynolds averaging. The term on the left hand side represents mean convection. The terms on the right hand side represent the pressure gradient, the viscous stress, the SGS stress, and the resolved turbulent stress, respectively. Note that the resolved stress, R_{ij}, represents the stress associated with the turbulent part of the resolved velocity field. Figure 4.8 shows the budget terms in the momentum equation at the middle section of the block with the FDS model. The SS model shows very similar distributions. In front of the block, the pressure term is not shown because it is much larger than the other terms. The contribution of the SGS stress term is much smaller than that of the resolved stress term in most regions around the block. Therefore, for the airflow around a bluff body with a Reynolds number as high as 100,000, most of the energy is contained in large eddies (resolved scales) and the SS and FDS models should give similar results.

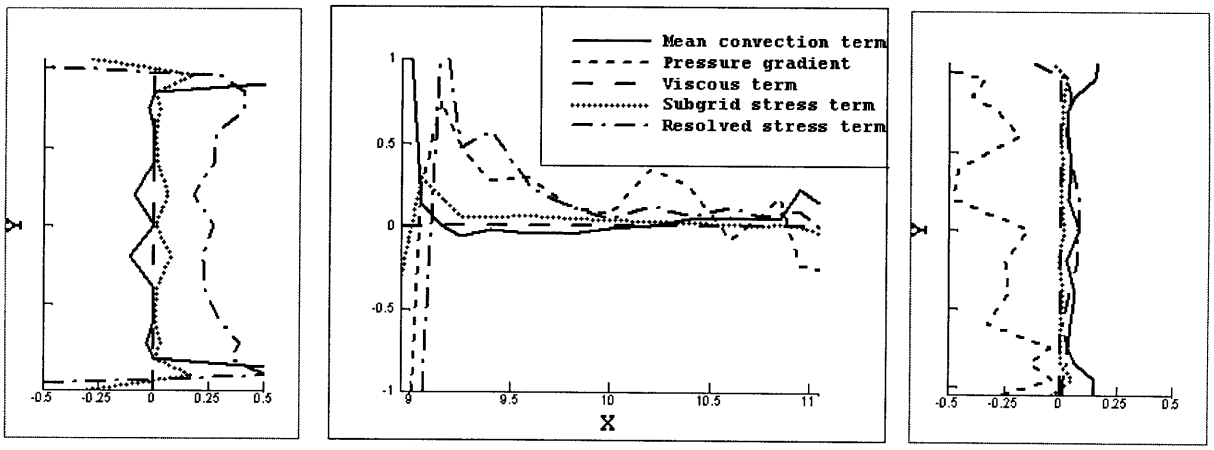

(a) in front of the block *(b) along the roof* *(c) behind the block*

Figure 4.8 *Contributions of different terms to the mean flow in the momentum equation at the middle section of the block.*

4.2 Indoor Airflow Study: Forced Convection

To check if LES models can correctly simulate indoor airflows, a forced convection case studied experimentally by Nielsen *et al.* (1978) was used for validation. This case represents a simple but typical indoor ventilation situation. Figure 4.9 shows a sketch of the case.

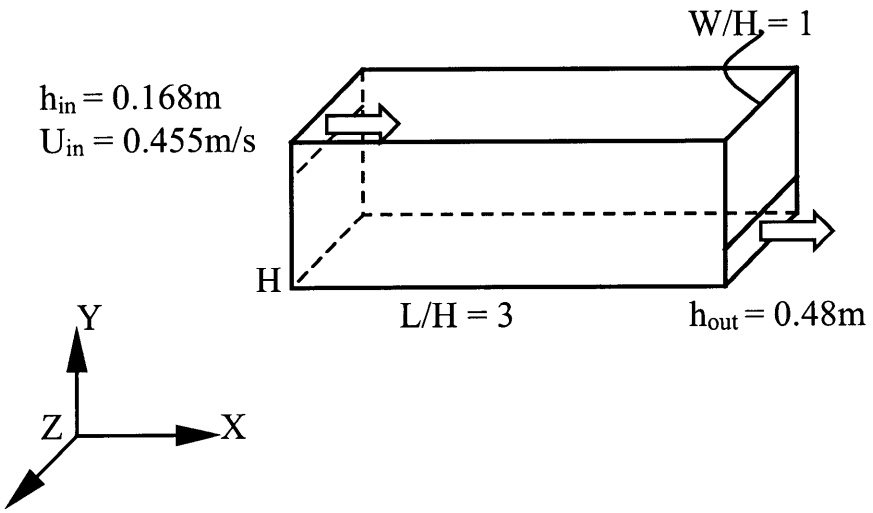

Figure 4.9 *Sketch of forced convection in a room.*

4.2.1 Case setup

In the numerical simulation, the Reynolds number is 5000 based on the inlet height and inlet velocity, and the non-dimensional characteristic length 1. The expected Kolmogorov scale is about 10^{-3}. The smallest non-dimensional grid size used in this investigation is 0.06, and the total grid number is 99,200. The non-dimensional time step size is 0.02.

4.2.2 Results and discussion

Figure 4.10 shows the distributions of the mean velocity and RMS velocity at two locations in the middle section of the room. It was found that the results computed with the FDS model agree reasonably well with the experimental data. Although different Smagorinsky constants, C_{SGS}, are used for the SS model, the model still cannot correctly predict the flow field. During this study, the C_{SGS} value was increased from 0.16 to 0.2, but this increase does not necessarily lead to a higher kinetic energy (Figures 4.10 (c) and (d)). This is

because the SGS eddy viscosity depends not only on C_{SGS}, but also on the strain rate and filter size (Equation (2.23)). Therefore, increasing C_{SGS} does not have a significant impact on flows with a small strain rate. This suggests that for indoor airflow cases, in which walls normally have significant effects and both turbulent and laminar flows exist, the SS model may not be appropriate.

The distributions of the velocity field and the model coefficient, C, show why the FDS model produces better results than the SS model. Figure 4.11 shows the mean flow field distributions at the middle section of the room. Figure 4.11 (b) illustrates that C is small both near the walls and in the regions of laminar flow, which correctly represents the physics of flow motions.

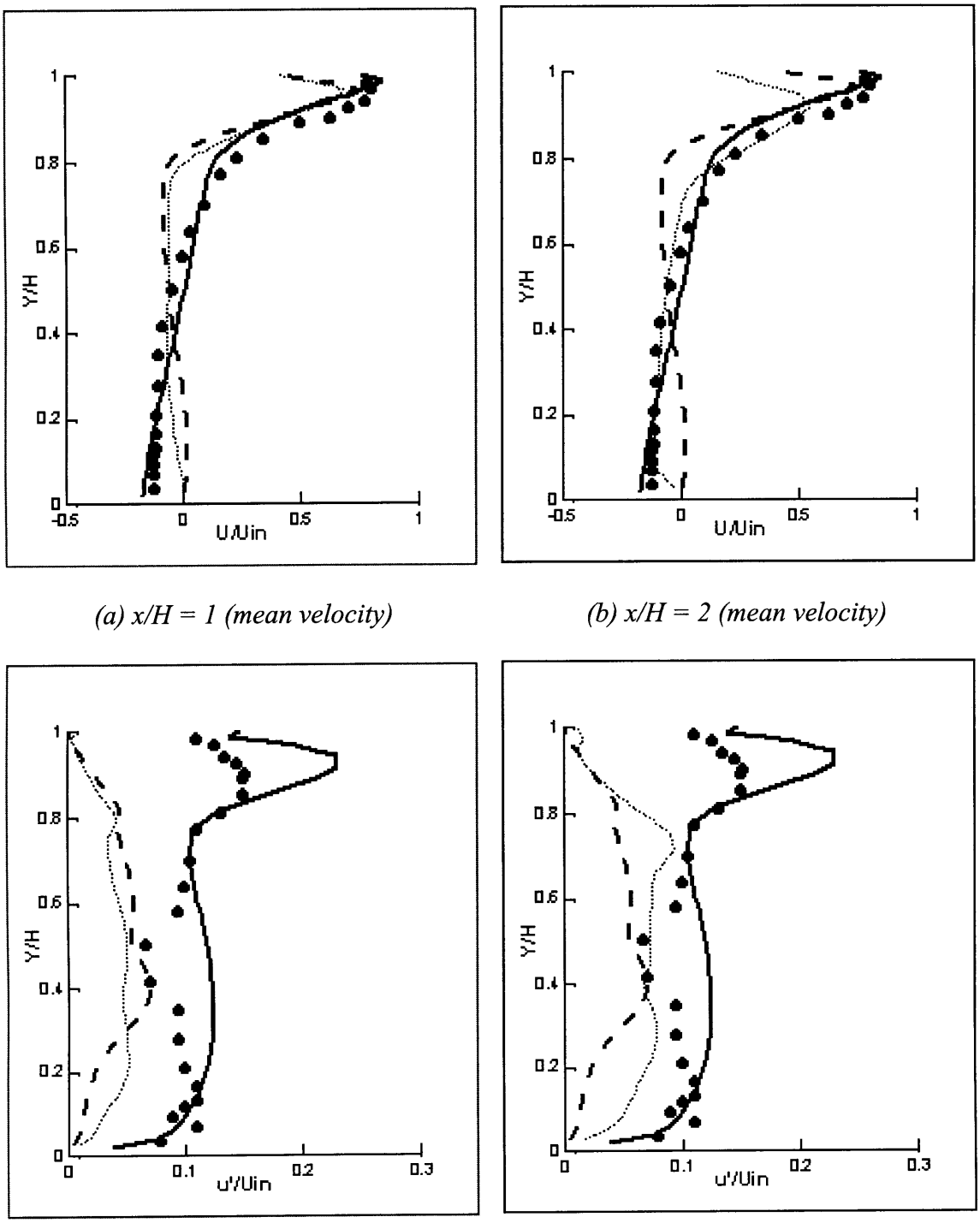

(a) x/H = 1 (mean velocity)

(b) x/H = 2 (mean velocity)

(c) x/H = 1 (RMS velocity)

(d) x/H = 2 (RMS velocity)

Figure 4.10 *Distributions of the mean velocity and RMS velocity at the middle of the room (Z = H/2). Dots: Experiment; Solid line: FDS model; Dashed line: SS model with C_{SGS} = 0.16; Dotted line: SS model with C_{SGS} = 0.2.*

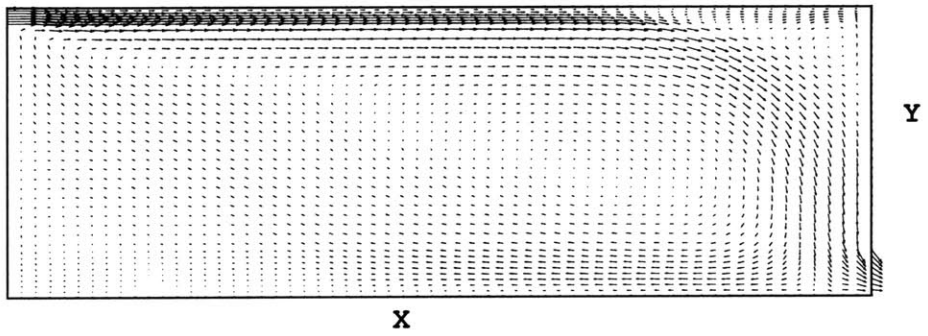

(a) velocity field

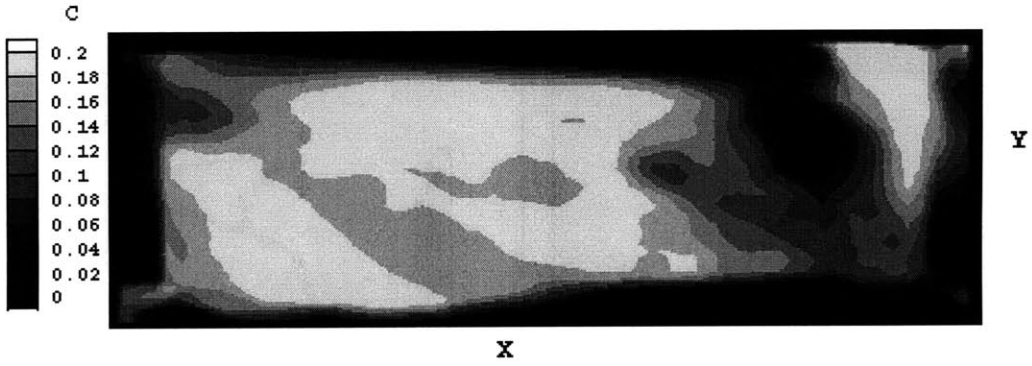

(b) model coefficient, C

Figure 4.11 *Distributions of the mean flow field and the mean model coefficient, C, at the middle section of the room.*

4.3 Indoor Airflow Study: Natural Convection

In the previous section, the indoor airflow driven by forced convection was studied with LES. To study the indoor airflow driven by buoyancy forces, the natural convection between a cold and a warm wall is investigated (Cheesewright *et al.*, 1986). Although in this case the airflow is not in a room, the airflow patterns are very similar to indoor airflows driven by buoyancy forces. Detailed air velocity, temperature, turbulence energy, and heat transfer were made experimentally and the LES models can therefore be well examined.

Figure 4.12 shows a sketch of the case. The heights of both the cold and warm walls were 2.5m, the distance between the two walls was 0.5m, and the depths of the walls were 0.5 m. All other surfaces were insulated. The corresponding Rayleigh number, Ra, was 2.5×10^{10}. Although this cavity type is not a real indoor condition, the airflow characteristics are very similar to those inside a room. Therefore, this case can be regarded as an indoor airflow driven by buoyancy forces.

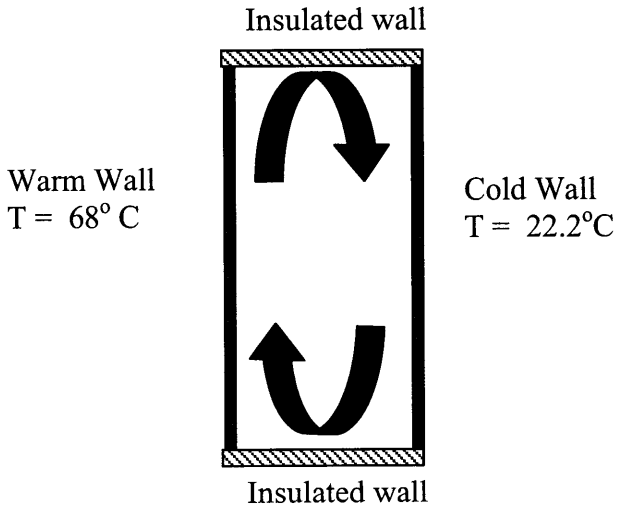

Figure 4.12 *Sketch of natural convection.*

4.3.1 Case setup

The numerical simulation used a non-dimensional grid system: 62 × 62 × 18. The smallest non-dimensional grid size is 10^{-3} m and the time step size is $2x10^{-4}$ s.

In the computation, the initial air velocities in the flow field were set to be 10^{-3} m/s to generate some initial momentum for the air. The initial air temperatures were set to be 45.1 °C, which was the average value between the cold and warm wall temperatures.

4.3.2 Results and discussion

Figure 4.13 shows the airflow distributions along the middle height of the cavity. In addition to the LES models, RANS modeling was also used as a comparison. The figure shows that all of the models gave good results for mean velocities and temperatures. However, for the turbulence kinetic energy, the SS model produced a much smaller value than the experimental data. The results computed with the FDS model were in good agreement with the experimental data. Again, this suggests that, for indoor airflows that normally contain both turbulent and laminar patterns, the FDS model should be used. On the other hand, RANS modeling predicts the experimental values well at both mean and turbulent levels.

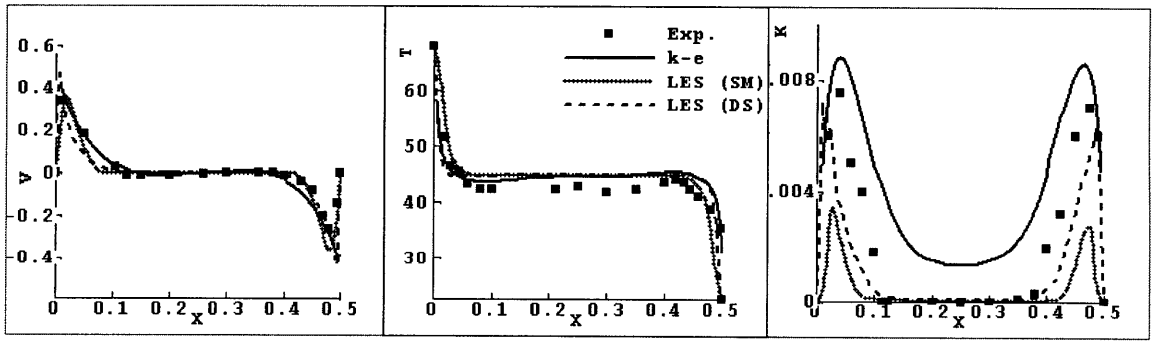

(a) Mean velocity *(b) Mean temperature* *(c) Turbulence kinetic energy*

Figure 4.13 *The airflow distributions along the mid section of the walls. Black dots: Experiment; Solid line: k-ε model of RANS modeling; Dotted line: SS model; Dashed line: FDS model with C_{SGS} = 0.16.*

4.4 Conclusions

Both the SS model and the FDS model of LES were used to study indoor and outdoor airflows. This study helps to understand the characteristics of the airflows in and around buildings and evaluate the performance of LES models applied to different types of airflows. The following conclusions were reached.

(1) In a highly turbulent flow, most energy is contained in large eddies. The large eddies therefore play a more important role in determining the airflow motions than the small eddies. Since both the SS and FDS models can directly solve the large-eddy motions and can model the dissipative nature of turbulence, they are both able to provide accurate flow results for the cases with highly turbulent flows. The flow investigated in this paper is the airflow around a bluff body, which is representative of an outdoor airflow. Since the SS model is much simpler than the FDS model, and requires less computing time than that needed by the FDS model, the SS model is more suitable for solving this type of problem.

(2) Using the SS model, the effect of the turbulence length scale on the mean pressure distribution around the bluff body was also investigated. It was found that, at the inflow, added turbulence with different frequencies produces different integral length scales. Although the mean velocity profile and turbulence intensity are the same, the varying turbulence length scales have a significant effect on the mean pressure distributions around a bluff body. When the incoming turbulence scale is in the range of the body-size scale, $L_x/h = 2\sim3$, the energy spectra analysis shows that the backward vortex shedding can be intensified through resonant interaction. As a result, the intensified vortex draws more fluids from the roof of the block, thus leading to a high negative peak pressure on the top surface of the block. When the incoming turbulence scale is much larger than the body-size scale, the vortex shedding in the wake behind the block cannot be stimulated and intensified. Thus, the negative peak pressure coefficient on the top surface is low.

(3) The SS model cannot predict laminar flows, such as the airflows near walls, because the model coefficient is a constant, and does not vary with flow type. The FDS model can give reasonable results in these cases because its model coefficient is a function of the flow type. The coefficient becomes zero in the laminar regions, which correctly represents the physics of flow motions. Therefore, the FDS model is more appropriate to study indoor airflows with both turbulent and laminar characteristics.

To study natural ventilation, a model that can correctly simulate both indoor and outdoor airflows should be used. The current study suggests that the FDS model is a suitable tool. However, this conclusion needs to be tested with natural ventilation cases, which the subject of Chapter 5.

Chapter 5

Large Eddy Simulation of Natural Ventilation

The research approach introduced in Chapter 2 and the experimental data obtained from the literature and measured in the wind tunnel and full-scale chamber as described in Chapter 3 are used to validate the LES models.

To investigate the model performance under wind-driven natural ventilation conditions, four sets of experimental data are applied. The first of these is a single-sided ventilation experiment that was conducted by Dascalaki et al. (1996) in a full-scale test room with measurement of the real wind speed and direction. The second is a cross ventilation experiment that was conducted by Katayama et al. (1992), who performed on-site measurements and wind tunnel tests for both indoor and outdoor airflows at a building site. Third is the experiment described in Section 3.1, which was conducted in a wind tunnel, and investigated three different types of ventilation conditions: single-sided with an opening in the windward direction, single-sided with an opening in the leeward direction, and cross ventilation. The fourth experiment is a cross ventilation test conducted by Murakami, et al. (1992) in a wind tunnel.

To investigate the model performance under buoyancy-driven natural ventilation conditions, the experimental measurements described in Section 3.2 are used. Two ventilation cases are studied: one with an open door and the other with an open window.

All of the experimental data are used to validate the two SGS models of LES, the SS model and the FDS model. Moreover, the standard k-ε model of RANS modeling and empirical models are used in some cases as a comparison.

5.1 Wind-driven Full-scale Single-sided Natural Ventilation

Dascalaki *et al.* (1996) did full-scale measurements for a single-opening house (Figure 5.1). They measured the wind speeds at various heights in the middle section of the opening, and applied the tracer-gas decay method to measure the ventilation rate of the house. This study simulated one of their cases with the LES models and with RANS modeling to examine whether it is appropriate for single-sided ventilation studies.

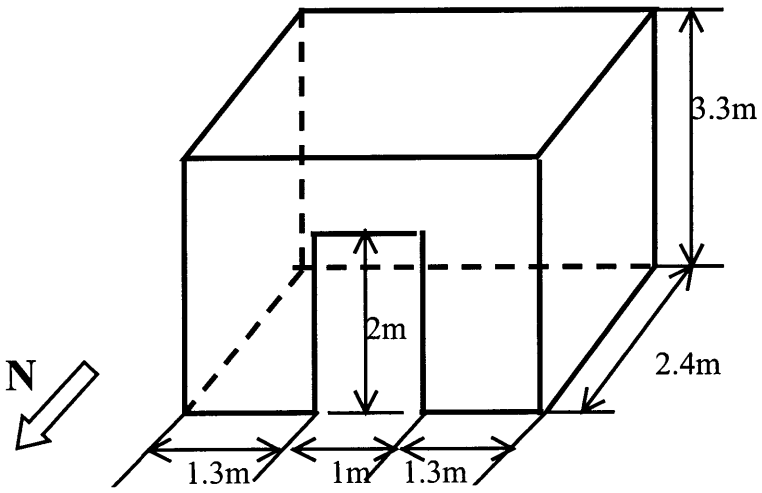

Figure 5.1 *A sketch of the single-opening house.*

5.1.1 Case setup

All of the numerical models, the LES models and the RANS model, used the same grid system with a total grid number of 604,200. The Reynolds number is 5×10^5, and the non-dimensional characteristic length 3.3. The expected Kolmogorov scale is about 10^{-4}. The smallest non-dimensional grid size is 0.015, and the non-dimensional time step is 0.002.

The simulation used the 1/7 power of the incoming wind profile. Table 5.1 gives the incoming wind information, in which WS_n is the mean wind speed normal to the opening.

Table 5.1 *Incoming wind information*

Mean wind speed at 1.5 m (m/s)	Mean WS_n at 1.5 m (m/s)	Mean wind direction (clockwise from south)
1.95 ± 0.52	0.98 ± 0.42	120 °

The experiment measured the indoor air temperatures at different heights. Although the temperature difference between indoor and outdoor airflows was 2.8 ± 0.1 °C, no significant air temperature stratification was observed during the measurement period. Dascalaki *et al.* (1996) compared the importance of wind force and buoyancy force in single-sided natural ventilation with the Archimedes number, Ar_D,

$$Ar_D = \frac{Gr}{Re_D^2} = \frac{\beta \Delta T g H^3/\gamma^2}{(UD/\gamma)^2} = 0.02 << 1 \qquad (5.1)$$

where Gr = Grashof number
Re_D, = Reynolds number
β = volumetric coefficient of expansion
g = gravitational force
H = the height of the opening
D = depth of the room
U = the wind speed at the building height.

Equation (5.1) shows that the natural convection due to the buoyancy effect is much smaller than the forced convection due to the wind effect. Therefore, for simplicity, the current simulation ignores the buoyancy effect, and this case can be regarded as wind-driven, single-sided, natural ventilation.

5.1.2 Results and discussion

Mean velocity profile

Figure 5.2 shows the distribution of the mean wind speed at the centerline of the opening. RANS modeling under-predicts the wind speeds at the bottom of the opening; the SS model over-predicts the speeds at the top; the FDS model gives the best agreement with the experimental data in terms of the profile shape and magnitude. The FDS model performs better than the SS model in this case. This is because the single-sided ventilation case involves fully developed turbulent flow around a building and laminar flow inside the building, where the turbulent and laminar flows have strong interactions at the opening (Figure 5.3). Furthermore, the walls have an important effect on the flow motions. As seen in Chapter 4, the SS model has difficulty (due to a constant model coefficient) in predicting flows in which walls have significant effects and both turbulent and laminar patterns exist. Since the model coefficient in the FDS model varies with different flow types, the FDS model is expected to be more suitable for the single-sided ventilation case, which involves many complex flows.

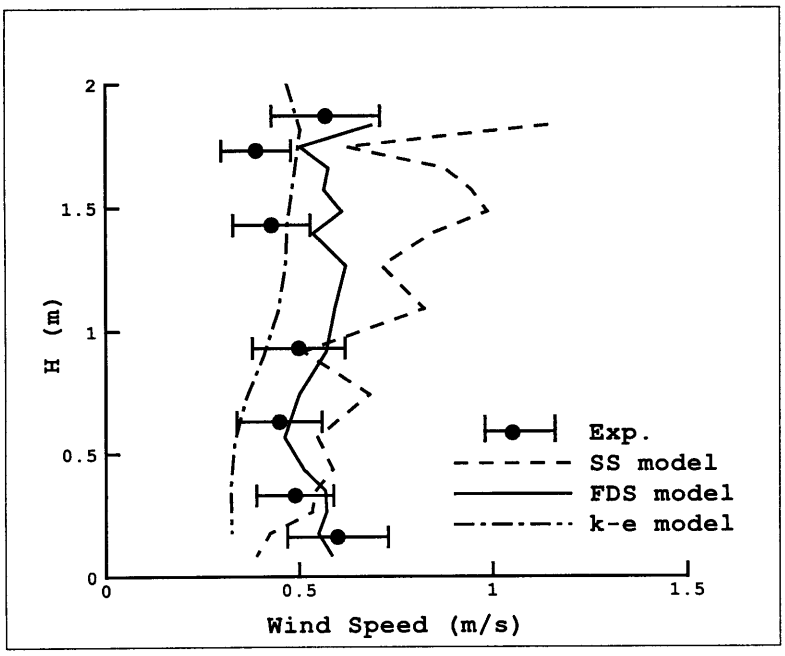

Figure 5.2 *The profiles of the mean wind speed at the centerline of the opening. Black dots with error bars: Experiment; Solid line: FDS model; Dashed line: SS model; Dash-dot line: standard k-ε model.*

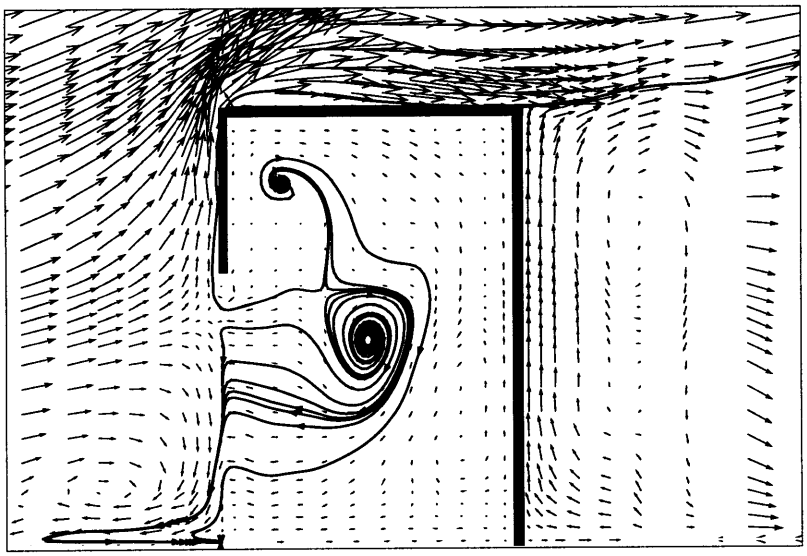

(a) mean

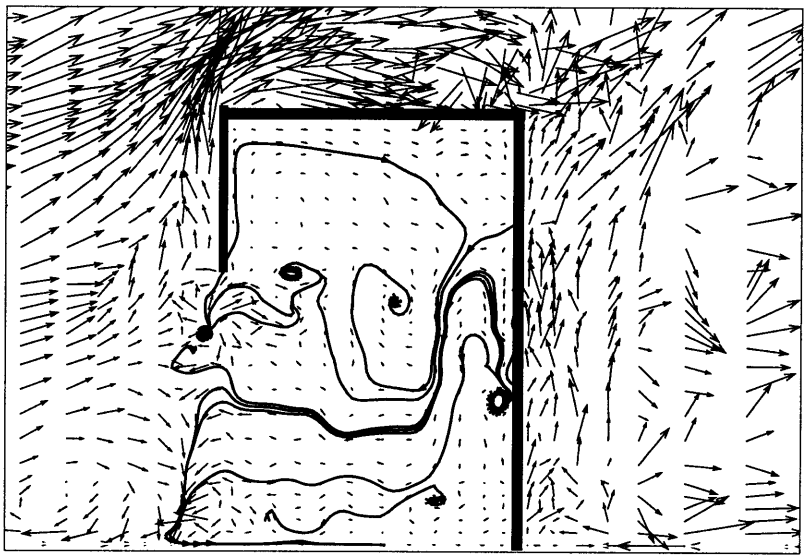

(b) instantaneous

Figure 5.3 *Flow field with the streamlines at the middle section of the room computed by LES with the FDS model.*

Ventilation rate

When studying natural ventilation in buildings, air change effectiveness is used to evaluate the ventilation performance. The air change effectiveness describes the ability of a ventilation system to deliver fresh air from the outside to the inside of a building (ASHRAE Fundamentals, 1997). These characteristics can be seen from the streamlines, as illustrated in Figure 5.3. The streamlines in the instantaneous velocity field show that fresh air can easily reach the wall opposite to the opening. However, the streamlines in the mean flow field show a recirculation zone so that the fresh air cannot penetrate deeply. The information from the mean flow field may mislead a designer in evaluating the ventilation performance for a particular design while the instantaneous flow field can provide information better suited to understanding ventilation.

Air change effectiveness cannot be determined by one index alone, since it varies at each point in the room if the room air is not perfectly mixed, which is a common situation in natural ventilation. In order to use one standard for ventilation assessment, ventilation rate or air change rate is introduced to describe the airflow rate from the outside into a building (ASHRAE Fundamentals, 1997). Although it is not an accurate measure of the ventilation performance of a building, ASHARE Standard 62 (1999) uses ventilation rate to provide a standard of proper minimum ventilation for acceptable indoor air quality.

Based on the definition, the ventilation rate in numerical simulations can be computed by integrating the air velocity at the opening. Appendix A derives the formula to calculate the

ventilation rate of a building (m^3/s) with this integration method. There are two ways to do integral calculations. The first is to extract the mean velocity normal to the opening, $U_{j,k}$, from the mean flow field. The computed value can be designated the mean ventilation rate, Q_{mean}.

$$Q_{mean} = \frac{1}{2}\sum_{j=ja}^{jb}\sum_{k=ka}^{kb}\left|U_{j,k}\right|\Delta y_j \Delta z_k \tag{5.2}$$

where $U_{j,k}$ = the mean velocity normal to the opening (m/s)
$[\Delta y_{ja}, \Delta y_{ja+1}, \ldots, \Delta y_{jb}]$ and $[\Delta z_{ka}, \Delta z_{ka+1}, \ldots, \Delta z_{kb}]$
= the grid sizes in the y and z directions within the opening (m).

Since LES can provide the instantaneous velocity field at each time step, another way to compute the ventilation rate of a building is to accumulate and average the instantaneous ventilation rates over a time period, T. The instantaneous ventilation rate at time t^n is defined as

$$q^n = \frac{1}{2}\sum_{j=ja}^{jb}\sum_{k=ka}^{kb}\left|u^n_{j,k}\right|\Delta y_j \Delta z_k \tag{5.3}$$

where $u^n_{j,k}$ = the instantaneous velocity normal to the opening at time t^n (m/s)

The cumulative and average instantaneous (CAI) ventilation rate over a time period of T, $Q_{ins,T}$, is defined as

$$Q_{ins,T} = \frac{\frac{1}{2}\sum_{n=1}^{N}\left(\sum_{j=ja}^{jb}\sum_{k=ka}^{kb}\left|u^n_{j,k}\right|\Delta y_j \Delta z_k\right)\cdot \Delta t^n}{\sum_{n=1}^{N}\Delta t^n} \tag{5.4}$$

where Δt^n = the time step size, $t^{n+1}-t^n$, (m/s)
N = the total number of the time steps, during which $Q_{ins,T}$ is calculated.

Equation (5.4) shows that when computing the ventilation rate by accumulating and averaging the instantaneous ventilation rate, the length of time over which the average is taken may be important. In $Q_{ins,T}$, the subscript "T" shows the duration over which the $Q_{ins,T}$ is computed.

Figure 5.4 shows the variations of the CAI ventilation rate, $Q_{ins,T}$, and the instantaneous ventilation rate, q^n, over time with the FDS model. Figure 5.4 (a) shows that the variation magnitude of variation of $Q_{ins,T}$ is high for small values of T, and the variation decreases as

T increases. When the averaging time T is increased to 120 seconds, $Q_{ins,T}$ is nearly constant at a value of 0.101 m^3/s. The variation of $Q_{ins,T}$ over time with the SS model shows a similar distribution, and $Q_{ins,T}$ is 0.159 m^3/s when T is increased to 120 seconds. For clarity, the result for the SS model is not shown in the figures. Figure 5.4 (b) also includes the mean ventilation rate as a reference. It clearly shows that the averaging procedure used to calculate the mean ventilation rate significantly cancels out the instantaneous air exchange between the indoor and outdoor airflows, which is theoretically proved in Appendix A. This can also be demonstrated physically. For example, an inflow in the upper part of the opening at one moment followed by an outflow at another moment leads to a zero mean ventilation rate. However, the instantaneous ventilation rate is definitely not zero. Therefore, the mean ventilation rate is calculated to be much smaller than the CAI value, which should represent real conditions. Obviously, the instantaneous flow field is crucial for the correct determination of ventilation rates with single-sided natural ventilation.

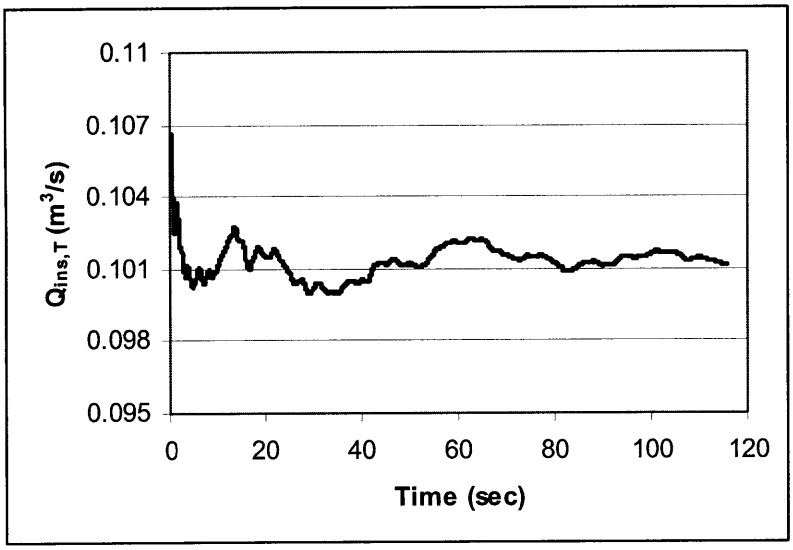

(a) Cumulative and average instantaneous ventilation rate

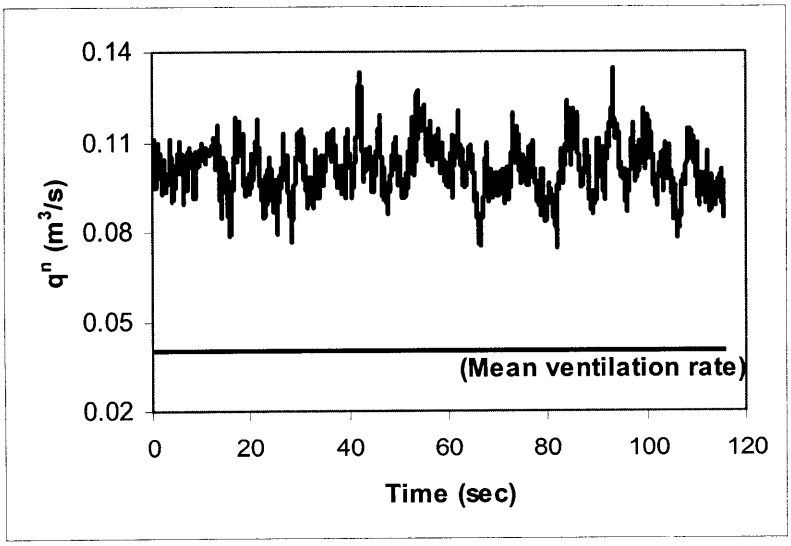

(b) Instantaneous ventilation rate

Figure 5.4 *Variation of the ventilation rate over time for the building with single-sided natural ventilation (FDS model).*

Table 5.2 compares the air exchange rate obtained by different numerical methods with that from the experiment. The air exchange rate (ASHRAE Fundamentals, 1997), which compares the ventilation rate of a room to the room volume, is also called air changes per hour (ACH). It is defined as

$$\mathrm{ACH} = \frac{Q}{V} \tag{5.5}$$

where Q is the volumetric airflow rate into the space (m^3/h), and V the interior volume of space (m^3). Since the incoming wind profile is parabolic due to ground effects, there are air exchanges between the indoors and outdoors. All the computed mean air exchange rates are at least 30% smaller than the measured one. Only the CAI air exchange rate computed by the FDS model agrees well with the experimental result, while the SS model over-predicts the air exchange rate. Table 5.2 also shows that the CAI air exchange rate is much larger than the mean one.

Table 5.2 *Air exchange rate for the building with single-sided natural ventilation.*

	Experiment	RANS (k-ε) Q_{mean}/V	LES (FDS model)		LES (SS model)	
			$Q_{ins,120\ sec}/V$	Q_{mean}/V	$Q_{ins,120\ sec}/V$	Q_{mean}/V
ACH	9.6 ~ 13.18	5.6	12.8	5.1	20.1	7.0

5.2 Wind-driven Full-scale Cross Natural Ventilation

5.2.1 Case description

Katayama *et al.* (1992) performed on-site measurements and wind tunnel tests for both indoor and outdoor airflows at a building site as shown in Figure 5.5. This site lies to the south of the Japanese Sea, and is seven kilometers away from the nearest beach. There is an open field located between the beach and the building site. The prevailing wind during the experimental period was from the north and northwest directions.

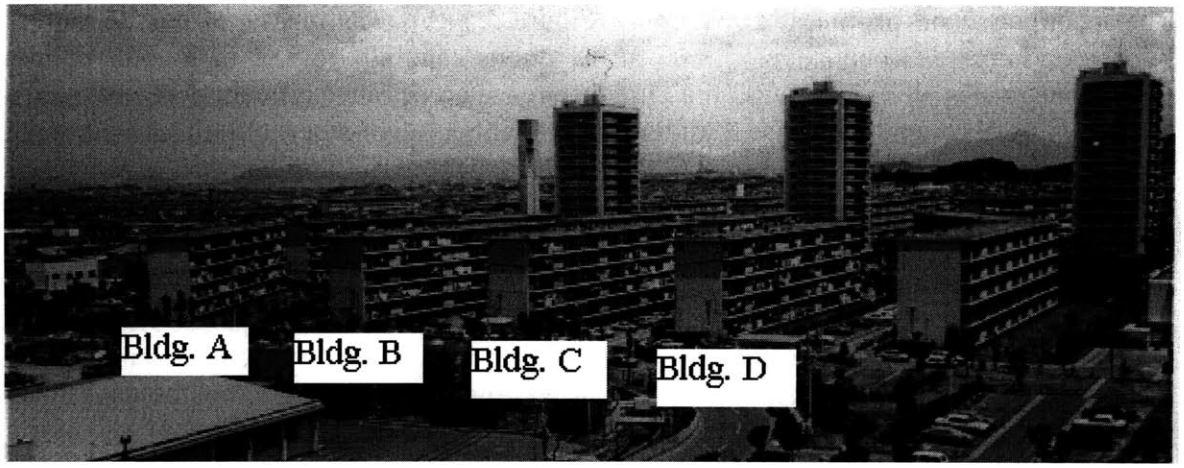

(a) Three-dimensional

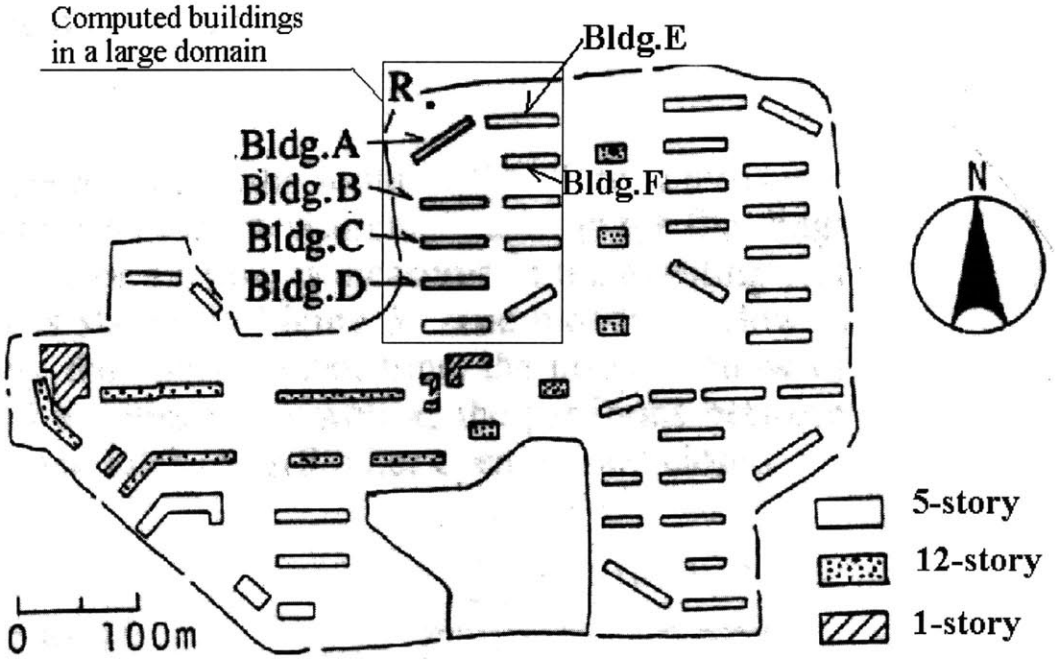

(b) Two-dimensional

Figure 5.5 *Layout of the building group*

The incoming wind profile at Location R (Figure 5.5 (b)) was measured on-site using a balloon system (a 3-cup anemometer) at 15 points ranging from 2 m to 160 m high (Katayama *et al.*, 1989). The wind-pressure difference across an apartment was measured at Buildings A through D. Those buildings are identical five-story buildings with eight apartments on each floor. Figure 5.6 shows the locations of the apartments where the pressure differences were measured, which varied from one building to another. Figure 5.7 diagrams the identical buildings, and gives the overall dimensions of the buildings: 56.43 m × 13.96 m × 6.66 m. The location marked as "indoor" in Figure 5.7 is an apartment in Building A where indoor airflow was measured at a height of 1.2 m from the floor. Figure 5.8 shows the plan of the investigated apartment. For indoor airflow, the distribution of the air speeds at the height of 1.2 m from the floor was measured. Furthermore, the wind speed at the center of the north window was recorded as a reference value (Figure 5.8).

Katayama *et al.* (1992) performed two wind tunnel tests of airflow in and around the buildings. The first test included about twenty buildings on the site with a model scale of 1/300, where the wind pressure differences around Buildings A through D were measured. The second test used only Building A with a model scale of 1/20 in order to obtain the detailed distributions of indoor airflow.

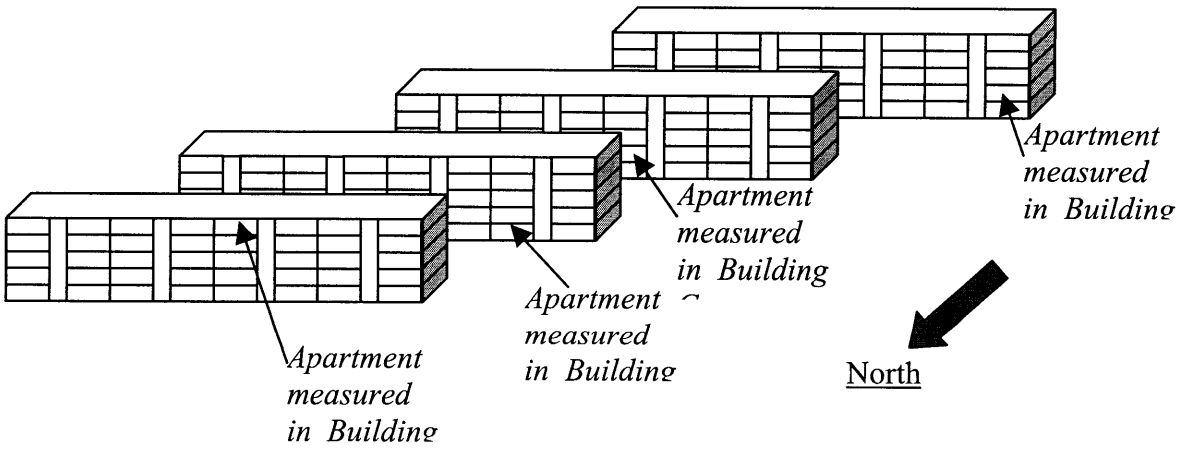

Figure 5.6 *The locations of the apartments where wind pressure difference across the buildings was measured.*

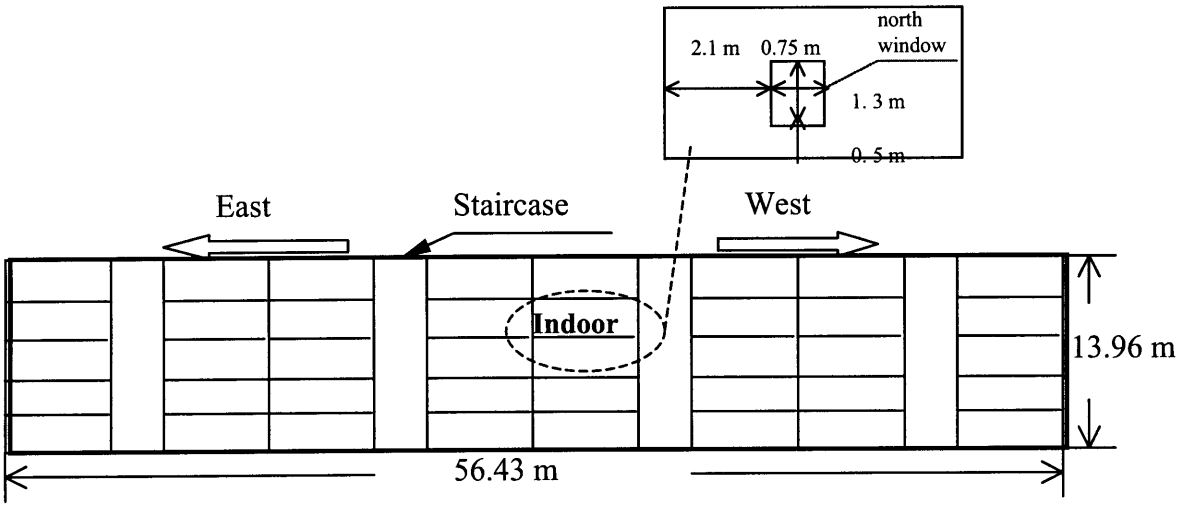

Figure 5.7 *The overall dimensions of the building (Length × height × width = 56.43 m × 13.96 m × 6.66 m), and the location of an apartment in Building A where indoor airflow was measured at a height of 1.2 m from the floor (north side elevation).*

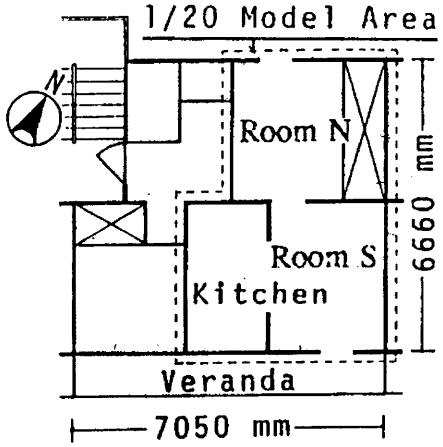

Figure 5.8 *Plan of an apartment in Building A*

5.2.2 Case setup

The LES model was applied to study cross ventilation in buildings. The governing equations and numerical schemes applied here were presented in Chapter 2. In the current simulation, the incoming wind to the building site and the computational domain size are the two key issues for studying airflow in and around the buildings correctly and efficiently with LES. The following two sections will discuss how to simulate the incoming wind and how to determine the computational domain to provide correct results with affordable computing time with LES. Then, the computational results are compared with the experimental data for airflow distributions in and around buildings.

Wind Simulation

The on-site measurements and wind tunnel experiments provide two sets of data on the incoming wind, both with a 1/4 power law mean-wind profile and the same turbulent intensity. Figure 5.9 shows the distributions of mean wind and turbulent intensity in the measurements and LES results. The data from the wind tunnel, from LES and from full-scale measurements are in good agreement.

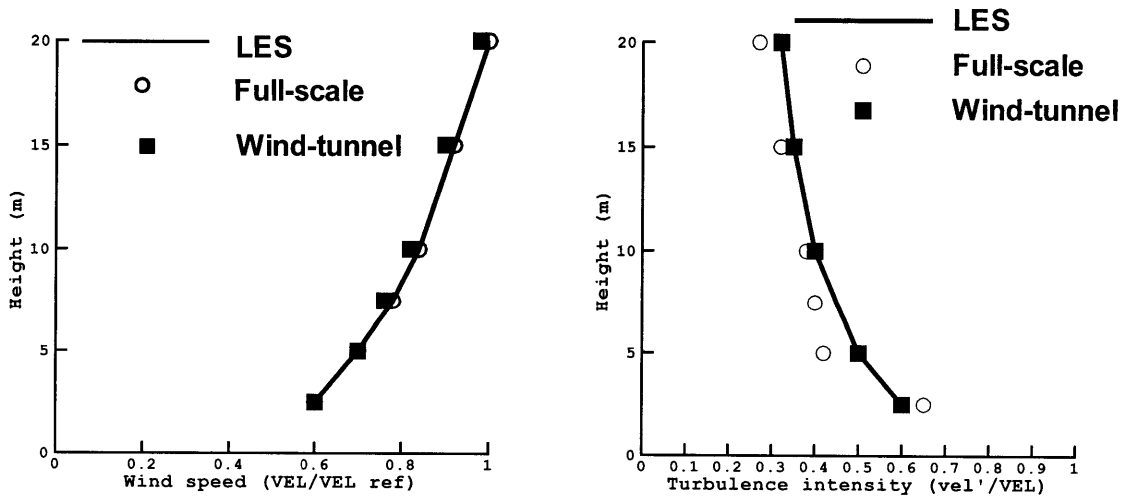

(a) Non-dimensional mean wind speed *(b) Non dimensional turbulent intensity*

Figure 5.9 *Profiles of incoming wind*

Although the wind tunnel produced the same incoming wind profile as the field wind in terms of mean velocity and turbulent intensity, Katayama *et al.* (1992) noticed some discrepancies in the wind-pressure differences across Buildings C and D and the indoor airflow distributions for these two sets of data. They explained these discrepancies by fluctuations of natural wind in both speed and direction, which were not simulated in the

wind tunnel. As pointed out by Surry (1989), Lin *et al.* (1995), and Zhao (1997), the wind direction is fixed in a conventional wind tunnel, which is different from real wind whose direction and speed vary over time. Hence, using a tunnel-generated wind to simulate real wind may cause significant errors.

Although natural wind direction changes over time, its histogram exhibits some rules. Nitta (1990) observed that, at a high wind speed (4.46 m/s), the histogram follows a normal distribution. At a low wind speed (1.17 m/s), however, the histogram tends to be uniform. Figure 5.10 shows the wind data from on-site measurement of a campus. The results lead to similar conclusions.

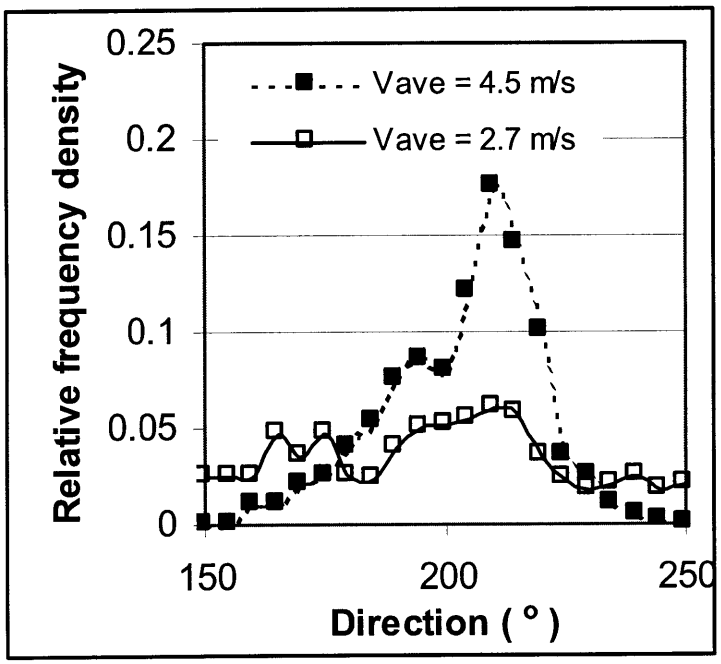

Figure 5.10 *Comparison of the histograms of wind data.*

Due to the different characteristics of natural wind and the incoming flow from a wind tunnel, LES in this investigation used different approaches to simulate the incoming flow. For the wind tunnel case, LES fixed the wind direction. For the on-site case, LES simulated the wind with either a normal or a uniform distribution depending on the magnitude of the incoming wind speed. Since the on-site measurement did not measure the variation of the incoming wind direction, the present investigation used the variation from other studies. Zhao (1997) found that a typical variation of wind direction is about 80° during a time period of 15 minutes. Because the real time in our simulations was about 10~20 minutes, the variation of wind direction was about 80°. The incoming wind speed ranged from 0.5~4 m/s above the building roof according to the on-site measurements. The wind speed below

the roof level would be much lower than this range. Therefore, in the present study, a uniform distribution was used for the variation of the incoming wind direction. As pointed out by Zhao (1997) a large fluctuation of wind direction could occur in a very short time. Fluctuations on the order of 60 ° or even higher could happen in one-tenth of a second. Therefore, in the current study, the wind direction was set to fluctuate on the order of 80° every one-tenth of a second. The real experimental data obtained from an on-site measurement of a campus were adjusted and adopted as the inflow boundary condition for the current study.

Determination of computational domain

The computational domain in LES must be large enough to generate correct flow information around the buildings. However, if the domain is too large, the computing time increases significantly. The outdoor measurements were performed only on Buildings A through D, and indoor measurements were conducted inside an apartment in Building A. Hence, our computational effort was to ensure correct simulation of the flow distributions around Buildings A through D and inside the apartment in Building A.

Since the wind came from the northwest, Buildings A through D were in the upwind direction. If we include ten buildings in LES as shown in Figure 5.5, the impact of the side and rear buildings on the flow distributions around Buildings A through D should be correctly simulated. For the study of the indoor airflow in the apartment in Building A, the computational grid size should be at least 0.2 m and the time step size should be sufficiently small (0.05 seconds) in order to obtain a stable simulation and detailed flow information. Even with a non-uniform grid system, the total grid number would be as high as eight million. This would require three months of computing time on a fast workstation. To save computing time, the indoor and outdoor calculations were separated.

The airflow distributions outside of buildings depend on the incoming wind speed and direction, the building size and shape, and the size and location of the building opening. If the area of the building openings is less than 1/6 of the total facade area, the effects of these openings on the outdoor airflow distributions can be neglected (Vickery and Karakatsanis, 1987). Since, the building opening area on the site was much smaller than 1/6 of the total facade area, the ten buildings can be simulated as concrete blocks. As a result, the smallest grid can be as large as 1 m and the corresponding time step can be as large as 0.1 seconds without numerical stability problems.

The study of the indoor airflow in Building A needs correct flow information only around that particular building. Therefore, the computational domain can be much smaller than that for the outdoor airflow study. Since Building A is in the windward direction, a computational domain that includes four buildings (A, B, E and F as shown Figure 5.5) would be sufficient. To ensure that this reduction in computational domain size can still generate correct airflow distribution around building A, the computed results with the small domain (four buildings) were compared with those for the large domain (ten buildings). The pressure difference between these two cases is less than 5% in most regions of

Building A, which is satisfactory for ventilation design. The separation of indoor and outdoor airflow calculations can reduce the computing time dramatically compared with the calculation of both indoor and outdoor flow simultaneously. Table 5.3 illustrates the computing time with different domains.

Table 5.3 *Comparison of total CPU time among different domain size and cell size*

No. of bldgs	Include indoor?	Domain size L × W × H (m × m × m)	Smallest grid size	Total grid number	Time step (s)	Total real time (min)	Total CPU (days)
10	Yes	450 × 80 × 400	0.2 m*	8×10^6	0.05	20	88
10	No	450 × 80 × 400	1.0 m	0.5×10^6	0.1	20	2.8
4	Yes	250 × 60 × 280	0.2 m*	1.8×10^6	0.05	10**	6

* Smaller cell size because the indoor calculation needs smaller time step size in order to stabilize the computation.
** A smaller domain requires a smaller total real time used in the simulation because the time for the wind to travel from one end to another is lower.

5.2.3 Results and discussion

Figure 5.11 shows the mean velocity distributions with two different wind conditions. When the wind is fixed from the northwest direction, the recirculation regions behind Buildings A through D are much larger than in the case where the wind direction varies from the north to the west with a mean direction of northwest. With a fixed wind direction, the wind blows to only certain regions of a building. There are some regions, such as those behind the building, where the wind can hardly reach. Therefore, large recirculation zones can easily be formed in these regions. On the other hand, with a variable wind direction, the wind will blow from the west at some moments (from the bottom to the top in Figure 5.11). The west wind would destroy the formation of the large recirculation zones behind the buildings leading to much smaller eddies. The different airflow distributions would cause different pressure distributions around the buildings.

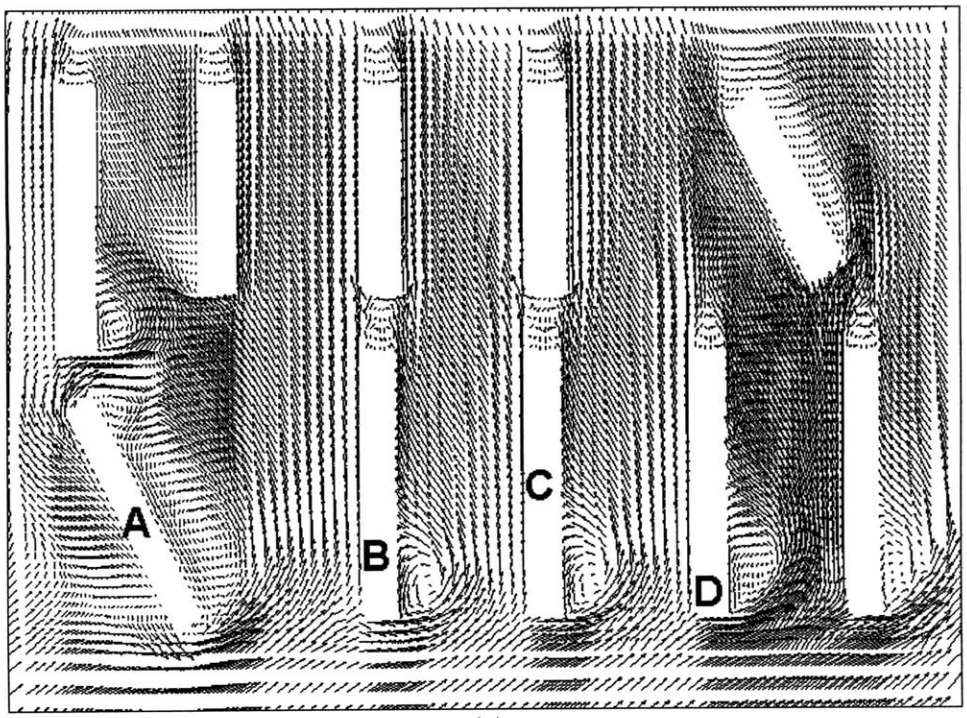

(a)

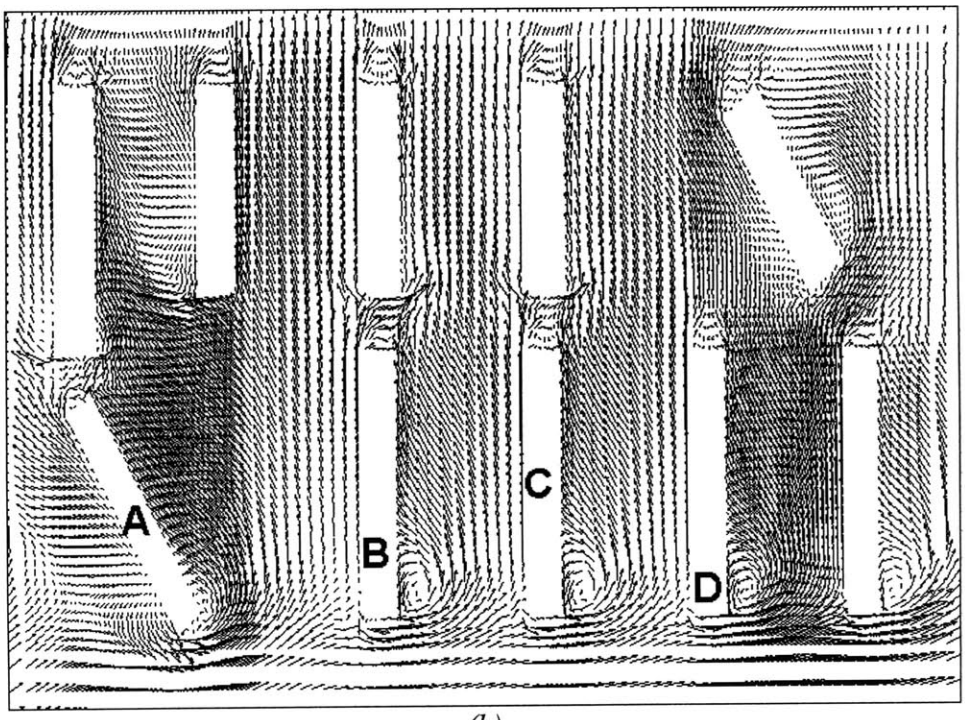

(b)

Figure 5.11 *The mean velocity distributions around the buildings at 3 m from the ground (a) With fixed wind direction from northwest; (b) With variable wind direction from north to west and a mean direction from northwest.*

Katayama *et al.* (1992) also reported the difference of the pressure coefficients across the selected apartments in Buildings A through D. The locations of the selected apartments are shown in Figure 5.6. The difference of the pressure coefficients, ΔCp, is defined as $\Delta Cp = \frac{P_{North} - P_{south}}{1/2\rho V_{ref}^2}$, where P_{North} is the measured pressure on the north wall of the selected apartment, P_{South} the measured pressure on the south wall of the selected apartment, ρ the air density, and V_{ref} the reference velocity measured at 1 m away from the north window of the selected apartment in Building A.

Figure 5.12 presents the pressure coefficients at the selected apartments in Buildings A through D. For Buildings A and B, the measured ΔCp values from the wind tunnel agree well with those from the on-site measurements. LES also gave reasonable results for two different wind conditions. For Buildings C and D, both the wind tunnel measurements and LES with fixed wind direction, show similar results. However, the wind tunnel over-predicted ΔCp values by nearly four times compared with the data obtained from on-site measurements. The LES results with varied wind direction are in good agreements with the on-site data. These results show that directional fluctuations of the incoming wind play an important role in determining wind pressure distributions around buildings. Unfortunately, this directional fluctuation is hard to reproduce in a wind tunnel.

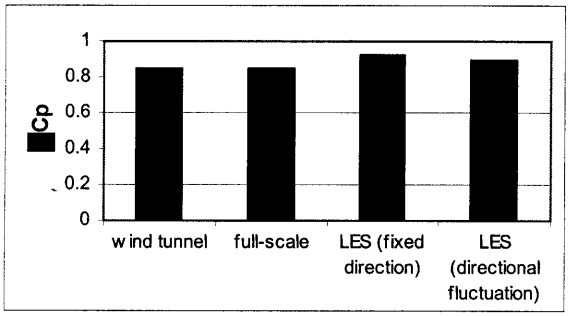

(a) Pressure difference in Building A

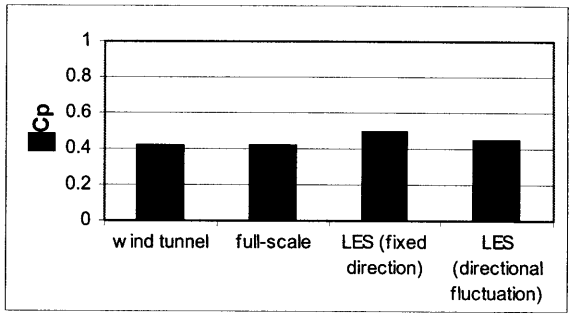

(b) Pressure difference in Building B

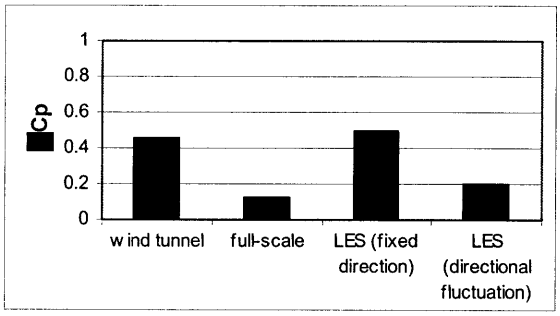

(c) Pressure difference in Building C

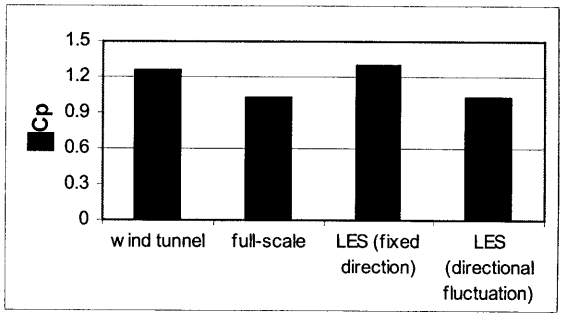

(d) Pressure difference in Building D

Figure 5.12 *Comparison of pressure difference with experimental data and LES simulations*

Figure 5.13 shows the distributions of the pressure coefficient difference, ΔCp, across Buildings A through D. When the wind direction varied from north to west, airflow was able to pass along the east-west facades of the building at times. This flow reduced the eddy size, and reduced the pressure gradient along the building facades.

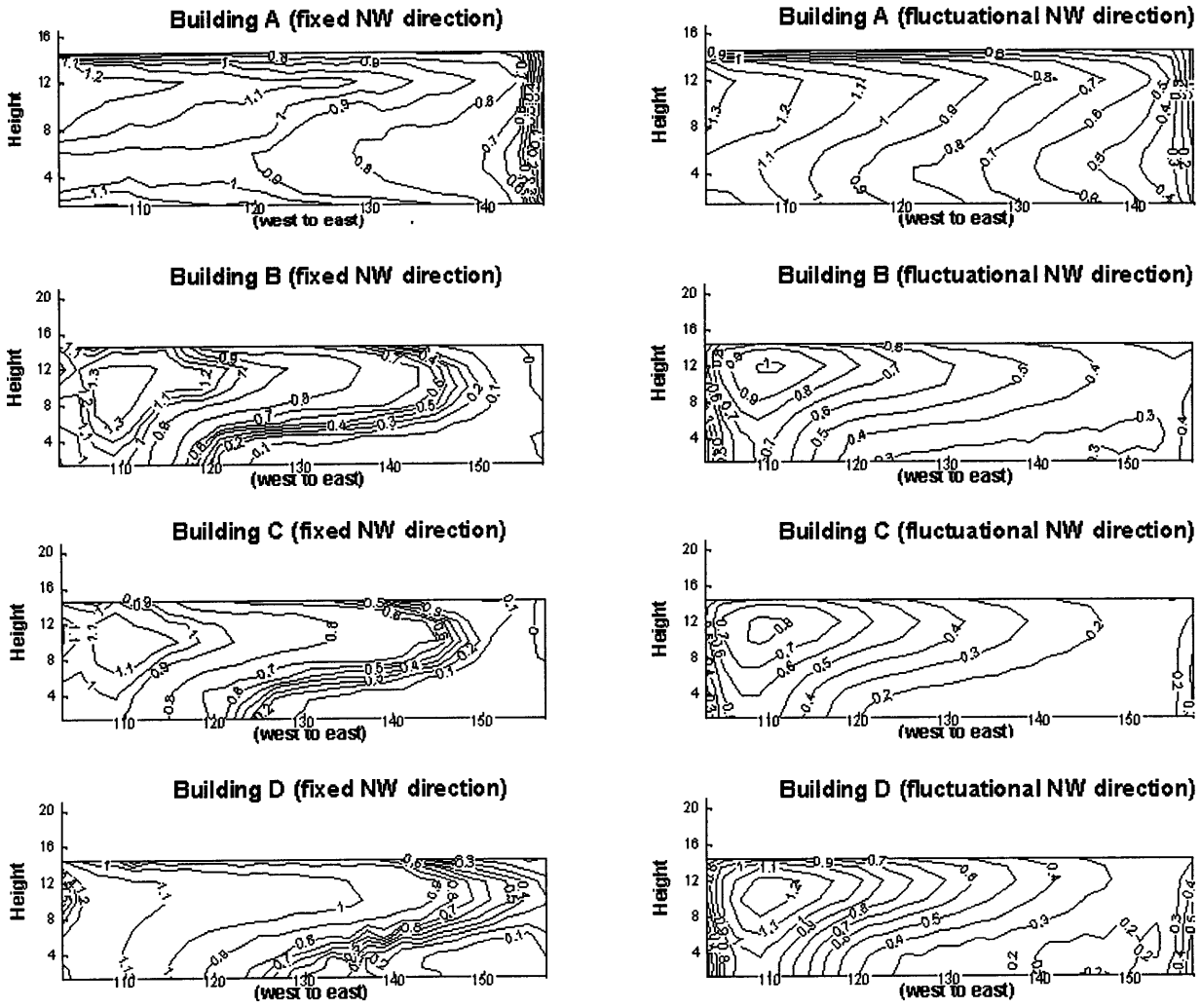

Figure 5.13 distributions of ΔCp across Building A-D

The study of indoor airflow only calculated the flow fields around four buildings (Buildings A, B, E and F) and inside a selected apartment in Building A, as shown in Figures 5.5 and 5.7. Figure 5.14 shows the wind speed distribution inside the apartment in Building A. The wind-tunnel data show a deep, thin and high velocity core in the north room (upper room). The LES results with fixed wind direction show a similar flow pattern. The on-site measurements show a shallower and wider high-speed region in both rooms. The LES results with varied wind direction are in reasonable agreement with the on-site data. Note that LES with the Smagorinsky subgrid-scale model may not accurately predict indoor airflow (Zhang and Chen, 2000). A perfect agreement between the LES results and the experimental data is difficult to achieve with the Smagorinsky model. Figure 5.15 shows the average and transient velocity distributions inside the apartment calculated by LES with varied wind direction.

These results illustrate that, with a fixed wind direction, the wind can pass through the room openings without too much oscillation and energy loss. Hence, a deep, thin and high-speed core is formed. On the other hand, with varied wind directions, the flow dissipates energy to the corners of the room, which reduces the depth and width of the high-speed core. The wind speed becomes more evenly distributed throughout the room than is the case for a fixed wind direction.

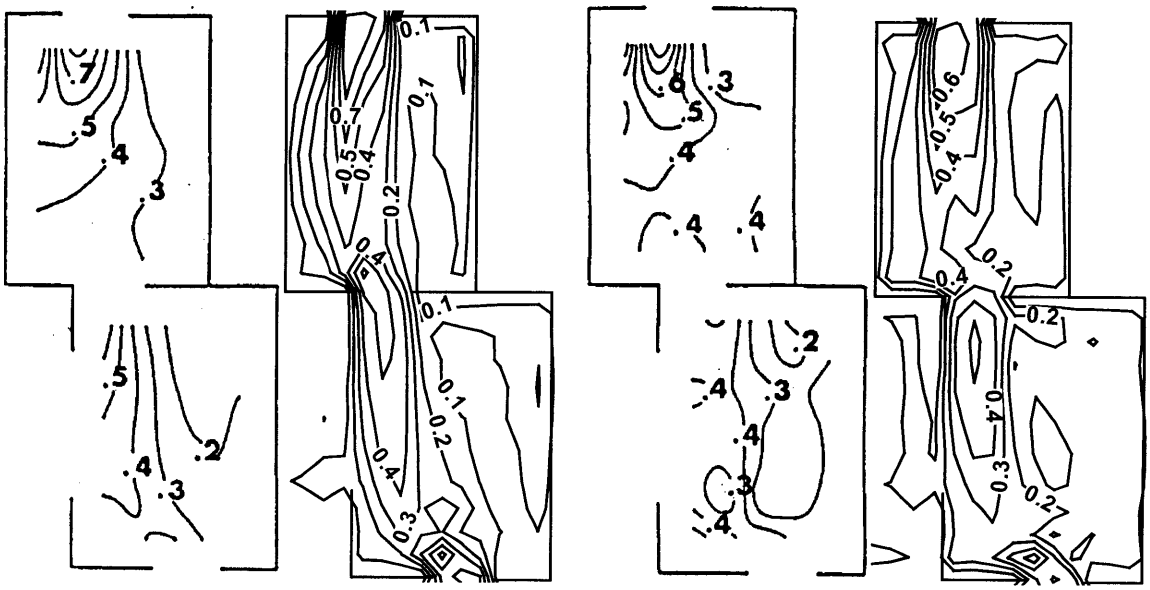

Figure 5.14 *Comparisons between the experimental data and LES results. (a) Wind-tunnel; (b) LES (fixed direction); (c) On-site; (d) LES (varied direction).*

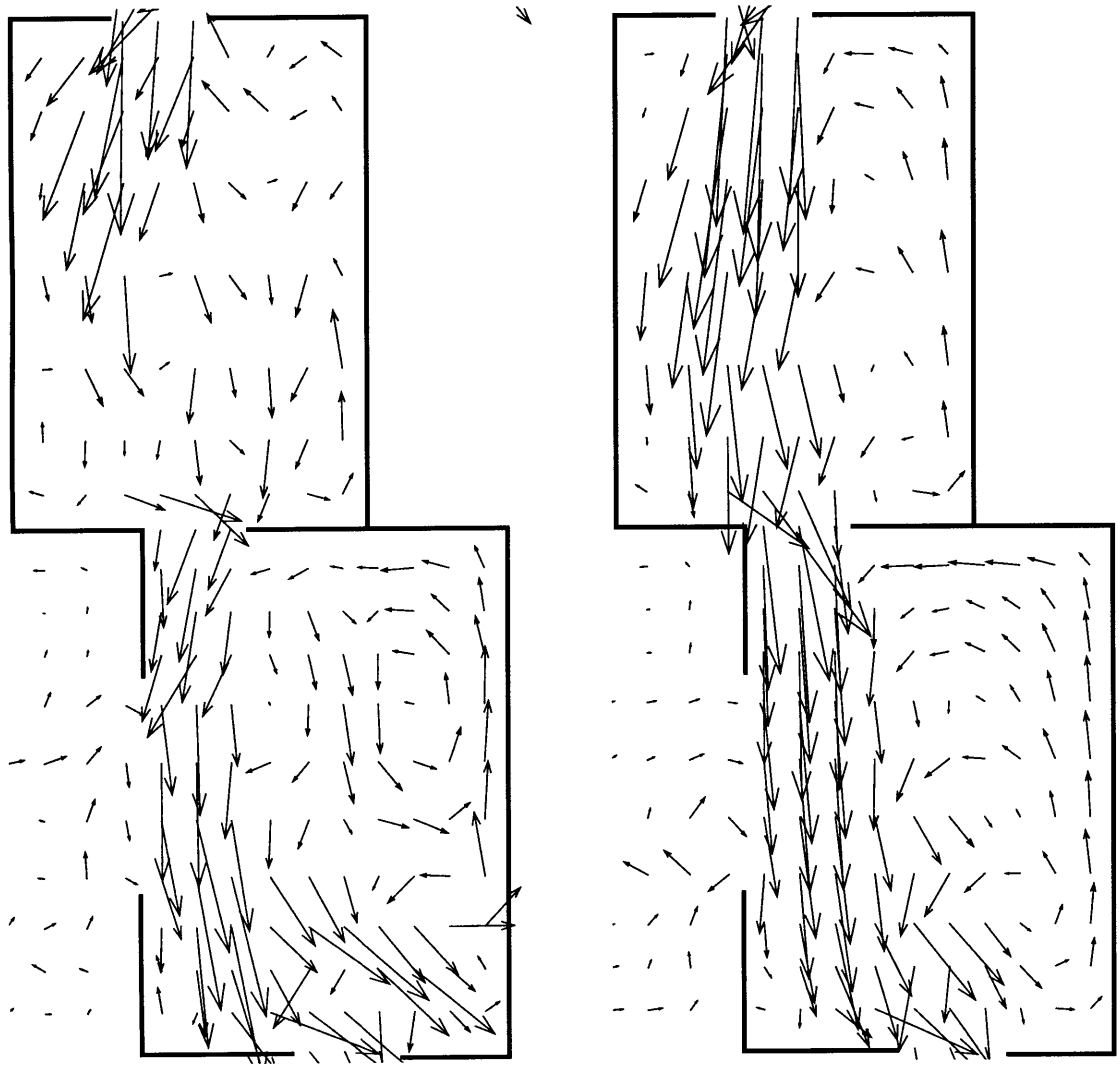

(a) Transient *(b) Mean*

Figure 5.15 *Velocity field computed by LES.*

5.3 Wind-driven Cross and Single-Sided Ventilation in a Wind Tunnel

As described in Section 3.1, detailed measurements of airflow around and within a simple building-like cubic body were made in a boundary layer wind tunnel. Two-dimensional mean and fluctuating velocity components were captured using Laser Doppler Anemometer (LDA) equipment. Measurement points were arranged in front, inside, and behind the body. The pressure distributions along the model surface were also measured. In this section, these experimental data are used to validate LES subgrid-scale models. Three different natural ventilation cases were studied: single-sided ventilation with an opening in the windward wall, single-sided ventilation with an opening in the leeward wall, and cross ventilation with openings in both windward and leeward walls. It is considered that, should the numerical results compare well to the physical model results in the wind tunnel, then the numerical method can be applied with confidence to simulations of full-scale buildings.

5.3.1 Case setup

In the experiments, both building models and their openings had the same dimensions, and they were placed at the same location in the wind tunnel (Section 3.1). In the numerical simulation, the same computational domain, meshes, and boundary conditions were used in all three cases. This investigation set the length of the building model, 250 mm, as a reference length (H). The computational domain had a downstream length of 8H, an upstream length of 4H, a lateral length of 4H on both sides of the building, and a height of 4H. The Reynolds number was 140,000 based on the velocity at the building height in the inlet of the computational domain.

A non-uniform mesh, $100 \times 65 \times 80$, was used in all three cases. Each case required one week of CPU time on an Alpha workstation. The time step was 4×10^{-4} seconds, and the smallest mesh was 10^{-2} H, which was close to the building edge dimension. This spacing was two orders higher than the expected Kolmogorov scale, 10^{-4} H.

Based on the experimental data, the profile of the mean velocity along the streamwise direction, U, follows a logarithmic law, and the mean velocities in the other two directions were zero. The impacts of the inflow condition with and without adding turbulence fluctuations on the pressure distributions around the body were investigated. It was found that the inflow with the turbulence fluctuations added generated accurate pressure distributions than that without the added turbulence fluctuations. The results suggested that it is better to add the turbulence fluctuations at the inflow. Although the reason for the better results is not clear, it seems to be related to the magnitude of the turbulence time scale. Therefore, turbulence was added to the mean velocity at the inflow: the fluctuations of the inflow velocity in all three directions are generated by superposing random perturbations with an intensity, u′/U, of 10%.

5.3.2 Results and discussion

Study of the ventilation performance in a building needs detailed airflow information around and inside the building. The information required includes the velocity and pressure distributions, which are used to determine the ventilation rate. The following sections present the numerical results for all three ventilation cases. The velocity distributions around and inside the buildings are presented first. Then the pressure distributions along building surfaces are presented. Finally, the ventilation rate and the energy spectra are studied.

Velocity

In all three ventilation cases, the mean and fluctuating velocities along the streamwise and vertical directions were measured along the center-section of the building models.

Figures 5.16-5.18 show the mean velocities computed from LES with a coarse mesh, 100 × 65 × 80. The difference between the experimental data and the LES results is less than 5% in most regions. This indicates that LES can be used to study natural ventilation driven by wind force with acceptable accuracy. However, there are also some discrepancies between the experimental data and the numerical results. In all three cases, LES under-predicted the mean velocities along the steamwise direction, U, in front of the building (X = -H) close to the ground. In addition, the computed mean velocities, U, right above the building roof, which were measured only in Case 2 (single-sided ventilation with an opening in the leeward wall), is 30% larger than the measurement data. This means that the eddy size above the roof is relatively larger in the experiment than in the simulation. Shah (1998) also observed this phenomenon when studying the airflow around a cube with LES. Kato, *et al.* (1992) pointed out that this problem might be attributed to the coarseness of the mesh. Figures 5.19-5.21 show that the fluctuating velocity components computed from LES are also in reasonable agreement with the experimental data.

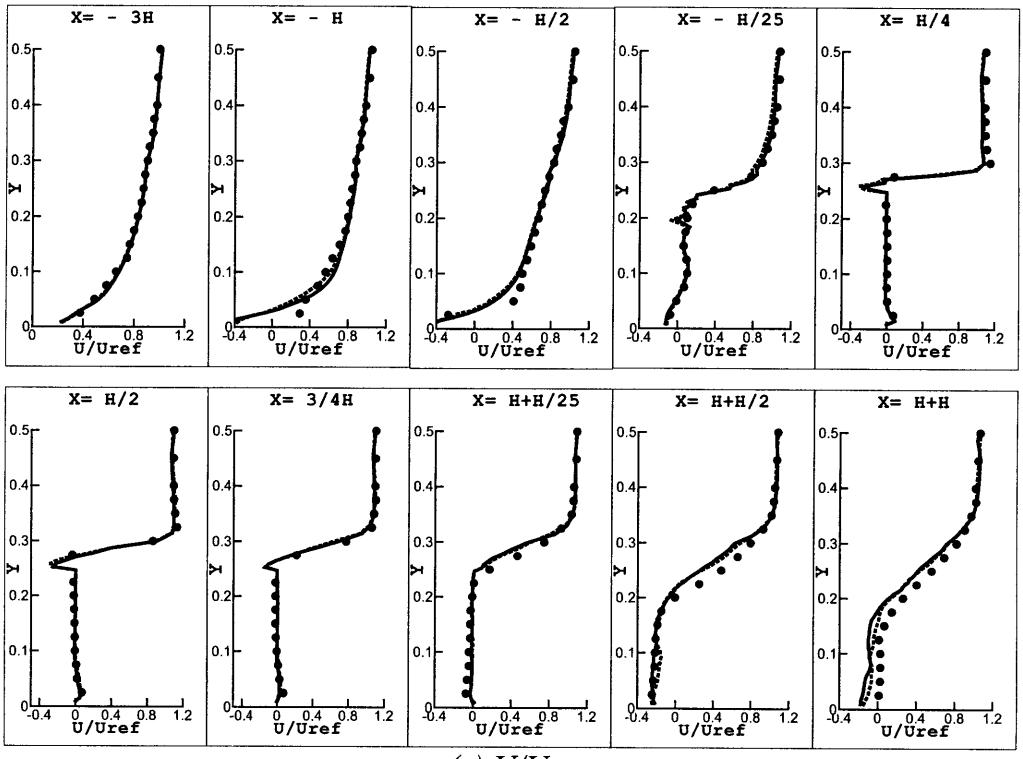

(a) U/U_{ref}

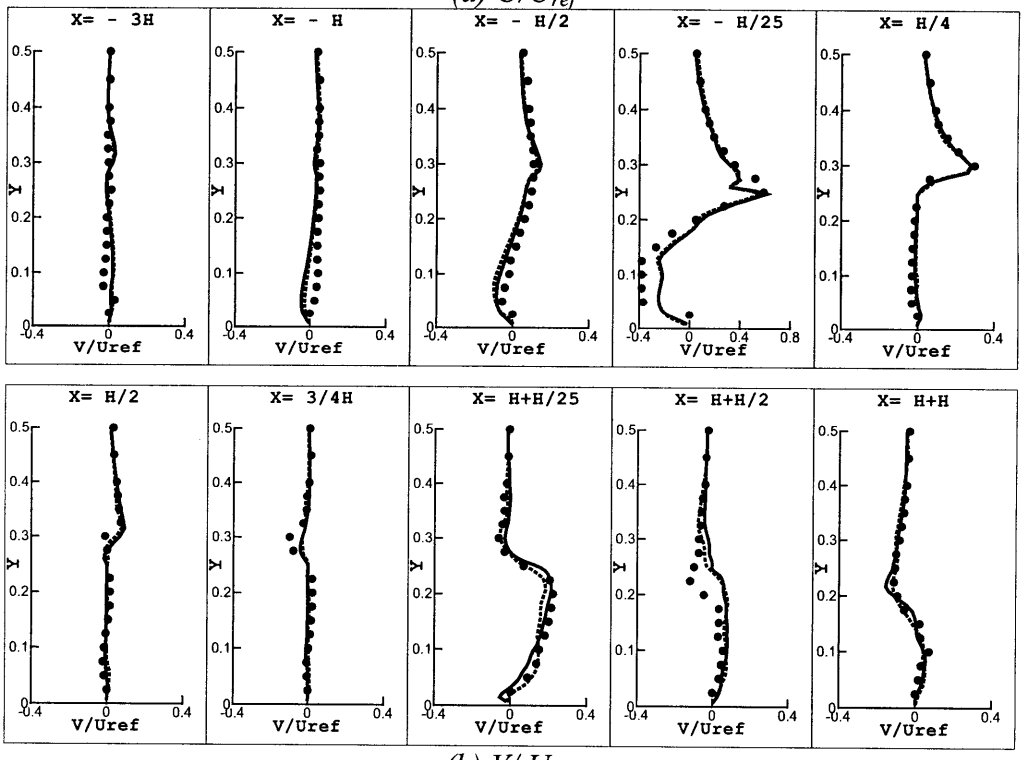

(b) V/U_{ref}

Figure 5.16 *Mean velocity distributions for the single-sided, windward ventilation. Black dots: Experiment; Solid line: SS model; Dashed line: FDS model.*

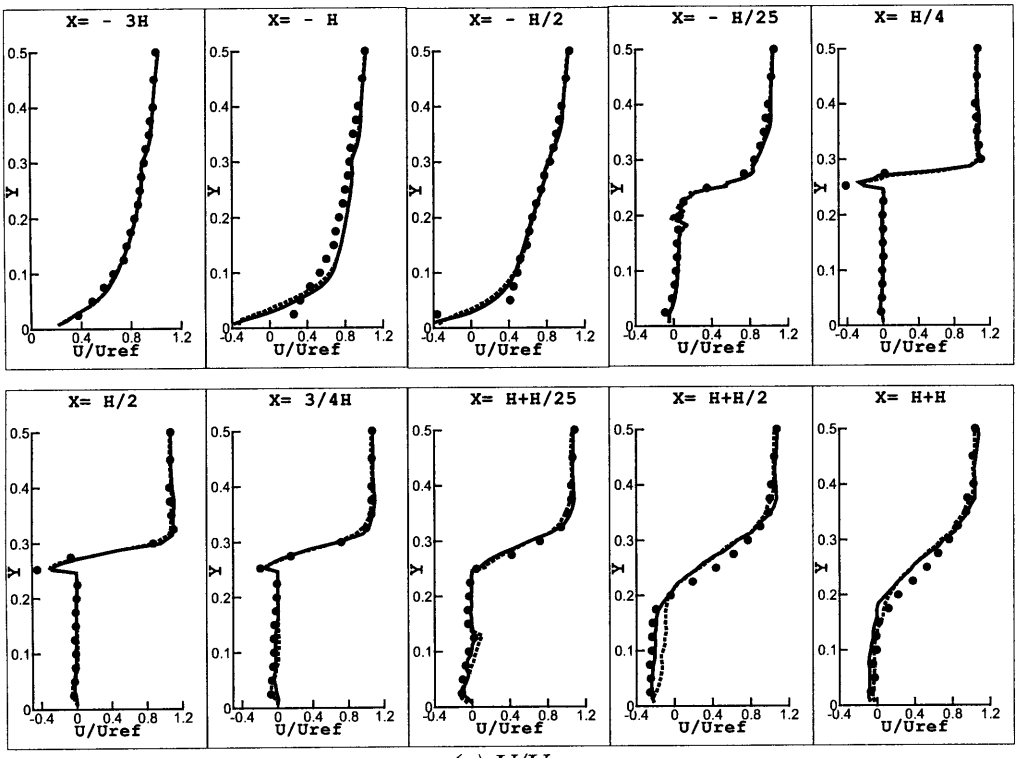

(a) U/U_{ref}

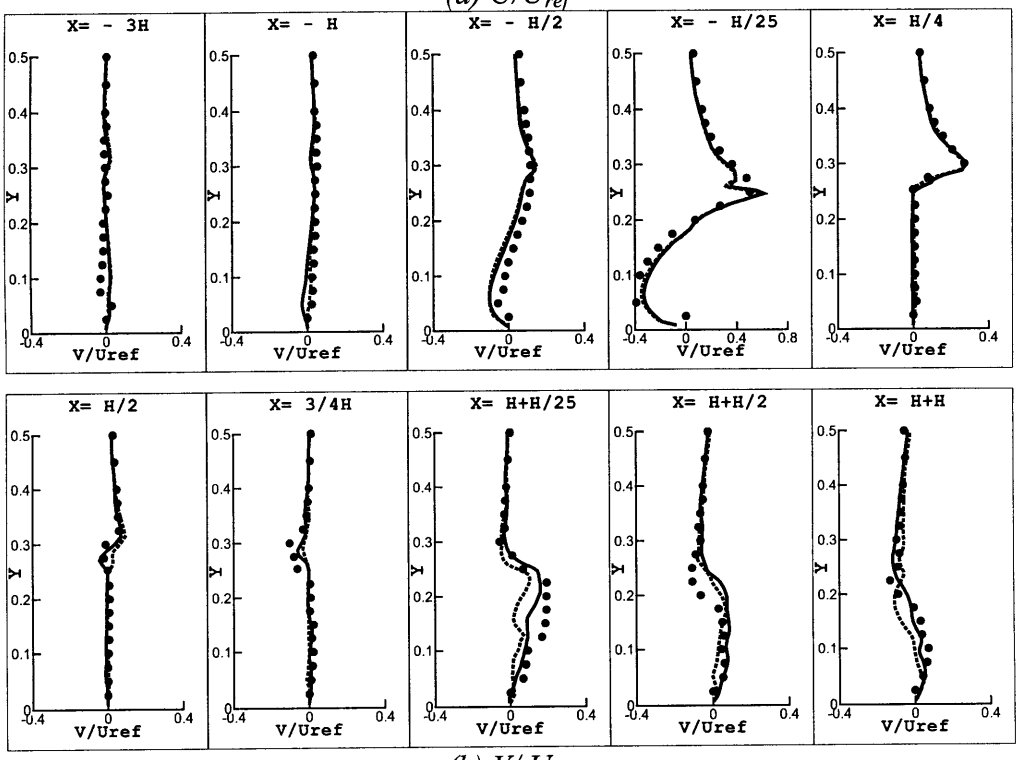

(b) V/U_{ref}

Figure 5.17 *Mean velocity distributions for the single-sided, leeward ventilation. Black dots: Experiment; Solid line: SS model; Dashed line: FDS model.*

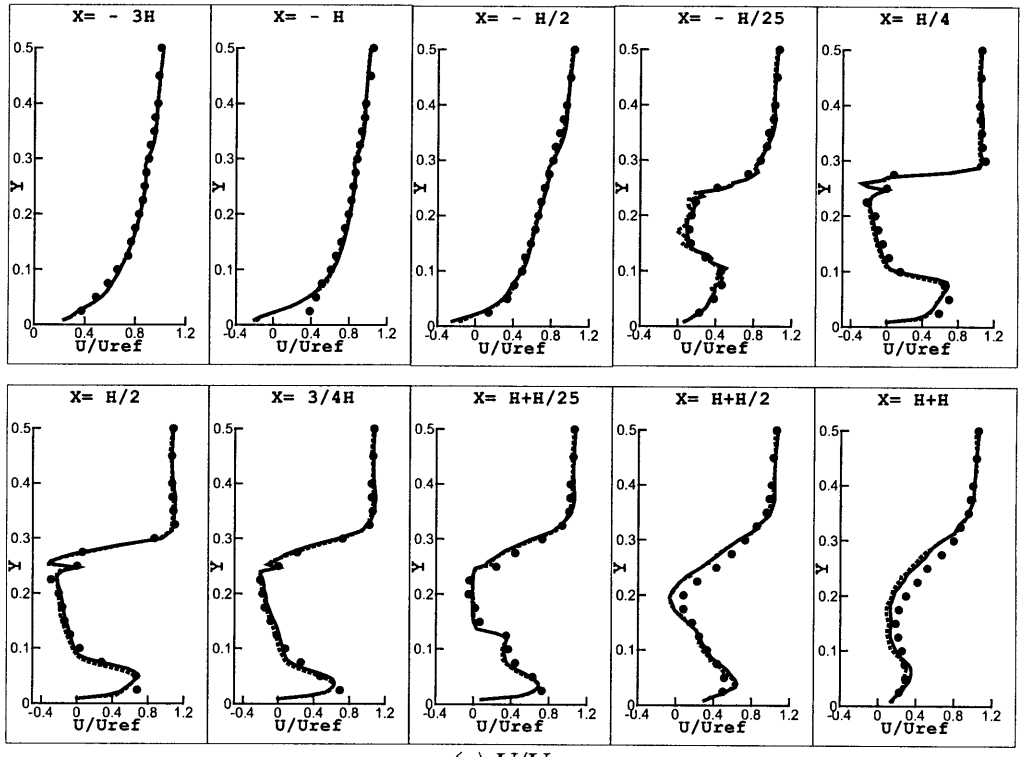

(a) U/U_{ref}

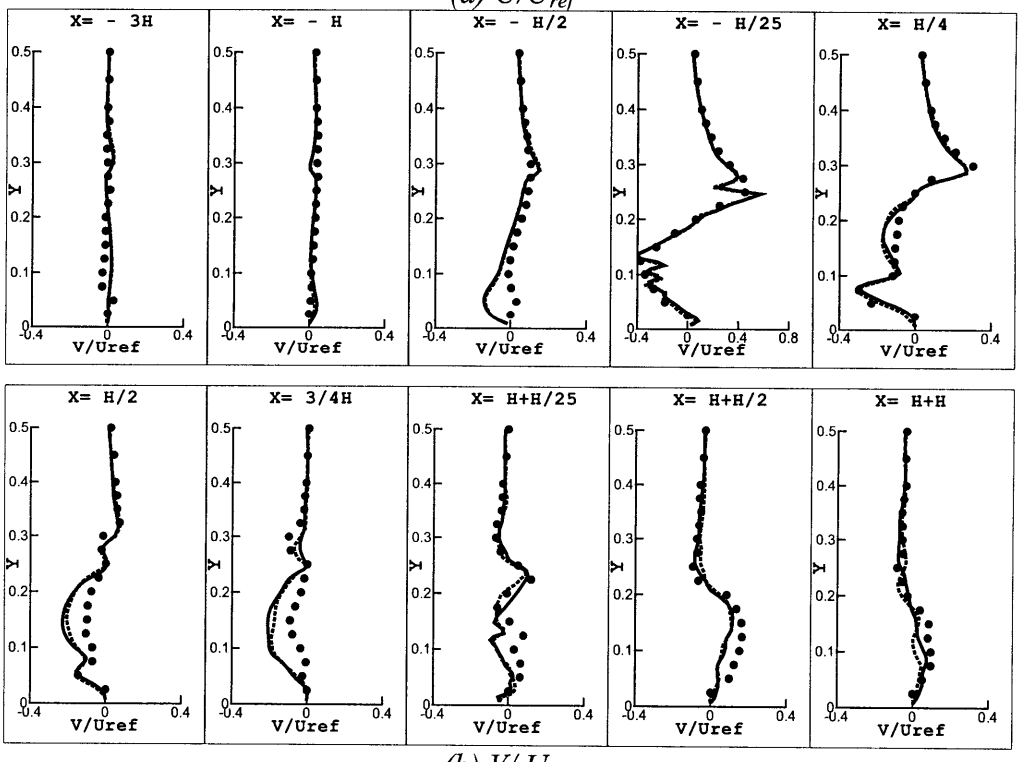

(b) V/U_{ref}

Figure 5.18 *Mean velocity distributions for the cross ventilation. Black dots: Experiment; Solid line: SS model; Dashed line: FDS model.*

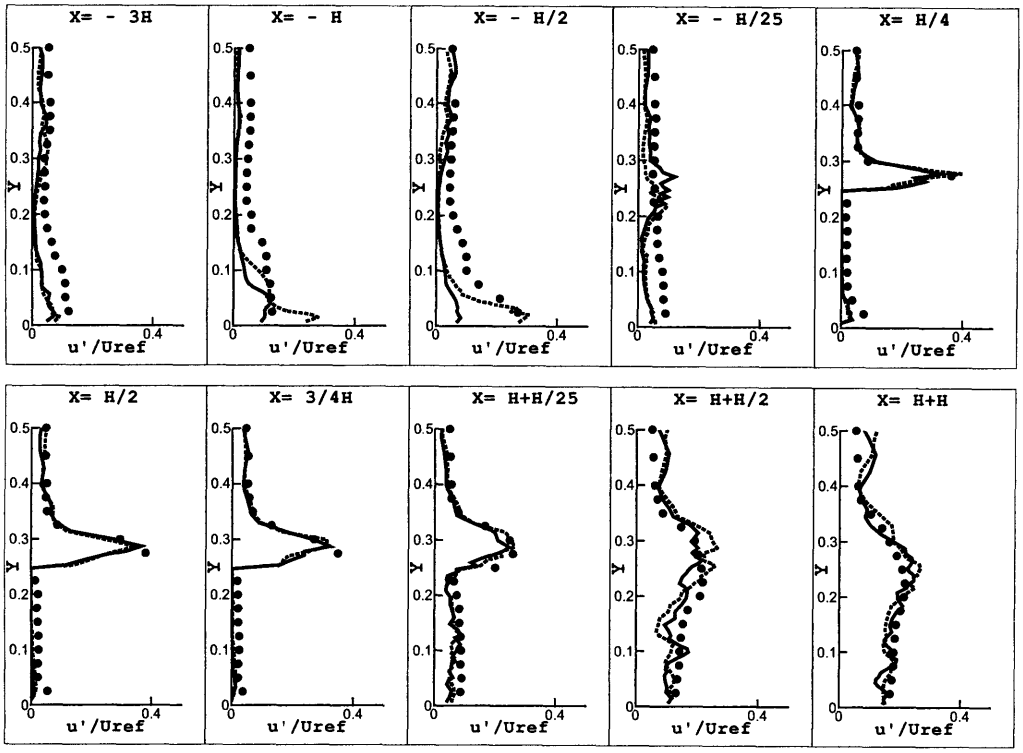

(a) u'/U_{ref}

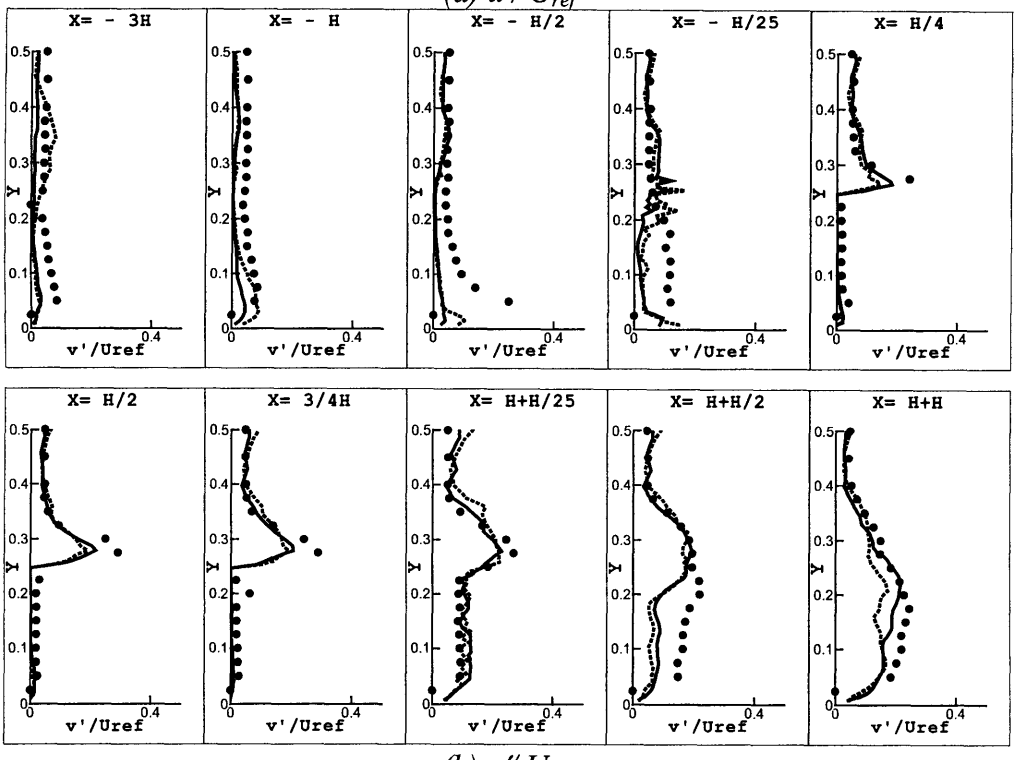

(b) v'/U_{ref}

Figure 5.19 *Fluctuating velocity distributions for the single-sided, windward ventilation. Black dots: Experiment; Solid line: SS model; Dashed line: FDS model.*

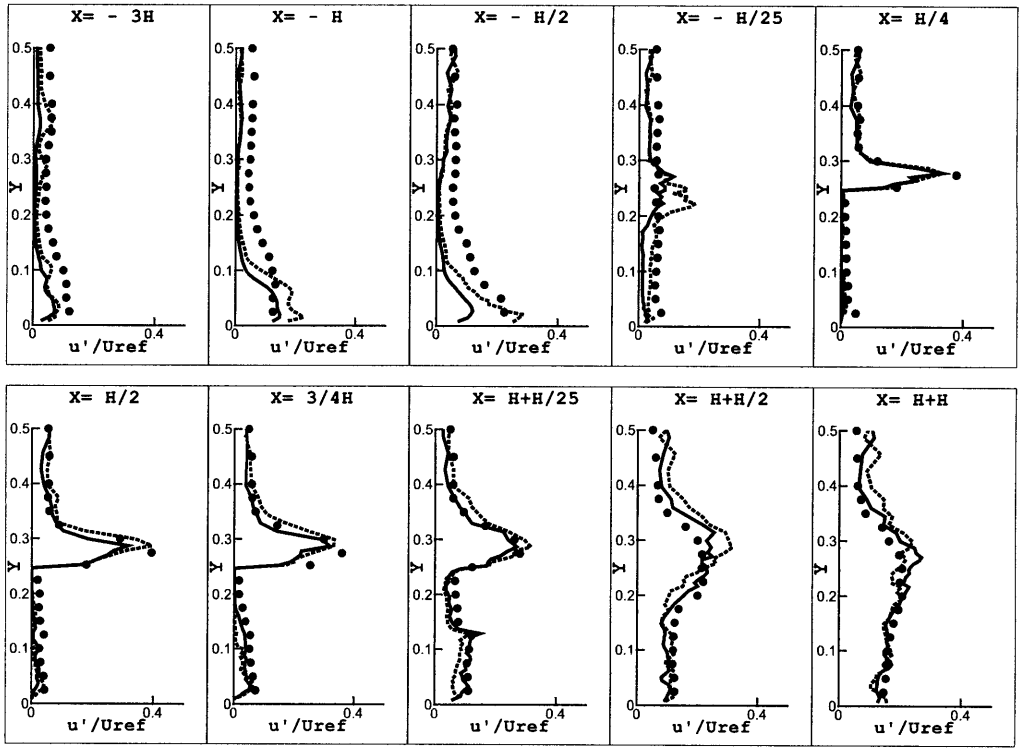

(a) u'/U_{ref}

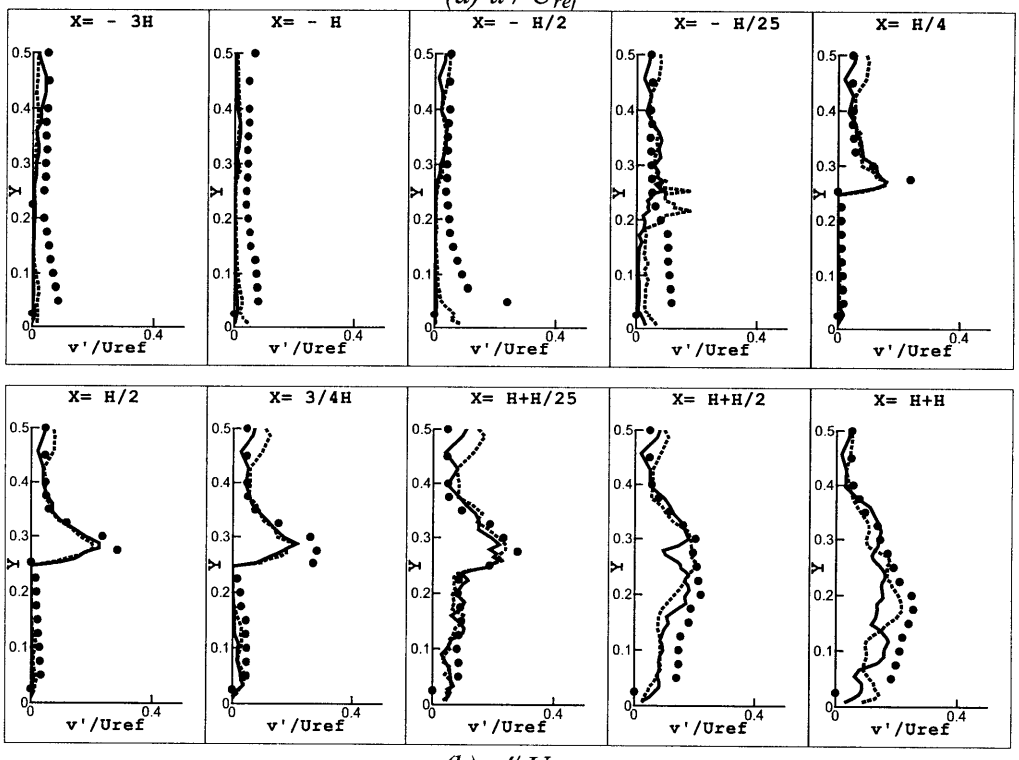

(b) v'/U_{ref}

Figure 5.20 *Fluctuating velocity distributions for the single-sided, leeward ventilation. Black dots: Experiment; Solid line: SS model; Dashed line: FDS model.*

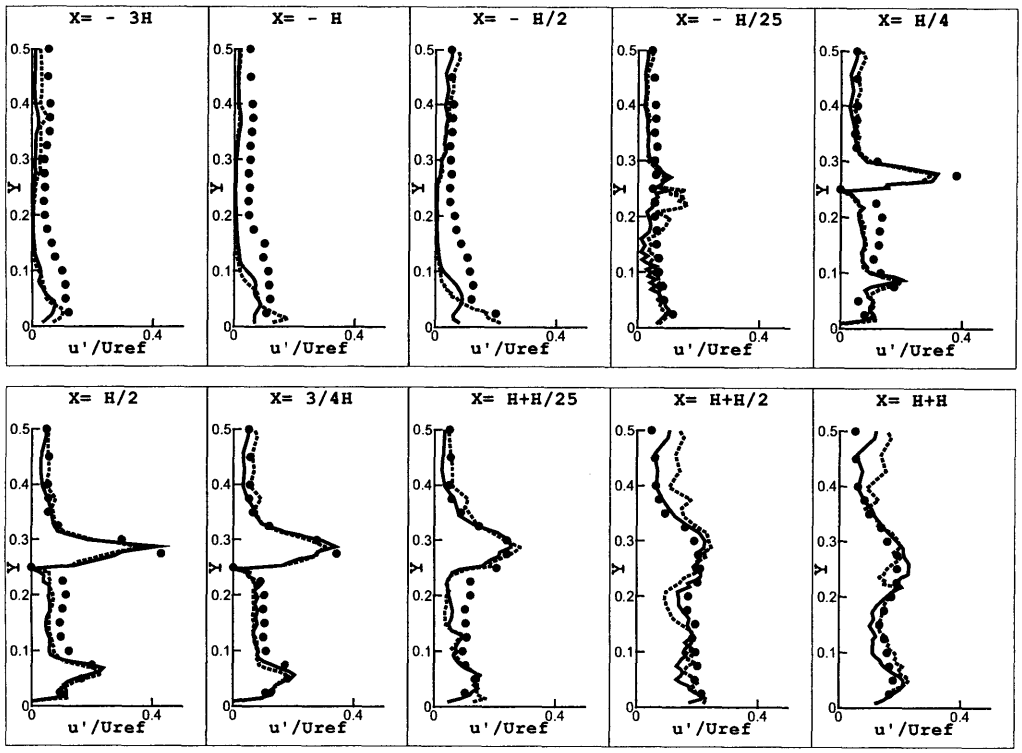

(a) u'/U_{ref}

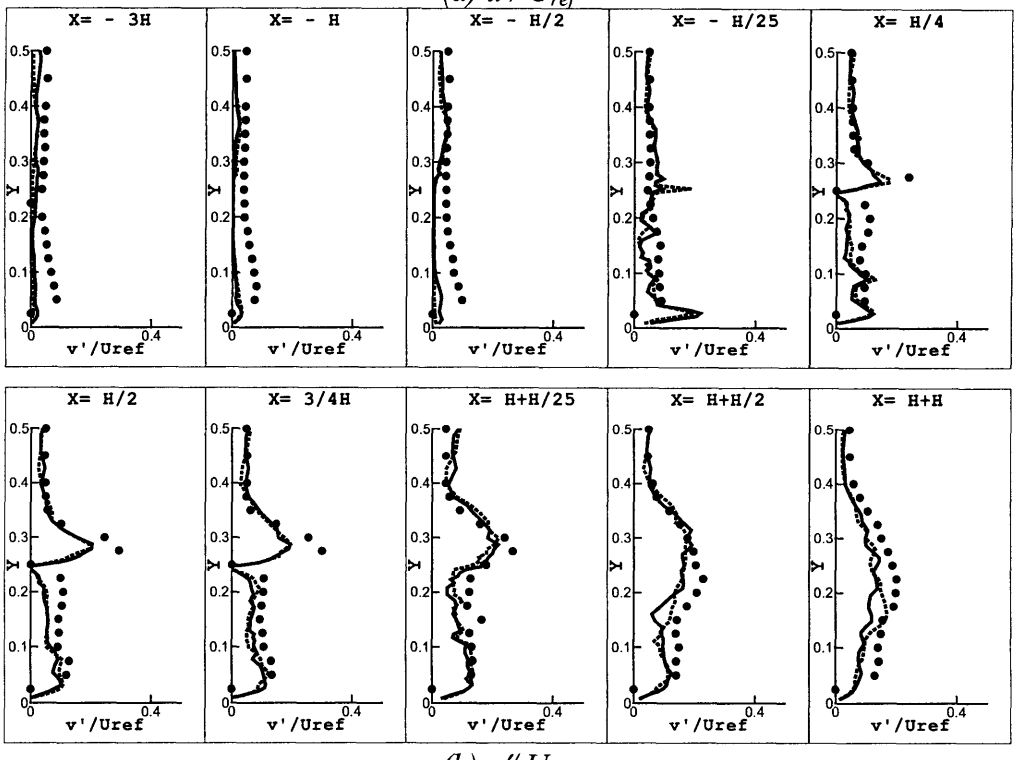

(b) v'/U_{ref}

Figure 5.21 *Fluctuating velocity distributions for the cross ventilation. Black dots: Experiment; Solid line: SS model; Dashed line: FDS model.*

To investigate whether the grid resolution causes LES to under-predict U in front of the building and over-predict U above the building roof, a finer mesh (140 × 80 × 110) was applied to Case 2 (single-sided ventilation with an opening in leeward wall), where the mean velocities above the building roof were measured in the experiment. Since both the SS and FDS models give similar results, only the SS model was used with the fine mesh. Figure 5.22 shows the distributions of the mean velocities along the streamwise direction, U, in front of the building (X = -H), and above the building roof (X = -H/4) with two different grid resolutions. The computed results show that the discrepancies found with the coarse mesh did not occur with the fine mesh, and the fine mesh provided better agreements with the experimental data. Therefore, the coarseness of the mesh is the reason for the two major discrepancies mentioned above.

However, when we use LES to study natural ventilation, the ventilation rate is the most important parameter that is determined by the flow field distributions at the opening. Since the distributions of the mean and fluctuating velocities close to building openings were correctly predicted with the coarse mesh (Figures 5.16-5.21), the ventilation rate can be calculated correctly with the coarse mesh. It was found that the difference between the computed ventilation rates with these two different grid resolutions is less than 3%. Therefore, the coarse mesh continued to be used in the current investigation.

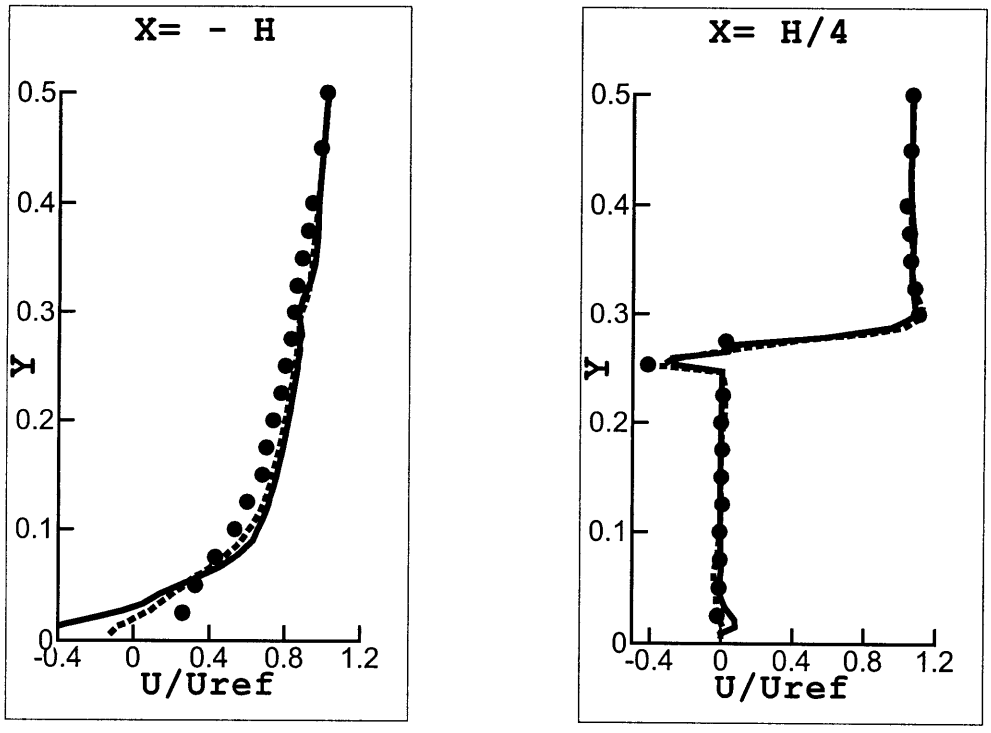

Figure 5.22 *Mean velocity distributions for the single-sided, leeward ventilation. Black dots: Experiment; Solid line: SS model with coarse mesh; Dashed line: SS model with fine mesh.*

Allocca (2001) used a standard k-ε model of the RANS modeling to simulate these three ventilation cases. It was found that, although the computed wind velocity distributions in front of the building model were in good agreement with the experimental data, the airflow distributions above and behind the building model were not correctly predicted, which has been confirmed in previous literature studies (Lakehal and Rodi, 1997). Figure 5.23 shows the computed mean velocity along the streamwise direction, U, with both the RANS modeling (Allocca, 2001) and the FDS model of LES for the single-sided leeward ventilation case. The results for other ventilation cases are very similar. The benefits of applying LES to study airflow around buildings are obvious from these comparisons.

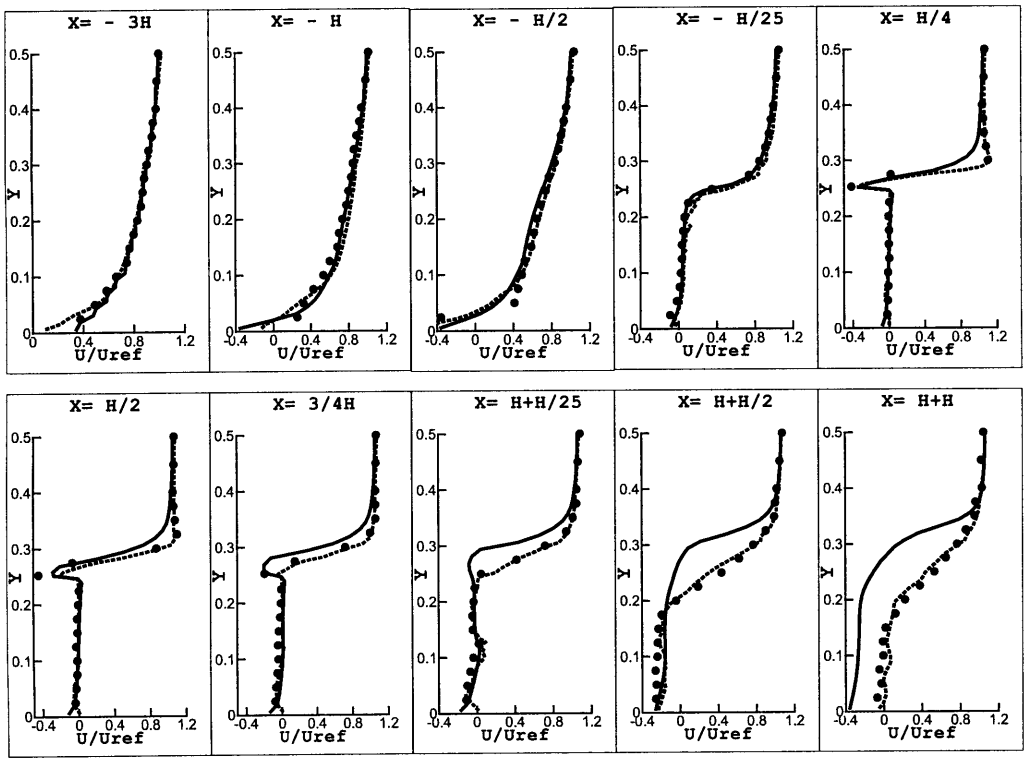

Figure 5.23 *Mean velocity distributions for the single-sided, leeward ventilation. Black dots: Experiment; Solid line: the RANS modeling (Allocca, 2001); Dashed line: FDS model of LES.*

The results from both SGS models of LES are almost the same. Shah (1998), Rodi, *et al.* (1997), and Jiang and Chen (2001) have observed that different subgrid-scale models have similar performance for predicting airflow around a block with high Reynolds numbers. By analyzing the magnitudes of different terms in the momentum equation, Jiang and Chen (2001) found that the contribution of the subgrid-scale stresses to the flow is much smaller than that of the resolved stresses in most regions around the block. Therefore, most energy is contained in large eddies, which play a more important role than the small eddies. Since both the SS and FDS models can directly solve the large-eddy motions, both models are able to provide accurate flow results. In the current study, although the building model is not a block, most of the airflows outside of the building model are fully or nearly fully developed turbulent flows, which are very similar to the airflows around a block. Hence, the computational results from the two subgrid-scale models are almost the same in most of the flow domain.

In some low velocity regions, such as the indoor airflow in the single-sided ventilation cases, the FDS model is expected to perform better than the SS model (Davidson and Nielson, 1996). However, in the current study, we did not do this comparison for two reasons. First, some measured interior velocities were as low as 0.05 m/s, which were within the error range. Secondly, the fluctuating velocities in most interior regions were higher than the magnitudes of the mean velocities. In order to obtain accurate velocity information, large number of data points would be needed at each measuring position. This would require abundant seeding particles entering the model. However, as discussed in Section 3.1, it was difficult to seed the interior of the model due to weak flow motion inside. Therefore, the comparison of the computed results with measurement data inside the building model is not very meaningful.

Figure 5.24 shows the time averaged velocity fields for the three cases with a coarse mesh. Since both the SS and FDS models provide very similar airflow fields, Figure 5.24 presents only the results computed by the SS model. The agreement between the LES results and the experimental data is fairly good with respect to flow patterns, in particular the leeward eddy sizes and positions. A reverse flow along the ground is observed in front of the windward wall even though there is an opening in the single-sided windward case and cross ventilation cases. This reverse flow was observed in the experiment for the single-sided windward case (Figure 5.24 (a) measurement). However, it was not found for the cross ventilation case (Figure 5.24 (c) measurement). As shown in Figures 5.16-5.18, when using the coarse mesh, LES under-predicted the mean velocities in the streamwise direction, U, in front of the building (X = -H) close to the ground. This suggests that a larger recirculating region was produced in LES compared to the experimental results. To correctly predict the recirculating region in front of the body, it is important to capture the characteristics of the boundary layer approaching the body (Martinuzzi and Tropea, 1993). Therefore, a finer mesh should be used to correctly compute the boundary layer in front of the body. Figure 5.22 shows that a fine mesh predicts the boundary layers in front of the body better than the coarse mesh does.

Another noticeable phenomenon in Figures 5.24 (a) and (b) is that, in the two single-sided ventilation cases, the eddy height in front of the building was nearly the same as the opening height. The eddy height behind the building, however, was approximately twice the opening height. Therefore, the opening in the leeward wall (Case 2) was within the lower part of the large eddy, so that a considerable amount of airflow entered the building. In case 1, the whole small eddy was right at the opening, and functioned like a barrier, preventing large airflows from entering. Therefore, a larger ventilation rate is expected in Case 2 (leeward openings) than in Case 1 (windward openings).

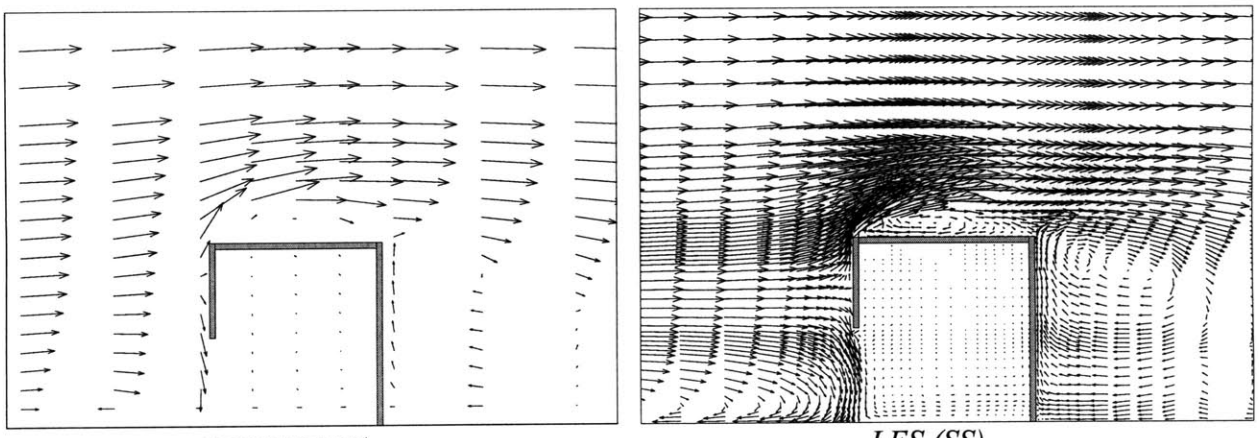

measurement *LES (SS)*

(a) single-sided, windward ventilation

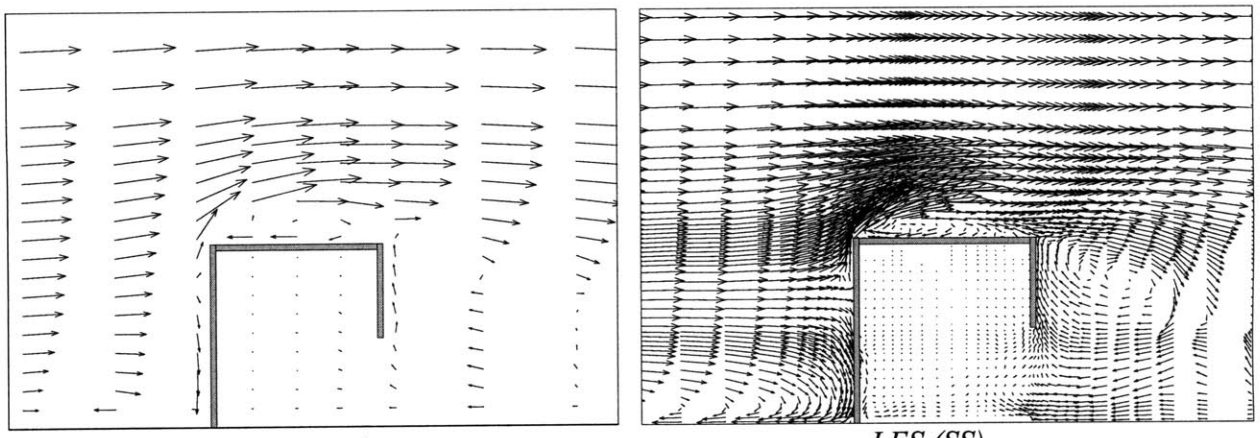

measurement *LES (SS)*

(b) single-sided, leeward ventilation

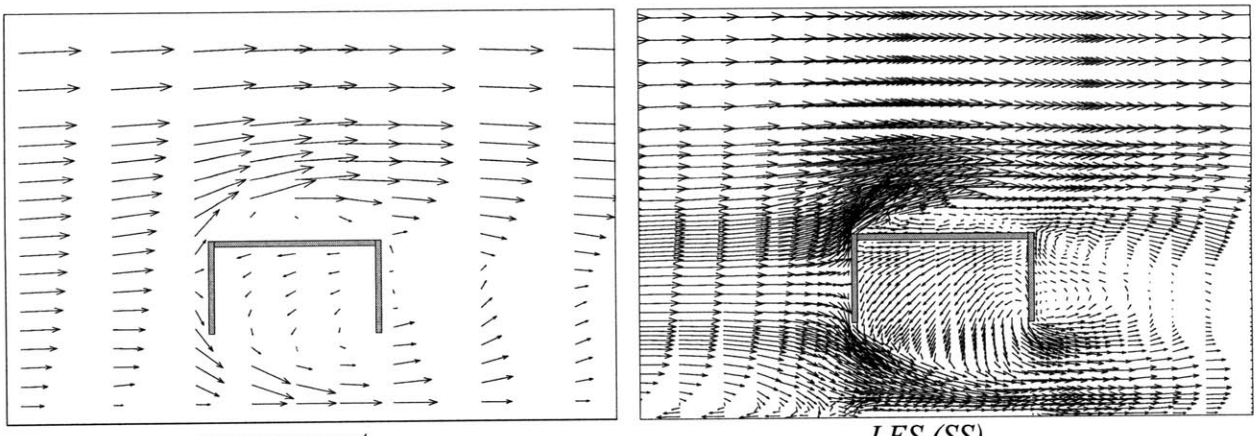

measurement *LES (SS)*

(c) cross ventilation

Figure 5.24 *The measured and computed mean velocities in the central section.*

Pressure

Figure 5.25 shows the distributions of mean pressure coefficient, $C_P = (P - P_{ref})/(\frac{1}{2}\rho U_{ref}^2)$, along the building surfaces for the three cases. Both the SS and FDS models can predict the coefficients well, although small discrepancies exist along the building roof, where the measured C_P is smaller than the computed one. As mentioned in Section 5.1, larger velocities in LES produce a smaller eddy size above the roof, thus leading to a larger Cp along the building roof.

Success in predicting surface pressures induces confidence in using the LES method to locate small ventilation openings (grills, smoke vents etc.) and to predict their performance even in highly disturbed flows.

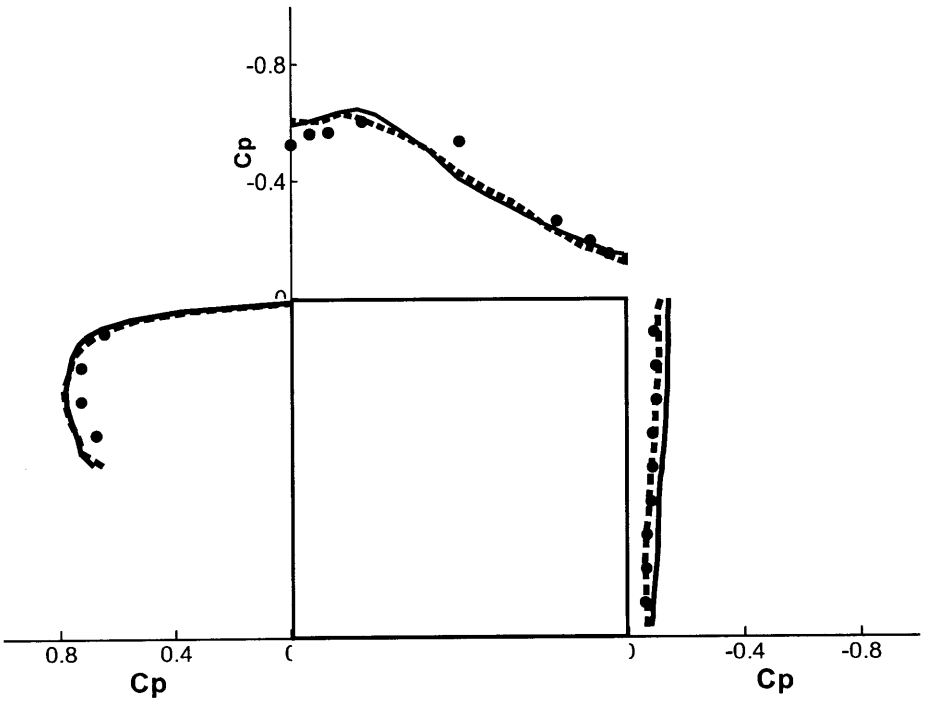

(a) single-sided, windward ventilation

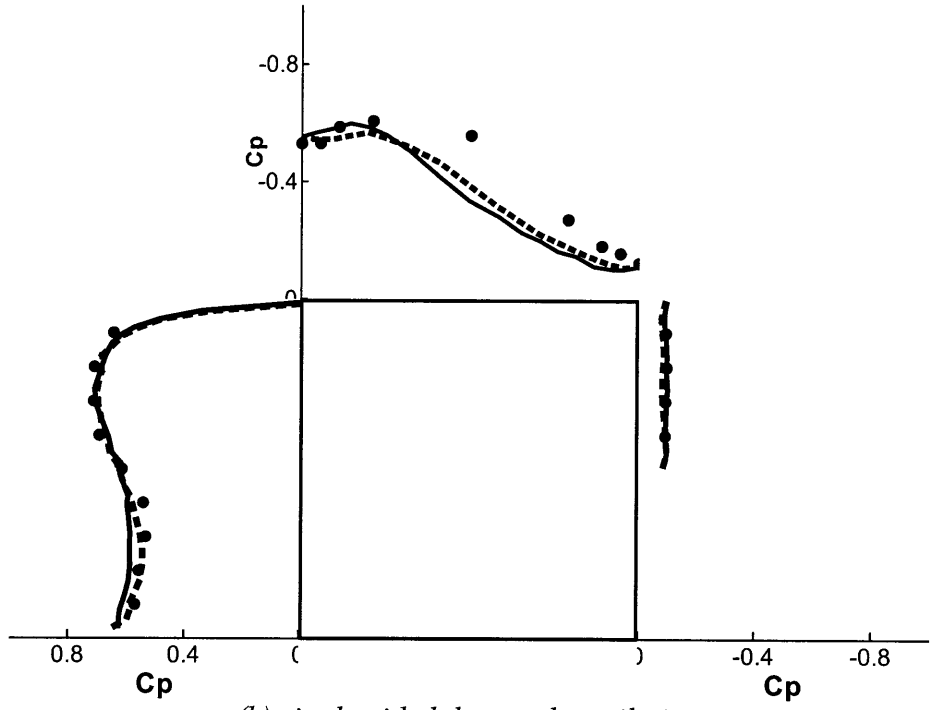

(b) single-sided, leeward ventilation

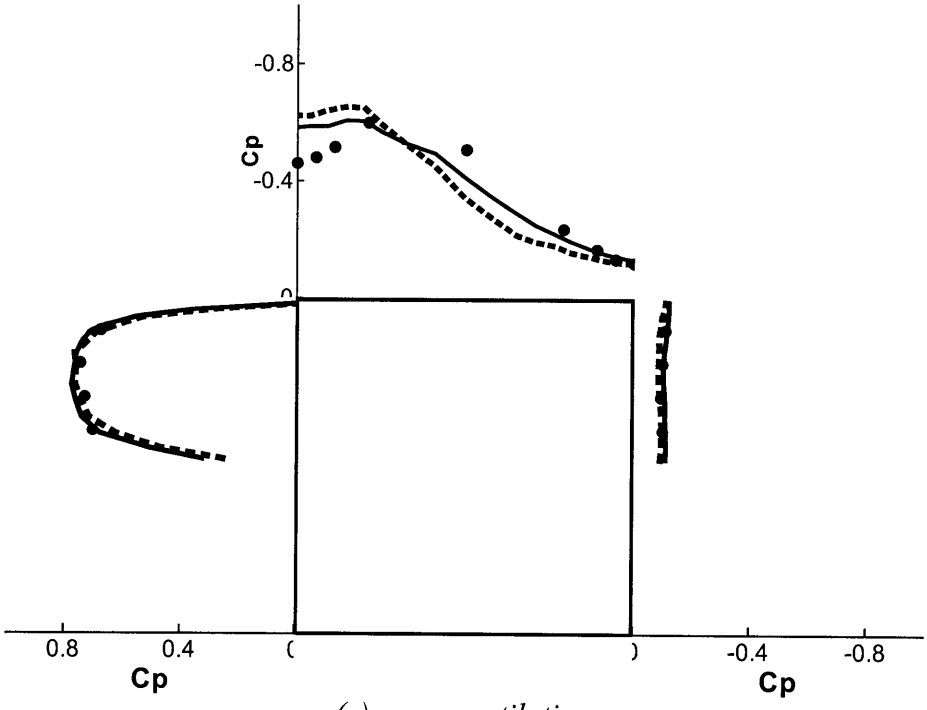

(c) cross ventilation

Figure 5.25 *The distributions of mean pressure coefficient, C_P ($C_P = \frac{P - P_{ref}}{\frac{1}{2}\rho U_{ref}^2}$), around the building model. Black dots: Experiment; Solid line: SS model; Dashed line: FDS model.*

Ventilation Rate

Ventilation rate or airflow rate is an important parameter for ventilation assessment. The current experiment was not able to measure the ventilation rate in the model due to time and resource limitations. However, if, as is shown here, boundary conditions of varying flow and pressure near openings can be predicted with confidence, then ventilation rates can be calculated with confidence through integrating the velocity across the openings. As mentioned in Section 5.1, there are two ways to do the integration. The first is to extract the mean velocity, $U_{j,k}$, from a mean flow field, and compute the mean ventilation rate, Q_{mean}. The other is to determine the cumulative and average instantaneous ventilation rate (CAI), $Q_{ins,T}$ as described in Section 5.1.2.

Figure 5.26 shows the variation of the CAI ventilation rate, $Q_{ins,T}$, over time, for both the SS and FDS models in the cross ventilation case. Although the difference in $Q_{ins,T}$ between the two subgrid-scale models is initially large, the CAI ventilation rate finally reached 0.0465 m^3/s with both models. This suggests that longer averaging times give more accurate ventilation rate results. $Q_{ins,T}$ were also computed for two single-sided ventilation cases.

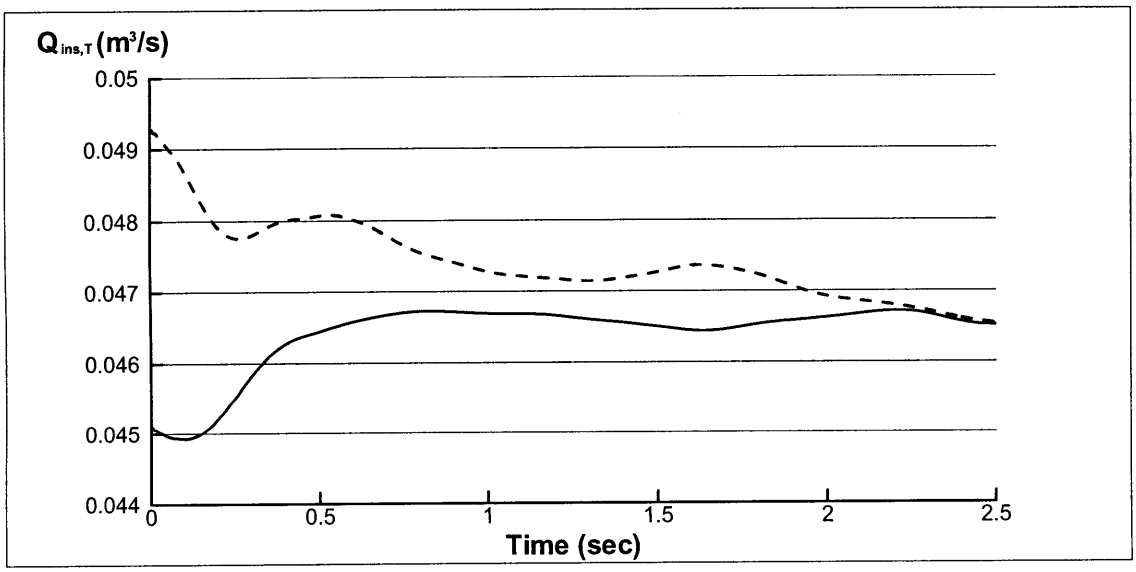

Figure 5.26 *The variation of the CAI ventilation rate, $Q_{ins,T}$, vs. averaging time with the two subgrid-scale models in the cross ventilation case. Solid line: SS model; Dashed line: FDS model.*

To compare results against simple design calculations, the cross ventilation rate expected in the model was computed by an empirical method based on the Bernoulli equation (Dascalaki, *et al.* 1995)

$$Q = C_d A U_{ref} \sqrt{\Delta C_p} \tag{5.6}$$

where C_d is the discharge coefficient of the openings, and can be set as 0.78 for a normal large sharp opening (Santamouris, 1992). The opening area, A, is computed as:

$$\frac{1}{A^2} = \frac{1}{A_{in}^2} + \frac{1}{A_{out}^2} \tag{5.7}$$

In our case A is 0.0074 m^2. The mean pressure coefficient across the openings is about 0.6 for a simple building shape (Etheridge and Sandberg, 1996), and the reference velocity at the building height is 10 m/s. The corresponding ventilation rate is 0.045 m^3/s, which agrees well with the LES result (0.0465 m^3/s). This may be because the building model studied is very simple, the two openings are identical, and there are no surrounding buildings. It is not surprising to see that the empirical model is capable of giving an accurate prediction of the ventilation rate. In a more complex real building design, where surrounding buildings or natural features affect wind flow, and where the configurations of openings are less ideal, the benefits of applying a general numerical method such as LES should become apparent.

An empirical model is also available for single-sided natural ventilation driven by wind (BS 5925, 1980). This model calculates the ventilation rate as

$$Q = 0.025\ A\ U \tag{5.8}$$

where A is the opening area, and U is the reference velocity normal to the opening. For our case, this gives Q = 0.0026 m^3/s. Although this empirical model, developed for full-scale buildings, should not be directly compared to our test cube, it is promising that there is an agreement with the LES result (0.0027 m^3/s) for the single-sided, windward ventilation case. However, this empirical model only considers the windward direction. The LES results indicate that the leeward ventilation case (at 0.0048 m^3/s) shows a significantly higher ventilation rate than the windward case.

The larger ventilation rate in Case 2 seems in conflict with common sense: one would expect a higher ventilation rate with a windward opening than with a leeward opening. However Melaragno (1982) has shown that for single-sided ventilation driven by wind force, the mean air velocity inside a building, which is closely correlated to ventilation rate, varies significantly with wind direction. He pointed out that the mean velocity inside a building with one opening in the windward wall could be smaller than that for an opening

in the leeward wall. In our wind-tunnel experiment, by visualizing the airflow within the cube, we observed that there was much stronger air movement within the cell in the leeward opening than in the windward opening case. The LDA measurements also indicate higher velocities and turbulence inside the opening in the leeward case. Table 5.4 gives the ventilation rates computed by LES and by empirical methods in three cases.

Table 5.4 *Ventilation rates in three natural ventilation cases*

Ventilation rate (m^3/s)	Empirical model	LES (FDS model)	
		$Q_{ins,\ 2.5\ sec}/V$	Q_{mean}/V
Case 1*	0.0026	0.0027	0.0026
Case 2**	–	0.0048	0.0032
Case 3***	0.045	0.0465	0.0465

Case 1*: single-sided ventilation with an opening in windward wall
Case 2**: single-sided ventilation with an opening in leeward wall
Case 3***: cross ventilation with openings in both windward and leeward walls

Turbulence Statistical Analysis

Haghighat, *et al.* (1991) studied the mechanism of single-sided ventilation due to wind-induced pressures. They performed a theoretical analysis by assuming a linear function of the wind pressure and employing an empirical formula for the wind velocity spectrum from experimental data. Their study found that the turbulent wind pressure has a direct impact on the ventilation performance of buildings. The effect is especially significant when the mean pressure differences across openings are low while their turbulent components are high, which usually occurs in single-sided ventilation situations.

Since LES directly provides both the mean and fluctuating pressure and the velocity, the mechanism of single-sided ventilation can be easily examined. The current study uses the single-sided, leeward case as an example. The overall internal pressure has a root-mean-square (RMS) value, σ_p^i, of 7.4 Pa, which is almost as large as that of the external wind RMS pressure acting on the opening, σ_p^e, of 7.6 Pa. The RMS values of pressure difference across the opening, $\sigma_{\Delta p}$ is 2 Pa, where $\Delta p = p^e - p^i$, while the mean pressure difference across the opening is only 0.4 Pa, which is much less than the fluctuating pressure. Therefore, the fluctuating pressure plays an important role in determining the airflow motions across the opening for this wind-induced, single-sided ventilation case.

Figure 5.27 shows the computed turbulence energy spectra in the vicinity of the opening using the SS model of LES for the single-sided leeward ventilation case. The shapes of the spectra distributions are very similar to those from the measurements (Figure 3.9). The energy spectra distributions at the opening were also computed, although they were not available from the measurements. At the lower part of the opening (Figure 5.27 (a)), the flow maintains its characteristics after going through the opening. However, at the higher parts of the opening and room (Figures 5.27 (b) and (c)), the outdoor airflow contains more high-frequency small eddies, and the indoor airflow in the recirculation and low-velocity region does not vary with time as strongly as the outdoor airflow does.

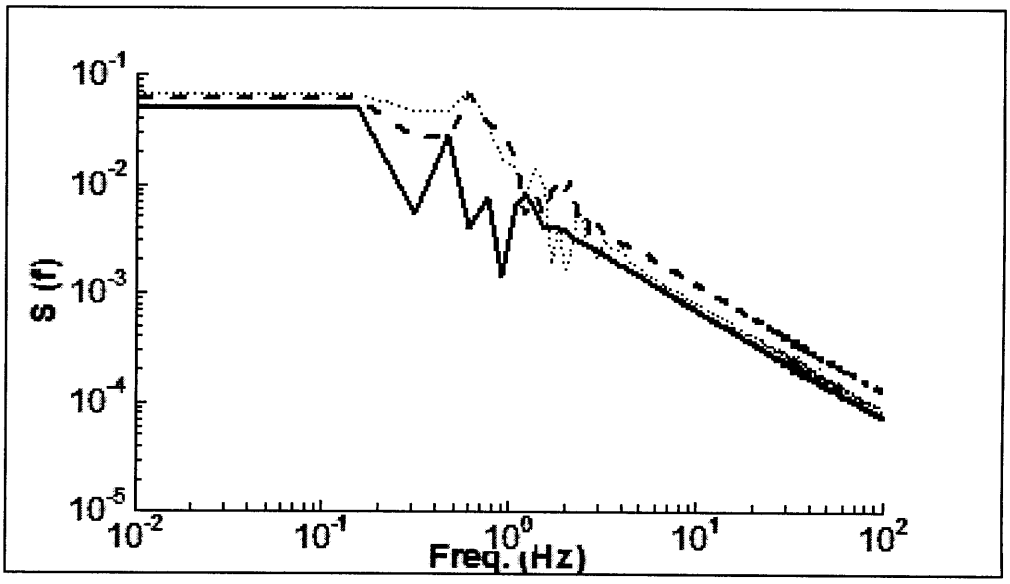

(a) Y = 0.3 H

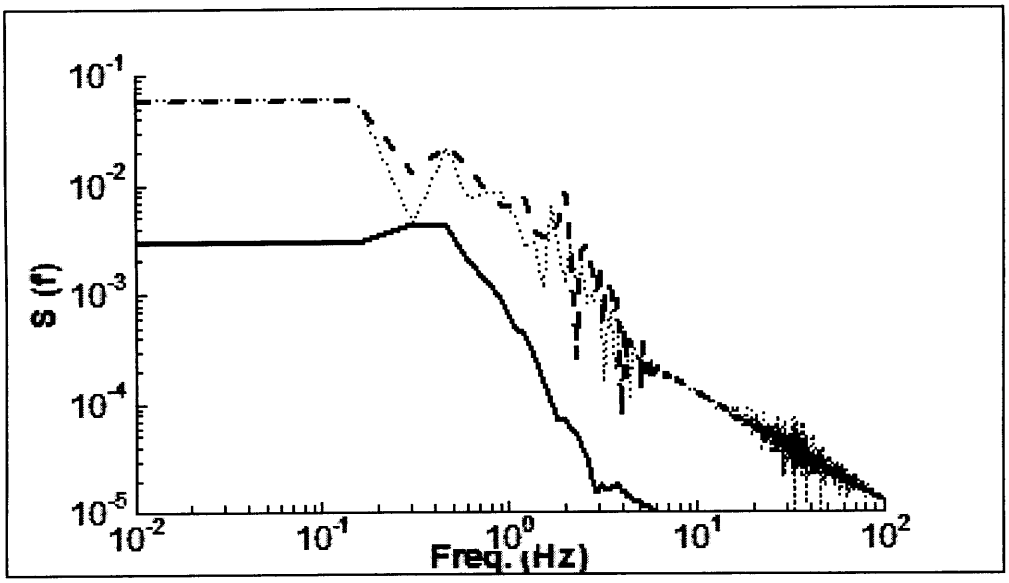

(b) Y = 0.5 H

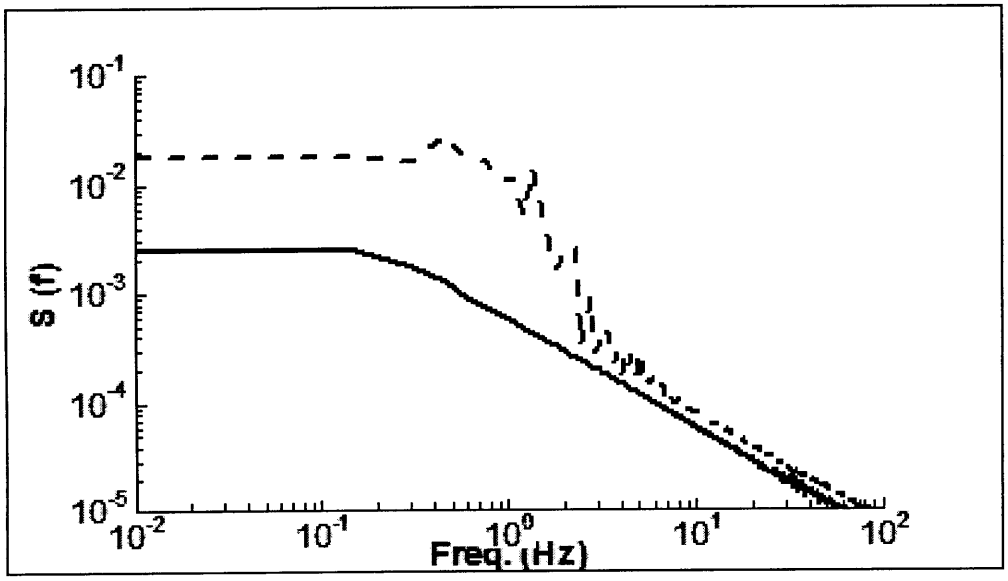

(c) Y = 0.8 H

Figure 5.27 *The computed turbulence energy spectra of u-component in the opening vicinity for the single-sided, leeward ventilation case. Solid line: X = 3/4 H (inside the model); Dotted line: X = H (at the opening); Dashed line: X = H + H/25 (outside of the model).*

Figure 5.28 shows the computed turbulence energy spectra in the vicinity of the opening with the SS model of LES for the cross ventilation case. Again, the shapes of the spectra distributions are very similar to those from the measurements (Figure 3.10). The airflow maintains its characteristics both inside and outside the building model. This suggests that, for this wind-tunnel simulation, the airflow motions in the cross ventilation case are very strong both outside and inside the building model. Therefore, most energy is contained in high-frequency regions.

For single-sided ventilation, however, the airflow varies strongly with time only in the high-velocity regions, such as the outside of the building model, and a large amount of high-frequency small eddies are generated. Inside the building model, if the airflow can enter directly from the outside, as in the lower region inside the building model, the energy is also contained in the high-frequency region, and the flow field maintains its characteristics. However, the upper areas of the model interior are low-velocity and recirculation regions, where airflow does not vary significantly with time. Therefore, most energy is contained in lower-frequency regions as shown in Figures 5.27 (b) and (c). However, whether this situation represents a real wind situation needs to be further tested with a full-scale experiment measuring real wind data both inside and outside a test chamber.

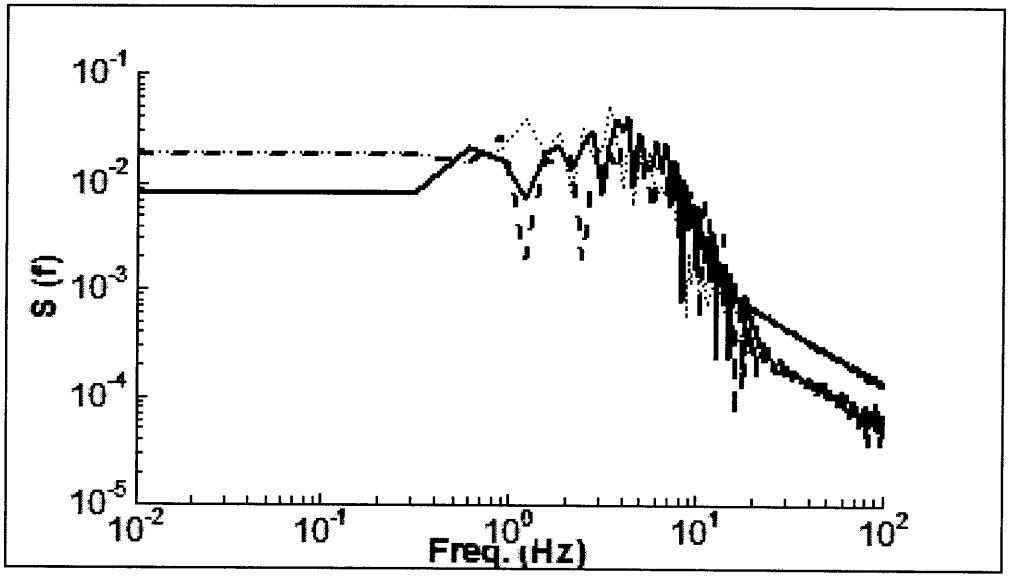

(a) Y = 0.3 H

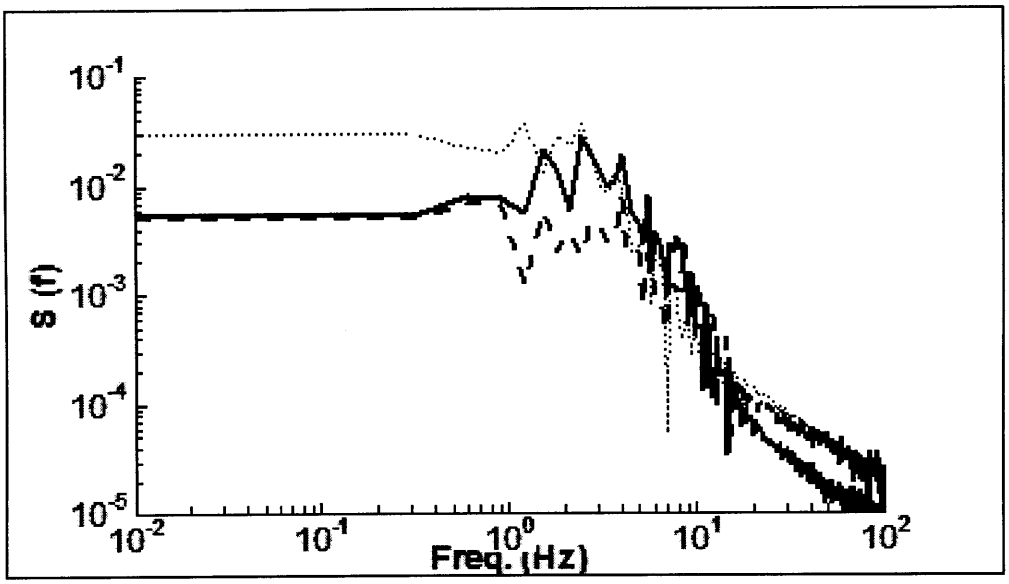

(b) Y = 0.5 H

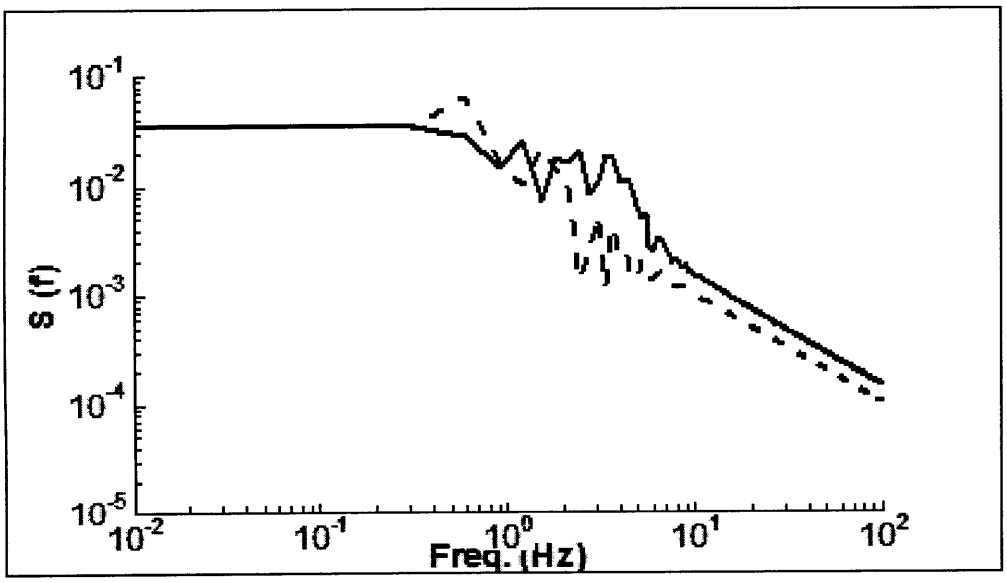

(c) Y = 0.8 H

Figure 5.28 *The computed turbulence energy spectra of u-component in the opening vicinity for the cross ventilation case. Solid line: X = H/4 (inside the model); Dotted line: X = 0 (at the opening); Dashed line: X = - H/25 (outside of the model).*

5.4 Wind-driven Cross Ventilation in a Wind Tunnel

Murakami *et al.* (1991) performed cross-ventilation experiments in a wind tunnel. The current study simulates one of their cases. Figure 5.29 shows a schematic view of the building model, which has a square duct connecting the inflow and outflow. In the experiment (Murakami *et al.*, 1991), a tracer gas technique with constant injection rate was used to measure the ventilation rate. The duct can be considered an "indoor" environment, and the case is thus a combined indoor and outdoor airflow study. In the numerical simulation, the Reynolds number is 50,000, and the non-dimensional characteristic length is 1. The expected Kolmogorov scale is about 10^{-4}. The smallest non-dimensional grid size is 0.02, and the total grid number is 261,184. The non-dimensional time step size is 0.004.

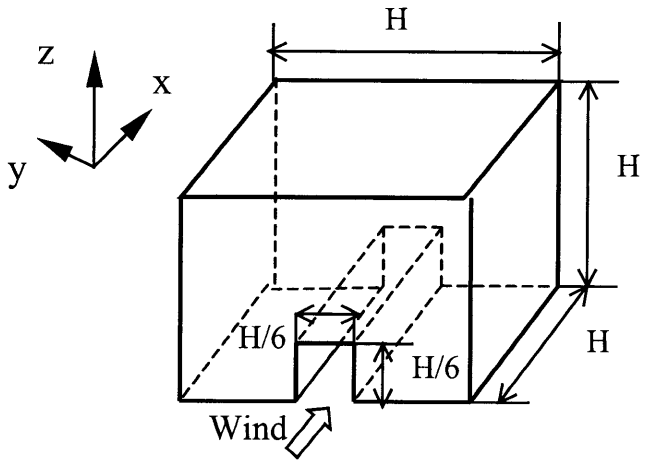

Figure 5.29 *A schematic view of the building model.*

Figure 5.30 shows the distributions of the mean pressure coefficients at the middle section of the building block. Very similarly to the outdoor airflow case reported in Chapter 4, both subgrid-scale models produce reasonable results compared with the experimental data.

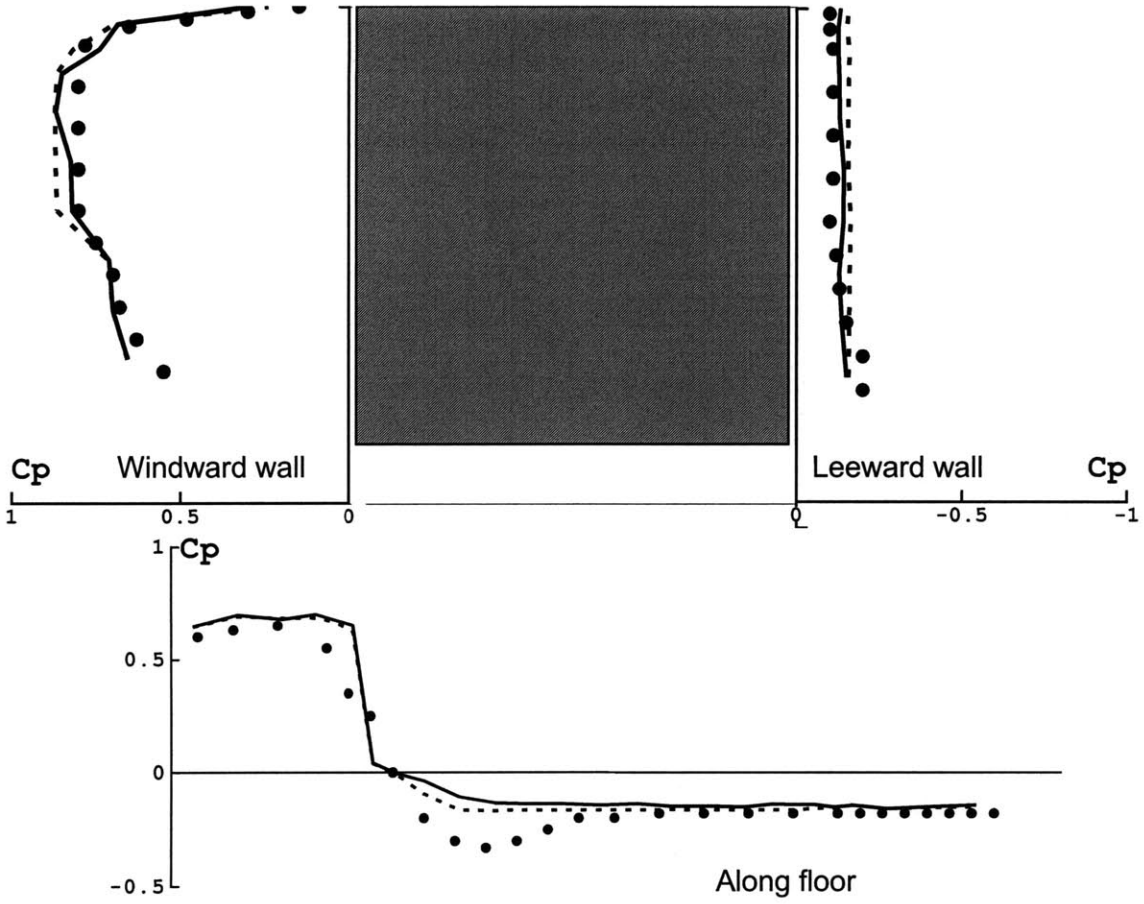

Figure 5.30 *The mean pressure distribution at the middle section of the building block. Black dots: Experiment; Solid line: SS model; Dashed line: FDS model.*

The velocity distributions around the building model, as shown in Figure 5.31, can explain why both subgrid-scale models produce good results. For simplicity, the figure presents the results computed with the FDS model. The results with the SS model are similar. Since the wind can easily travel through the duct without a major recirculation region, the "indoor" airflow is a nearly fully developed turbulent one. Therefore, both subgrid-scale models are able to correctly predict the flow.

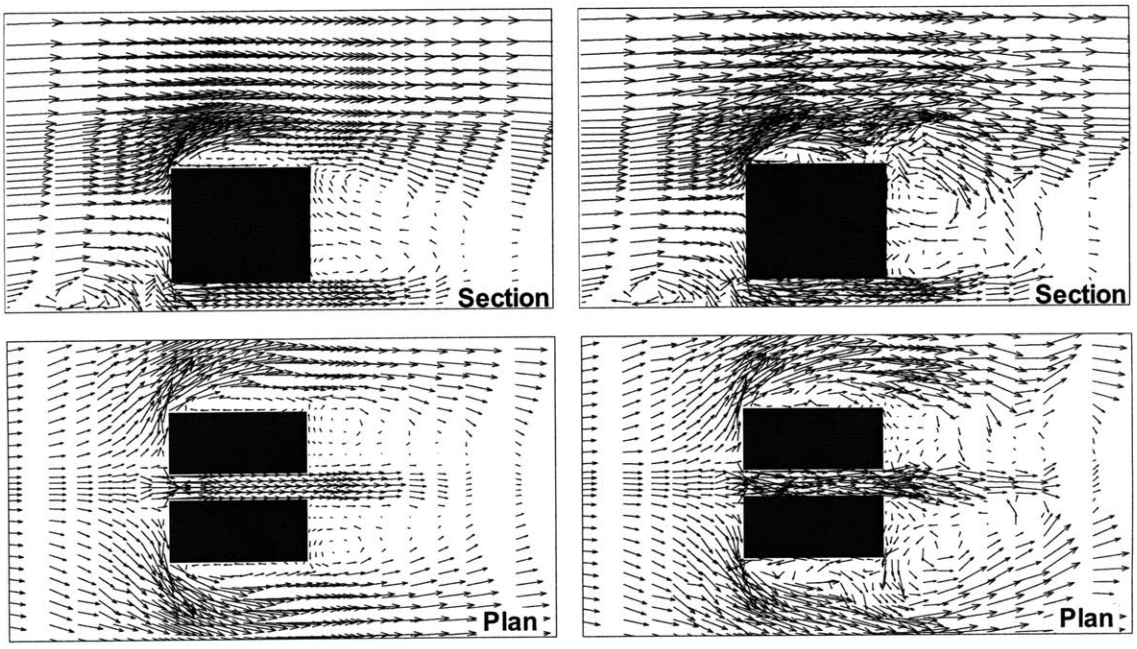

(a) Mean *(b) Instantaneous*

Figure 5.31 *The velocity distributions for cross ventilation with the FDS model.*

Table 5.5 shows that both subgrid-scale models can correctly predict the ventilation rate. Furthermore, the difference between the CAI and mean ventilation rates is small. Since the flow can easily enter and exit the "room", and the mean and instantaneous flow fields are similar, the corresponding calculated ventilation rates should be close to each other.

Table 5.5 *The ventilation rate in the cross ventilation case*

Ventilation rate (m^3/s)	SS model		FDS model		Experiment
	$Q_{ins,100\ sec}$	Q_{mean}	$Q_{ins,100\ sec}$	Q_{mean}	
	0.025	0.021	0.024	0.021	0.023

5.5 Buoyancy-driven Full-scale Single-sided Natural Ventilation

As described in Section 3.2, the experimental measurements for buoyancy-driven, single-sided natural ventilation with large openings were conducted to measure detailed airflow characteristics inside and outside of the room and the ventilation rate of the room. In this section, these experimental data are used to validate the LES models. Steady RANS modeling and an empirical model are also used as a comparison. Two ventilation cases are studied: one with an open door and the other one with an open window.

5.5.1 Case setup

The LES study used a non-uniform grid system. Since the Reynolds number was 40,000 and the expected Kolmogorov scale was about 10^{-4}, the smallest non-dimensional grid size was chosen as 0.03 m and the total grid number was 700,000. The time step size was 0.02 s. With this grid number and time step size, the simulation would require 10 days of computing time on a workstation. However, for RANS modeling, the grid number was less than half of that required by LES, and the simulation only required 2 days of computing time on a PC.

Since all the walls of the test chamber had a high thermal-resistance of 5.3 Km^2/W, they were simulated as adiabatic. The surface temperatures of the laboratory in Tests 3 and 4 (Section 3.2.2) were used as the boundary conditions for the door case and the window case, respectively. As discussed in Section 3.2.2, any set of surface temperatures of the laboratory could be used, since they would lead to the same results.

5.5.2 Results and discussion

This section presents the numerical results for the door and window cases, including the distributions of the air temperature and velocity and the ventilation rate of the room. Furthermore, the mechanism of single-sided ventilation is investigated with turbulence statistical analysis.

The airflow distributions

Figure 5.32 compares the computed temperature profiles with the experimental data at five positions for the door and window cases. In general, the computed results are in good agreement with the data. The LES models give slightly better results than the RANS modeling. The results show that, within the chamber, the air temperature increases with the room height. But the temperature profile is not linearly distributed, and the largest temperature stratification occurs in the middle section of the room (0.9 m ~ 1.3 m from the floor).

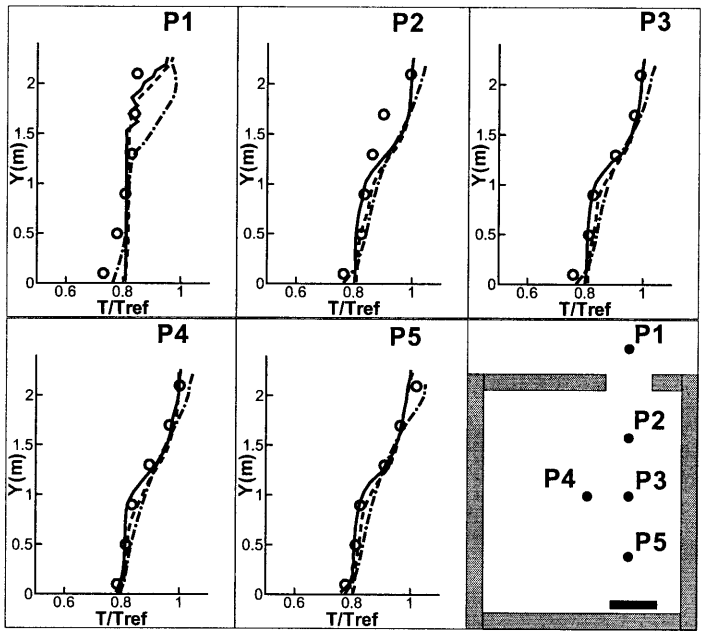

(a) Door Case

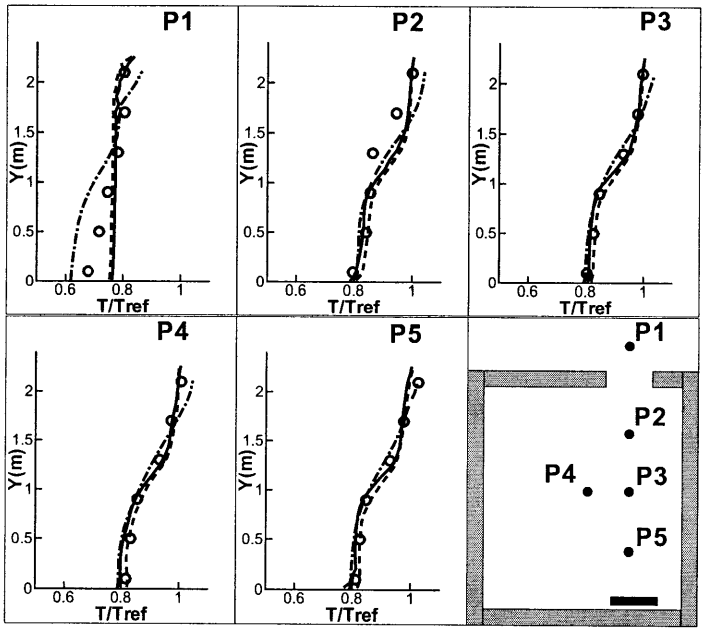

(b) Window Case

Figure 5.32 *Comparison of the computed temperature profiles with the measured data at five positions in and around the chamber with an open door or window. Circles: Experimental data; Solid lines: the SS model; Dashed lines: the FDS model; Dash-dot lines: the RANS modeling.*

LES can provide both mean and root-mean-square (RMS) air velocity. Although RANS modeling can provide turbulence kinetic energy that is related to the RMS velocity, this kinetic energy cannot be converted to the RMS values of the air speed. Figures 5.33 and 5.34 compare the computed mean and RMS air velocity with the corresponding measured data. In Figure 5.33, the door case, the RANS modeling seems to perform better at the upper part of P2 than the LES models, but it over-predicts the speeds at the bottom parts of P2, P3 and P4. The results obtained with the FDS model of the LES are in the best agreement with the experimental data in these regions. Nevertheless, the agreement in air velocity is not as good as that in air temperature. One possible reason is that the air velocity in this room was low (most regions were less than 0.1 m/s), which would affect the accuracy of the measurements. Figures 5.33 and 5.34 also show that the high-speed regions are along the top and bottom parts of the room. In the middle section, the air speeds are very low. This can explain why the temperature stratification in the middle section is very high (Figure 5.21), since there is not much air mixing in this region. Figure 5.34 shows that the computed RMS velocity by LES is in reasonable agreement with the experimental data.

In the experiment, a small air current kit (smoke "puffer") was used to observe the flow patterns in some particular areas. It was found that, in the door case, a small recirculation region occurred at the upper right part of the room as shown in Figure 5.35 (a). Figure 5.35 (b) shows that the airflow pattern obtained with the FDS model provides a much clearer recirculation in this region than does the RANS modeling. In an earlier study, Chen (1996) found that RANS modeling had difficulty predicting some secondary recirculations for indoor airflows.

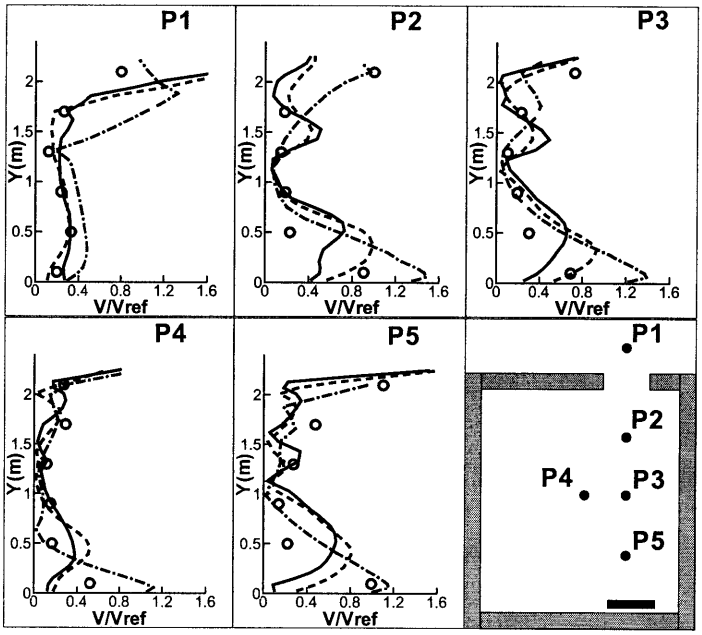

(a) Door Case

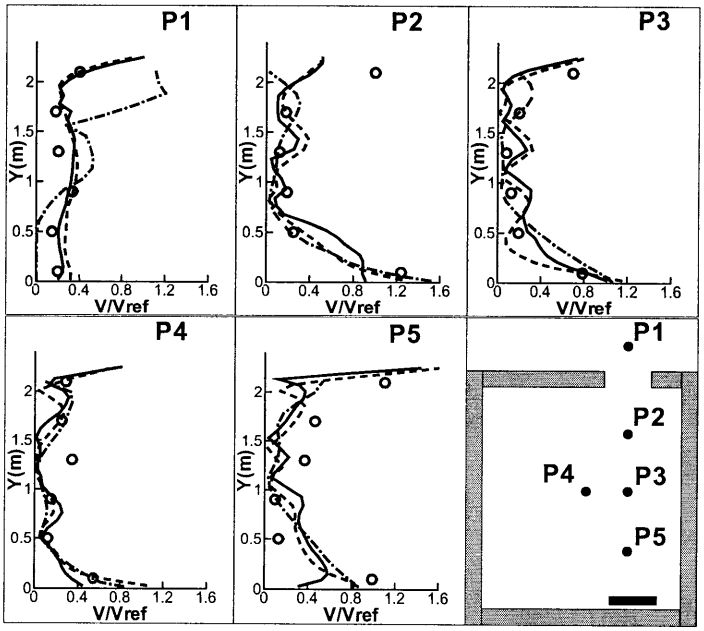

(b) Window Case

Figure 5.33 *Comparison of the computed mean air velocity profiles with the measured data at the five positions in and around the chamber with an open door or window. Circles: Experimental data; Solid lines: the SS model; Dashed lines: the FDS model; Dash-dot lines: the RANS modeling*

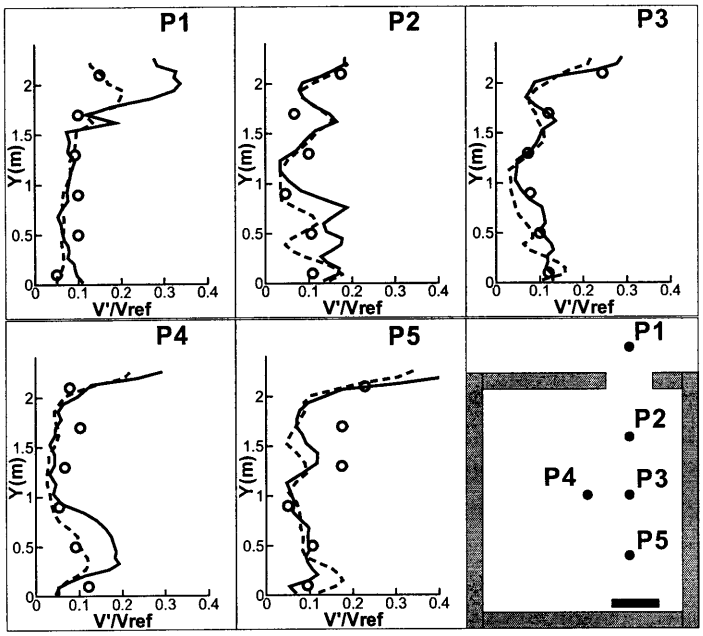

(a) Door Case

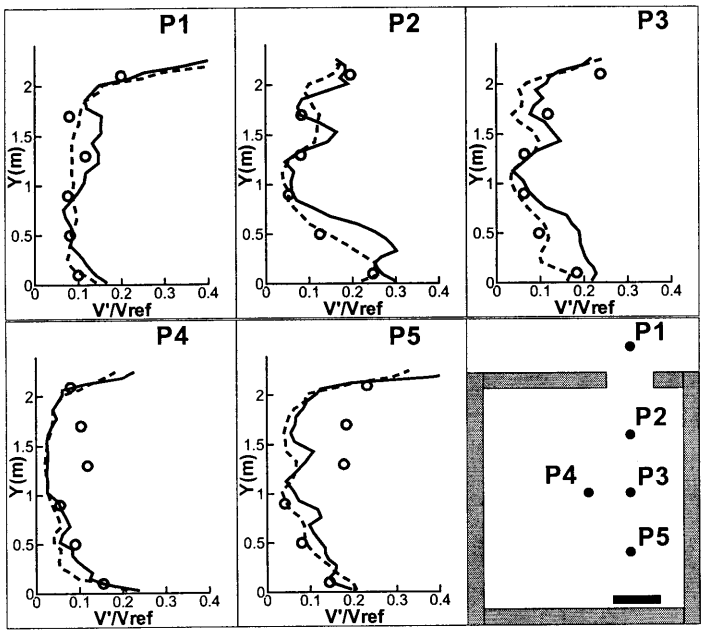

(b) Window case

Figure 5.34 *Comparison of the computed RMS velocity profiles with the measured data at the five positions in and around the chamber with an open door or window. Circles: Experimental data; Solid lines: the SS model; Dash-dot lines: the FDS model.*

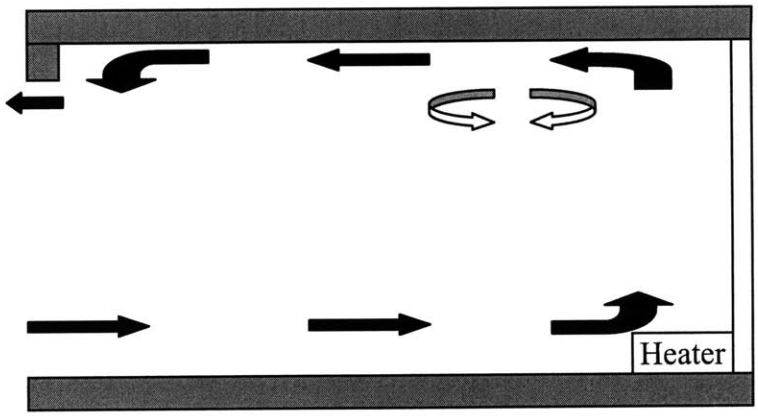

(a) The airflow pattern observed.

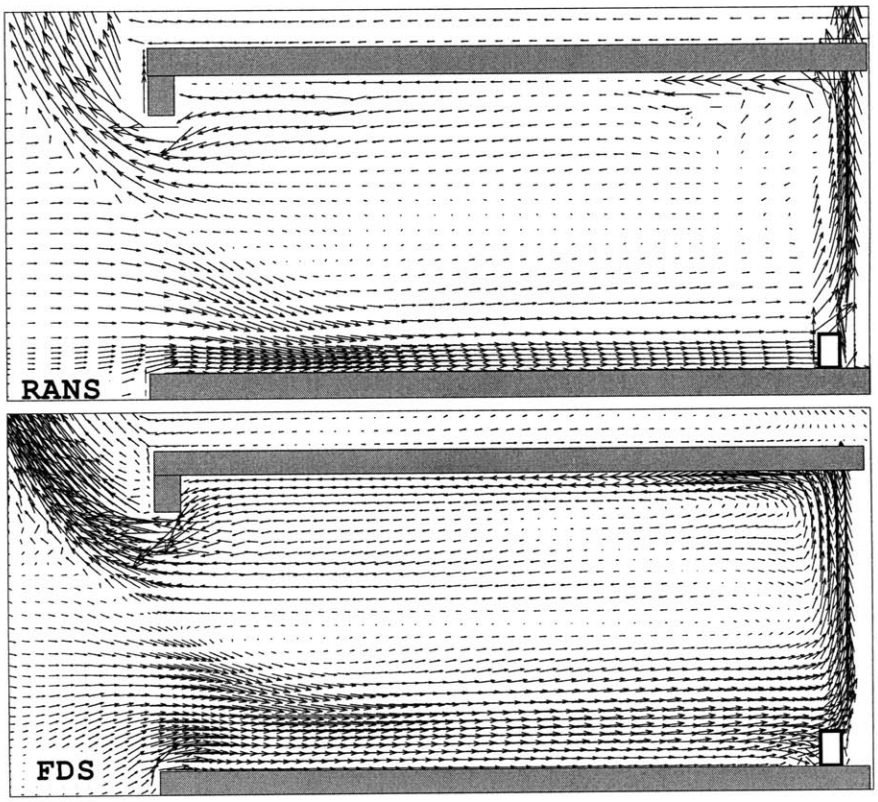

(b) The airflow pattern computed by RANS and LES with FDS.

Figure 5.35 *Comparison of observed and computed airflow pattern along the section at P1, P2, P3, and P5.*

Ventilation rate

The current experiment used a modified constant injection method to measure the ventilation rate. Based on the definition, the ventilation rate in numerical simulations can be computed by integrating the velocity at the opening. There are two ways to do the integration. The first is to extract the mean velocity, $U_{j,k}$, from the mean flow field and compute the mean ventilation rate, Q_{mean}. The other is to determine the accumulative and average instantaneous ventilation rate (CAI), $Q_{ins,T}$, which were described in Section 5.1. Since the calculation of $Q_{ins,T}$ requires the transient flow field, only LES can provide it in the current study.

This investigation also used a semi-analytical method from Awbi (1996) to calculate single-sided ventilation rate as a basis for comparison:

$$Q = \frac{C_d A}{3}\sqrt{gh\frac{\Delta T}{(T_{out}+273.15)}} \tag{5.9}$$

where C_d = the discharge coefficient
A = opening area (m^2)
g = gravity acceleration (m/s^2)
h = the height of the opening (m)
ΔT = the temperature between T_{in} and T_{out} (°C)
T_{out} = the outside air temperature (°C)
T_{in} = the average inside air temperature (°C)

In Equation (5.9), the discharge coefficient, C_d, depends on the characteristics of both the opening shape and the flow field. The current investigation set C_d as 0.61 (a value for a sharp-edged orifice). ΔT is the temperature difference between the outdoor and indoor air. Although an energy balance equation

$$W = \rho Q C_p \Delta T_{inlet-outlet} \tag{5.10}$$

where W = total heat load within the room (watt)
ρ = air density (m^3/s)
Q = ventilation rate (m^3/s)
C_p = specific heat of air (J/kg K)
$\Delta T_{inlet-outlet}$ = the temperature difference between the air at the inlet opening and the air at the outlet opening

can provide $\Delta T_{inlet-outlet}$, which is not the same as ΔT. With the assumption of a linear temperature profile within the space, ΔT would be approximately half of $\Delta T_{inlet-outlet}$. Therefore,

$$W = 2\rho Q C_p \Delta T \tag{5.11}$$

By combining Equations (5.9) and (5.11), one can obtain the ventilation rate:

$$Q = h\left(\frac{WgC_D^2 w^2}{18\rho 8_p (T_{out} + 273.15)}\right)^{1/3} \tag{5.12}$$

This equation suggests that the ventilation rate is proportional to the opening height, h. But the measured data show that the ventilation rate of the window case is more than half of that of the door case (Table 3.2). This incorrect conclusion drawn from Equation (5.12) is due to the linear assumption of the temperature profile, which does not match the real situation (Figure 5.32). The determination of the temperature difference, ΔT, is not a trivial issue, and a semi-analytical method may give incorrect results. Nevertheless, the current investigation used Equation (5.14) to calculate the ventilation rate for a comparison with other methods.

Tables 5.6 and 5.7 show the ventilation rates computed by different methods. The LES results agree well with the experimental data. The RANS modeling gives much higher ventilation rates. The empirical model gives a reasonable estimation for the window case, but predicts a higher value for the door case. Tables 5.6 and 5.7 also show that there is no significant difference between the mean ventilation rate and the average instantaneous ventilation rate. This is different from wind-driven, single-sided ventilation, where the average instantaneous ventilation rate is much higher than the mean value, and the fluctuating flow field plays a more important role in determining the airflow motions across the opening (Section 5.3). The following section will explain these results using a statistical analysis.

Table 5.6 *Air exchange rate for the door case.*

Experimental measurement	Empirical model	RANS (k-ε) Q_{mean}/V	LES (FDS model)		LES (SS model)	
			Q_{ins}/V	Q_{mean}/V	Q_{ins}/V	Q_{mean}/V
9.18-12.6	13.6	15.2	10.6	10.5	10.4	10.2

Table 5.7 *Air exchange rate for the window case.*

Experimental measurement	Empirical model	RANS (k-ε) Q_{mean}/V	LES (FDS model)		LES (SS model)	
			Q_{ins}/V	Q_{mean}/V	Q_{ins}/V	Q_{mean}/V
6.75~7.92	6.8	8.55	6.97	6.96	6.73	6.72

Turbulence statistical analysis

Since LES calculates the mean and fluctuating pressure and velocity, it is possible to study the mechanism of single-sided ventilation through turbulence statistical analysis.

Figure 5.36 shows the mean pressure distributions in the vicinity of the opening computed by the FDS model for the door and window cases. The higher internal pressure at the upper opening drives outflow and the lower internal pressure at the lower opening drives inflow. The neutral level is the height that separates the outflow and inflow. The mean pressure difference across the opening can be calculated with

$$\Delta\overline{P}_{open} = \frac{\int_0^h \left|\overline{P}^i - \overline{P}^e\right| dy}{2h} \tag{5.13}$$

where $\Delta\overline{P}_{open}$ = the mean pressure difference across the opening (Pa)

$\overline{P}^i$ = internal mean air pressure (Pa)

$\overline{P}^e$ = external mean air pressure (Pa)

Table 5.8 shows the computed mean pressure difference across the opening and the average internal and external RMS pressures. The internal pressure has a RMS value, σ_p^i, on the order of 10^{-3}, which is of the same order as that of the external wind RMS pressure acting on the opening, σ_p^e. The mean pressure difference across the opening is on the order of 10^{-2}, which is almost ten times larger than the fluctuating pressure. Therefore, the mean flow field plays a more important role in this single-sided and buoyancy-driven natural ventilation. That is why the mean ventilation rate and the average instantaneous ventilation rate are almost the same.

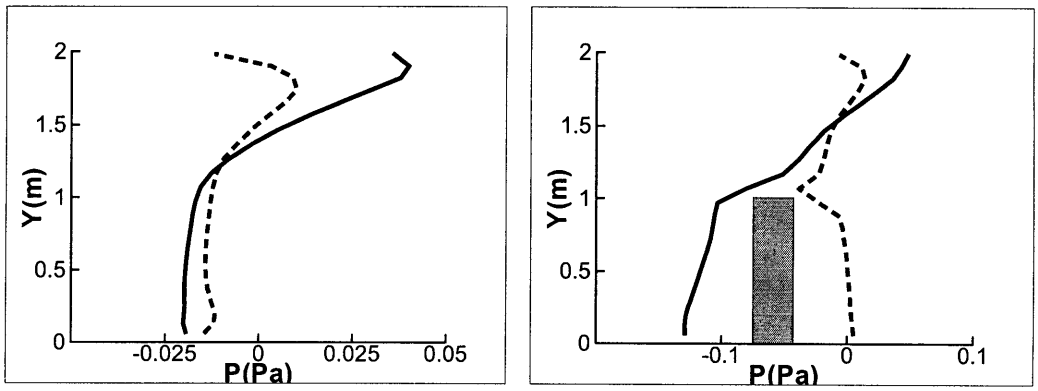

(a) Door case *(b) Window case*

Figure 5.36 *Distributions of mean pressure in the vicinity of the opening. Solid lines: internal pressure (0.06 m from the opening); Dashed lines: external pressure (0.06 m from the opening).*

Table 5.8 *The computed mean and RMS pressure distributions across the opening.*

Door Case			Window Case		
$\Delta\overline{P}_{open}$ (Pa)	σ_p^i (Pa)	σ_p^e (Pa)	$\Delta\overline{P}_{open}$ (Pa)	σ_p^i (Pa)	σ_p^e (Pa)
0.012	0.0012	0.0019	0.022	0.0027	0.0033

Figures 5.37 and 5.38 show the computed turbulence energy spectra with the FDS model of LES. The shapes of the spectra distributions are very similar to those from the measurements. Again, the energy is contained in low-frequency regions for both outside and inside air. The energy spectra distributions at the opening were also computed, although they were not available from the measurements. For the door case (Figure 5.37), the energy spectra at the lower part of the opening (H=0.5 m from the floor) are similar to those inside and outside of the room. At the upper part of the opening, however, the peak energy is shifted to the high-frequency region (close to 1 Hz). This is because the sharp upper frame of the opening disturbs the flow field (Figure 5.39 (a)); thus, more energy is drawn from large eddies to small eddies. For the lower part, there is no obstacle blocking the airflow (Figure 5.39 (a)), the airflow enters the room smoothly, and most energy is still contained in low-frequency region. For the window case (Figure 5.38), there are sharp frames at both the lower and upper parts of the opening (Figure 5.39 (b)). The peak energy is shifted to a high-frequency region in both areas (Figure 5.38). The disturbances from the opening frame can be clearly observed in Figure 5.39 (b).

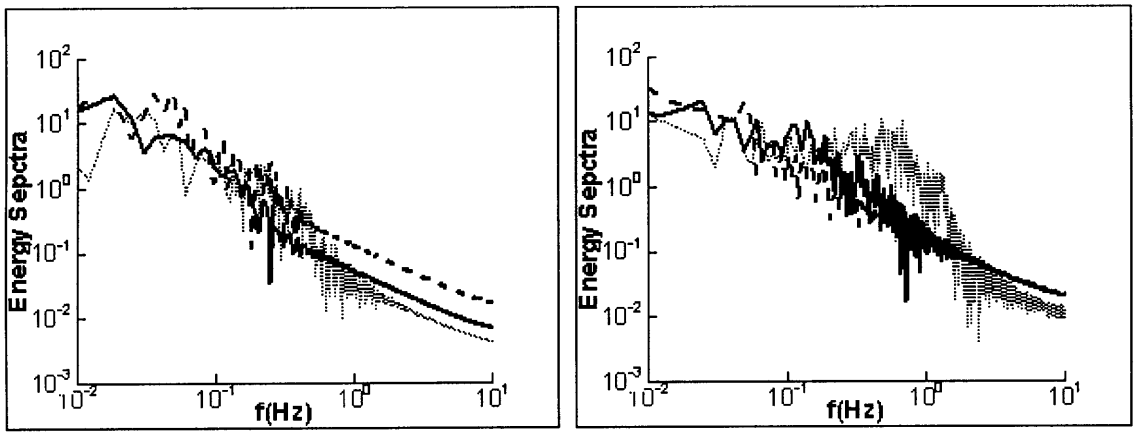

(a) H=0.5 m from the floor *(b) H=1.7 m from the floor*

Figure 5.37 *The computed turbulence energy spectra in the opening vicinity for the open door case. Solid lines: P1 (outside of the room); Dashed lines: P2 (inside of the room); Dotted lines: at the opening.*

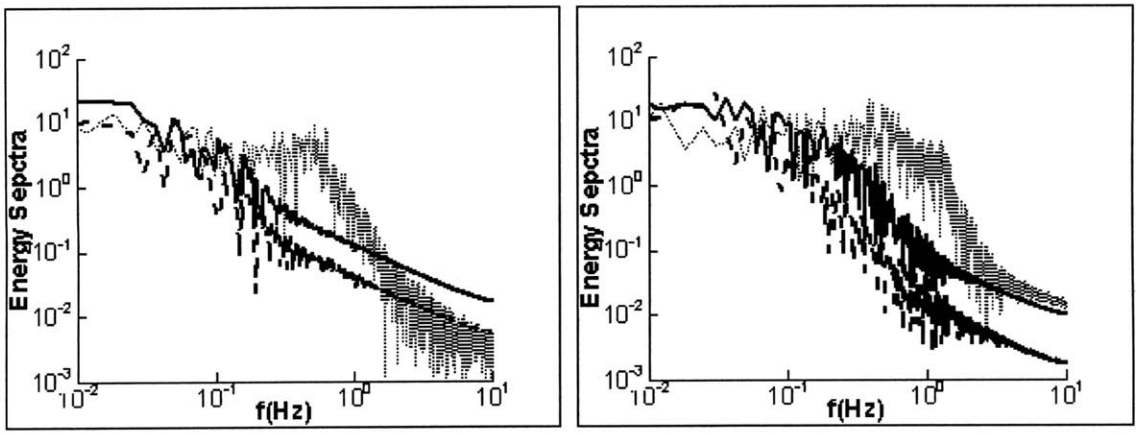

(a) H=1.3 m from the floor *(b) H=1.7 m from the floor*

Figure 5.38 *The computed turbulence energy spectra in the opening vicinity for the open window case. Solid lines: P1 (outside of the room); Dashed lines: P2 (inside of the room); Dotted lines: at the opening.*

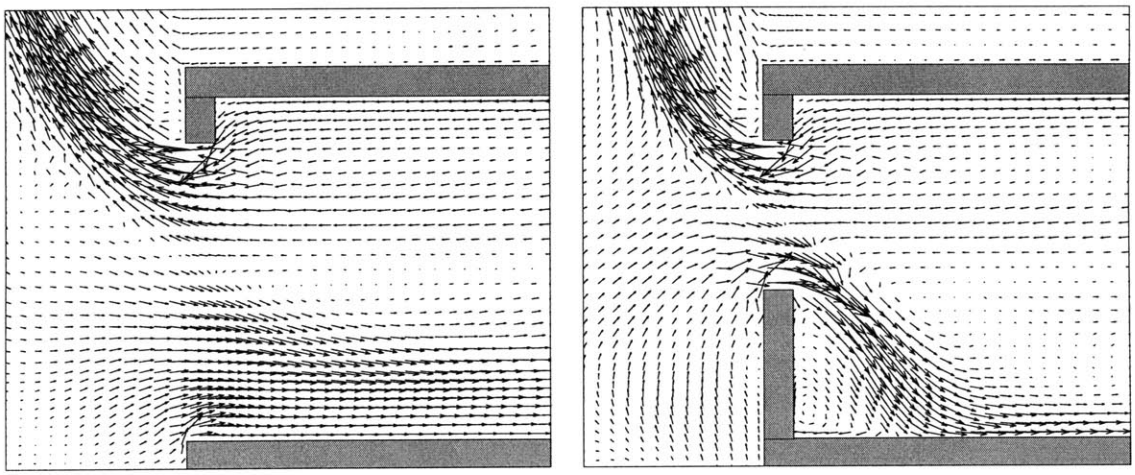

(a) Open door case *(b) Open window case*

Figure 5.39 *The mean air velocity distribution at the opening vicinity.*

5.6 Conclusions

Both the SS model and the FDS model were used to simulate and investigate wind-driven and buoyancy-driven natural ventilation. The numerical results from LES methods are in generally good agreement with the experimental data, in the prediction of gross flow patterns, in mean and fluctuating velocities and temperature around and within the building, and in surface pressures. RANS modeling and empirical models were also used as a comparison. The study has led to the following conclusions.

5.6.1 Wind-driven natural ventilation

For the wind-driven natural ventilation studies, the experiments conducted both on site and in a wind tunnel were used, and both cross and single-sided ventilation were investigated.

Evaluations of model performance

In highly turbulent flows with a high Reynolds number, most energy is contained in large eddies. The large eddies therefore play a more important role than the small eddies. Since both the SS and FDS models can directly solve the large-eddy motions, and can model the dissipative nature of turbulence, both models are able to provide accurate flow results for most natural ventilation cases with highly turbulent flows, such as wind-driven cross natural ventilation. Since the SS model is much simpler than the FDS model, and requires less computing time, the SS model is more suitable to solve for this type of problem.

The SS model cannot predict laminar flows, such as the airflows near walls, because the model coefficient is a constant and does not vary with flow type. The FDS model can give reasonable results in these cases because its model coefficient is a function of the flow type. The coefficient becomes zero in the laminar regions, which correctly represents the physics of flow motions. Therefore, the FDS model is more appropriate to study natural ventilation flows with both turbulent and laminar characteristics, such as single-sided natural ventilation.

Importance of using LES for single-sided ventilation studies

For single-sided ventilation, the information obtained from a mean flow field may restrict the designer's perspective on the ventilation performance of a design. This is because the averaging procedure of calculating the airflow significantly cancels out the instantaneous air exchange between indoor and outdoor air. This procedure leads to lower ventilation rate and air change effectiveness prediction than the instantaneous or measured ones. RANS modeling might not be appropriate for determining the ventilation rate and air change effectiveness due to the averaging procedure used in this model. The instantaneous flow field, which can be provided by LES, might be more useful to determine the ventilation rate and air change effectiveness in a single-sided natural ventilation design.

Furthermore, for single-sided ventilation designs, there are no concrete and reliable empirical models available. The LES method provides a suitable choice for simulation to allow design development and testing.

Turbulence statistical analysis

The results from LES enable us to analyze the velocity and pressure fields of complicated turbulence flows in detail, and to give a detailed and accurate assessment of the ventilation performance of a building. Hence, LES is capable of examining the mechanism of wind-driven ventilation with a turbulence statistical analysis. It is found that, for outdoor airflow, energy is contained in high-frequency regions. For strong indoor airflow, such as in the cross ventilation case, the energy is also contained in the high-frequency region. However, in the low-velocity and recirculation regions, the airflow does not vary significantly with time, and most energy is contained in lower-frequency regions. Whether this situation represents a real wind situation needs to be further tested with full-scale measurements. Moreover, for single-sided ventilation, the mean pressure difference across the opening is much less than the fluctuating pressure. Therefore, the fluctuating pressure plays an important role in determining the airflow motions across the opening.

Effect of fluctuating wind direction on cross natural ventilation in buildings

Natural wind changes direction over time, which is hard to reproduce in a conventional wind tunnel, where the "wind" direction is fixed. LES can simulate both cases by adjusting inlet boundary conditions: a fixed incoming wind direction for the wind-tunnel test, and a varied incoming wind direction for the on-site measurements. The measured data and computed results show three significant differences in the airflows for a real building site and for a wind tunnel.

(1) Natural wind fluctuations can inhibit the formation of large recirculation zones behind a building, and only small eddies can exist. With a fixed wind direction in the wind tunnel, the wind cannot reach some regions of the building facades. Therefore, large recirculation zones are easily formed in the downwind direction.

(2) The gradient of the pressure coefficient difference across a building, ΔCp, is more uniform with a varied wind direction than with a fixed wind direction.

(3) Indoor airflow with a fixed wind direction has a thinner, deeper and higher speed core than that with a variable wind direction. This is because the wind in the former case does not oscillate and loses less energy.

5.6.2 Buoyancy-driven natural ventilation

The experimental measurements for single-sided natural ventilation driven by buoyancy forces were used to validate LES models. Steady RANS modeling was also used as a comparison. The air temperature, air velocity, and ventilation rate predicted by the LES models are in better agreement with the measured data than those computed by RANS modeling. But the LES models need much longer computing time than does RANS modeling. An empirical model can give a reasonable estimation of the ventilation rate, provided that the discharge coefficient of the opening and the temperature difference between inside and outside air are correctly specified. However, correct prediction of the temperature difference is not easy and the information obtained from empirical models is limited. Based on the accuracy of the results and the equipment and labor costs, the FDS model of LES is a suitable tool to study buoyancy-driven natural ventilation.

Using the mean and fluctuating pressures and velocities, this investigation studied the mechanism of single-sided ventilation with a turbulence statistical analysis. The turbulence energy is mostly contained in low-frequency regions for both indoor and outdoor air. Local disturbances, such as a sharp geometry, could shift the energy to high-frequency regions. The magnitude of the fluctuating pressures close to openings is much smaller than the mean pressure difference across the opening. Therefore, the mean flow fields play a more important role in determining the airflow motions across openings in the buoyancy-driven, single-sided natural ventilation cases.

Chapter 6

Further Application of Large Eddy Simulation to Particle Dispersion in Buildings

LES was successfully validated with experimental data. The results show that LES is a suitable tool to study natural ventilation. In a naturally ventilated building, outside pollutants can be introduced to a building and indoor pollutants can be removed to the outside. To design an effective natural ventilation system to provide good indoor air quality, a Lagrangian particle model was implemented in LES to study particle dispersion in buildings. The particle model is first used to calculate the motions of three different types of solid particles in a decaying, homogeneous, isotropic, turbulent airflow. The model is then applied to particle dispersion in a six-room office building with a pollutant source in the corridor.

6.1 Introduction

Currently, in developed countries, people spend most of their time in an indoor environment. Indoor air quality has become more important than ever before. In a naturally ventilated building, outdoor pollutants, such as dusts, fuels, and pollens, can be transported to the indoor environment, which may lead to an indoor air quality problem. On the other hand, the pollutants produced inside a building, such as tobacco smoke and volatile organic compound emissions from various building materials and furnishings, can be removed to the outside of the building. Therefore, to maintain a healthy indoor environment, it is necessary to design an effective ventilation system to prevent outdoor pollutants from entering the building, to remove the indoor pollutants, and to control the transportation of pollutant sources within buildings. This requires a better understanding of the pollutant trajectory in buildings, which is determined by airflow patterns and pollutant properties.

As discussed in Chapter 1, airflow patterns in buildings are very complex and cannot be easily calculated with simple numerical methods, such as an empirical model or a zonal method. Therefore, CFD modeling should be used. Of two possible CFD methods, RANS modeling and the LES method, RANS modeling requires less computing time. However, RANS modeling is inaccurate when predicting airflows around and inside buildings as was discussed in Chapters 1, 4 and 5. Moreover, if airflow in buildings is turbulent, which occurs in most cases, the instantaneous velocity field will significantly affect particle dispersion (Armenio, *et al.*, 1999). Since steady RANS modeling only solves for mean velocity fields, the effect of the turbulent fluctuations on the particle motions should be taken into account. Normally, a stochastic model is used to produce a fluctuating flow field (Belermont *et al.*, 1990). Although the stochastic model tries to produce a fluctuation flow field, the resulting stochastic characteristics cannot account for the coherence of the turbulent motions. Furthermore, the stochastic model generally requires empirical coefficients, but the determination of those values is not a trivial issue, and it will affect the

accuracy of the results. Therefore, LES is a good compromise because it generates instantaneous flow and particle information, with moderate computing costs.

The flow field generated by LES is used to calculate pollutant trajectories and dispersion patterns. Indoor pollutants can be classified into solid, liquid, and gas types based on the contaminant phase. The current investigation focuses on solid particulates, which include dust, smoke, fumes, and mists (ASHRAE Fundamentals, 1997). There are two generic approaches for the numerical simulation of a cloud of particle trajectories and dispersion patterns in airflows: namely, the Lagrangian approach and the Eulerian approach. In the Lagrangian approach, the velocity, mass and temperature history of each particle in the cloud is calculated. The local cumulative motion and state of each particle in the cloud represents the spatial properties of the cloud. In the Eulerian approach, the cloud of particles is considered to be a second fluid that behaves like a continuum, and equations are developed for the average properties of the particles in the cloud (Crowe, *et al.*, 1998). Each approach has its relative advantages and disadvantages depending on the nature of the flow. Compared to the Eulerian method, the main drawback of the Lagrangian approach is that a large number of particles must be injected into the flow field in order to obtain statistically independent results. Thus, a large amount of computing time is required. Nevertheless, to study particle dispersion patterns in airflows inside and around buildings, the Lagrangian method is applied because it is easier to consider the impacts of complex boundary conditions on particle motions.

6.2 Particle Model

LES solves the turbulence flow field over the spectrum of length scales by solving a filtered form of the continuity and momentum equations for the larger scales of turbulence, and by using an eddy viscosity model for the smaller scale. The flow field generated by this scheme is used to calculate particle trajectories and dispersion patterns. The current study investigated particle dispersion patterns in turbulent airflows with a Lagrangian method. The interaction between the carrier air and the particles was treated as a one-way coupling, assuming the effect of particles on air turbulence is negligible due to low solid loadings and comparatively small particle settling velocities.

When using the Lagrangian method, the trajectory of each particle can be computed by solving the momentum equation based on Newton's second law,

$$\frac{d(m\vec{v})}{dt} = \sum \vec{F} \tag{6.1}$$

with

$$\frac{d\vec{X}_P}{dt} = \vec{v} \tag{6.2}$$

where $\vec{v}$ = particle velocity, m/s

m = particle mass, kg

$\sum \vec{F}$ = Total forces acted on a particle, N

$\vec{X}_P$ = Coordinates of particle, m

Momentum is transferred between air and particles through inter-phase drag and lift forces, which can be divided into, but not limited to, the following parts: the drag force, pressure gradient and buoyancy forces, unsteady forces which include Basset force and virtual mass force, Brownian force, and body forces, such as gravity force (Crowe, *et al.*, 1998). For particles with a certain size and density, some of the forces may be very small compared to others, and thus are be ignored. In the current study, the particles are solid, and the particle shape is assumed to be spherical for simplicity. The particle diameter ranges from 10 to 100 μm, and the density is on the order of 10^3 kg/m^3. The following sections discuss which forces can be ignored.

6.2.1 Drag force

When studying particle motion in airflows, one of the most important forces is the drag force, which acts on the particle in a uniform pressure field when there is no acceleration of the relative velocity between the particle and the conveying fluid. The force is quantified by the drag coefficient, C_D, through the equation

$$\vec{F}_D = \frac{1}{2}\rho C_D A \left|\vec{u} - \vec{v}\right| (\vec{u} - \vec{v}) \tag{6.3}$$

where $\vec{F}_D$ = drag force acted on a particle, N

A = particle surface area, m^2

$\vec{u}$ = air velocity, m/s

In general, the drag coefficient will depend on the particle shape and orientation with respect to the flow as well as on the flow parameters such as Reynolds number, Mach number, turbulence level, etc. Hinds (1982) computed the drag coefficient for a spherical solid particle under low a March number condition

$$C_D = \frac{24.0\left(1.0 + 0.15 Re_P^{0.687}\right)}{Re_P} \text{ if } Re_P \le 1000 \tag{6.4}$$

$$C_D = 0.44 \text{ if } Re_P > 1000 \tag{6.5}$$

where Re_P is the particle Reynolds number :

$$Re_P = \frac{\left|\vec{u} - \vec{v}\right| d_P}{\nu} \tag{6.6}$$

where d_P = particle diameter, m
ν = air kinematic viscosity, m/s^2

6.2.2 Pressure gradient and buoyancy forces

When a particle is placed in a flow field, the effect of the local gradient gives rise to a force in the direction of the pressure gradient. The pressure gradient produced by a hydrostatic pressure is

$$\nabla p = -g\rho\vec{e}_z \tag{6.7}$$

where z = in the direction opposed to gravity (upward)
g = magnitude of gravy force per unit mass

The corresponding pressure force is

$$F_P = \rho g V_P \tag{6.8}$$

where V_P = particle volume, m^3

Equation (6.8) states that the force is equal to the weight of the fluid displaced. This is known as Archimedes principle. In a similar fashion, there is also a force on the particle due to the shear stress in the conveying fluid (Crowe, *et al.*, 1998).

An estimate of the importance of the force due to the pressure gradient is obtained as follows. The magnitude of the pressure gradient in the continuous phase is on the order of the flow acceleration.

$$\frac{\partial p}{\partial x} \sim \rho \frac{Du}{Dt} \tag{6.9}$$

Thus the ratio of the pressure force to the force to accelerate a particle is

$$\frac{V_P \dfrac{\partial p}{\partial x}}{m\dfrac{dv}{dt}} \sim \frac{\rho}{\rho_P}\frac{Du/Dt}{Dv/Dt} \tag{6.10}$$

where ρ_p = particle density, kg/m^3

If the accelerations of the two phases are of the same order, then the ratio of the pressure force to the acceleration is

$$\frac{V_P \frac{\partial p}{\partial x}}{m\frac{dv}{dt}} \sim \frac{\rho}{\rho_P} \tag{6.11}$$

In the current gas-particle flow, the ratio of ρ/ρ_p is of the order of 10^{-3} so the pressure gradient force can be neglected.

6.2.3 Unsteady forces: virtual mass force (added-mass force) and Basset force

The forces due to acceleration of the relative velocity can be divided into two parts: the virtual mass force and the Basset force.

The virtual mass force is also called the added-mass force, which relates to the force required to accelerate the surrounding fluid. When a body is accelerated through a fluid, there is a corresponding acceleration of the fluid which occurs at the expense of work done by the body.

The virtual mass force acting on the particle is given by

$$F_{Ai} = C_a V_P \rho \left(\frac{du_i}{dt} - \frac{dv_i}{dt} \right) \tag{6.12}$$

where C_a = the virtual-mass force coefficient.
v_i = component of the particle velocity in the x_i direction, m/s

Odar and Hamilton (1964) suggested the following empirical equation for the coefficient, C_a, as a function of the acceleration parameter,

$$C_a = 1.05 - \frac{0.066}{A_C^2 + 0.12} \tag{6.13}$$

$$A_C = \frac{\left|\vec{u} - \vec{v}\right|^2}{d_P \left| \frac{d\vec{v}}{dt} - \frac{d\vec{u}}{dt} \right|} \tag{6.14}$$

The Basset force describes the force due to the lagging boundary layer development with changing relative velocity. This term therefore accounts for viscous effects. It addresses the

temporal delay in boundary layer development as the relative velocity changes with time. The value of the Basset force depends on the acceleration history up to the present time

$$F_{Basset,i} = \frac{3}{2} d_p^{\,2} \sqrt{\pi \rho \mu} \int_0^t \frac{u_i - v_i}{\sqrt{t - t'}} dt' \tag{6.15}$$

This term is often difficult to evaluate although it is important in many unsteady applications. According to the calculations of Hjemfelt and Mockros (1966), the Basset term and virtual mass term become insignificant for $\rho/\rho_p \sim 10^{-3}$. Thus, in the current study, these two unsteady forces are ignored.

6.2.4 Brownian force

If the size of a particle suspended in a fluid is very small (less than a micron), the discrete nature of molecular motion affects the motion of the particle, exhibiting a random motion due to collisions of molecules with particles. This is called Brownian motion. Since the particle sizes in the current study are greater than 10 microns, the Brownian force is not considered.

6.2.5 Body force

The only body force in the current study is the gravity force, which can be expressed as

$$\vec{F}_B = m\vec{g} \tag{6.16}$$

Therefore, only the drag force and the body force are considered in the current study. The term on the right side in Equation (6.1) can be expanded as

$$\sum \vec{F} = \vec{F}_D + \vec{F}_B \tag{6.17}$$

Substituting Equations (6.3) and (6.16) into Equation (6.1) and dividing the mass of particles, m, on both sides, one can obtain the particle motion equation:

$$\begin{aligned} \frac{d\vec{v}}{dt} &= \frac{3\ \rho C_D}{4 d_P\ \rho_P} \left|\vec{u} - \vec{v}\right| \left(\vec{u} - \vec{v}\right) + \vec{g} \\ &= f_P \left(\vec{u} - \vec{v}\right) + \vec{g} \end{aligned} \tag{6.18}$$

where

$$f_P = \frac{3\ \rho C_D \left|\vec{u} - \vec{v}\right|}{4 d_P\ \rho_P} \tag{6.19}$$

is the response "frequency" of the particle to changes in flow conditions surrounding the particle.

6.3 Numerical Methods

This section discusses the numerical scheme employed for solving particle equations, the boundary conditions, and determination of the time step when coupling the airflow and particle equations.

The flow velocity used to integrate the equation of particle motion is obtained by interpolation and the particle motion equations (Equations (6.1) and (6.2)) can be integrated with the fifth order Runge-Kutta method (William, 1992).

To solve the equations of flow field and particle motion, two different time step sizes could be used, one for the flow field and the other one for the particle motion. However, in order to avoid errors due to time interpolation, the flow field and the particle motion are advanced with the same time step, Δt. Such a time step must satisfy both the CFL condition of the flow field (discussed in Section 2.3.5) and the time step requirement for the particle motion. The CFL condition requires that

$$\Delta t \leq \Delta t_f = \Delta_{min}/u_{max} \tag{6.20}$$

where u_{max} = the maximum speed over all the grids in the physical domain
Δ_{min} = the minimum grid space.

In order to correctly simulate the response of the particle to the fluctuating flow field, the time step for advancement is also required to satisfy

$$\Delta t \leq \Delta t_P = \varepsilon f_P^{-1} \tag{6.21}$$

where f_P^{-1} in Equation (6.21) is the characteristic time for the particle motion, and ε is a constant and is taken to be of the order $o(10^{-1})$. In practice, Δt_P can be much less than Δt_f for small particles. The time step size is determined by

$$\Delta t = \min(\Delta t_f, \Delta t_P) \tag{6.22}$$

6.4 Boundary Conditions

The particle motion equation determines the particle trajectories in airflows. However, when particles travel via airflow in buildings, the particles may hit building walls. Therefore, the interaction between the particles and building surfaces should be considered. Several experiments have been carried out to determine whether a particle would bounce back from a wall or not (Okuyanna, *et al.*, 1986, Holub, *et al.*, 1988, Abadie, *et al.* 2001).

Abadie *et al.* (2001) investigated the deposition patterns of several types of particles on real wall textures found in buildings. They used a critical deposition velocity, V_{crit}, to evaluate the particle motions after hitting a wall. Figure 6.1 illustrates the use of V_{crit}. When a particle hits a wall, the particle velocity normal to the wall, V_n, is compared with the critical deposition velocity, V_{crit}. If V_n is greater than V_{crit}, then the particle would bounce back. If not, the particle would be attached to the wall.

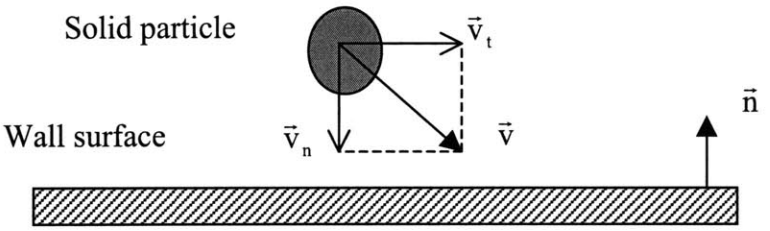

Figure 6.1 *Plot of a particle close to a wall*

The critical deposition velocity is determined by the particle type, including such parameters as particle density and size, wall texture, and wall position, such as a vertical wall, a ceiling or a floor. All of these factors significantly affect the magnitude of V_{crit}. In the current study, the critical velocity provided by Abadie *et al.* (2000) is used.

6.5 Results and Discussions

The above numerical method was used to study particle dispersion in turbulent airflows. The method was first validated by an experimental measurement conducted by Snyder and Lumley (1971), who measured the dispersions of different types of particles in a channel flow. Then the validated numerical method was used to study particulate transport in buildings.

6.5.1 Particle dispersion in a channel flow

The motions of small spherical solid particles are simulated numerically in decaying homogeneous isotropic turbulent gas flow fields generated by the large eddy simulation. Snyder and Lumley (1971) studied the particle motion in a vertical wind tunnel with air flowing upward and the gravity vector opposite to the flow direction. The wind tunnel was operated with the mean speed U = 6.55 m/sec. Snyder and Lumley (1971) measured the turbulent intensity of the airflow in the tunnel. Figure 6.2 shows a sketch of their wind tunnel. The test section was 16 in. x 16 in x 16 ft (0.4 m x 0.4 m x 4.8 m). The biplane grid was made from 3/16-inch (0.476 cm) square brass rods spaced on 1-inch (2.54 cm) centers.

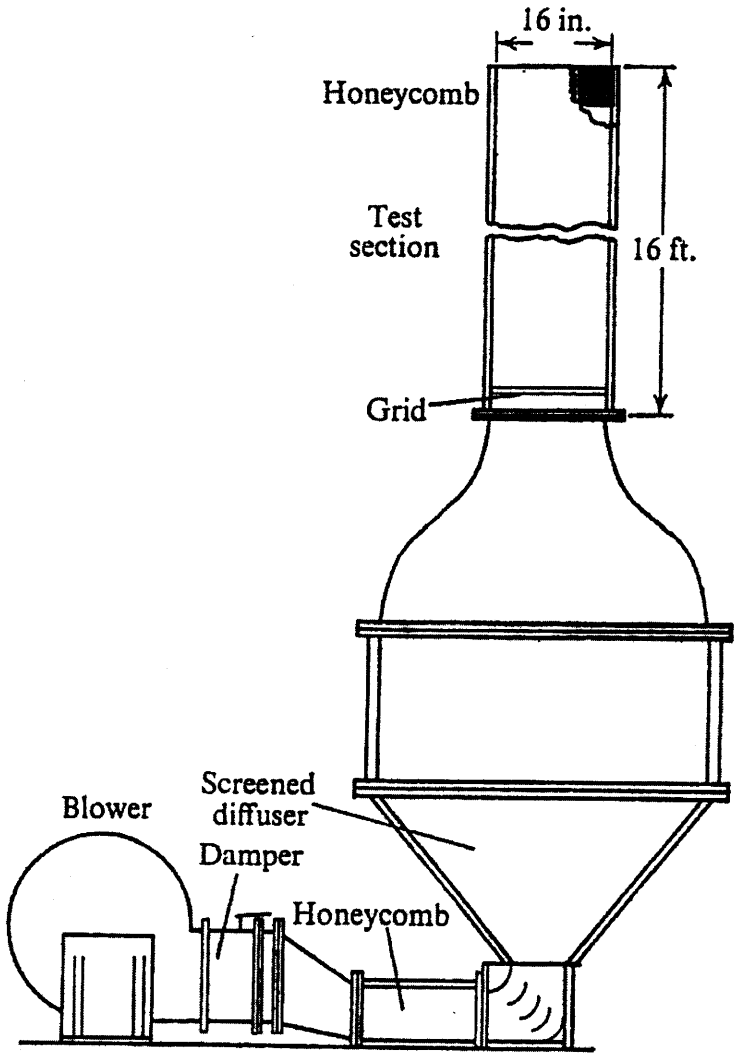

Figure 6.2 *The wind tunnel*

In the experiment, particles were ejected at the wind tunnel centerline with a mean velocity the same as the tunnel speed, and the injection position was 20 mesh lengths (1 mesh length = 1 inch = 2.54 cm) from the grid. A photographic system was used to measure the instantaneous positions of the particles at 10 separate locations. The injections were independent and about 700 measurements at each location were made. Since the flow was isotropic in planes perpendicular to the mean flow in Eulerian variables, it was isotropic in particle variables. Therefore, particle position distributions in cross sections perpendicular to the streamwise direction were circular. Since perpendicular displacements were uncorrelated with each other and had equal variances, all information was obtained from the measurements of a single component. Therefore, only the lateral particle displacements, Y(t), were measured.

In the numerical simulation, a biplane grid, which had the same geometry as that in the experiment, was placed in the windward direction to generate the isotropic and homogeneous airflow field. The smallest grid size was the same as the size of the brass rods, 3/16-inch (0.476 cm). A non-uniform grid system was used, and the grid numbers were 200 × 67 × 67 along the streamwise direction, x, and lateral directions, y and z. The time step size was 0.0002 seconds, determined by Equation (6.22).

Figure 6.3 shows the decay of root-mean-square velocity fluctuation. The LES results agree well with the experimental data. Therefore, the airflow field can be correctly simulated by LES.

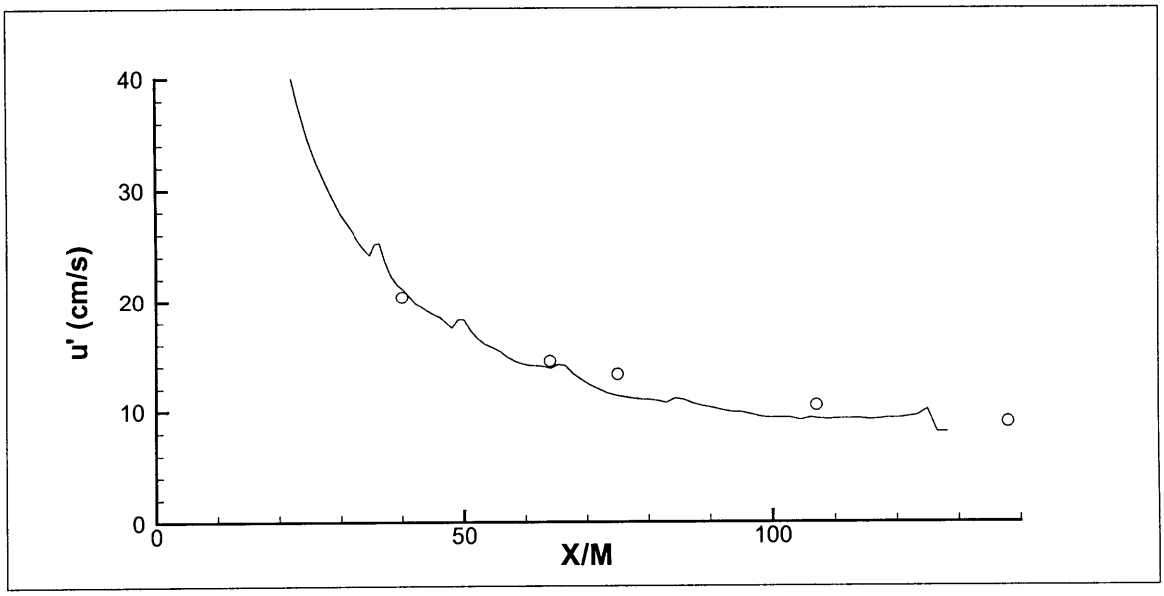

Figure 6.3 *Decay of the root-mean-square velocity fluctuation along the streamwise direction. The solid line: results from LES; Circle: Experimental data.*

Three different types of particles: hollow glass particles with diameter of 46.5 μm and density of 260 kg/m^3, corn particles with diameter of 87 μm and density of 1000 kg/m^3, and copper particles with diameter of 46.5 μm and density of 8900 kg/m^3 were studied. For each type of particle, one thousand samples were independently introduced to the centerline of the flow field. The magnitude of the relative velocity between the local fluid point and the particle, $\left|\vec{u}-\vec{v}\right|$, increases to a maximum value and then decays slowly as time develops. The time required for $\left|\vec{u}-\vec{v}\right|$ to reach the maximum is of the same order as the particle's characteristic time, f_P^{-1} (in Equation 6.20). Therefore, particles with larger density and size would require longer time to reach the maximum than particles with smaller values. Statistical properties of the particle motion that are free from the effect of initial conditions can be calculated after $\left|\vec{u}-\vec{v}\right|$ has reached the maximum value (Riley and Patterson, 1974). In the experiment, the position for a given particle obtained by the first camera, which was located at (X/M) = 68.4 (M is the mesh length), was chosen to be the reference position for that particle. In the simulation, the reference positions were set at (X/M) = 30 – 64 M, depending on the different values of f_P^{-1}.

Figure 6.4 shows the mean-square displacements of three different types of particles from the present calculation and from the experiments. Again, the computational results are in good agreement with the experimental data. Since the reference positions to begin displacement calculations vary for different types of particles, the time durations for the displacement calculations are also different. The copper particles have the largest f_P^{-1} and require the reference position farther from the injection point. Therefore, the time duration for the displacement calculation of the copper particles is the shortest (Figure 6.4).

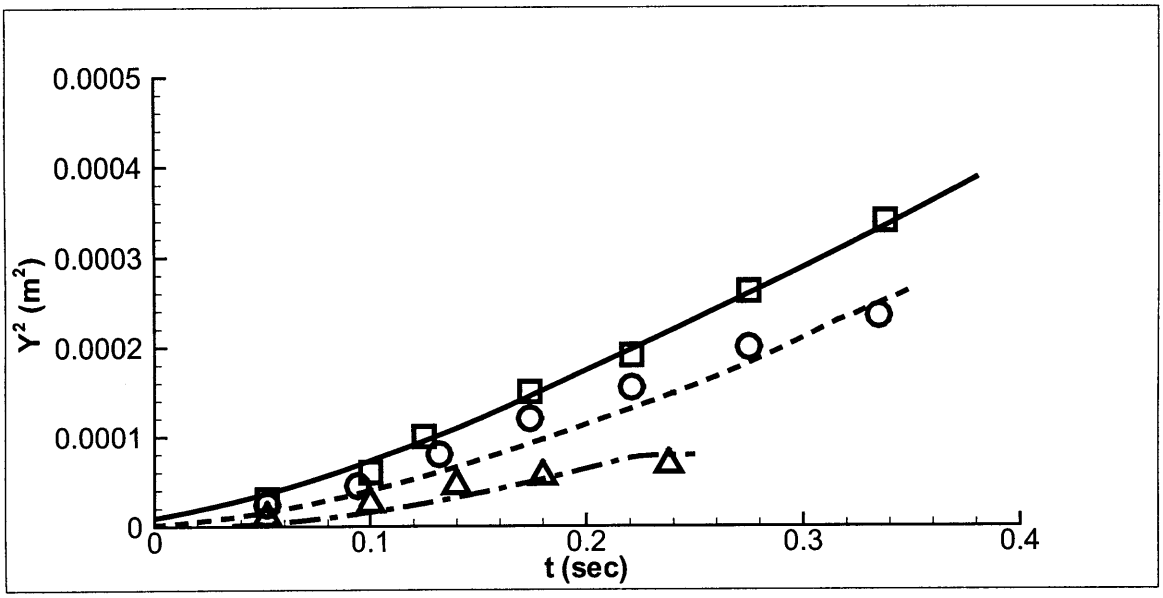

Figure 6.4 *Comparison of the development of the mean-square displacement of the particles between the LES results (lines) and the experimental results (symbols). Solid line: LES results for hollow particles; Dashed line: LES results for corn particles; Dash-dot line: LES results for copper particles; Square: Experimental results for hollow particles; Circle: Experimental results for corn particles; Delta: Experimental results for copper particles.*

6.5.2 Particle dispersion in a six-room building

In this case, a cloud of particles for the simulation of an assumed particulate source was injected into a six-room building. Figure 6.5 shows the building plan and the position of the particulate source. For the corn-type particles used in the simulation, the gravity force plays an important role. However, if the gravity force were considered in the current calculation, the particles would not travel through the whole building before falling to the ground.

Although reducing the particle size and density could lessen the impact of the gravity force, the time step size would have had to be decreased as well, in order to simulate the correct response of the particle to the fluctuating flow field. As shown in Equation (6.21), the time step to advance particle motion must be decreased with the reduction of the characteristic time for the particle motion, f_P^{-1}, which is proportional to the particle diameter times particle density, $d_P \rho_P$, (Equation (6.19)). Therefore, the time step for particle motion is proportional to $d_P \rho_P$. For example, if a hollow-glass particle is used, the time step size needs to be decreased by an order of magnitude. To save computing time, as well as to show how particles could travel through the whole building, corn-type particles without considering the impact of the gravity force were applied. Simulation of light particles with

the impacts of the gravity force, such as hollow-glass particles, is suggested for a future study.

There is one inlet in each of the six rooms and one general outlet at the other end of the corridor. The inlet air velocity is 3.2 m/s, and outlet velocity 1 m/s. The dimension of each room is 5 m long, 3.85 m wide and 2.53 m high, and the size of each inlet is 0.15 m wide and 0.05 m high. The dimension of the outlet is 0.32 m wide and 0.45 m high. The particles were assumed to be airborne, corn-type with a diameter of 87 μm. The gravity force of the particle is neglected to reduce the computing time. Simulation of these light particles also allows them to be transported to the entire building without deposition.

In the numerical simulation, a non-uniform grid system was used. Since the Reynolds number is 38,000, the expected Kolmogorov scale is about 10^{-4}. Therefore, ideally, the smallest grid size should be 0.01 m, and the required total grid number about 10^{6}, which would require more than a month of computing time on a fast workstation. To save computing time, the current study applied a coarse grid system to demonstrate that LES is capable of doing the study. Therefore, the smallest non-dimensional grid size was chosen as 0.05, and the total grid number was 110,000. The time step size was 0.02 seconds.

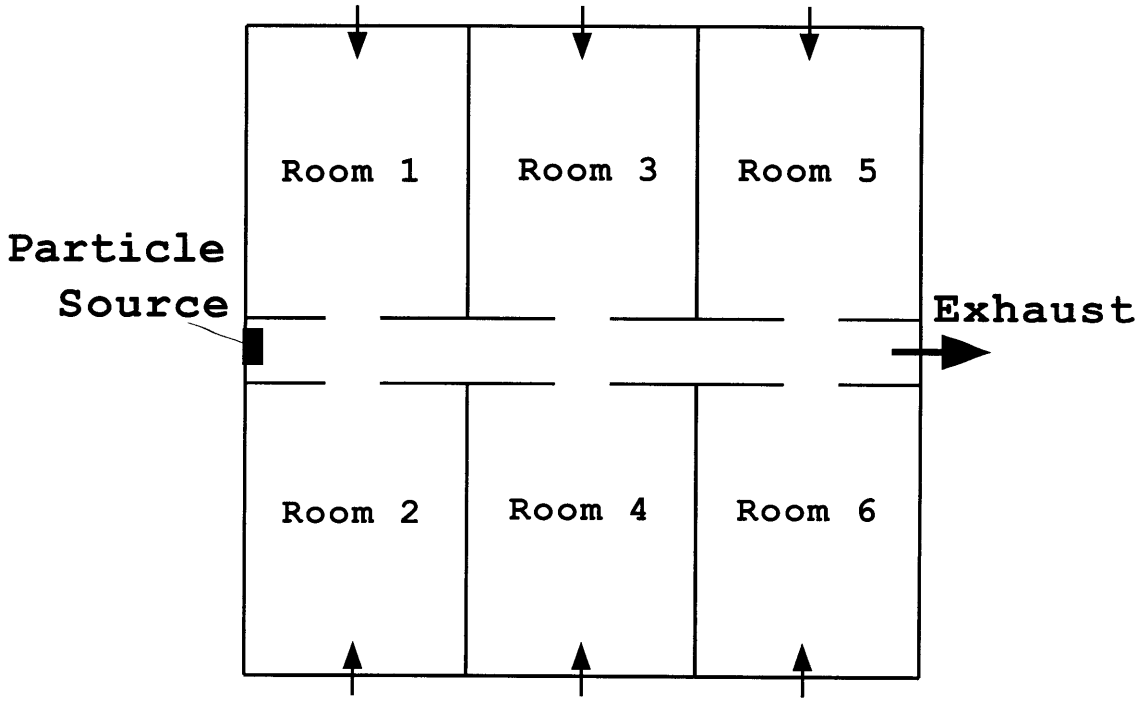

Figure 6.5 *Plan of a six-room building used for the particle transport study.*

One thousand corn-type particles were injected into the corridor at the same time. They were dispersed into different rooms with time, and some of them were removed through the exhaust. Figure 6.6 shows the trajectories of the particles after 1 and 4 minutes respectively. Figure 6.7 shows the number of particles accumulated in each room and corridor with time. It was found that most particles were contained in the corridor, Room 1 and Room 2. Since all the particles were injected at the same time, the instantaneous flow field (Figure 6.8) had a significant impact on the particle dispersion and distribution in space. Therefore, the numbers of particles dispersed into Room 1 and 2, Room 3 and 4, and Room 5 and 6 were not equal even though the rooms were placed symmetrically and the injection position was central. It is expected that if the particles are injected constantly from the source, the numbers of particles in each pair of symmetric rooms will be equal.

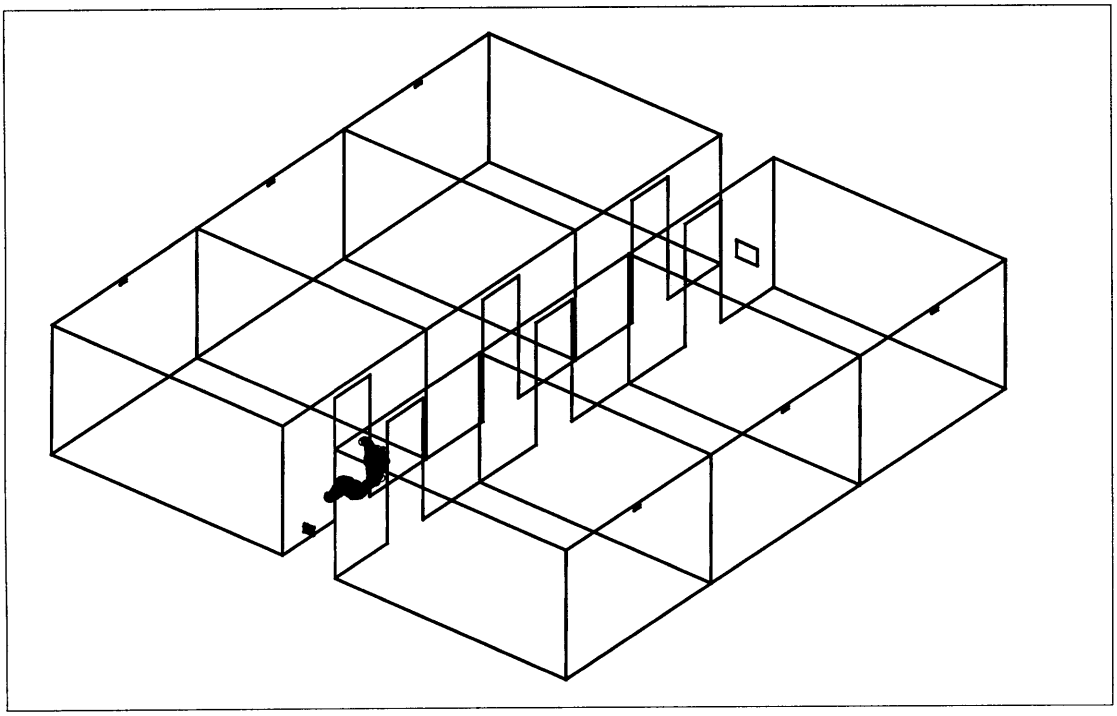

(a) t = 1 minute

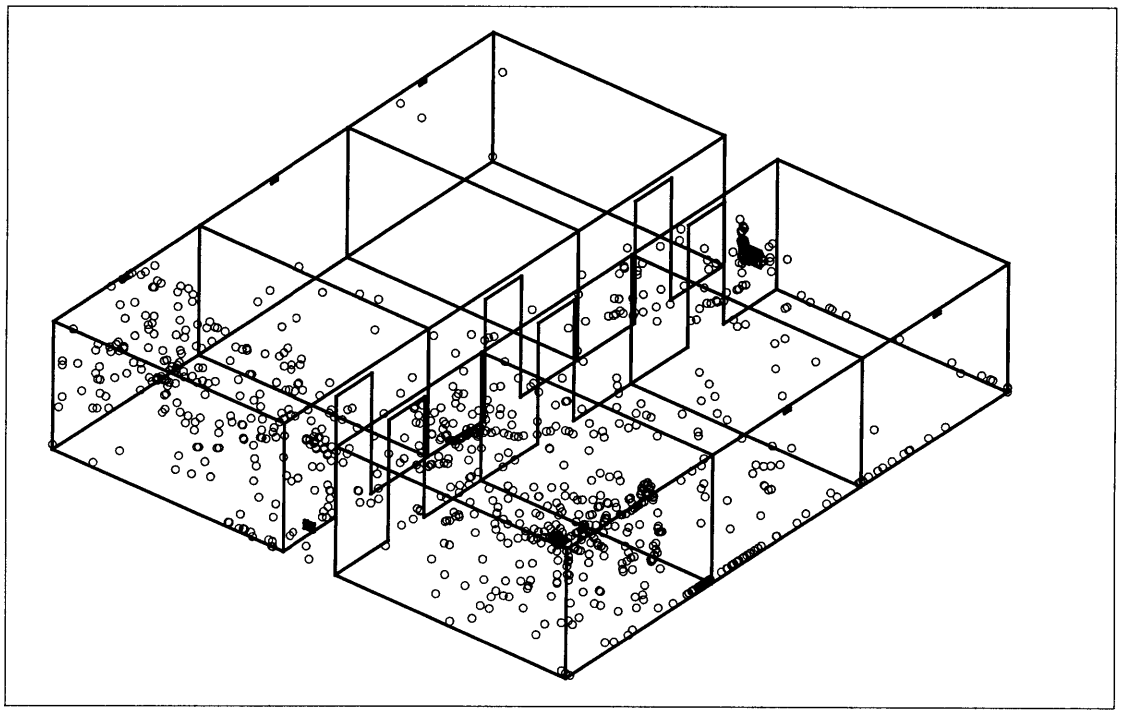

(b) t = 4 minutes

Figure 6.6 *Trajectories of 1,000 particles at different times.*

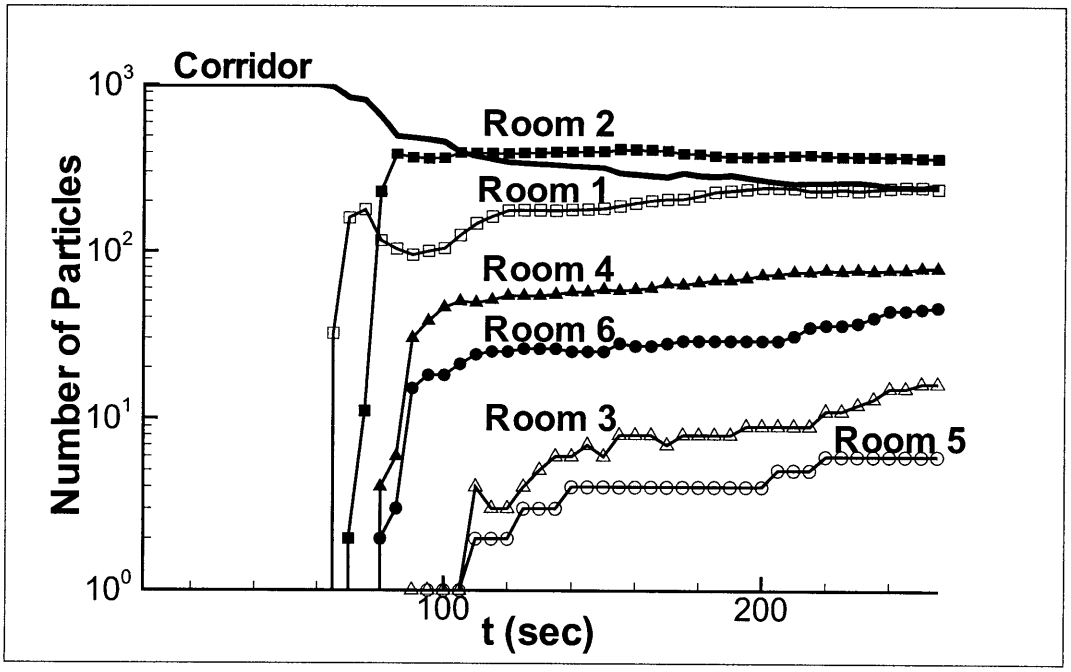

Figure 6.7 *Number of particles accumulated in each room and corridor with time.*

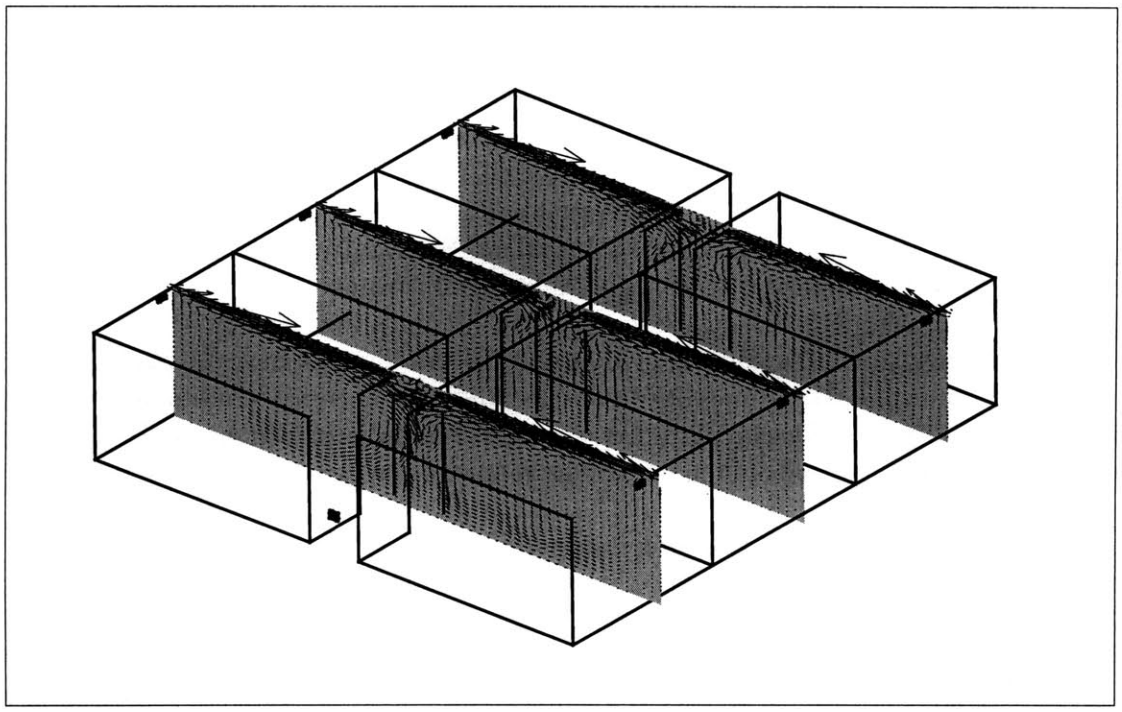

(a) across inlets

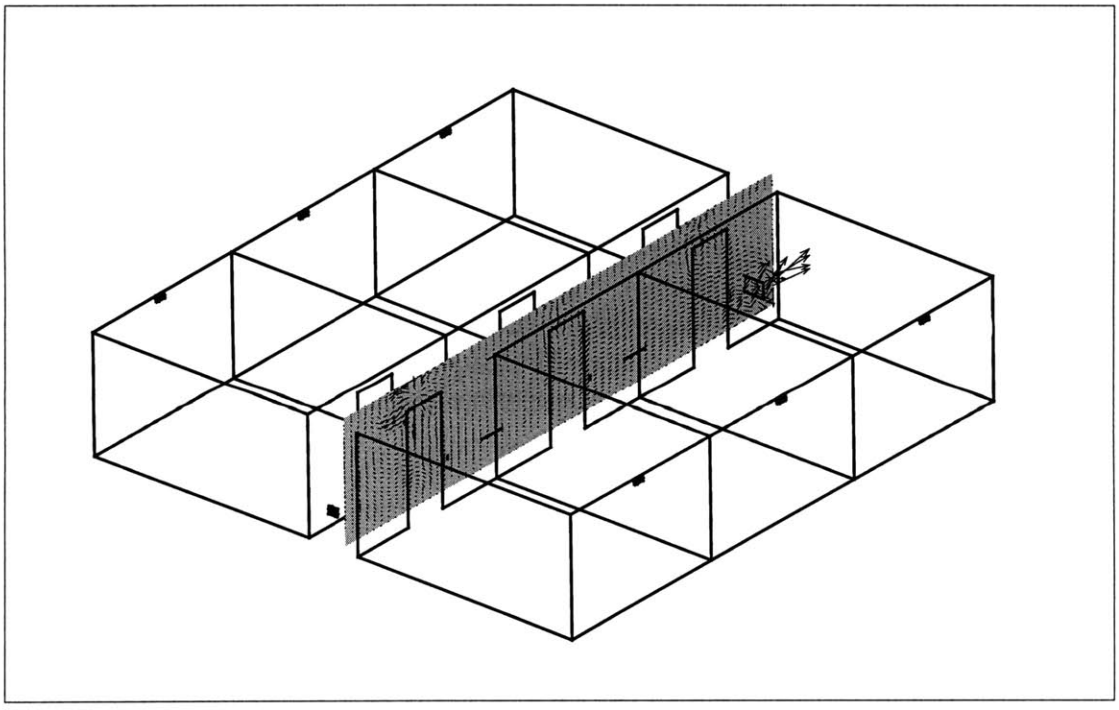

(b) across outlet (mid-section of the corridor)

Figure 6.8 *Instantaneous velocity fields at t = 0 (All sections are shown in gray color).*

6.6 Conclusions

Indoor airborne particles have a significant influence on human health and indoor air quality. To understand the particle trajectory in buildings, it is necessary to learn the characteristics of both airflow and particles.

Most airflow in and around buildings is turbulent. Study of particle motion in turbulent airflow requires an instantaneous airflow field, which cannot be provided with a time-averaged numerical method, such as steady RANS modeling. Therefore, in addition to RANS modeling, stochastic models with empirical coefficients have to be employed to produce instantaneous flow properties. However, these models may lead to some accuracy problems. LES, which always performs transient simulations, can be used to simulate particle movement directly with the implementation of a Lagrangian particle model.

The motion of three different types of solid particles in a decaying, homogeneous, isotropic, turbulent airflow was calculated. By comparing the computed results with the previous experimental and theoretical studies, the present method was found to be a successful tool to predict the properties of particle motion with regard to the second-order statistics, such as the mean-square displacement and turbulent intensity. The particle model with LES was further applied successfully to investigate particle dispersion in a six-room office building with a pollutant source in the corridor. It was found that the positions of the ventilation system and the geometry layout inside a building affect airflow distributions, and thus have impacts on the particle dispersion in the building. Furthermore, the location of the pollutant source determined how particles were transported inside the building. The study showed that the developed LES program with the implementation of the Lagrangian particle model is a suitable numerical tool to study particulate dispersion and transport in buildings.

Chapter 7

Conclusions and Recommendations

This chapter summarizes the results and conclusions obtained from the study. Some limitations of the current work and future perspectives for natural ventilation studies are also discussed.

The objective of this thesis work was to study natural ventilation in buildings with LES. The objective was achieved by applying LES models and other methods to study natural ventilation and analyze the characteristics of turbulent flow in natural ventilation. LES was also successfully applied to study of particle transport in buildings.

The major conclusions from the study are summarized as follows.

7.1 Characteristics of Turbulent Flows in Natural Ventilation

Using experimental, numerical and analytical methods, the characteristics of turbulent flow in natural ventilation, such as velocity, temperature, pressure, and energy spectrum, were investigated. For wind-driven natural ventilation, both cross and single-sided ventilation types were studied. A buoyancy-driven natural ventilation case with single-sided ventilation and one opening was also studied.

7.1.1 Velocity distributions and ventilation rate

Wind-driven ventilation

For cross ventilation with large openings on both the windward and leeward walls of a building the wind can easily travel through the building without generating major low-speed regions, and the airflows outside and inside of the building are therefore highly turbulent. For single-sided ventilation, however, major recirculation and low-speed regions are generated inside a building. In this case the airflows involve highly turbulent flow around the building and laminar flow inside the building, and the turbulent and laminar flows interact strongly at the opening. Therefore, the airflow motions in cross ventilation are much stronger than those in single-sided ventilation and the ventilation rate is also much higher.

In the single-sided ventilation cases, the overall air velocity inside a building varies significantly with wind direction. The air velocity inside a building with one opening in a windward wall could be smaller than for a leeward wall opening, and therefore, the ventilation rate in the windward case would be lower than that in the leeward case. Whether this situation occurs is determined by outdoor airflow distributions and the opening size, type and location.

For single-sided ventilation, a mean flow field, which can be obtained by RANS modeling or LES, may not allow designers to correctly evaluate the ventilation effectiveness of their design. This is because the averaging procedure of calculating the airflow significantly cancels out the instantaneous air exchange between indoor and outdoor air. This procedure leads to lower predicted ventilation rate and air change effectiveness than is predicted by instantaneous methods or measured in practice. Therefore, the instantaneous flow field is important for the study of wind-driven, single-sided ventilation.

Buoyancy-driven ventilation

In buoyancy-driven single-sided ventilation cases, high-speed regions were found to be in the top and bottom of the room. At intermediate heights, the air speeds were very low.

7.1.2 Temperature distributions

In the buoyancy-driven, single-sided ventilation case, the air temperature increases with height within the room. The temperature profile, which depends on the interior layout, the opening size, type and location, and the temperature difference between indoor and outdoor air, is hard to predict using an empirical model. The commonly used linear assumption about the temperature profile may not be correct. In the current investigation, the linear assumption was not made and the largest temperature stratification was found at intermediate heights.

7.1.3 Pressure distributions

For wind-driven, single-sided natural ventilation, the mean pressure difference across the opening is much less than the fluctuating pressure close to the opening. Therefore, the fluctuating flow fields play an important role in determining the airflow across the opening.

For buoyancy-driven, single-sided natural ventilation, the magnitude of the fluctuating pressures close to the openings is much smaller than the mean pressure difference across the opening. Therefore, mean flow fields play an important role in determining the airflow motion across the opening.

7.1.4 Energy spectral distributions

The study of energy spectra helps to reveal the impacts of turbulence on thermal comfort, an important factor to evaluate natural ventilation performance.

For wind-driven airflows, the energy spectra of the velocity contain a wide range of eddy sizes from 0.1 Hz to 100 Hz. However, for the buoyancy-driven airflows, the spectral curve contains eddies from 0.01 Hz to 1 Hz. Furthermore, the peak energy of the wind-driven airflows is about 1 Hz, which is an order of magnitude higher than that in the buoyancy-driven cases. This suggests that the wind-driven airflows contain a large range of eddies

from high-frequency small eddies to low-frequency large eddies. For buoyancy-driven airflows, most energy is contained in low-frequency large eddies. Therefore, the airflow fluctuates more strongly in a wind-driven case than in a buoyancy-driven case.

In wind-driven cases, most of the energy is contained in high-frequency regions for the outdoor airflows due to highly turbulent patterns. For indoor airflow, if the airflow is still highly turbulent, which might occur in a cross ventilation case, most of the energy is still contained in the high-frequency regions. However, in the low-velocity and recirculation regions, which are characteristic of single-sided ventilation cases, the airflow does not vary significantly with time, and most energy is contained in low-frequency regions.

In buoyancy-driven natural ventilation cases, most of the energy is contained in low-frequency regions for both indoor and outdoor airflows because the flows do not vary significantly with time. However, local disturbances, such as a sharp edge, could shift the energy to high-frequency regions.

7.2 Methods to Study Natural Ventilation

The current investigation uses mainly LES to study natural ventilation. Several other methods, which include full-scale and wind-tunnel measurements, an empirical method, and RANS modeling, were also used for a comparison, and the pros and cons of those methods are summarized here.

7.2.1 LES

LES can give accurate results for complex meteorological and geometrical conditions. LES can provide detailed flow field information to investigate the mechanism of natural ventilation, but it is computationally intensively.

Accuracy

Experimental data from a natural ventilation study were used to validate two subgrid-scale models of LES, the SS model and the FDS model. The following conclusions were obtained.

Both the SS and FDS models can provide accurate flow results for natural ventilation with highly turbulent flows, such as those found in wind-driven, cross-flow ventilation. In these highly turbulent flows with a high Reynolds number, most energy is contained in large eddies. The large eddies therefore play a more important role than small eddies. Since both models can directly solve the large-eddy motions and can model the dissipative nature of turbulence, both of them work well for these cases.

The SS model has difficulty in predicting single-sided ventilation driven by wind or buoyancy forces. The FDS model can still give accurate results in these cases. This is because in most single-sided ventilation cases, airflows are partially turbulent and partially

laminar and walls have a significant impact on the airflow motions. Since the model coefficient of the SS model is a constant and does not vary with flow type, it cannot predict laminar flows, such as the airflows near the walls. The FDS model can give reasonable results because its model coefficient is a function of the flow type. The coefficient becomes zero in the laminar regions, which correctly represents the physics of flow motions. Therefore, the FDS model is a suitable tool to study single-sided natural ventilation driven by wind or buoyancy forces.

Simulation of complex situations

A study of natural ventilation needs to take into account many phenomena and criteria, such as the wind force and/or buoyancy force, incoming wind velocity with respect to direction and magnitude, building shape and adjacent condition, and opening size, type and location, among others. LES can take into account all of these factors.

One special feature of LES should be noted. Natural wind direction varies over time, which are not easily dealt with by other methods except for full-scale measurement, can be handled by LES. LES can also simulate the changes due to adjusting inflow boundary conditions, and its results are accurate in terms of wind-pressure difference across buildings, eddy size behind buildings, and wind speed distributions.

Detailed airflow information

LES can provide three-dimensional, time-dependent airflow fields, including parameters such as air velocity, temperature, pressure and concentration distributions. This information can be used to estimate thermal comfort effects and evaluate indoor air quality risks, which are important factors to consider when designing natural ventilation.

LES provides instantaneous flow fields, which makes possible investigation of the mechanism of natural ventilation. First, as mentioned in Section 7.1.1, the instantaneous flow field is crucial in correctly determining the ventilation rate and air change effectiveness for wind-driven, single-sided ventilation. Second, since ventilation through building openings is driven by pressure forces, the instantaneous flow fields can be used to determine whether the mean pressure difference across the opening or the fluctuating pressure at the opening is more important to the airflow motion. Third, the instantaneous flow fields can be used for energy spectra analysis to reveal the impacts of turbulence on thermal comfort.

Computing time

LES has been applied to study natural ventilation in buildings. However, it requires large amount of computing time. For example, one week of computer time is required on a fast workstation to study natural ventilation in a simply shaped building and more than a month of computing time is required to study natural ventilation in multiple buildings. Therefore, when studying natural ventilation in multi-buildings, the current study separated the indoor

and outdoor calculations to save computing time, and the airflow fields surrounding the investigated buildings were examined to ensure that the separation could still generate correct ventilation information.

Since the SS model of LES is much simpler than the FDS model, the SS model requires 20% less computing time than the FDS model. Therefore, to save computing time, the SS model should be used to solve highly turbulent flows, such as wind-driven cross-flow natural ventilation.

7.2.2 Other methods to study natural ventilation

Full-scale experimental method

A full-scale facility used for natural ventilation studies can provide reliable airflow information. However, there are several difficulties associated with this approach.

First, full-scale experiments are expensive due to time and equipment costs. For example, in a buoyancy-driven case, a long time is required to obtain steady flow conditions. Expensive measuring equipment, such as anemometers and a tracer-gas analyzer, needs to be used to measure the distributions of air temperature and speed and ventilation rate.

Second, it is difficult to control the environment in a full-scale measurement. For wind-driven natural ventilation, the impacts of the wind speed and direction variations are coupled, and it is hard to differentiate the individual impacts on the measured results. For buoyancy-driven natural ventilation, it is hard to find a completely windless situation in nature. Although an artificial "outdoor" environment can be produced in a large laboratory as described in Section 3.2, the control of this "outdoor" environment is difficult due to impacts from the real outdoor weather on the enclosure of the laboratory.

Third, the information obtained is limited, and some measured data may not be correct due to facility limitations. For example, it is difficult to measure low air velocities with a common anemometer and some measuring equipment may disturb flow fields and produce incorrect data.

Finally, some modified methods have to be developed to provide correct airflow information due to facility limitations. In the experiment described in Section 3.2, since the "outdoor" space was limited and the airflow distributions inside the room were not uniform, a modified constant injection method had to be developed to correctly predict the ventilation rate.

Wind-tunnel experimental method

Wind-tunnel tests are often used to study natural ventilation driven by wind forces. Since wind tunnels have difficulties simulating Grashof number by similarity theory, the impact of buoyancy is neglected. Several other difficulties are commonly encountered. First, although the mean flow characteristics can be adequately modeled in a wind tunnel, the fluctuating components of the flow characteristics, such as the directional variation of an incoming wind, are difficult to reproduce in a traditional wind tunnel. Therefore, the data obtained from a wind tunnel measurement may lead to significant errors. Second, it is difficult to measure some of the fluctuating velocities inside a building model even if sophisticated equipment, such as Laser Doppler Anemometer (LDA), is available. This problem arises in recirculation and low-speed areas where seeding particles do not adequately penetrate, even over long measurement times. Again, this can lead to inaccuracies in the measurements of fluctuating velocities and energy spectral distributions.

Empirical methods

Although it is very easy to use an empirical model, the model provides very limited information. Furthermore, the predicted results, such as ventilation rate, may have significant inaccuracies due to the simplifications required for application of these methods.

For cross ventilation, if the building shape is very simple, the two openings are identical, and there are no surrounding buildings around the building model, an empirical model can give an accurate prediction of the ventilation rate. However, in real building design, where surrounding buildings and topography may affect wind flow and the openings are not simple, the empirical model may not give reasonable results.

For single-sided ventilation, there are also no concrete and reliable empirical models available. In wind-driven cases, the wind direction has a major impact on ventilation rates and indoor air velocity distributions. In buoyancy-driven cases, the indoor temperature profiles must be known to accurately calculate the ventilation rate.

Steady RANS modeling

Steady RANS modeling was adopted in the current study and unsteady RANS modeling is not used due to its accuracy problems and long computing time requirements compared to steady RANS modeling.

Steady RANS modeling requires less computing time than LES and it can provide detailed airflow field distributions. However, RANS modeling has several difficulties. First, RANS modeling is not as accurate as LES. Both the literature and current studies show that RANS modeling cannot correctly predict airflow around buildings, such as the separation region on the roof and the recirculation region behind a building. Second, natural wind varies in both speed and direction, so that a transient simulation is required to fully describe the

incoming wind. Steady RANS modeling cannot do this type of simulation. Third, the turbulence characterization provided by steady RANS modeling is limited, and it cannot be used to study wind-driven, single-sided ventilation. Such a ventilation study requires instantaneous flow fields to determine the ventilation rate and air change effectiveness to investigate the impacts of the pressure on ventilation rate and to do energy spectral analysis.

Table 7.1 compares the natural ventilation study methods in terms of costs, available airflow information and accuracy.

Table 7.1 *Comparison among different methods used to study natural ventilation.*

	Computing costs	Labor costs	Equipment cost	Flow information	Accuracy
Experiment	N/A	High	High	Limited	Reliable
Empirical	N/A	Low	N/A	Little	Low
RANS	Low	Moderate	Low	Moderate	Moderate
LES	High	Moderate	Moderate	Detailed	High

7.3 Further Applications of Large Eddy Simulation

The results show that LES is a suitable tool to study natural ventilation. In a naturally ventilated building, outside pollutants can be introduced to a building and indoor pollutants can be removed to the outside. To design an effective natural ventilation system to provide good indoor air quality, a Lagrangian particle model has been implemented to LES to study particle dispersion in buildings. Study of particle motion in turbulent airflow requires an instantaneous airflow field, which cannot be provided by a time-averaged numerical method, such as RANS modeling. LES, which always performs transient simulations, can be used to simulate particle movement directly with the implementation of the Lagrangian particle model. The study showed that this approach provides a suitable numerical tool to study particulate dispersion and transportation in buildings.

7.4 Limitations of the Current Work

Apart from the limitations that were discussed elsewhere, the current work is still subject to further improvements or extensions in several areas.

(1) For wind-driven natural ventilation, both cross ventilation and single-sided ventilation were studied. For buoyancy-driven natural ventilation, however, only single-sided ventilation was investigated. Buoyancy-driven cross ventilation and wind/buoyancy-driven ventilation with multiple openings should be studied analytically, experimentally and numerically.

(2) The experiments conducted in the current study focus on the separate impacts of wind and buoyancy forces. It is necessary to extend this study to the combined effects of wind and buoyancy forces, a common scenario in natural ventilation cases so that the interactions between wind and buoyancy forces can be analyzed and their combined impacts on natural ventilation can be investigated.

(3) The investigation of energy spectra was limited to the two experiments conducted in a wind tunnel and an environmental chamber. Whether this study represents a real situation should be further tested by detailed measurements of real winds around and inside a building.

(4) The particle size studied in the current investigation was over 10 μm. For a smaller particle, whose size ranges from 1 μm to 10 μm, the particle model needs to be adjusted to consider some extra forces. Furthermore, the small eddies in airflows may play an important role in determining the particle motion and the subgrid-scale model used to simulate those small eddies may need to be modified in order to correctly account for the impacts of the small eddies on the particle motion.

7.5 Future Perspectives

Natural ventilation is one of the most attractive options to reduce energy consumption while ensuring good indoor air quality and acceptable comfort. Through the current investigation, LES has been proved to be a suitable tool to study natural ventilation by providing accurate and detailed airflow information. Several related areas that need further investigation are:

(1) Currently, applying LES to study natural ventilation demands extensive computing time. The reduction of the computing time while preserving the model's accuracy should be further investigated. One possible approach is the development of parallel algorithms.

(2) Most designers use empirical models for their designs for simplicity even though those methods are not generally applicable. LES can be used to develop empirical models by providing suitable empirical coefficients under different ventilation situations.

(3) The study of energy spectra helps to reveal the impacts of turbulence on thermal comfort of human beings, which is an important factor in evaluating natural ventilation performance. On-site measurements of natural and mechanical winds in terms of turbulence statistical characteristics, such as energy spectra, and their impacts on thermal comfort should be investigated. LES can be used to generate these turbulence characteristics and evaluate whether a ventilation design can provide a comfortable indoor environment.

References

Abadie M., Limam K., Allard F., 2001, Indoor particle pollution: effect of wall textures on particle deposition. Building and Environment 36: 821-827.

AIJ Working Group, 1994, Numerical prediction of wind loading on buildings and structures. division for wind loading design, Architecture Institute of Japan. (in Japanese)

Akselvoll, K., and Moin, P., 1995, Large eddy simulation of turbulent confined coannular jets and turbulent flow over a backward facing step. Report TF-63, Thermosciences Division, Department of Mechanical Engineering, Stanford University.

Allard, F., 1998, *Natural ventilation in buildings: a design handbook.* James & James, London, UK.

Allocca, C., 2001, *Single-sided natural ventilation: design analysis and general guidelines.* Master thesis, Department of mechanical engineering, Massachusetts Institute of Technology.

Armenio, V., Piomelli, U., and Fiorotto, V., 1999, Effect of the subgrid scales on particle motion. Phys. Fluids, 11: 3030-3042.

ASHRAE Fundamentals Handbook, 1997. American Society of Heating, Refrigerating and Air-Conditioning Engineers, Inc., Atlanta, GA.

ASHRAE Standard 62, 1999, *Ventilation for acceptable indoor air quality.* American Society of Heating, Refrigerating and Air-Conditioning Engineers, Inc., Atlanta, GA.

Awbi, H.B., 1996, Air movement in naturally-ventilated buildings. Department of Construction Management & Engineering, The University of Reading, WREC.

Axley, J. and Persily, A., 1988, Integral mass balances and pulse injection tracer techniques. Report NISTIR 88-3855. U.S. Department of Commerce. National Institute of Standards and Technology.

Aynsley, R.M., Melbourn, W., and Vickery, B.J., 1977, *Architectural aerodynamics.* Applied Science Publishers, London, UK.

Belermont, A., Desjonqueres, P., and Gouesbet, G., 1990, Particle Lagrangian simulation in turbulent flows. Int. J. Multiphase Flow 16: 19-34.

Brager, G.S. and De Dear, R., 2000, A standard for natural ventilation. ASHRAE J. 42 (10): 21-28.

Brown, G.Z., Dekay, M., and Barbhaya, D., 2000, *Sun, Wind, and Light: Architectural design strategies*. 2nd edition, John Wiley & Sons.

BS 5925, 1980, *Code of practice for design of buildings: ventilation principles and designing for natural ventilation*. British Standards Institution, London.

Busch, J.F., 1992, A Tale of Two Populations: Thermal Comfort in Air-conditioned and Naturally Ventilated Offices in Thailand. Energy and Buildings 18 (3-4): 235-49.

Cheesewright, R., King, K.J., and Ziai, S., 1986, Experimental data for the validation of computer codes for the prediction of two-dimensional buoyant cavity flows. HTD-60, ASME winter Annual Meeting, Anaheim, December, 1986, 75.

Chen, Q., 1996, Prediction of room air motion by Reynolds-stress models. Building and Environment. 31 (3): 233-244.

Choiniere, Y. and Munroe, J.A., 1994, A wind-tunnel study of wind direction effects on air-flow patterns in naturally ventilated swine buildings. Canadian Agricultural Engineering, 36 (2): 93-101.

Clarke, J., 1993, *Manual of ESP*. Glasgow, UK: University of Strathclyde.

Crowe, C., Sommerfeld, M., and Tsuji, Y., 1998, *Multiphase flows with droplets and particles.* CRC Press, Boca Raton, Florida.

Dagliesh, W.A., 1975, Comparison of model/full-scale wind pressures on high-rise building. J. Ind. Aerodyn. 1: 55-66.

Dascalaki, E., Santamouris, M., Argiriou, A., Helmis, C., Asimakopoulos, D., Papadopoulos, K. and Soilemes, A., 1995, Predicting single sided natural ventilation rates in buildings. Solar Energy 55 (5): 327-341.

Dascalaki, E., and Santamouris, M., 1995, *Manual of PASSPORT-AIR, Final Report.* PASCOOL Research Program, European Commission, D.G. XII.

Dascalaki, E., Santamouris, M., Argiriou, A., Helmis, C., Asimakopoulos, D., Papadopoulos, K. and Soilemes, A., 1996, On the combination of air velocity and flow measurements in single sided natural ventilation configurations, Energy and Buildings 24: 155-165.

Davidson, L. and Nielsen, P., 1996, Large eddy simulation of the flow in a three-dimensional ventilation room, 5th International Conference on Air Distribution in Rooms, ROOMVENT'96, July 17-19, 1996.

Deardorff, J. W. 1970. A numerical study of three-dimensional turbulent channel flow at large Reynolds numbers. Journal of Fluid Mechanics, 41: 453-480.

De Gidds, W. and Phaff, H., 1982, Ventilation rates and energy consumption due to open windows, Air Infiltration Review, 4 (1): 4-5.

Dols, W.S., Walton, G.N., and Denton, K.R., 2000, *CONTAMW 1.0 User Manual: Multizone Airflow and Contaminant Transport Analysis Software*, NISTIR 6476.

Doughty M.J., Blades, K.A., Ibrahim, N., 2002, Assessment of the number of eye symptoms and the impact of some confounding variables for office staff in non-air-conditioned buildings, Ophthalmic and Physiological Optics, 22 (2): 143-155.

Durbin, P.A., 1995, Separated flow computations with the k-ε-υ model. AIAA Journal, 33 (4): 659-664.

Ellis, R., 1994, The British office market – the workplace of tomorrow; the consumer's view.

Emmerich S. J., and McGrattan, K. B., 1998, Application of a large eddy simulation model to study room airflow. ASHRAE Transactions, 104: 1128-1140.

Etheridge, D., 2000, Unsteady flow effects due to fluctuating wind pressures in natural ventilation design – instantaneous flow rates. Building and Environment, 35: 321-337.

Etheridge, D. and Nolan, J., 1979, Ventilation measurements at model scale in a turbulent flow. Building and Environment, 14: 53-64

Etheridge, D. and Sandberg, M., 1996, *Building ventilation: theory and measurement*, John Wiley and Sons, Chichester; New York.

Fernandez, J.E. and Bailey, B.J., 1992, Measurement and prediction of greenhouse ventilation rates, Agricultural and Forest Meteorology, 58 (3-4): 229-245.

Feustel, H.E., Allard, F., Dorer, V.B., Garcia Rodriguez E., Herrlin, M.K., Mingsheng, L., Phaff, H.C., Utsumi, Y., and Yoshino, H., 1990, Fundamentals of the multizone air flow model – COMIS." Tech. Note AIVC 29. Coventry, UK: International Energy Agency, Air Infiltration and Ventilation Centre.

Fisk, W.J., 2000, Health and productivity gains from better indoor environments and their relationship with building energy efficiency. Annu. Review Energy Environ. 25: 537-66.

Flourentzou, F., Van der Maas, J., and Roulet, C.A., 1998, Natural ventilation for passive cooling: measurement of discharge coefficients. Energy and Buildings 27: 283-292.

Germano, M., Piomelli, U., Moin, P., and Cabot, W. H. 1991. A dynamic subgrid-scale eddy viscosity model. Physics of Fluids, A 3 (7): 1760-1765.

Ghosal, S., Lund, T., Moin, P. and Akselvoll, K., 1995, A dynamic localization model for large-eddy simulation of turbulent flows, J. Fluid Mech. 286: 229.

Gianluca, I., and Durbin, P., 2000, Unsteady 3D RANS simulations using the v^2-f model. Annual Research Briefs, Center for Turbulence Research, Stanford University, USA.

Godish, T., and Spengler, J.D., 1996, Relationship between ventilation and indoor air quality: a review. Indoor Air, 6: 135-145.

Haan Jr., F. L., Kareem, A., and Szewczyk, A. A. 1998. The effects of turbulence on the pressure distribution around a rectangular prism. Journal of Wind Engineering and Industrial Aerodynamics, 77 & 78: 381-392.

Haghighat, F., Rao, J., and Fazio, P., 1991, The influence of turbulent wind on air change rates — a modeling approach. Building and Environment, 26 (2): 95-109.

Hanzawa, H., Melikow, A.K., and Fanger, P.O., 1987, Airflow characteristics in the occupied zone of ventilated spaces, ASHRAE Transactions, 93 (1): 524-539.

Harlow F. H. and Welch, J. E. 1965. Numerical calculation of time-dependent viscous incompressible flow. Physics of Fluids, 8 (12): 2182-2189.

Haymore, C. and Odom, R., 1993, Economic effects of poor IAQ, EPA Journal, 19(4): 28-29

Hinds, W.C., 1982, *Aerosol technology : properties, behaviour, and measurement of airborne particles*, John Wiley and Sons, Inc.

Hjelmfelt, A.T. and Mockros, L.F., 1966, Motion of discrete particles in a turbulent fluid, App. Sci. Res., 16:149.

Holub, R.F., Raes, F., Van Dingenen, R., and Vanmarcke, H., 1988, Deposition of aerosols and unattached radon daughters in different chambers: theory and experiment. Radiation Protection Dosimetry, 24: 217-220.

Jaakkola, J.J.K., Miettinen, P., 1995, Type of ventilation system in office buildings and sick building syndrome. American Journal of Epidemiology, 141 (8): 755-765.

Jiang, Y. and Chen, Q., 2001, Study of natural ventilation in buildings by large eddy simulation. J. Wind Eng. Ind. Aerodyn. 89 (13): 1155-1178.

Katayama, T. Tsutsumi, J. Ishii, A. Nishida, M. and Hashida, M., 1989, Observations of heat flux in an urban area with a large pond by kytoons. J. Wind Eng. Ind. Aerodyn. 32: 41-50.

Katayama T., Tsutsumi J., and Ishii A., 1992, Full-scale measurements and wind tunnel tests on cross-ventilation. J. Wind Eng. Ind. Aerodyn. 41-44: 2553-2562.

Kato S, Murakami S., Mochida, A, Akabyashi S., Tominaga Y. 1992. Velocity-pressure field of cross ventilation with open windows analyzed by wind-tunnel and numerical-simulation. J. Wind Eng. Ind. Aerodyn., 44 (1-3): 2575-2586.

Lakehal, D., and Rodi, W. 1997. Calculation of the flow past a surface-mounted cube with two-layer turbulence models. J. Wind Eng. Ind. Aerodyn., 67 & 68: 65-78.

Leonard, A., 1974, Energy cascade in large eddy simulation of turbulent fluid flows. Adv. In Geophys., 18A: 237-248.

Li, Q. S., and Melbourne, W. H., 1995, An experimental investigation of the effects of free-stream turbulence on streamwise surface pressures in separated and reattaching flows. J. Wind Eng. Ind. Aerodyn., 54 & 55: 313-323.

Lilly, D.K., 1992, A proposed modification of Germano subgrid-scale closure method, Phys. Fluids A 4 (3): 633-635.

Lilly, D. K. 1965. On the computational stability of numerical solutions of time-dependent non-linear geophysical fluid dynamics problems. Monthly Weather Review, 93 (1): 11-26.

Lin, J.X., Surry, D., and Tieleman, H.W., 1995, The distribution of pressure near roof corners of flat roof low buildings. J. Wind Eng. Ind. Aerodyn., 56: 235-265.

Linden, P.F., Lane-Serff, G.F., Smeed, D.A., 1990, Emptying filling boxes, the fluid mechanics of natural ventilation. J. Fluid Mech., 212: 309-335.

Lubcke, H., Schmidt, St., Rung, T., and Thiele, F., 2001, Comparison of LES and RANS in bluff-body flows, J. Wind Eng. Ind. Aerodyn., 89: 1471-1485.

Martinuzzi, R. and Tropea, C., 1993, The flow around a surface-mounted prismatic obstacle placed in a fully developed channel flow. J. Fluid Eng. 115: 85-92.

Melaragno, M., 1982, *Wind in architectural and environmental design*, Van Nostrand Reinhold, New York.

Meneveau, C., Lund, T. and Cabot, W., 1996, A Lagrangian Dynamic Sub-grid scale Model of Turbulence. J. Fluid Mech., 315: 353.

Metais, O., and Lesieur, M., 1992. Spectral large-eddy simulation of isotropic and stably stratified turbulence. J. of Fluid Mech., 239: 157-194.

Mittal R. and Moin P., 1997, Suitability of upwind-biased finite-difference schemes for large eddy simulation of turbulent flows. AIAA Journal, 35 (8): 1415-1417.

Murakami, S. 1998. Overview of turbulence models applied in CWE-1997. J. Wind Eng. Ind. Aerodyn., 74-76: 1-24.

Murakami, S., and Mochida A. 1995. On turbulent vortex shedding flow past 2D square cylinder predicted by CFD. J. Wind Eng. Ind. Aerodyn., 54 & 55: 191-211.

Murakami, S., Kato, S., Akabayashi, S., Mizutani, K. and Kim, Y.D., 1991, Wind tunnel test on velocity-pressure field of cross-ventilation with open windows, ASHRAE Transactions 97 part 1: 525-538.

Muzi, G., Abbritti, G., Accattoli, M.P., dell'Omo, M. 1998, Prevalence of irritative symptoms in a nonproblem air-conditioned office building, International Archives of Occupational and Environmental Health, 71 (6): 372-378.

Nakamura, Y. 1993. Bluff-body aerodynamics and turbulence. J. Wind Eng. Ind. Aerodyn., 49: 65-78.

Nakamura, Y., and Ozono, S., 1987, The effect of turbulence on a separated and reattaching flow. J. Fluid Mech., 178: 477-490.

Nielsen, P.V., Restivo, A. and Whitelaw, J.H., 1978, The velocity characteristics of ventilated room. J. Fluids Eng. 100: 291-298.

NIOSH (National Institute for Occupational Safety and Health), 1999, http://www.cdc.gov/niosh/nrinev.html

Nitta K., 1990/1991, Cross-correlation between speed and direction of urban wind fluctuation. Energy and Buildings 15-16: 357-363.

Odar, F. and Hamilton, W.S., 1964, Forces on a sphere accelerating in a viscous fluid. J. Fluid Mech., 18: 302.

Ohba, M., Irie K., and Kurabuchi, T., 2001, Study on airflow characteristics inside and outside a cross-ventilation model, and ventilation flow rates using wind tunnel experiments, J. Wind Eng. Ind. Aerodyn. 89: 1513-1524.

Okuyanna, K., Kousaka, Y., Yamamoto, S., and Hosokaya, T., 1986, Particle loss of aerosols in a stirred tank, J. Chemical Eng. Japan, 10(2): 142-147.

Olson, D., L. Glicksman, and H. Ferm., 1990, Steady-state natural convection in empty and partitioned enclosures at high Rayleigh numbers. Transactions of the American Society of Mechanical Engineers, Journal of Heat Transfer, 112: 640-647.

Petersen, R.L., 1987, Wind tunnel investigation of the effect of platform-type structures on dispersion of effluents from short stacks. J. Air Pollution Control Association, 36: 1347-1352.

Piomelli, U., Zang T. A., Speziale, C. G., and Hussaini, M. Y. 1990. On the large-eddy simulation of transitional wall-bounded flows. Phys. Fluids, A 2 (2): 257-265.

Piomelli, U., Ferziger, J.H., and Moin, P., 1988, Models for large eddy simulations of turbulent channel flows including transpiration. Report TF-32, Thermosciences Division, Dept. of Mech. Engr., Stanford Unversity.

Piomelli, U., Ferziger, J.H., 1987, Model consistency in large eddy simulation of turbulent channel flows. Phys. Fluids 31 (7): 1884-1891.

Reynolds, A. J. 1974, *Turbulent Flows in Engineering.* John Wiley & Sons, New York.

Riley, J.J., and Patterson, G.S., 1974, Diffusion experiments with numerically integrated isotropic turbulence. Phys. Fluids 17(2): 292-297.

Rodi, W., Ferziger, J.H., Breuer, M., and Pourquié, M. 1997. Status of large eddy simulation: results of a workshop. Journal of Fluids Engineering, Vol. 119, pp. 248-262.

Santamouris, M., 1992, Natural convection heat and mass transfer through large openings. Internal report, PASCAL Research Program, European Commission DGX11.

Scotti, A., and Piomelli, U., 2002, Turbulence models in pulsating flows. AIAA Journal, 40(3): 537-544.

Shah, K. B. 1998. *Large eddy simulations of flow past a cubic obstacle.* Ph.D. dissertation, Department of Mechanical Engineering, Stanford University.

Shur, M., Spalart, P.R., Strelets, M., and Travin, A., 1996, Navier-Stokes simulationof shedding turbulent flow past a circular cylinder and a cylinder with a backward splitter plate. Third European CFD Conference, Paris.

Singh, J., 2001, Occupational exposure to moulds in buildings, Indoor and Built Environment, 10 (3-4): 172-178.

Smagorinsky, J., 1963, General circulation experiments with the primitive equations. I. The basic experiment. Monthly Weather Review, 91: 99-164.

Snyder, W.H. and Lumley, J.L., 1971, Some measurements of particle velocity autocorrelation functions in a turbulent flow. J. Fluid Mech. 48 (1): 41-71.

Spalart, P. R., 2000, Strategies for turbulence modelling and simulations. International journal of heat and fluid flow, 21 (3): 252-263.

Spalart, P.R., and Allmaras, S.R., 1994, A one-equation turbulence model for aerodynamic flows. La Recherche Aerospatiale, 1 (1): 5-21.

Stone, H. L. 1968, Iterative solution of implicit approximations of multidimensional partial differential equations. SIAM Journal of Numerical Analysis, 5 (3): 530-558.

Surry, D., 1989, Pressure measurements on the Texas Tech Building-II: Wind tunnel measurements and comparison with full scale. Proceedings of the 8th colloquium on Industrial Aerodynamics, Aachen, West Germany, September 4-7, 1989; 25-35.

Tieleman, H.W., Akins, R.E., and Sparks, P.R., 1981, A comparison of wind-tunnel and full-scale wind pressure measurements on low-rise structures. J. Wind Eng. Ind. Aerodyn., 8: 3-19.

Travin, A., Shur, M., Strelets, M., and Spalart, P., 2000, Detached-eddy simulations past a circular cylinder. Flow, Turbulence and Combustion, 63 (1-4): 293-313.

U.S. Department of Energy, 1997, Scenarios of U.S. Carbon Reductions. Prepared for the Office of Energy Efficiency and Renewable Energy, September 22, 1997.

U.S. Energy Information Administration, 1995, *State energy data report 1995*, Tables 3-7.

Vickery, B.J., and Karakatsanis, C., 1987, External pressure distributions and induced internal ventilation flow in low-rise industrial and domestic structures. ASHRAE Transactions 98(2): 2198-2213.

Walton, G., 1988, AIRNET, A computer program for building airflow network modeling. MISTR 89-4072, National Institute of Standards and Technology.

Werner, H., and Wengle, H., 1991, Large eddy simulation of turbulent flow over and around a cube in a plate channel. Eighth Symposium on Turbulent Shear Flows, Technical University Munich, September 9-11, 1991, pp. 155-168.

William, H., 1992, *Numerical recipes in FORTRAN : the art of scientific computing.* Cambridge University Press, Cambridge [England] ; New York, NY, USA.

Wolkoff, P., 1999, How to measure and evaluate volatile organic compound emissions from building products. A perspective. Science of the Total Environment, 227 (2-3): 197-213.

Zhang, W., and Chen, Q., 2000, Large eddy simulation of indoor airflow with a filtered dynamic subgrid scale model. Inter. J. of Heat and Mass Transfer, 43 (17): 3219-3231.

Zhao, R. and Xia, Y., 1998, Effective Non-isothermal and Intermittent Air Movement on Human Thermal Responses. Proc. of Roomvent 98, Stockholm. 351-57.

Zhao, Z., 1997, *Wind flow characteristics and their effects on low-rise buildings.* Ph.D. dissertation, Department of civil engineering, Texas Tech University.

Zweers, T., Preller, L., Brunekreef, B., and Boleij, J.S.M., 1992, Health and indoor climate complaints of 2043 office workers in 61 buildings in the Netherlands. Indoor Air, 2: 127-136.

Appendix A

Calculation of airflow rate into a building with integration method

In CFD, the airflow rate into or out of a building can be calculated by integrating the normal velocity at all openings of a building if the flow is incompressible, which is true in most natural ventilation studies. Based on a mass balance of the airflow within a building, there will be as much fluid leaving the building in some regions, as there will be fluid entering the building. Therefore, the total amount of airflow out of a building equals to the total amount of airflow into a building, $Q_{in} = Q_{out}$ by assuming a constant air density. In the integration calculation, if an absolute value sign is put around the velocity normal to the openings, we can get

$$Q_{in} + Q_{out} = \sum_{j=ja}^{jb} \sum_{k=ka}^{kb} \left| U_{j,k} \right| \Delta y_j \Delta z_k \tag{A.1}$$

$$Q_{in} = \frac{1}{2} \sum_{j=ja}^{jb} \sum_{k=ka}^{kb} \left| U_{j,k} \right| \Delta y_j \Delta z_k \tag{A.2}$$

where $[\Delta y_{ja}, \Delta y_{ja+1}, \ldots, \Delta y_{jb}]$ and $[\Delta z_{ka}, \Delta z_{ka+1}, \ldots, \Delta z_{kb}]$ are the grid sizes in the y and z directions within the opening, respectively, and $U_{j,k}$ is the mean normal velocity corresponding to the grid $(\Delta y_j, \Delta z_k)$ at the openings. Please note that the above calculation extracts $U_{j,k}$ from a mean velocity field. The computed airflow rate into a building can be called the mean ventilation rate, Q_{mean}. Since LES can provide the instantaneous velocity field at each time step, the airflow rate into a building can be also calculated by cumulating and averaging the instantaneous ventilation rate over a time period of T. The instantaneous ventilation rate at time t^n is defined as

$$q^n = \frac{1}{2} \sum_{j=ja}^{jb} \sum_{k=ka}^{kb} \left| u_{j,k}^n \right| \Delta y_j \Delta z_k \tag{A.3}$$

The cumulative and average instantaneous (CAI) ventilation rate over a time period of T, $Q_{ins,T}$, is defined as

$$Q_{ins,T} = \frac{\frac{1}{2} \sum_{n=1}^{N} \left(\sum_{j=ja}^{jb} \sum_{k=ka}^{kb} \left| u_{j,k}^n \right| \Delta y_j \Delta z_k \right) \cdot \Delta t^n}{\sum_{n=1}^{N} \Delta t^n}$$

$$= \frac{\frac{1}{2}\sum_{j=ja}^{jb}\sum_{k=ka}^{kb}\sum_{n=1}^{N}\left|u_{j,k}^{n}\Delta t^{n}\right|\Delta y_j \Delta z_k}{T} \tag{A.4}$$

where $u_{j,k}^{n}$ is the instantaneous normal velocity at the opening at time t^n, Δt^n is the time step size; $(t^{n+1}-t^n)$, and N is the total number of the time steps, during which $Q_{ins,T}$ is calculated. Since the relationship between the mean velocity, $U_{j,k}$, and the instantaneous velocity $u_{j,k}$, is

$$U_{j,k} = \frac{\sum_{n=1}^{N} u_{j,k}^{n} \cdot \Delta t^{n}}{T} \tag{A.5}$$

Eq. (A.2) can be derived as

$$Q_{mean} = \frac{\frac{1}{2}\sum_{j=ja}^{jb}\sum_{k=ka}^{kb}\left|\sum_{n=1}^{N} u_{j,k}^{n}\Delta t^{n}\right|\Delta y_j \Delta z_k}{T} \tag{A.6}$$

Since

$$\sum_{n=1}^{N}\left|u_{j,k}^{n}\Delta t^{n}\right| \geq \left|\sum_{n=1}^{N} u_{j,k}^{n}\Delta t^{n}\right| \qquad (\Delta t^{n} > 0) \tag{A.7}$$

We can get

$$\frac{\frac{1}{2}\sum_{j=ja}^{jb}\sum_{k=ka}^{kb}\sum_{n=1}^{N}\left|u_{j,k}^{n}\Delta t^{n}\right|\Delta y_j \Delta z_k}{T} \geq \frac{\frac{1}{2}\sum_{j=ja}^{jb}\sum_{k=ka}^{kb}\left|\sum_{n=1}^{N} u_{j,k}^{n}\Delta t^{n}\right|\Delta y_j \Delta z_k}{T}$$

$$Q_{ins,T} \geq Q_{mean} \tag{A.8}$$

In Eq. (A.7), only when $u_{j,k}^{n}$ keeps the same sign over the whole time period of T, which means that $u_{j,k}^{n}$ should be always negative or positive, $Q_{ins,T}$ can equal Q_{mean}. This situation may happen in a simple cross-ventilation case, such as a tunnel type. However, for complex ventilation type, such as single-sided ventilation, the instantaneous velocity at an opening changes direction all the time due to strong interactions between turbulent and laminar flows.